In-Vivo Feasibility Study and Developments for Cardiac Arrhythmia Ablation using Scanned Carbon Ions

In-Vivo Machbarkeitsstudie und Entwicklungen zur Behandlung von Herzrhythmusstörungen mit gescannten Kohlenstoffionen
Vom Fachbereich Physik der Technischen Universität Darmstadt
zur Erlangung des Grades eines Doktors der Naturwissenschaften (Dr. rer. nat.)
genehmigte Dissertation von M.Sc. Anna Vera Eichhorn aus Heppenheim
Tag der Einreichung: 20.12.2016, Tag der Prüfung: 06.02.2017
Darmstadt 2017 — D 17

1. Gutachten: Prof. Dr. Marco Durante
2. Gutachten: Prof. Dr. Thomas Aumann

TECHNISCHE
UNIVERSITÄT
DARMSTADT

In-Vivo Feasibility Study and Developments for Cardiac Arrhythmia Ablation using Scanned Carbon Ions
In-Vivo Machbarkeitsstudie und Entwicklungen zur Behandlung von Herzrhythmusstörungen mit gescannten Kohlenstoffionen

Genehmigte Dissertation von M.Sc. Anna Vera Eichhorn aus Heppenheim

1. Gutachten: Prof. Dr. Marco Durante
2. Gutachten: Prof. Dr. Thomas Aumann

Tag der Einreichung: 20.12.2016
Tag der Prüfung: 06.02.2017

Darmstadt — D 17

Bitte zitieren Sie dieses Dokument als:
URN: urn:nbn:de:tuda-tuprints-60822
URL: http://tuprints.ulb.tu-darmstadt.de/6082

Abstract

Cardiac arrhythmia are a widely spread global health burden. Currently, the standard treatments are anti-arrhythmic drugs and radio-frequency catheter ablation. The latter is an invasive procedure with varying success rates. For the treatment of atrial fibrillation, the most common cardiac disorder, repetitions of the procedure are necessary in a significant amount of cases. Furthermore, radio-frequency catheter ablation is particularly ineffective against ventricular tachycardia, another common cardiac arrhythmia, as the thickness of the myocardium in the ventricles often prevents transmural scar formation. A promising alternative is the use of radiotherapy. During the last few years, several studies showed that ionizing radiation can alter electrical pathways within the heart muscle. The use of carbon ions instead of photons should offer significant dosimetric advantages, due to the inverse depth-dose profile. Accurate treatment of moving targets with scanned ion beams remains challenging and is still not a clinical routine. For the high doses needed for cardiac targets, careful consideration of motion mitigation is necessary.

In this work, the first in-vivo feasibility study in pigs using scanned carbon ions to induce targeted changes of the cardiac electrophysiology is presented. The focus lies on the 4D treatment planning approach and the motion mitigation techniques applied in the study. In total, 15 pigs were irradiated in three different target groups: atrioventricular node (AVN), pulmonary vein, and left ventricular freewall. In each group, a specific heart structure was ablated using single-fraction doses of 40 Gy, except for the AVN group were doses of 25, 40 and 55 Gy were applied to carry out a dose escalation study.

Electrophysiological changes were found in all target groups after the experiment. Nevertheless, due to heterogeneous results among animals of the same dose group, the success rate was not satisfactory. A critical discussion of 4D treatment planning and delivery revealed the accuracy of deformable image registration as a potential source of error. The influence on 4D dose calculation could potentially explain limited results in single pigs and dose groups. Furthermore, a scan path optimization was developed to reduce treatment time while improving interplay reduction compared to methods employed in the in-vivo study. This optimization could also facilitate single-fraction and hypofractionated treatments in clinical radiotherapy. The scan path optimization and a dynamic intensity control were implemented in a simulation software which was subsequently validated and tested at the Heidelberg Ion-Beam Therapy Center (Germany).

This work summarizes the current status of ion beam cardiac ablations and identifies and realizes possible improvements for future in-vivo studies in support of a fast clinical transition of catheter-free ablation using carbon ions.

Zusammenfassung

Herzrhythmusstörungen sind ein weitverbreitetes Gesundheitsproblem mit steigender Inzidenz aufgrund einer alternden Bevölkerung. Die heutige Standardbehandlung für Herzrhythmusstörungen ist, neben der Gabe von Medikamenten, die Katheterablation. Die Erfolgsaussichten der Katheterablation sind vor allem abhängig von der behandelten Herzregion. Während Behandlungen von Vorhofflimmern, der am häufigsten auftretenden Herzrhythmusstörung, zwar oftmals wiederholt werden müssen, bietet die Katheterablation dennoch eine Möglichkeit der Heilung für einen großen Teil der Patienten. Deutlich schlechter hingegen sind die Aussichten für die Behandlung von ventrikulären Tachykardien, da aufgrund der Dicke des Myokards oftmals keine transmurale Narbe induziert werden kann.

Eine vielversprechende Alternative ist die strahlentherapeutische Behandlung. In den letzten Jahren wurden mehrere Studien publiziert, welche die Möglichkeit erforschen, die elektrische Leitfähigkeit des Myokards durch Bestrahlung zu verändern. Hierfür sollte die Verwendung von Kohlenstoffionen durch das inverse Tiefendosisprofil große Vorteile bieten. Allerdings stellt die konforme Bestrahlung von bewegten Zielen immer noch eine große Herausforderung dar und wird noch nicht in der klinischen Routine angewendet. Besonders für die hohen Dosen, die für die Behandlung von Herzrhythmusstörungen nötig sind, ist eine sorgfältige Bewegungskompensation notwendig. In dieser Arbeit wird die erste in-vivo Studie zur Behandlung von Herzrhythmusstörungen mit gescannten Kohlenstoffionen, mit dem Ziel elektrophysiologische Änderungen im Herzmuskel zu induzieren, vorgestellt. Eine Gesamtübersicht über das Experiment und die Ergebnisse befinden sich in dieser Arbeit, der Fokus liegt hierbei auf der durchgeführten 4D Bestrahlungsplanung und Bewegungskompensation. Insgesamt wurden 15 Schweine bestrahlt, welche in drei Gruppen aufgeteilt wurden: atrioventrikulärer Knoten (AVN), freie Wand des linken Ventrikels und obere Pulmonalvene. In allen Gruppen wurden Tiere mit Einzelfraktionsdosen von 40 Gy bestrahlt, mit Ausnahme der AVN Gruppe. In dieser Gruppe wurden Tiere mit Dosen von 25, 40 und 55 Gy behandelt.

In der vorgestellten Studie war eine erfolgreiche Bestrahlungen für alle Ziele möglich. Dennoch waren die Ergebnisse auch für gleiche Dosisgruppen heterogen und dementsprechend die Erfolgsraten nicht zufriedenstellend. Eine kritische Diskussion über 4D Bestrahlungsplanung und Strahlapplikation zeigte auf, dass die deformierbare Bildregistrierung eine potentielle Fehlerquelle darstellt. Dies könnte potentielle Einschränkungen der Ergebnisse erklären. Zusätzlich wurden nach dem Experiment verschiedene Strategien entwickelt, um die Behandlungszeiten von bewegten, einzelfraktionierten oder hypofraktionierten Plänen zu verringern und zusätzlich Interplay Effekte besser zu kompensieren als die in der präsentierten Studie verwendeten Methoden. Diese Ansätze wurden in einem Simulationstool implementiert und anschließend an der Heidelberger Ionenstrahl-Therapie Anlage getestet und validiert.

Diese Arbeit fasst den aktuellen Stand der katheterlosen Ablation mit Kohlenstoffionen zusammen und stellt nötige Änderungen für zukünftige in-vivo Studien in diesem Feld dar. Dies unterstützt eine zügige Translation der katheterlosen Ablation mit Kohlenstoffionen in die klinische Routine.

Contents

List of Abbreviations

4DCT	time-resolved computed tomography
4DMRI	time-resolved magnetic resonance imaging
AF	atrial fibrillation
AVN	atrioventricular node
BD	base damage
BDS	beam delivery sequence
CA	catheter ablation
CBCT	cone-beam CT
CDSB	clustered double strand break
CNAO	Centro Nazionale di Adroterapia Oncologica
CT	computed tomography
DAQ	data acquisition system
DIC	dynamic intensity control
DIR	deformable image registration
DIRQA	deformable image registration quality assurance
DKFZ	German Cancer Research Center
DNA	deoxyribonucleic acid
DSB	double strand break
DSim	beam delivery sequence simulation
ECG	electrocardiogram
GSI	GSI Helmholtz Center for Heavy Ion Research
GUI	graphical user interface
HZDR	Helmholtzcenter Dresden Rossendorf
HIMAC	Heavy Ion Medical Accelerator in Chiba
HIT	Heidelberg Ion-Beam Therapy Center
HU	Hounsfield unit
IBF	’Interfakultäre Biomedizinische Forschungseinrichtung’
ICD	implantable cardioverter-defibrillator
ICE	inverse consistency error
ICRU	International Commission on Radiation Units and Measurements
IES	iso-energy slice
IMRT	intensity-modulated radiation therapy
IMPT	intensity-modulated particle therapy
ITV	internal target volume
LBL	Lawrence Berkeley Laboratory
LCA	left coronary artery
LEM	local effect model
LET	linear energy transfer
LV	left ventricular free-wall
Mayo	Mayo Clinics
MIT	Marburg Ion-Beam Therapy Center
MRI	magnetic resonance imaging
NIRS	National Institute of Radiological Sciences
OAR	organ at risk
PA	pulmonary artery
PET	positron emmission tomography
PRSC	perfect rescanning
PSI	Paul Scherrer Institut
PTV	planning target volume
QA	quality assurance
RBE	relative biological effectiveness
RCA	right coronary artery

RiFi	ripple-filter
RMSE	root-mean-square error
ROI	region of interest
RTOG	Radiation Therapy Oncology Group
SBRT	stereotactic body radiation therapy
SFUD	single field uniform dose
SOBP	spread-out Bragg peak
SPO	scan path optimization
SPV	superior pulmonary vein
SSB	single strand break
SVC	superior vena cava
TCS	treatment control system
TPS	treatment planning system
TSP	traveling salesman problem
TV	target volume
UCHD	University Clinic Heidelberg
VMAT	volumetric arc therapy
VT	ventricular tachycardia

Motivation

Cardiac arrhythmia are a widely spread global health burden caused by changes in the hearts' conduction system. Due to an aging society the incidence of cardiac disorders has been increasing over the last decades. Depending on the type of cardiac arrhythmia, the severity of the symptoms as well as the influence on the patients' quality of life varies significantly. Transient, mild forms can be harmless, not requiring any treatment; but others advanced forms are associated with severe complications, such as stroke, heart failure or even sudden cardiac death. To make matters worse, specific cardiac disorders, as for instance, atrial fibrillation (AF), can occur silently [Cam10] and are often only diagnosed after severe complications. The incidence of AF, the most common cardiac disorder, is 2 % in the European population, causing about 5 % of the diagnosed strokes every year [Rah14]. Due to the strong association with age, it is expected that between 14 to 17 million people will suffer from AF in 2030 [ZB14].

Another common type of cardiac arrhythmia is ventricular tachycardia (VT), which is estimated to be responsible for 50 % to 85 % of all sudden cardiac deaths. Thus, VT poses a serious health problem with higher absolute mortality than breast, lung and colon cancer combined [Hai16].

Treatment modalities for AF and, especially, VT are limited. Even though anti-arrhythmic drugs can reduce the symptoms, they often induce severe side effects and thus, patient compliance is low. To cure cardiac arrhythmia, it is necessary to alter electrical pathways in the heart muscle, which is currently only possible using catheter ablation. However, the procedure is time intensive, invasive and can have major complications. In addition, due to a poor general state of health, a lot of patients cannot undergo the procedure. Furthermore, a recurrence of the symptoms cannot be avoided in a large number of patients [Cap05, Cap10, Wis12, Din14].

Even though catheter ablation could cure some patients suffering from VT, in many cases the thickness of the ventricular wall does not allow a successful treatment, as the penetration depth is not sufficient to create transmural scar tissue. To overcome this limitation epi- as well as endo-cardial catheter ablation has to be combined. Although this method shows increased success rates, the number of clinics providing this approach is extremely limited. Furthermore, the risk of complications is increased [Di 12]. Therefore the standard treatment for VT is still the implantable cardioverter-defibrillator (ICD) [Bah13] interrupting acute VT episodes and, hence, reducing the risk of sudden cardiac death. However, an ICD does not actually cure VT and the defibrillation shocks are painful, can cause anxiety and occur unnecessarily in 30 % of the cases [Bor13].

A promising non-invasive alternative to treat cardiac arrhythmia is radiotherapy. In 2010, Sharma et al. showed that photon irradiation has the potential to alter electrical pathways in the myocardium [Sha10b]. Inspired by the success of carbon ion cancer therapy, especially for the treatment of deep seated tumors and those close to critical structures, Bert at al. proposed the use of carbon ions to ablate cardiac structures in 2012 [Ber12]. The inverse depth-dose profile of carbon ions combined with the precision of the raster scanning system [Hab93] provides a highly conformal therapy with a superior depth dose distribution compared to conventional photon treatments. A feasibility study irradiating Langendorff-perfused pig hearts was carried out in 2013 [Leh15, Pra15] and a first carbon ion treatment planning study was published in 2014 [Con14, Con16]. Both indicate that carbon ions are an excellent choice for catheter-free ablation. Motivated by the previous findings, a first in-vivo experiment was designed to demonstrate the feasibility of ablating cardiac structures using carbon ions.

Scope of this Work

This thesis presents the results of the first in-vivo feasibility study using carbon ions to ablate cardiac structures, carried out at GSI Helmholtz Center for Heavy Ion Research (GSI) in July 2014 by an interdisciplinary team. My work during this time focused on the 4D treatment planning process and the applied motion mitigation techniques necessary to allow a successful irradiation of beating hearts.

A combination of rescanning and repeated breath-holds was chosen to overcome cardiac and respiratory motion, respectively. Three different anatomical sites were targeted in single-fraction treatments to investigate the feasibility of carbon ions for catheter-free ablations. The aim was to ablate the atrioventricular node (AVN) and the superior pulmonary vein (SPV) as well as to induce a homogeneous and transmural scar in the left ventricular free-wall (LV).

The study results were heterogeneous and motivated a critical investigation of the deformable image registration (DIR) used for 4D treatment planning, dose calculation and dose reconstruction of the feasibility study. Different alternative approaches to improve the DIR results were tested. Finally, the influence of the registration uncertainties on the dose distributions was determined to estimate the impact of the registration problems on the study outcome.

To support the transition of catheter-free ablation into clinical routine, new approaches are warranted to reduce the treatment time; both to ensure the patients' comfort and to increase the number of patients treated yearly. The main factor influencing treatment duration is the maximum beam intensity which still permits accurate detection of small beam spots. The irradiation times for the catheter-free ablation with a traditional rescanning scheme were lengthy. Thus, a new rescanning scheme was applied with the drawback of a slightly reduced target coverage. Within this work a scan path optimization was developed to overcome these limitations. For this approach as well as for the dynamic intensity control (DIC) implemented at Heidelberg Ion-Beam Therapy Center (HIT), the influence on 4D dose distributions due to the changes in the beam delivery sequence (BDS) were investigated. For realistic simulations a beam delivery sequence simulation (DSim) Software, capable of calculating BDSs for different accelerator settings and the scan path optimization (SPO) algorithm, was validated. In addition, the developed strategies can also be applied to hypofractionated or single-fraction treatments of cancerous disease using particles. Hence, the potential time saving is also determined for lung cancer patients.

The presented work is structured as follows. In Chapter 1, an overview of the underlying physical and radiobiological basics of radiotherapy is given. In addition, photon and particle therapy are compared, followed by a discussion about problems of motion in particle therapy and how to overcome interplay effects. The first chapter is closed with an overview of different types of cardiac arrhythmia and conventional and new treatment modalities. In Chapter 2, the in-vivo feasibility study of catheter free-ablation in pigs is described focusing on the treatment planning process. In Chapter 3 problems of the deformable image registration for the pig study are discussed including an estimate of the uncertainties of the study outcome. Finally, in Chapter 5 new techniques to decrease the treatment time of rescanned treatments with a high target dose are presented and their influence on 4D dose distributions is discussed. In Chapter 5 the results of this work are discussed and an outlook is given.

1 Scientific background

The following chapter gives an overview of the relevant physical processes involved in radiotherapy, explaining the concept and advantages of heavy ion therapy. Furthermore, this chapter provides background information for the understanding of the following chapters.

The chapter is separated into two sections. In the first part the physical, biological and technical background of particle therapy are explained, focusing on the advantages, the process of treatment planning and the influence of motion in particle therapy. The second part addresses the fundamentals of the heart conduction system and different kinds of cardiac arrhythmia, which are important for the understanding of Chapter 2. In addition, a short overview of already published data on using radiation to ablate cardiac structures is given.

1.1 Radiotherapy

The history of radiotherapy goes back to the discovery of the X-rays in 1895 by Wilhelm Conrad Roentgen [Rön95]. Only seven months after, first patients suffering from eczema and lupus were treated using X-rays. The first treatment of malignant tissues followed shortly afterwards. First targets were superficial tumors as the penetration depth of X-rays is limited [Con09].

Later on, in 1946, the use of protons was proposed due to the inverse depth-dose profile. Already in the 1950's first patients were treated [Wil46]. From there on, the development of photon and particle therapy continued in parallel. Over the next decades, the achievements of radiotherapy improved the survival of patients suffering from cancerous disease. A more detailed overview on the history and the development of both therapy alternatives follows in the next two sections.

1.1.1 Photon Therapy

The first attempts in radiotherapy used X-rays produced by an X-ray tube, which was positioned in close proximity to the patient. The number of cured patients was small and always connected with a high damage to the healthy tissue, as the available energies were too low to reach deep seated tumors without severely damaging the skin [Hel96]. In 1913 the heated X-ray tube was invented enabling external beam radiotherapy [Pat48].

As an alternative for deep seated tumors, brachytherapy was invented shortly after the discovery of the radioactive element radium. During the 1920's, brachytherapy was widely used to treat accessible tumors inside the body, for instance, ovarian cancer [Cur50].

After the 50 keV equipment was invented by Philipps it was possible to treat not only superficial tumors. The next big step forward in radiotherapy was the installation of the first machine using Cobalt-60 for photon production in 1948. With this machine it was possible to deposit a high dose (45 - 60 Gy) to deep seated tumors without violating organ at risk (OAR) limits due to the 1.2 MeV photon beams emitted by Cobalt-60. In the early 1950's, first linear accelerators became available, which could produce 6 - 20 MeV beams for deep seated lesions as well as electron beams for superficial lesions. Up to this time, all treatment planning was performed in 2D and in the 1970's treatment planning was improved by 2D simulators. A major step forward was achieved using computed tomographys (CTs) for a 3D treatment planning. Also the introduction of the multileaf collimator, which transformed the 2D external-beam radiotherapy to a 3D conformal therapy, was a big step towards modern radiotherapy. A detailed description of the multileaf collimator can be found in [Moh95].

In 1996, the development of intensity-modulated radiation therapy (IMRT), combined with the multileaf collimator, enabled inverse dose planning and dose sculpting around concave volumes. The development of radiotherapy continued with the introduction of stereotactic body radiation therapy (SBRT). The latest development in photon therapy is volumetric arc therapy (VMAT), which further improved the volume conformity. More detailed reviews targeting the history and developments of conventional radiotherapy can be found in [Tha12, Con09]

1.1.2 Particle Therapy

During the last decades, particle therapy has developed to a promising branch of radiotherapy. Particle therapy offers a highly conformal dose distribution within the targeted volume while depositing less dose in the surrounding healthy tissue compared to photon therapy. In Figure 1.1 a comparison of an IMRT and an intensity-modulated particle therapy (IMPT) dose distribution is shown, indicating the reduced dose to healthy tissue using particle therapy.

Robert R. Wilson was the first who proposed the use of an inverse depth-dose profile for an application in radiotherapy [Wil46]. Only a few years later, in the 1950's, the first patient treatments with proton beams were conducted at the Lawrence Berkeley Laboratory (LBL), USA. After the physical and biological properties of protons were investigated in several research projects, a proton trial was successfully carried

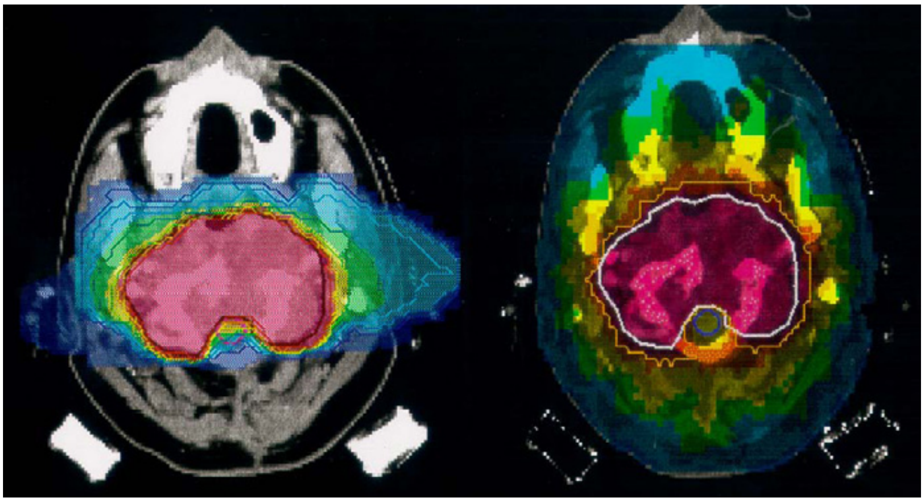

Figure 1.1.: Comparison of a photon and a carbon ion treatment plan for a skull tumor. To reach a conformal dose coverage intensity-modulated photon therapy needs 9 fields causing a dose bath in the healthy tissue. In contrast to this, carbon ion therapy significantly reduces the dose to normal tissue using only two fields [Ama05].

out. The first clinical proton facility started operation in 1990 at Loma Linda University Medical Center, USA. Soon after, several other centres were established. Today 60 proton centres are operating world wide and 29 additional ones are under construction [PTC].

In the 1970's, research on the use of heavier ions for particle therapy started at LBL. The idea behind this step was to benefit from an increased biological effectiveness of ions like helium and neon. After the treatment of 3000 patients at LBL, the therapy program was stopped in 1993 due to the shutdown of the accelerator. In 1994 the National Institute of Radiological Sciences, Chiba (Japan), started treating patients using similar techniques as previously used at LBL. At the same time, the Paul Scherrer Institut (PSI), Villigen (Switzerland), and the GSI Helmholtz Center for Heavy Ion Research (GSI), Darmstadt (Germany), investigated more advanced and conformal delivery systems for protons and carbon ions, respectively.

A pilot study using scanned carbon ions was carried out at GSI in collaboration with the German Cancer Research Center (DKFZ), the University Clinic Heidelberg (UCHD) and the Helmholtzcenter Dresden Rossendorf (HZDR) from 1997 to 2008. Over 440 patients, most of them suffering from tumors in the head and neck region or at the skull base, were treated during the study. For skull-based chordoma the 5 year survival rate could be increased from roughly 20 % using photons or 60 % using protons to almost 100 % using carbon ions. This success became possible by significantly increasing the median dose deposited in the tumor volume increased without increasing the damage to the healthy tissue [SE07]. The range of treated tumors was extended to prostate and spinal cord tumors within the pilot project. For treatment planning, an in-house treatment planning system was developed, which includes biological modeling for the increased relative biological effectiveness (RBE) of carbon ions. Clinical follow-up examinations showed high clinical success rates and low side effects. These findings enabled the construction and planning of several heavy ion centers following the basic concepts of the treatment room at GSI. The first clinical heavy ion center using scanned carbon ions, Heidelberg Ion-Beam Therapy Center (HIT), started operation in 2009. In the following years several other facilities either upgraded their system to scanned carbon ions or directly started operation using raster scanning. In Europe Centro Nazionale di Adroterapia Oncologica (CNAO) and Marburg Ion-Beam Therapy Center (MIT) started operation in 2011 and 2015, respectively, and MedAustron is planned to follow in 2016. Nowadays, 10 carbon ion facilities are running worldwide and over 70 proton facilities are in operation, under construction or in the planning state. For carbon ions as well as for protons the trend goes to the use of scanned particles and about 50 % of all facilities are already using this technique [PTC].

The following sections give a brief explanation of the physical, biological and technical basics of particle therapy. It starts with an introduction to the underlying physics, continues with an overview of radio-biology and ends with relevant technical knowledge on beam delivery, focusing on the active beam delivery system.

1.1.2.1 Physical Basics

The advantage of using charged particles in radiotherapy lies in the favorable depth-dose profile, the so-called Bragg Peak. A comparison of the depth-dose distributions of photons and carbon ions is given in Figure 1.2 showing the beneficial depth-dose profile of carbon ions.

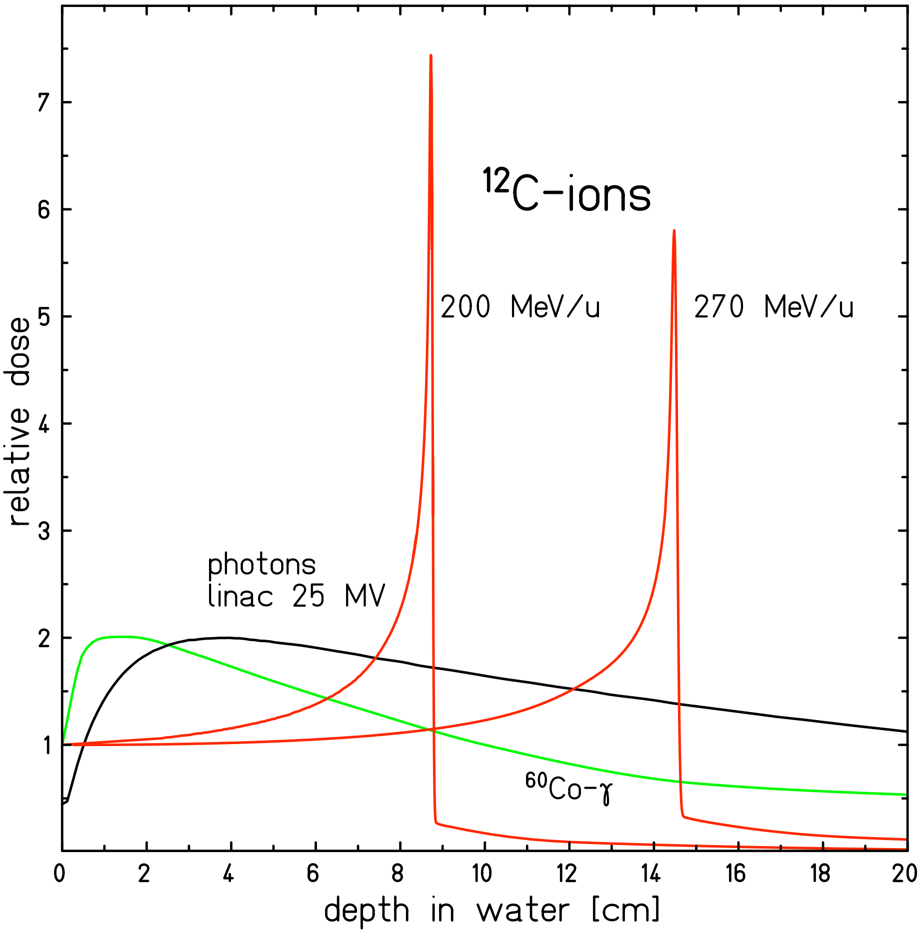

Figure 1.2.: Depth-dose profiles for photons and carbon ions at different energies in water. While the depth-dose curve of photons shows an exponential decay after penetrating a short distance through water (build-up effect), the deposited dose for carbon ions shows a sharp maximum at the penetration depth, which is determined by the initial beam energy. The reduced Bragg peak height at higher energies is caused by the increased energy straggling. The dose tail after the Bragg peak is caused by fragments created in nuclear reactions [Sch10].

Compared to photons, charged ions deposit a significantly lower amount of dose in the entrance channel and additionally a sharp dose fall-off a the end of their range allowing a successful sparing of healthy tissue.

Interactions of Ions with Matter

Two effects, not influencing the structure of the ion itself, are important for the interaction of ions with matter in particle therapy. They can either interact via elastic Coulomb scattering (nuclear stopping) or via inelastic collisions with target electrons (electronic stopping). For the particle energies used for radiotherapy the most likely effect for interactions is electronic stopping, causing ionization and excitation of target electrons. The stopping power is defined as

$$S = -\frac{dE}{dx}, \tag{1.1}$$

where dE is the energy loss over the length dx. For a description of the specific energy loss the Bethe-Bloch [Bet30] formula is used.

$$S = \frac{4\pi e^4 z^2 Z}{m_e c^2 \beta^2}\left[\ln\left(\frac{2\, m_e c^2 \beta^2}{I(1-\beta^2)}\right) - \beta^2 - \frac{C}{Z}\right]. \tag{1.2}$$

The quantities m_e and z represent the electron mass and the charge of the primary particle; z and Z are the nuclear charges of the projectile and the target, respectively; m_e and e are the rest mass and charge of the electron; $\beta = v/c$ is the velocity v of the incident particle normalized to the speed of light c. The parameter I denotes the average excitation and ionization potential of the absorber and has to be determined experimentally. For further details of the relativistic corrections the reader is referred to [Zie99]. A decreasing particle velocity yields an increasing stopping power. For non-relativistic incoming particles the energy loss is increasing with $1/v^2$ or $1/E$. The reason of this behavior is rather simple. Due to the lower velocity of the ion the interaction time increases, i.e the particle spends more time close to the electrons and thus the energy transfer increases. For a given velocity, the energy loss increases with increasing ion charge. Materials with a high electron density (high density, high atomic number) are characterized by a larger linear stopping power.

The Bethe-Bloch equation becomes inexact and eventually fails when the particle energy decreases below a certain threshold. In this region the charge exchange between the incoming particles and the absorber material cannot be neglected anymore. The parameter z has to be replaced by the effective charge z_{eff} which takes into account the charge changes through ionization and recombination. The effective charge z_{eff} can be calculated using Barkas' formula [Bar63].

Dose Definition

The absorbed dose D, an important quantity for radiotherapy, is given by the deposited energy dE per mass element dm:

$$D = \frac{dE}{dm} \quad [1Gy = 1\frac{J}{kg}]. \tag{1.3}$$

Range Straggling and Lateral Spreading

A Bragg curve depicts the energy loss of a charged particle over the thickness of the traversed absorber material. The energy of the incoming ion determines the range of the particle and at the end of the track sharp peak, the so-called Bragg peak, occurs. Due to statistical fluctuations the energy released by each ion varies slightly, causing a broadening of the Bragg peak. The equation

$$\frac{\sigma_R}{R} = \frac{1}{\sqrt{M}} f\left(\frac{E}{M\, c^2}\right) \tag{1.4}$$

describes the ratio of the energy straggling width σ_R and the mean particle range R. The function f depends on the absorber material while E and M denote the mass and the energy of the particle, respectively. The term $1/\sqrt{M}$ indicates that the range straggling is higher for lighter ions [Ros52].

Together with range straggling, also lateral spreading of a beam has to be taken into account for treatment planning. The lateral spreading is caused by elastic Coulomb interactions with the target nuclei and is higher for lighter particles. This process can be described by Moliere's theory [Mol48]. As a rough approximation it can be assumed that the effect is proportional to $\frac{Z_{\text{proj}}}{A_{\text{proj}}} \times v_{\text{proj}}$, where Z_{proj},A_{proj} and v_{proj} are the atomic number, the number of nucleons and the velocity of the projectile, respectively [Kra00a].

Nuclear Fragmentation

For an accurate description of the depth-dose profile, especially for the fragment tail after the Bragg Peak, nuclear fragmentation has to be taken into account. The probability of nuclear fragmentation is proportional to the penetration depth. In such a process both nuclei, the projectile as well as the target, can change their charge due to nucleon loss and thus secondary particles (fragments) are created. Nuclear fragmentation can be described as a two step process by the abrasion-ablation model of Serber [Ser47]. Figure 1.3 shows a schematic of the abrasion-ablation process. In the first step, called abrasion, the projectile and the target collide with a certain overlap. The nucleons in the overlapping region, typically called 'reaction zone', are abraded. The nucleons outside the reaction zone are almost unaffected by the collision, although the target and projectile fragments are now in a highly excited state. The nucleons involved in the collision are called 'fireball'. In a second step, called ablation, deexcitation processes in the target and the projectile cause evaporation of nucleons or nucleon clusters.

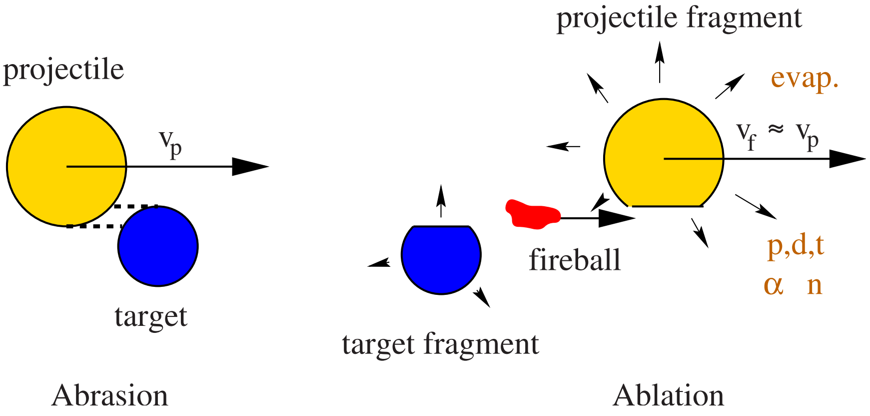

Figure 1.3.: Schematic of the abrasion-ablation model [Sch10]

Even though the cross sections for nuclear fragmentation are orders of magnitude smaller compared to Coulomb interactions, they cannot be neglected for particle therapy especially for larger penetration depths. For ions heavier than protons nuclear fragmentation, especially projectile fragmentation, contributes mainly to the dose tail after the Bragg peak. The contribution of target fragments is significantly smaller.

In ion beam therapy three different effects related to fragmentation are relevant [Sch10]:

- The amount of primary ions reaching the target volume decreases with increasing tumor depth, while the amount of low Z fragments is increasing.

- Light ions produced by fragmentation have almost the same momentum as the primary ions. As lighter particles have a higher range than the primary ions, fragmentation causes a dose tail behind the Bragg peak.

- Even if most fragments are produced in beam direction, their angular distribution adds to the lateral spread of the depth-dose distribution.

Track Structure

The energy loss of ions in the therapeutic energy range is mainly caused by ionization and excitation of the target material. The liberated electrons, called δ-electrons, undergo elastic and inelastic scattering processes, in which additional electrons can be created, depending on the initial energy. For δ-electrons with energies higher than 50 eV, ionization is the dominant process [Kra00a, Sch10].

The track structure is defined by the energy distribution of the δ-electrons. The energy distribution of the secondary electrons influences the radial dose profile of the track as well as the track diameter. As the momentum transfer is generally low and mainly in forward direction, most energy is deposited

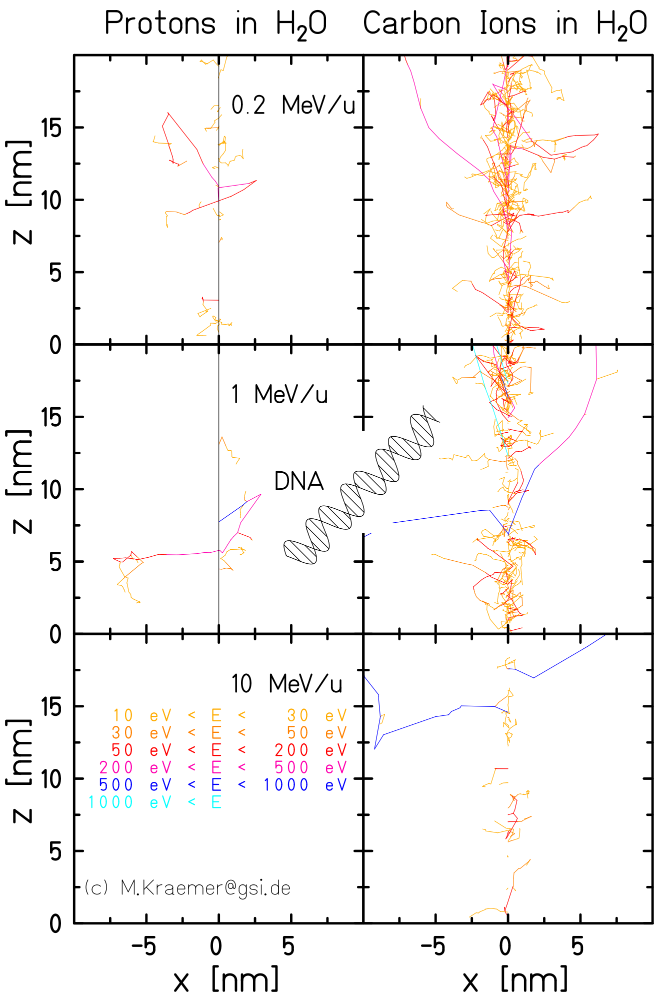

Figure 1.4.: Simulation of track structure of protons (left) and carbon ions (right) at different energies. The energies of the created secondary electrons can be distinguished by different colors. A sketch of a DNA molecule is included for scale. Figure courtesy of Michael Krämer.

in a small cylinder around the track. Several models can be used to predict the radial dose fall off [Cha76,Kat99]. In addition, track structures can be simulated with Monte-Carlo methods [Krä05,Par86]. All methods consistently predict a radial dose fall-off with a $\frac{1}{\mathrm{r}^2}$ dependence, which was also confirmed by measurements [Var77]. In general, the range of δ-electrons is restricted by the kinematics of the collision between projectile and target electron. The maximum range can be approximated empirically by $r_{max} \propto \mathrm{E}^{1.7}$ [Kie86], where E is the Energy of the incoming primary ion. As the energy deposition depends on the kind of incoming ion and the initial energy, that is, a dependence on $\frac{1}{\mathrm{r}^2}$ and z^2 in equation 1.2, the track structure depends on the incoming ion type as well as the initial energy of the ion. Figure 1.4 shows a Monte-Carlo simulation of the track structure for protons and carbon ions at different energies [Krä10].

The energy deposited in the material by the δ-electrons is often described as linear energy transfer (LET) or restricted energy loss. The LET is given by dE/dx and describes the energy locally transferred to the absorber material. The contributions of electrons with a higher energy than a certain threshold are not taken into account for the LET calculations [ICR93,ICR95].

1.1.2.2 Radiobiology

Radiotherapy aims to kill tumor cells to inhibit a further growth of malignant tissue. The actual damage to a single cell depends heavily on the location of the particle tracks within the cell. The most critical damage is observed when radiation damage occurs within the cell nucleus, especially within the deoxyribonucleic acid (DNA). The DNA carries the genetic information of the cell and a damaged DNA can cause cell mutations, carcinogenesis or cell death. The DNA is compounded of two sugar and phosphate backbones and for different bases (adenine (A), cytosine (C), guanine (G) and thymine (T)). This four bases always form base pairs allowing only the combination of A and T or C and G. Depending on the structures hit, the incident radiation can cause different kinds of radiation damage.

The following different kinds of DNA damage can be distinguished:

- **single strand break (SSB)** - SSBs are defined as one destroyed DNA strand, which can be repaired without errors.
- **double strand break (DSB)** - DSBs are defined as breaks in both strands within a short distance. Repair is not always possible and repair mistakes are possible.
- **clustered double strand break (CDSB)** - CDSBs are defined as several breaks in both strands within a few base pairs. The available repair mechanisms cannot repair this kind of damage successfully.
- **base damage (BD)** - BDs occur when bases are knocked out of the DNA structure. Depending on the amount of released bases the repair is possible, even without mistakes if the number of knocked out bases is small.

DNA damage is usually caused by the production of δ-electrons. Two different ways to create radiation damage can are distinguished. Direct effects occur due to ionization of compounds of the DNA and indirect effects are caused by hydroxyl groups which are created through the hydrolysis of water on the particle track, which can travel for up to two nanometres. Indirect effects mainly appear after low linear energy transfer (LET) radiation as, for instance, photons, whereas direct effects are the main cause for DNA damage under high LET radiation, for instance, heavy ions. Nevertheless, both kinds of effects occur in parallel and can cause unrepairable damage. The structure of the DNA as well as a scheme of the direct and indirect effect are shown in Figure 1.5.

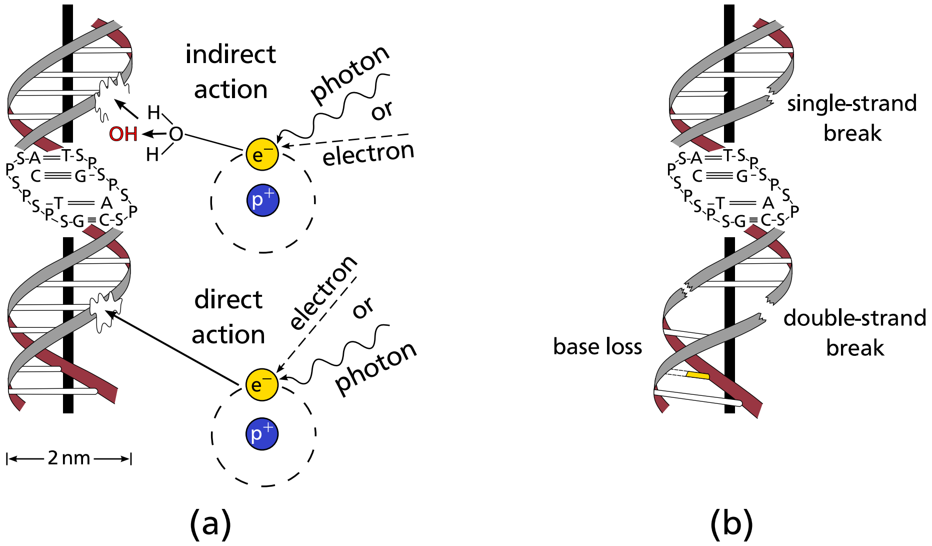

Figure 1.5.: In a) direct and indirect damage due to ionizing radiation is shown. While direct damage is caused by electrons liberated from ions in ionizing processes, indirect damage occurs due to free hydroxyl radicals created during the hydrolysis of water. In b) a scheme of different types of DNA damage is given. Figure taken from [Ric12].

The knowledge of radiation effects in cells and tissue is mainly gained from studies with photon radiation. As the interactions are assumed to be comparable for photons and ions and only the dose pattern changes, the differences between both radiation types can be expressed using the RBE. The RBE is defined as

$$\mathrm{RBE}_{\mathrm{isoeffect}} = \frac{D_{\mathrm{ref}}}{D_{\mathrm{ion}}} \tag{1.5}$$

where D_{ion} is the absorbed heavy ion dose and D_{ref} is the absorbed dose of a reference radiation, usually photons, yielding the same cell survival as D_{ion}. The RBE expresses the increased biological effectiveness of ions and can be only determined for the same biological endpoint.

The relevant endpoint of radiotherapy is the cell survival and therefore cell survival curves of different cell types, for different dose levels and different radiation types are compared. An example for a cell survival comparing photons and heavy ions is given in Figure 1.6. In general the survival curves of ions are steeper and the ones of photons have a more pronounced shoulder before they start to drop almost linearly.

To compare the outcome of treatment or OAR doses for photon and ion radiation, the photon equivalent dose is defined and can be expressed either as GyE or Gy (RBE). The latter is the one recommended by the ICRU. To be able to predict the outcome for a treatment, simulations of cell survival are necessary, especially as the RBE depends on the LET and is highly variable over the whole depth-dose distribution. The cell survival can be approximated with the linear quadratic model

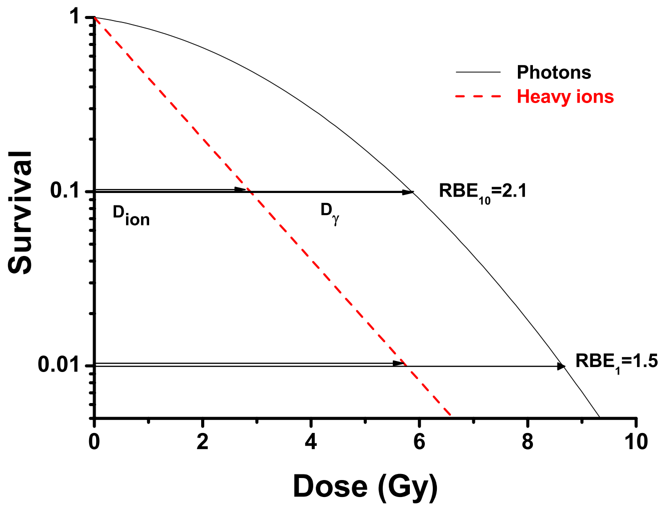

Figure 1.6.: The cell survival curve indicates the differences between photon and ion survival curves and explains how the RBE can be calculated using a cell survival curve. Figure taken from [Sch10].

$$S(D) = e^{(-\alpha D - \beta D^2)}, \tag{1.6}$$

where S is the survival depending on the deposited dose D, and α and β are tissue dependent values.

For biological treatment planning, a model was developed at GSI to consider the changing RBE within the whole dose distribution to deposit a homogeneous biological dose to the patient. The local effect model (LEM) was developed within the context of the pilot project [Krä06, Krä00b, Sch97] and has received revisions over the years [Els07, Fri12]. Different versions of the model are in use for carbon ion therapy and recently a company started implementing LEM for proton and carbon therapy [Ray]. While a LET dependent RBE for carbon ions has been accepted for years, it is still a heavily discussed topic for proton therapy, where a constant RBE of 1.1 is still used in the clinical routine.

1.1.2.3 Beam Delivery Systems

Particle therapy requires a complex accelerator to deliver therapeutic ions. The maximum particle range necessary is about 30 cm, requiring that protons are accelerated up to 200 MeV/u and carbon ions up to 430 MeV/u. The beam needs to be transported from the accelerator to treatment rooms and a high precision delivery on the target volume must to be guaranteed. Nowadays mainly two kinds of accelerators are in use for this task:

- **Cyclotron** - The big advantage of cyclotrons is their compact design and they are used for most of the proton facilities. Cyclotrons offer a beam with a constant energy and intensity. Therefore, passive degraders are necessary to adjust the beam energy and the particle intensity, resulting in a high loss of primary ions.

- **Synchrotron** - A fully active spill-by-spill energy variation can be performed with a synchrotron. All heavy ion facilities are using a synchrotron, even though complicated ion optics are necessary to control and adjust the beam to meet therapy quality standards.

To deliver a conformal and homogeneous treatment plan, an energy and intensity variation is not sufficient. Additionally, lateral and longitudinal beam shaping is necessary to obtain a patient-specific spread-out Bragg peak (SOBP). Two main beam shaping techniques are used - active and passive beam shaping. However, today the trend goes toward active scanning systems, which provide a superior dose conformity.

Passive Beam Delivery

The passive beam delivery system was the first method available for treating patients with heavy ions. Passive beam shaping offered a reliable method, especially in times, when particle therapy was only applied at research facilities and accelerators were less stable and sophisticated than today.

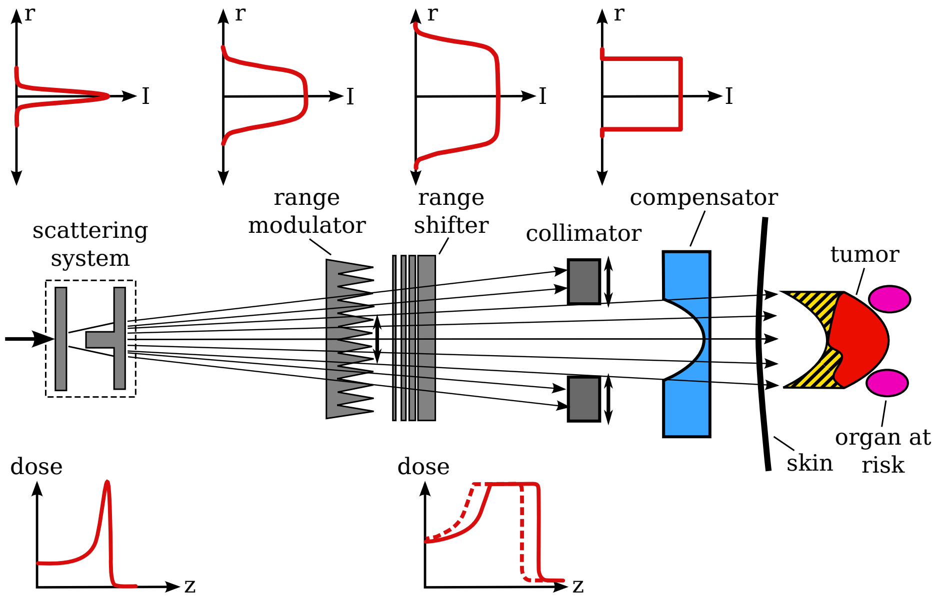

Figure 1.7.: Scheme of a passive beam delivery system. In the first step, the narrow beam is scattered to the required lateral width. A system composed of range modulator, range shifter and collimator ensures the adaption of the beam shape to the lateral and longitudinal extend. Finally, the distal edge is determined by a patient-specific compensator. The hatched area in front of the tumor volume indicates the volume of irradiated healthy tissue. Figure taken from [Ric12].

For a passive beam delivery system several devices need to be placed in the beam line to adjust the narrow incoming beam in lateral and longitudinal direction. A scheme of a passive beam delivery set-up is shown in Figure 1.7. The first step is to laterally scatter the narrow incoming beam to a certain width to reach a broad and flat beam profile. Passive double scattering or a magnetic wobbler are typically used in this case [Kra00a]. In the next step, range modulators are used to extend the beam in depth to create a SOBP with the depth of the target volume. This can be done by either using ridge filters or rotating wheels, for details see [Chu93]. After that, the beam energy is reduced with a range shifter, a passive absorber, to reach the needed penetration depth. All devices up to this point in the beam-line are required for every patient and are installed permanently. However, different settings are necessary for each patient.

In the next step, patient-specific devices are used to adjust the SOBP as precisely as possible to the specific patient geometry. A collimator determines the lateral extend of the SOBP and a compensator forms the distal edge of the SOBP. A large variety of devices is used to achieve a conformal dose distribution. H However, a passive beam delivery system is always limited in dose conformity, as doses as high as the target dose are delivered to the healthy tissue in front of the targeted volume. Besides the limited conformity, additional drawbacks are the necessity of a patient-specific hardware and the production of fragments, especially neutrons, in the beam shaping devices. For a more detailed description of the passive beam delivery method see [Chu93, Kra00a]. Even though the passive beam delivery system was significantly improved over the last decades, it is still inferior to an active scanning system regarding dose shaping.

Active Beam Delivery

An active beam delivery system deflects the beam via dipole magnets to reach a highly conformal depth-dose distribution. The technology needed for beam scanning is more advanced compared to a passive scattering system and brings the following advantages:

- No additional devices are needed in the beam line to shape the beam reducing the additional neutron dose [Kad12]
- No patient-specific hardware needs to be manufactured
- Increased volume conformity, especially in front of the target volume

The basic idea of beam scanning is to divide the target volume in several iso-energy slices (IESs) and rasterize each slice, yielding a grid of raster points covering the volume. A pencil beam is then used to deposit a predetermined number of particles at each raster point.

This allows to integrate a variable RBE in the planning process, as each raster point is optimized separately in the treatment planning system (TPS). Hence, it is possible to deliver not only a highly conformal but also biologically homogeneous dose to the patient. Two different kinds of scanning techniques have been developed in parallel in the 1990s: spot scanning [Ped95] and raster scanning [Hab93].

The idea of PSI was to use a cyclotron and passive degraders to adjust the beam energy. In addition, the beam was scanned in horizontal direction by dipole magnets, while the vertical displacement was reached by a couch shift. Between the single raster points the beam was always switched on and off. In the next generation of the gantry at PSI, scanning was performed in vertical and horizontal direction by beam deflection. The raster scanning approach developed at GSI offers a fully active 3D scanning system, with spill-by-spill energy variation and scanning in vertical and horizontal direction. A schematic overview of the GSI raster scanning system is shown in Figure 1.8.

A narrow pencil beam with a fixed energy is extracted from the synchrotron. Using the mono-energetic beam, the dose is delivered to each IES. The beam is continuously scanned over each IES following a predefined path. Two dipole magnets are responsible for the horizontal and vertical deflection of the beam. The beam stays on each position until the planned number or particles is delivered. This is controlled by a beam monitoring system that checks and, if necessary, adjusts the number of particles as well as the beam position.

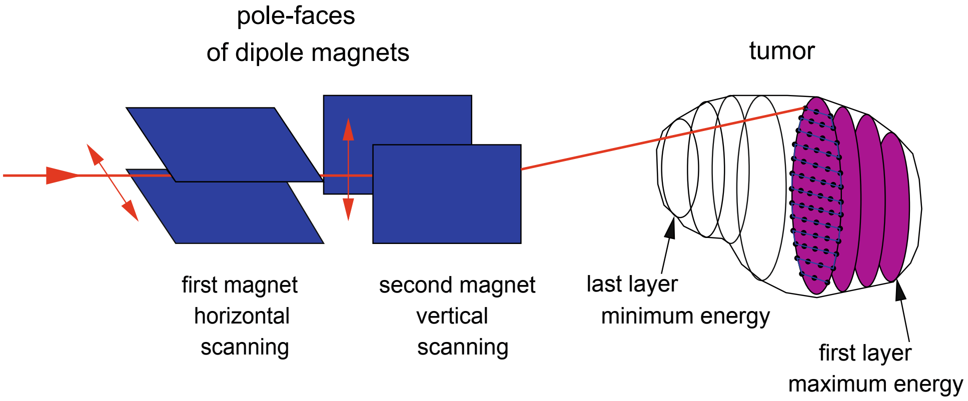

Figure 1.8.: Scheme of the GSI raster scanner. The target volume is divided in iso-energy slices and the beam is moved across the slice following a predetermined scan path. A treatment control system always checks the beam position to avoid deviations between planned and irradiated dose. Figure taken from [Krä09].

The target dose homogeneity is achieved with the help of two different concepts. The lateral overlap of the pencil beams is chosen big enough to compensate for position uncertainties and the spacing between the IESs is chosen sufficiently to obtain a homogeneous dose distribution from the overlapping Bragg peaks. At the same time the number of IESs is kept as low as possible to reduce the treatment time. The only passive device used is a ripple-filter (RiFi) behind the exit-window to slightly broaden the Bragg peak which allows to achieve a homogeneous dose distribution with fewer IESs. The thickness of the used RiFi is usually 3 mm allowing a satisfying homogeneous longitudinal dose distribution [Web99]. In Figure 1.9 schematics are shown which illustrate the overlapping of multiple beams in longitudinal and lateral direction.

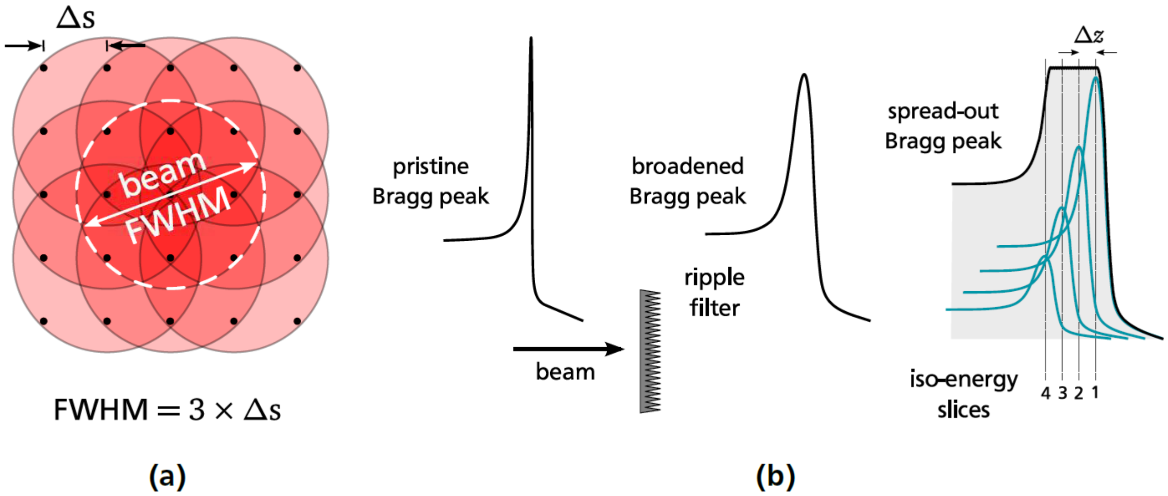

Figure 1.9.: Schematic to indicate how the homogeneous target dose in lateral (a) and longitudinal (b) direction is achieved by overlaying of multiple beams. Figure taken from [Ric12]

1.1.2.4 Treatment of Moving Tumors

Radiotherapy has improved within the last decades and the number of applications is constantly increasing. While nowadays a good homogeneity and conformity of the dose distribution can be achieved for static tumors, moving tumors are still challenging for photon as well as particle therapy and remain a major research topic in the field of radiotherapy.

Different motion types are distinguished and can, in general, be separated into three different categories:

1. **Patient positioning** summarizes uncertainties during the positioning process. This can cause tumor deformation as well as changes of the water-equivalent depth of the tumor volume. Positioning errors can arise due to changes between the planning CT and the treatment positioning and due to positioning changes between the single therapy fractions. Patient fixation systems and positioning protocols are used to avoid systematic errors and minimize uncertainties and thus enabling a successful treatment.
2. **Inter-fractional motion** occurs on a time-scale of hours to days and is correlated to anatomical changes between different fractions. The reasons for inter-fractional motion are manifold. For lung tumors, shrinkage as well as lung density changes over the course of a treatment can cause severe overshooting. Additionally, the breathing pattern can change over time [Son08]. The varying filling of gut and bladder is an important source of uncertainties for prostate cancer patients [Fok04]. To reduce the effect of inter-fractional motion frequent 3D imaging is necessary to control the changes between treatments sessions.
3. **Intra-fractional motion** occurs on a time-scale of seconds to minutes and is mainly correlated with breathing or the heartbeat. This is the type of motion that is usually counteracted with motion mitigation techniques during therapy, which are explained in detail in Section 1.1.2.5.

Tumor motion usually causes dose blurring or a deformation of the dose distribution, as the tumor is partly moving out of the field. This effect is also known from photon therapy, but less critical than for particle therapy. Density changes have a significant influence on the range of particles and therefore can cause severe under- and over-dosage. These range changes can significantly increase the dose deposited in normal tissue and decrease the dose deposited in the targeted volume.

In contrast to photon and passive particle therapy, the delivery time of active particle therapy is in the order of several minutes so that for breathing and heartbeat movements several motion cycles occur during the treatment. This can lead to interference effects, so-called interplay effects, between the target motion and the motion of the scanned pencil beam, causing local over- and under-dosage in the target volume as well as additional irradiation of normal tissue. The severity of this effects depends on the motion amplitude of the target volume, the extraction rate of the accelerator and therefore the scanning speed and the relative direction between target motion and scanning motion [Ber08a, Grö06]. In Figure 1.10 film measurements are shown indicating the consequences of interplay effects in particle therapy.

In the next Sections different motion mitigation techniques are introduced, which are used to counter interference effects during the irradiation of moving targets.

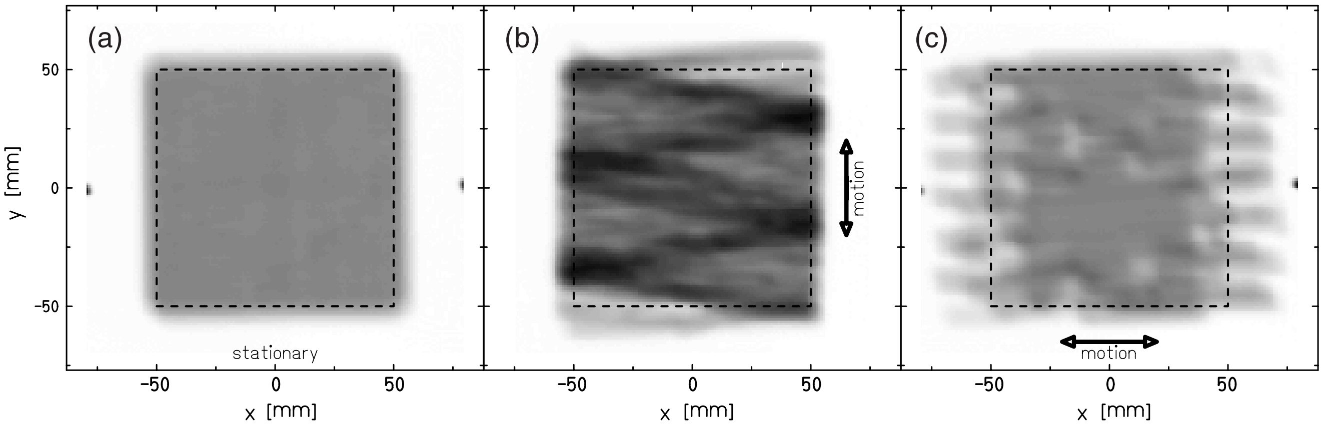

Figure 1.10.: Impact of the interplay effect illustrated with a radio-graphic film measurement. In (a) a static dose distribution is shown. Interplay patterns caused by a vertical (b) and horizontal (c) motion of the films are shown. The heterogeneity of the optical density in the films (b) and (c) is clearly visible and corresponds to over- and under-dosage [Ber08a].

1.1.2.5 Motion Compensation for Moving Tumors

Various different strategies have been developed to counter intra-fractional motion. The following Sections introduce the ones most important for this work. A full overview of motion mitigation techniques can be found in [Ber11].

Motion mitigation techniques can be applied either during the treatment planning process or at patient set-up. For the latter, the motion in the patient is reduced as much as possible, for instance with abdominal compression or jet ventilation for liver or lung cancer patients, respectively. For the former, the target volume is enlarged for planning, so that the targeted tumor cannot move outside the irradiated volume during the treatment.

Apart from considering the motion during the planning and positioning process, additional methods are known for adapting the treatment itself. The most important ones are rescanning and gating, which will be explained within this section. An additional possibility is beam tracking, for more details concerning this approach the reader is referred to [Ber07b, Ber10, Web00].

Rescanning

Motion mitigation via rescanning is only possible for raster or spot scanning. The aim of this approach is to use statistical averaging to overcome the dose inhomogeneities caused by the interference effects between target and beam motion. The basic idea is simple: instead of irradiating each raster point once, multiple rescans are performed, where raster points are irradiated multiple times with a corresponding lower dose. Different versions of rescanning have been proposed. The most common ones are slice-by-slice and volumetric rescanning. Furthermore, phase-controlled and breath-sampled rescanning have been proposed [Sec09, Fur07]. They offer an even better motion mitigation at the cost of a more challenging delivery. The effect of a rescanned irradiation can be seen in Figure 1.11.

The major drawbacks of rescanning are the increased treatment time and the enlarged target volume. As the target must be covered in all motion states an extended volume needs to be irradiated, which

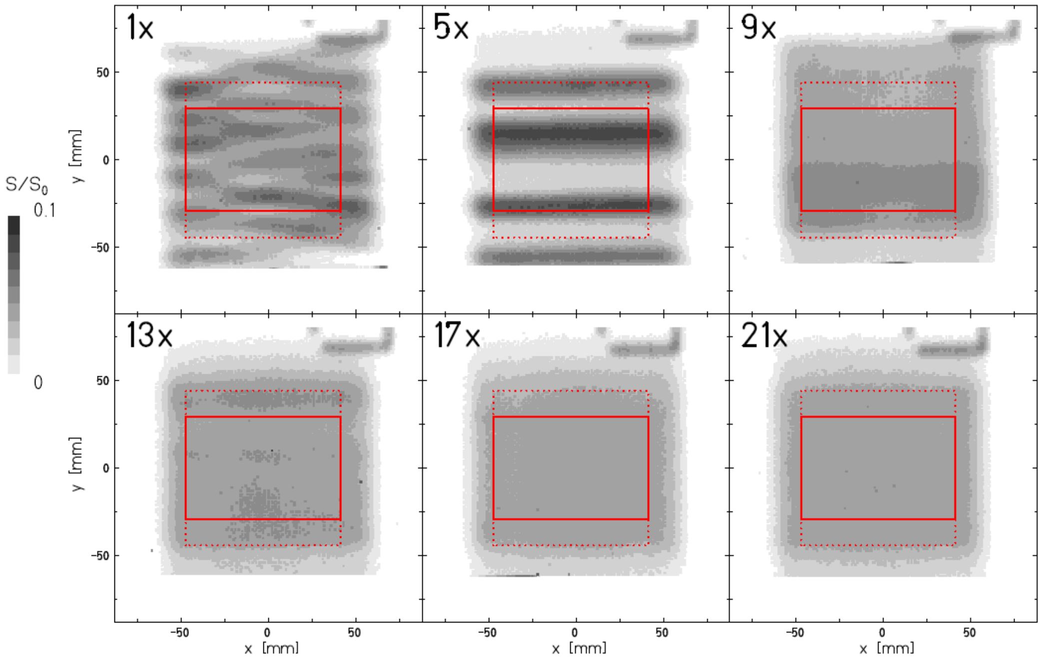

Figure 1.11.: Films irradiated with different numbers of rescans. With an increasing number of rescans, hence with an improved statistical averaging, the interplay pattern becomes homogeneous indicating the effectiveness of rescanning to compensate motion patterns. Figure taken from [Ber08b]

increases the dose delivered to normal tissues. The major advantage is the simple delivery, especially for slice-by-slice and volumetric rescanning. Different kinds of rescanning are already in clinical use [Ros15].

Gating

For gating, a certain part of the motion cycle is selected in which the motion amplitude is small. The beam is only extracted when the target volume is within this window. The technique needs a sophisticated motion monitoring and beam extraction system, which can start and stop the beam extraction without a significant time delay. A drawback of this technique is the prolonged treatment time, as the irradiation is only possible when the gating window and the accelerator extraction overlap.

For complicated cases a combination of gating and rescanning is possible, where gating is used to reduce the motion amplitude and rescanning to compensate the residual motion effects [Mor14].

1.1.2.6 Treatment Planning

Nowadays, treatment planning is based on a CT of the corresponding volume. The target as well as the OARs are delineated by a physician and this structures are then used for the optimization of the treatment plan. Additionally, positron emmission tomography (PET) and magnetic resonance imaging (MRI) are used to gain additional information of the tumor, which facilities a more precise contouring.

The tumor region and the OARs have to be defined and different volumes have to be determined following the International Commission on Radiation Units and Measurements (ICRU) [ICR95, ICR99]:

- **GTV** (Gross Tumor Volume) - *'The GTV is the gross palpable or visible extent and location of malignant growth.'*

- **CTV** (Clinical Target Volume) - *'The CTV is a tissue volume that contains a demonstrable GTV and/or subclinical microscopic malignant disease, which has to be eliminated. This volume thus has to be treated adequately in order to achieve the aim of therapy, cure or palliation.'*

- **PTV** (Planning Target Volume) - *'The PTV is a geometrical concept, and it is defined to select an appropriate beam size and beam arrangements, taking into consideration the net effect of all the possible geometrical variations, in order to ensure that the prescribed dose is actually absorbed in the CTV.'*

- **ITV** (Internal Target Volume) - *'This is the margin that must be added to the CTV to compensate for expected physiological movements and variations in size, shape and position of the CTV during therapy.'*

- **OAR** (Organ at risk) - *'OARs are normal tissues whose radiation sensitivity may significantly influence treatment planning and/or prescribed dose.'*

During the treatment planning process the beam entry angles and the beam parameters need to be set. Yet, as major task remains the optimization of the dose distribution. The aim of the TPS is to optimize a treatment plan satisfying all constraints given by the physician. For heavy ion therapy the RBE as well as projectile and target fragments need to be taken into account increasing the complexity of the planning process.

The TPS used throughout the thesis is TRiP4D, a further development of TRiP98, which was developed at GSI during the pilot project. A detailed description of TRiP98 can be found in [Krä00b, Krä00c, Krä10] and the upgrade to the 4D version is described in detail in [Ric13].

4D Treatment Planning

Particle therapy, especially actively delivered particle therapy, is very sensitive to target motion. Therefore a dedicated 4D treatment planning can increase the dose conformity, which allows a higher target dose while sparing the OARs. TRiP4D [Ric13] was introduced to handle 4D dose calculations as well as 4D dose optimization [Gra13, Gra14].

The basis for 4D treatment planning is representative 4D imaging data gained by a time-resolved computed tomography (4DCT). The 4DCT was developed in the last decade and is now routinely performed in the clinical workflow. The 4DCT allows adapting a treatment plan to the present motion in the patient. However, a 4DCT only represents a single motion cycle, which is assumed to be valid during the whole treatment. Additional 4D image information can be gained from time-resolved magnetic resonance imaging (4DMRI) allowing to record several motion cycles.

Typically, one 4DCT is divided in 10 motion phases, either with an amplitude or phased based algorithm. From this phases one is selected as reference phase and all others are registered to it. The image registration process provides deformation maps between each motion phase and the reference phase. The resulting deformation maps are required input data for the 4D treatment planning process. The image registration needs to be done before the 4D treatment planning process can be started. At GSI external programs are used for this step, for instance Slicer3D [Fed12].

An image registration can be done between different motion phases in an image modality (intra-modality registration) or between different image modalities (inter-modality), for instance contrast CT to native CT or CT to MRI. As mentioned, the result of the image registration is a deformation map, which specifies the transformation of every voxel in the moving image. In Figure 1.12 a deformation map is shown and in Figure 1.13 displays the process of registering two images.

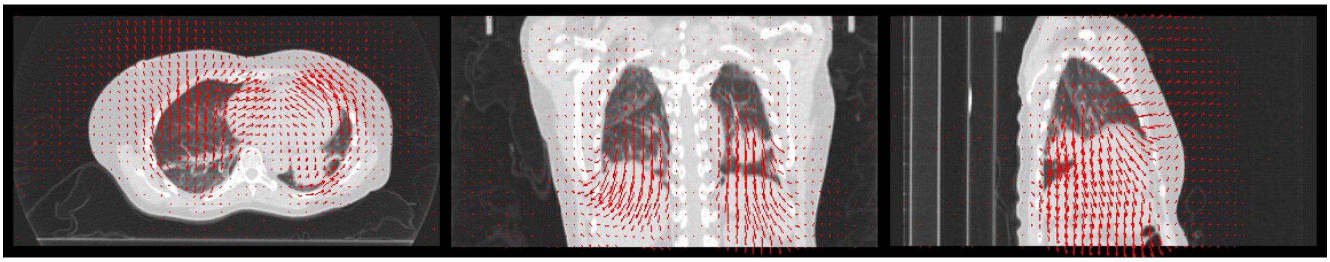

Figure 1.12.: Deformation map of a 4DCT of a lung cancer patient in the reference phase (end-exhale). The vector fields visualize the necessary deformations to convert it to the end-inhale phase. From left to right axial, coronal and sagittal views are shown [Ric12].

Different registration types are known and can be used for different purposes in treatment planning. A Rigid registration provides limited degrees of freedom including changes such as translation, rotation and scaling. Deformable registrations allow arbitrary transformations.

To calculate the 4D dose distribution, the treatment plan is divided into sub-plans corresponding to the motion phases that are irradiated. To determine the sub-plans a time correlation between the beam delivery and the present motion phase needs to be available, hence beam delivery sequences need to be simulated.

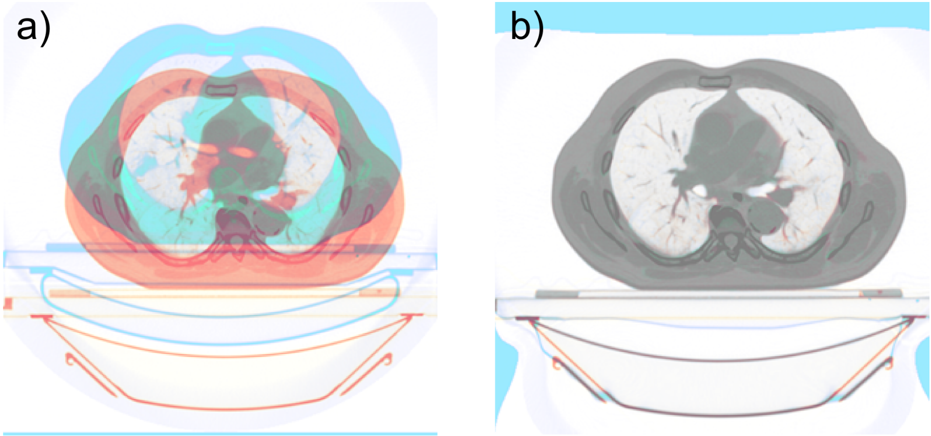

Figure 1.13.: Overlay of two different 4DCTs is shown without image registration in (a). In (b) the overlay of the fixed and the corresponding image after registration is shown. As inverse colors are used in both CTs perfectly matching areas are displayed in gray [And16a].

Simulation of Beam Delivery Sequences

A tool was develop at GSI which can use different accelerator settings and simulate the time the irradiation of each raster point [Ric12]. Doing this for all raster points yields the timings for the complete beam delivery, including the timing of the begin and end of each spill, the chosen particle intensity for each IES or for each raster point, depending on the accelerator, the structure of the beam extraction and the extraction duration.

1.2 Cardiac Arrhythmia

Cardiac arrhythmia is the general term for any disruption of the cardiac conduction system. It includes heart rates at rest that are too high (above 100 bpm as resting pulse rate - tachycardia), too low (below 60 bpm - bradycardia) and also all types of irregular beating of the heart. Furthermore, cardiac arrhythmia can arise from almost any anatomical site of the heart.

The types of cardiac arrhythmia and their corresponding symptoms vary extremely. While several kinds of arrhythmia are harmless, others can have severe complications like strokes, heart failure and decreased quality of life or can even cause sudden cardiac death. The risk to develop cardiac arrhythmia rises with increasing age and they are a serious problem for an aging society.

The effectiveness of the available treatment modalities depends on the type of cardiac arrhythmia and range from good to very complicated to control. Within this section more details are given for two types of cardiac arrhythmia: Atrial fibrillation (AF) and ventricular tachycardia (VT). The symptoms, causes and prevalence is discussed as well as conventional treatment modalities and possible future ones.

1.2.1 Conduction System of the Heart

From a mechanical point of view the heart works like a pump. The control system of the heart is the heart's conduction system which takes care that the pumping action occurs regularly and effectively. The starting point of every healthy heart contraction is the sinoatrial node (SA), in which electrical impulses, so called action potentials, are created. The action potentials are propagated by specialized cells over the atria to the atrioventricular node (AVN) and from there over the atrioventricular bundle to the left and right ventricle. The timing of the propagation of the action potentials is very important to guarantee an effective heartbeat. The atria beat shortly before the ventricles to allow an effective pumping of blood through the heart muscle. A scheme of the conduction system and the hearts anatomy is given in Figure 1.14.

The electrical impulses can be measured on the body surface and are displayed in an electrocardiogram (ECG), which is used for medical diagnostics. In Figure 1.15, a schematic of the human sinus rhythm is shown as it can be seen on an ECG. Different wave forms can be distinguished representing different actions of the heart muscle. The first small wave, the so-called P wave, is formed due to the electrical impulses causing the atria to contract. The QRS complex, the big spike after the P wave, is created by the contracting ventricles. The next rising structure, the T wave, measures the release of the action potentials within the ventricles. For medical diagnostics not only the appearance of the different waves is important, but also the timing of the ECG. The PQ interval is defined as the elapsing time between the beginning of the P wave until the beginning of the QRS complex, indicating the necessary time for

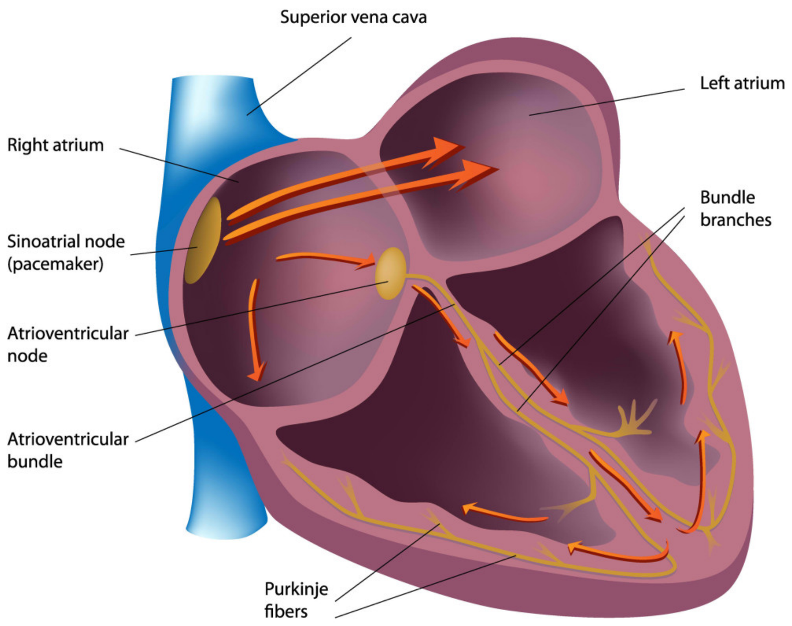

Figure 1.14.: Scheme of the conduction system of a human heart. The figure is taken from [Hea].

the action potentials to propagate from the atria across the AVN to the ventricles. The interval from the beginning of the QRS complex to the end of the T wave is called QT interval and represents the stimulation of the ventricle. The ST segment corresponds to the time necessary for the relaxing of the ventricles.

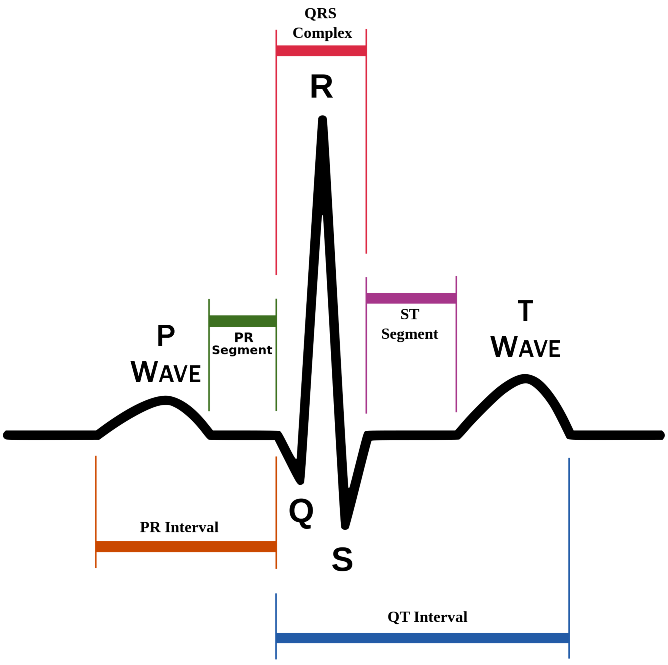

Figure 1.15.: Scheme of a human sinus rhythm as it can be seen on an ECG of a healthy human [ECG].

1.2.2 Types of Arrhythmia

The next part focuses on atrial fibrillation as well as ventricular tachycardia, since both are types of cardiac disorders for which a non-invasive treatment modality was investigated in this work, especially in Chapter 2. In addition, a short review of conventional treatment modalities for cardiac arrhythmia as well as an introduction to the current sate of research on radiotherapy as an alternative treatment is given.

1.2.2.1 Atrial Fibrillation

Atrial fibrillation is the most common cardiac arrhythmia with severe complications [Mun14]. The number of affected patients is dramatically increasing due to an aging society, especially in developing countries. The 2010 Global Burden of Disease Study estimated, that 596 out of 100.000 men and 373 out of 100.000 women suffer from atrial fibrillation (AF) [Chu14]. This sums up to a total of 33 million people worldwide and the global prevalence of AF is expected to double until 2050. The lifetime risk for people above 40 years is estimated with approximately 25 % and already today about 2 % of the European population already suffers from AF [Rah14].

AF is not directly life threatening, but can have severe complications like stroke, cardiac infarction and sudden cardiac death. However, even without severe complications AF decreases the quality of life significantly. Aside from genetic predisposition, age is the most important risk factor. The AF prevalence is almost doubling within each decade for people older than 50 years and the average age of patients suffering from AF in high-income countries is above 65 years. Obesity, hypertension, diabetes, coronary heart disease and all other conditions related to cardiovascular diseases are risk factors related to AF. AF is caused by misfunctions of the heart conduction system. During an AF episode additional electrical impulses are generated by either the entries of the pulmonary veins or some other random cardiacmyocytes. These irregular and erratic signals lead to an irregular beating of the atria, which is marked by a missing P wave on the ECG. A schematic comparison of a normal sinus rhythm and atrial fibrillation is given in Figure 1.16.

AF can cause severe symptoms but can also occur silently for the patient, it is assumed that about 20 % of all strokes are caused by AF. Especially for patients with silent AF, it is often diagnosed after a stroke. Therefore every stroke patient should be checked for AF [Cam10].

In general several types of AF can be distinguished based on the duration of the attacks and the presentation:

- **Paroxysmal** - Attacks last a maximum of 48 hours
- **Persistent** - Attacks last longer than 7 days or require cardioversion
- **Long-standing persistent** - Attacks last longer than a year
- **Permanent (accepted)** - Attacks are not ending anymore and no cardioversion is performed. The wrong heart rhythm gets accepted.

Usually the different versions of AF develop into each other and the process can only be stopped by an efficient treatment.

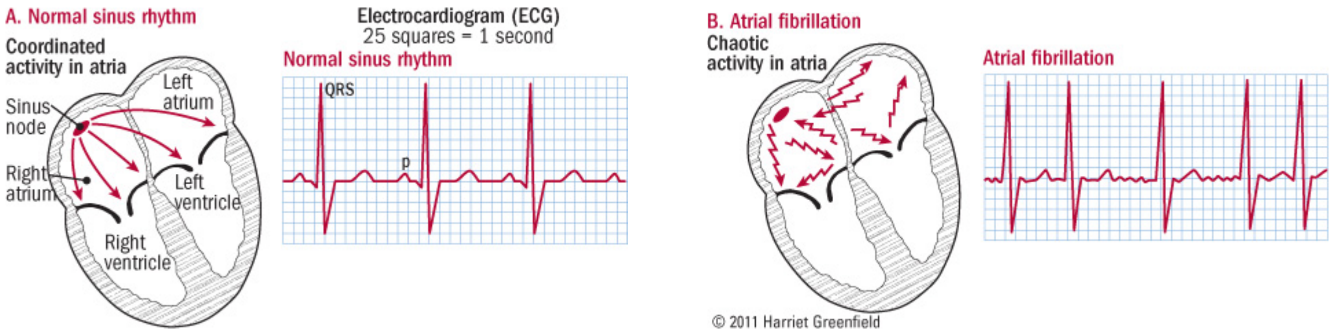

© 2011 Harriet Greenfield

(a) Schematic of electrical impulse propagation during a sinus rhythm of the heart on the left and the corresponding ECG on the right. In normal sinus rhythm, the sinus node initiates the electrical activity that triggers each heartbeat. The electrical impulse travels through the atria, signaling the muscle to contract. Each atrial contraction shows on the ECG as a p wave.

(b) Schematic of electrical impulse propagation during an AF episode on the left and the corresponding ECG on the right. In atrial fibrillation, the atria's electrical signals are very rapid and erratic. The atria do not contract and there is no p wave visible in the ECG. Without a coordinated signal to guide them, the ventricles contract in an irregular rhythm.

Figure 1.16.: Schematic comparison of the electrical impulse propagation in the atria between a sinus rhythm and an AF episode with corresponding ECGs. Both figures are taken from [Fib]

Conventional Treatment Modalities

After AF is diagnosed several treatment options are available. The choice depends mainly on the present form and duration of the AF, the influence of AF on the quality of life and the cause of AF. The main aims are either to reset the heart rhythm or to control the heart rate and to avoid the formation of blood clots. In general, the common treatment options are: Anti-coagulation drugs, drugs for rate and rhythm control, cardioversion, pulmonary vein isolation and, as a final step, AVN ablation.

The first aim is always to reset the heart to the sinus rhythm. This is why a cardioversion, either with medication or with an external defibrillator is applied. Even when anti-arrhythmic drugs are effective the side effects should be considered.

Whether anti-coagulation drugs are necessary and which ones, can be decided with the help of the CHADS_2 score [Cam10], which classifies risk factors and supports the decision pro or against drugs. Major risk factors which always require antithrombotic therapy are, for instance, a prior stroke, transient ischemic attack, or thromboembolism and age above 75 years. Clinically relevant but non-major risk factors are, for instance, heart failure, hypertension or diabetes. In the presence of several non-major risk factors, anti-coagulation drugs are also recommended.

If controlling the heart rhythm is not possible a rate control of the ventricles is necessary. This can either be achieved with medication or an ablation of the AVN and the implantation of a pacemaker. The AVN ablation should always be the last step and is only applied if all other treatment modalities are unsuccessful.

A cure of AF can be achieved by a radio-frequency catheter ablation of the pulmonary veins. However, the treatment requires anesthesia, is lengthy and severe side effects can occur. Furthermore, the outcome is varying and in about 30 % of all patients a recurrence of the symptoms is found [Cap05,Cap10] making a repetition of the treatment necessary.

1.2.2.2 Ventricular Tachycardia

Another type of cardiac arrhythmia is ventricular tachycardia (VT), which causes most of the sudden cardiac deaths in the US. It is a cardiac disorder like AF, but VT is potentially life-threatening as it is defined as a fast rate of ventricular contractions. These fast contractions are inefficient and slow down or even interrupt the blood flow, causing an extremely low blood pressure which can develop into ventricular fibrillation and sudden cardiac death. A schematic of an ECG recorded during a VT attack is shown in Figure 1.17.

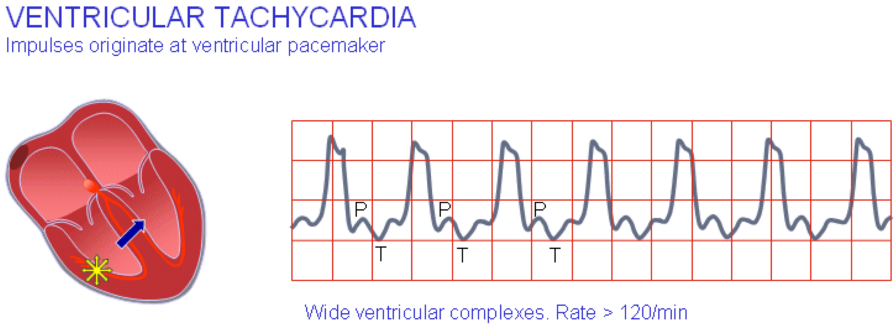

Figure 1.17.: Schematic of the origin of the electrical impulses within the heart on the left and a typical VT ECG on the right [VT].

During a VT attack an ECG shows 3 or more consecutive QRS complexes at a minimum heart rate of 100 bpm. During VT episodes the heartbeat can easily reach between 160 and 250 bpm. The electrical impulses do not propagated from the atria through the AVN to the ventricles, instead they originate directly from the ventricles. Mostly they are caused by an interaction between an arrhythmogenic substrate, for instance the border zone of a scar after a myocardial infarction, and electrophysiological properties of the heart muscle cells.

Comparable to AF, different kinds of VT can be classified. Important factors to classify VT are the duration of an attack, the morphology, the hemodynamic characteristics and the underlying mechanism. A detailed overview of definitions and classifications can be found in [Mit15].

The most common cause of VT is an ischemic heart disease in which scar tissue is created due to under-supply of the myocardium with oxygen. However, other structural heart diseases can cause VT as, for instance, cardiomyopathy and surgical incisions in the ventricle. In addition, VT can also occur in the absence of a structural heart disease and can be triggered by electrolyte deficiencies, digitalis toxicity or drugs that influence the heartbeat.

Conventional Treatment Modalities

The standard treatment for VT depends on the classification of the VT. While anti-arrhythmic drugs are successful for patients with idiopathic VT, they are not a stand-alone therapy for patients with structural heart diseases anymore. For those patients, using an implantable cardioverter-defibrillator (ICD) is the first treatment choice nowadays. An ICD is able to perform cardioversion, defibrillation and even pacing and thus reduces the risk of sudden cardiac death and can prolong the lifetime of a patient. However, ICDs do not offer a cure of ventricular tachycardia and cannot completely avoid sudden cardiac death [Red07].

In addition, ICDs are a psychological burden and repeated shocks are challenging. First of all they are painful for the patient and not well tolerated. Secondly, especially for patients with a heart failure, repeated shocks can worsen the hemodynamic within the heart and therefore increase the mortality [Poo08]. To reduce the number of ICD shocks the use of anti-arrhythmic drugs is indicated, even though they are not well tolerated and can even increase the number of deaths. In patients with severe structural heart diseases they are even less effective.

Radio-frequency catheter ablations, as a prophylactic measure together with ICD implantation or after repeated ICD shocks, offer an additional treatment modality. For patients with idiopathic VT, radio-frequency ablation can even be used as a stand-alone therapy with the aim to cure patients. The success for radio-frequency catheter ablations is increasing as the technology is developing further. Thus, a study was carried out to investigate the benefit of radio-frequency ablation for patients. The complication risks during the procedure were found to be below 5 % and the number of ICD shocks decreased from 53.7 % in the control group, to 32.7 % in the ablation group. [Bah13]

Radio-frequency catheter ablation is still limited by the thickness of the myocardium as transmural scars are necessary to control the electrical impulses, as the penetration depth is limited. Hence, for several patients an additional epicardial ablation is necessary which is correlated with higher risks of complications and, in addition, only carried out at a very limited number of clinics [Di 12].

1.2.3 Radio-ablation as Catheter-Free Ablation for Atrial Fibrillation and Ventricular Tachycardia

As the conventional treatment of cardiac arrhythmia is not always satisfying or even insufficient for some patient groups, a potential solution is radiotherapy. It is a non-invasive approach with a sufficient penetration depth and accuracy. First animal studies were carried out in the last years, showing the possibility to alter electrical pathways in the heart muscle using ionizing radiation [Sha10b, Bla14]. Trials to isolate pulmonary veins in pigs followed and showed the feasibility to ablate cardiac structures using photon radiation. However, an improved dose distribution is necessary to avoid radiation related side effects, especially with conventional linear accelerators.

First patient trials followed that indicated the successful application of photon therapy for cardiac arrhythmia [Cve14, Loo15]. However, until the method can be used in clinical routine further studies are necessary. A phase I/II study with more than one patient was carried out at Washington University St. Louis (USA) irradiating five patients, which showed the feasibility of a fully non-invasive VT ablation (www.clinicaltrials.gov: NCT02919618). Due to the larger patient number of this study the outcome could provide more information on advantages, success and side effects of the therapy.

One possibility to further improve the dose distribution and to avoid side-effects reported by [Bod15] is the use of heavy ions. Therefore a study with Langendorff-perfused porcine hearts was carried out to investigate the feasibility to ablate cardiac structures using carbon ions [Leh15, Pra15]. In addition, a treatment planning study for carbon ions of ablating pulmonary veins was published by [Con16, Con14] to show the feasibility of a carbon treatment for humans. A twin study followed, where the use of photons and carbon ions for catheter-free ablation was compared. The study was carried out at Mayo Clinics (Mayo) (Rochester,Minnesota, USA) and GSI (Darmstadt, Germany) [Leh15, Leh16a, Eic15]. The carbon ion arm of the study and the study's results are discussed in detail in Chapter 2.

2 Feasibility Study of Catheter-Free Ablation using Carbon Ions in Pigs as an Animal Model

Radio-frequency catheter ablation is a widely spread treatment modality for treating cardiac arrhythmia. The aim of catheter ablation is to alter electrical pathways within the heart muscle to prevent the propagation of action potentials disturbing the normal sinus rhythm of the heart. The procedure itself is time intensive and requires repetition in about 30 % of all treatments due to a recurrence of the symptoms [Cap05, Cap10]. Therefore, innovative treatment modalities are highly warranted and radiotherapy emerges as a promising non-invasive alternative.

First in-vivo studies using photons for cardiac ablations demonstrated the feasibility to alter the electrical conductivity of the heart muscle using radiation [Sha10b, Bla14, Bod15]. In addition, first patient trials were conducted [Cve14, Loo15]. In none of the two treated patients, radiation induced side effects were observed, while Bode et al. reported severe side effects in pigs. In one of the patient trials no treatment effect was found and the patient died 9 months after the treatment due to the underlying disease [Loo15]. In the other one, no clear connection between the reduced number of ventricular tachycardia (VT) attacks starting 4 weeks after the irradiation and the treatment could be shown [Cve14]. Motivated from these findings a phase I/II clinical trial was initiated at Washington University, St. Louis, USA (www.clinicaltrials.gov: NCT02919618). The outcome of this study is still pending.

Apart from photon irradiation, the potential of scanned carbon ions beams for non-cancerous diseases was already discussed in 2012 [Ber12]. In 2013, a feasibility study was carried out irradiating Langendorff-perfused pig hearts with carbon ions [Leh15, Pra15]. In addition, a first treatment planning study was conducted, proposing the use of carbon ions to ablate pulmonary veins in humans [Con16, Con14]. The results showed that carbon ions offer an excellent non-invasive alternative with superior dose distributions compared to photons due to the inverse depth-dose profile. However, carbon ions are prone to interplay effects and need a careful consideration of breathing as well as heartbeat motion during the treatment planning process and the irradiation itself. This causes a more complex treatment compared to photons. Nevertheless, the conformity of the depth dose distribution and the sparing of the critical structures in close proximity to the target volume is superior.

The following chapter describes the first in-vivo feasibility study on catheter-free ablation using carbon ions in pigs. Pigs are widely used as an animal model for heart experiments, although anatomical differences to human hearts are present [Cri98]. The aim of the study was to investigate the potential of carbon ions as a non-invasive treatment alternative to ablate anatomical structures in the heart. The study was carried out at GSI Helmholtz Center for Heavy Ion Research (GSI) in Darmstadt (Germany) in July 2014 in collaboration with Mayo Clinics (Rochester, Minnesota, USA), University Clinic Heidelberg (Germany) and Helmholtzcenter Dresden Rossendorf (Germany). The focus of this work is the treatment planning and motion mitigation performed for the experiment. In addition, a summary of the whole experiment and results is given for completeness. For further details on the experiment the reader is referred to [Leh16b, Leh15, Gra15, Erb15, Eic15, Hel14, Pra14b].

2.1 Material and Methods

2.1.1 Patient Cohort and Targets

In total, 22 pigs were included in this study. 16 of them were prepared for irradiation, 3 pigs were kept as a control group and, in addition, the workflow was tested with 3 pigs prior to the experiment. This was essential to establish imaging protocols for treatment planning as well as for positioning, to test the infrastructure at GSI, the transportation to GSI and to investigate the anatomical variability. One of the pigs prepared for irradiation had to be euthanized prior to the treatment due to a vascular obliteration. In addition, one of the 15 irradiated pigs suffered from a heart malformation and was thus excluded from the analysis as the results could not be compared to the healthy pigs. All other pigs were healthy and did not suffer from any cardiac disorder. At the time of irradiation, all pigs were 10 weeks old and weighted between 29.0 and 39.1 kg.

For the study, all pigs were randomly separated in three target groups corresponding to three different target volumes:

- The **atrioventricular node (AVN)** is part of the electrical conduction system of the heart and propagates the action potentials from the atria to the ventricles. The ablation of the AVN is used for patients suffering from permanent atrial fibrillation (AF), which influences the ventricular rhythm. The AVN was irradiated in order to create a complete AV block preventing any electrical signals to emerge from the atria to the ventricles. As a complete AV block can be lethal due to slow ventricular excitation, all pigs in the AVN group were equipped with pacemakers.

- The **left ventricular free-wall (LV)** was irradiated to create a homogeneous and transmural lesion. This is a potential treatment for VT, which can occur due to the creation of inhomogeneous scar tissue in the heart muscle after a myocardial infarction. Ablating the LV is the only possible cure for patients suffering from VT. The standard treatment, implantation of an implantable cardioverter-defibrillator (ICD), can only reduce the risk of sudden cardiac death.

- The **superior pulmonary vein (SPV)** ablation was carried out as an alternative and innovative treatment for AF. In several cases AF is caused by action potentials that are created in the pulmonary veins and propagate to the atria. A homogeneous scar at the transition between SPV and atrium can avoid the propagation of action potentials and, hence, cure AF.

In Table 2.1 an overview of all pigs is given including a numbering system, which is used throughout this work. In addition, target doses as well as the size of the target volumes are stated.

Selection of Dose Groups

All pigs were irradiated with a single-fraction treatment. The dose groups were selected corresponding to the findings of previous photon studies [Sha10b, Bla14]. The reported doses necessary to reach a permanent alteration of the electrical pathways varied between at least 25 Gy [Sha10b] and above 30 Gy [Bla14]. Sharma et al. reported bidirectional cavotricuspid isthmus block after 30 days and a dose of 40 Gy and an AVN conduction block after 49 days and 70 Gy. Blanck et al. found that the 50 %

Target	Dose [Gy]	ID	Target Volume [cm^3]	Treated Volume [cm^3]	Optimization
AVN	55	1	0.065	1.76	SFUD
		2	0.065	1.76	
		3	0.065	1.74	
	40	4	0.065	1.73	
		5	0.065	1.76	
		6	0.065	1.80	
	25	7	0.065	1.73	
		8	0.065	1.73	
SPV	40	12	1.30	16.09	IMPT
		13	0.95	11.11	
		14	0.96	12.58	
LV	40	15	2.11	-	SFUD
		16	2.28	-	
		17	2.38	-	

Table 2.1.: Overview of the treated animals and the corresponding targets, target doses and target volumes. The stated IDs are used throughout this work. Pigs with ID 9, 10 and 11 were sham-irradiated control animals. Due to the applied range margins it was not possible to determine a geometric treated volume for the LV group.

effective dose to induce fibrotic tissue was 31.3 Gy with a follow-up time of 6 months and suggests doses above 32.5 Gy to ensure a successful treatment.

These findings motivated the use of 25, 40 and 55 Gy for the AVN group to carry out a dose escalation study within the presented feasibility study. For the pigs with 25 Gy no AV-block was expected, for the ones with 40 Gy permanent changes were likely and the 55 Gy group was chosen to definitely induce AV-blocks. For the SPV and LV irradiations only one target dose was applied. Hence, 40 Gy was chosen to ensure a dose high enough to create fibrotic tissue, while at the same time trying to keep the organ at risk (OAR) doses as low as possible to avoid radiation induced side effects.

All treatment plans were optimized using physical doses due to insufficient knowledge of the relative biological effectiveness (RBE). Even though biological effective doses are typically prescribed in carbon ion therapy, the RBE at such high single-fraction doses is expected to be only slightly above 1 [Fri14a].

2.1.2 Study Outline

Two to three weeks before irradiation all pigs were examined and an electrophysiological mapping of the heart was performed to collect baseline data as reference for the final analysis. Additionally, skin biopsies and blood samples were taken. Pigs selected for AVN group underwent a pacemaker implantation to ensure the survival after a successful treatment. During the experiment and the follow-up time all animals were kept at the 'Interfakultäre Biomedizinische Forschungseinrichtung' (IBF) of the University Clinic Heidelberg (UCHD). All medical examinations of the study were carried out at the IBF. The pigs were transported to GSI for the catheter-free ablation with an adequately equipped truck.

In total, three follow-ups were carried out 4, 8 and 13 or 24 weeks after the treatment. All follow-ups consisted of the recording of 12-channel electrocardiograms (ECGs), taking of blood samples and examination of the skin in the area of the entrance channels to check for side effects. In addition, the second and the third follow-up included skin biopsies. During the final follow-up an electrophysiological cardiac mapping was performed to detect electrical changes in the heart muscle. In-between the follow-ups regular ECGs were performed for the AVN pigs checking for AV-blocks. After the final follow-up the pigs were euthanized and heart, lung, trachea, esophagus and phrenic nerve were removed *'en bloc'* with a possibly intact pericardium. Finally, a pathological examination was carried out to assess and document tissue changes. In Figure 2.1 the complete workflow for each pig is described.

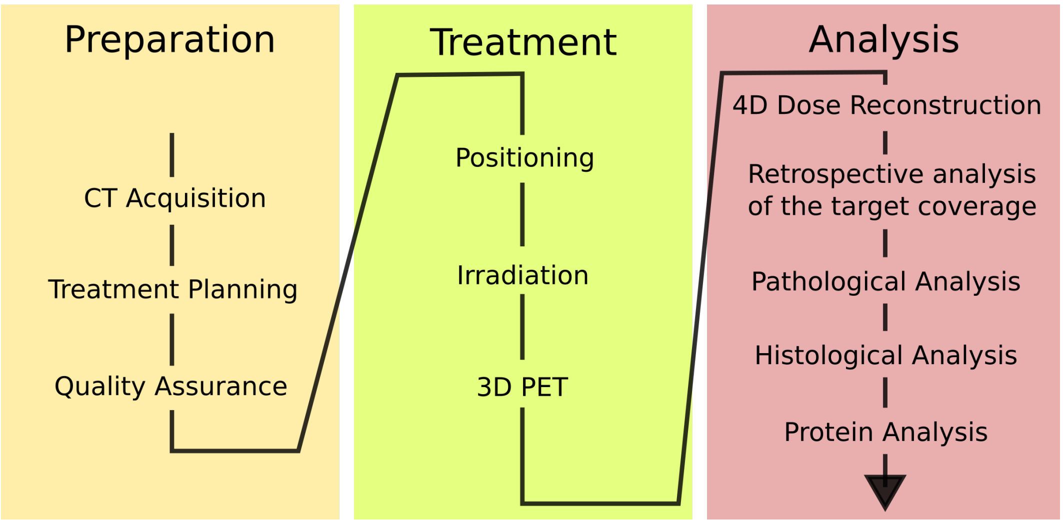

Figure 2.1.: Overview of the workflow carried out for each pig during the feasibility study.

2.1.3 Fixation

A fixation device was constructed to allow a reproducible positioning of the animals during the computed tomography (CT) acquisition at Heidelberg Ion-Beam Therapy Center (HIT) and the catheter-free ablation at GSI [Pra14b].

Figure 2.2 shows a drawing of a pig positioned in the fixation device. All pigs were fixed in a PMMA frame containing a vacuum mattress (BlueBAG^{TM}, 750×1025 mm^2, ITV Austria) for hip and lower body as well as a thermoplastic mask for the chest. The vacuum mattress was formed for the first pig and then reused for all remaining ones. An individual thermoplastic mask was modeled for each pig to ensure a stable and reproducible positioning of the chest. On each mask the orthogonal laser lines, indicating the room iso-center, were marked and Beekley spots were placed on the laser intersections. In addition, the laser intersections and the upper and the lower edge of the thermoplastic mask were tattooed on the pigs. The marks, especially at the upper edge of the mask, provided a reproducible position of the front legs avoiding additional tissue in the beam entrance channel.

The fore and hind legs were attached to PMMA bridges, which were connected to the ground plate, using gauze bandages. Therefore the legs were slightly stretched. A supine position of the pigs was chosen as this increased the reproducibility, offered a stable positioning of the animals and facilitated the targeting without additional material in the beam entrance channel. More details on the reproducibility of the positioning will be published in [Pra].

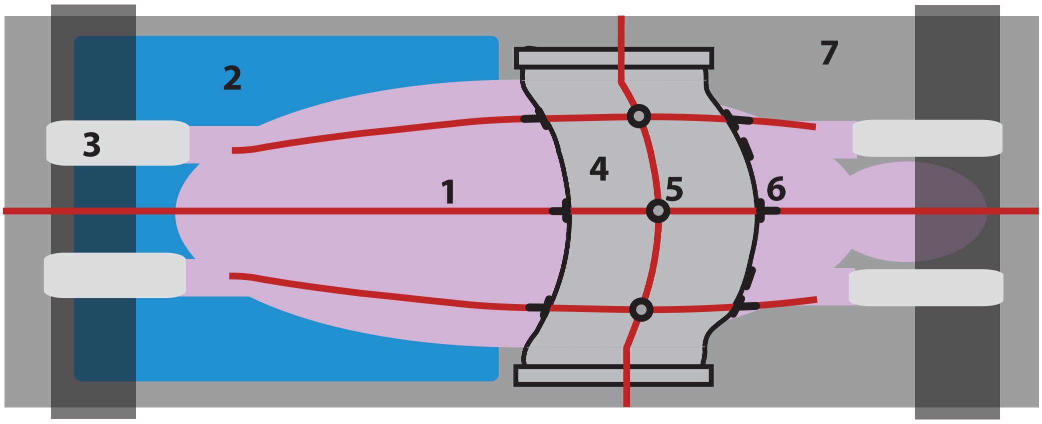

Figure 2.2.: Schematic view of a pig positioned in the fixation device. 1) orthogonal laser lines, 2) vacuum mattress, 3) gauze bandages for the fixation of the legs, 4) thermoplastic mask, 5) Beekley spots at intersections of laser lines on thermoplastic mask 6) tattoos of the outline of the thermoplastic mask and laser lines, 7) fixation device. Figure courtesy of Matthias Prall.

2.1.4 CT Acquisition

Cardiac-gated time-resolved computed tomographys (4DCTs) for treatment planning were recorded at HIT using a multidetector 64 row Siemens Somatom Definition Flash Scanner (Siemens Healthcare, Forchheim, Germany). The full cardiac cycle was divided into 10 motion phases and a 3DCT was recorded for each. A reference phase, phase 0, corresponding to the diastole and the onset of the QRS-complex was selected, as the rising edge in the voltage can easily be detected. The CT was recorded at end-exhale and a respirator was remotely controlled via a Labview interface (National Instruments, Austin, TX, USA) to interrupt the ventilation at end-exhale shortly during image acquisition.

A CT protocol was established to generate 4DCTs with Hounsfield units (HUs) comparable to the planning CTs currently in clinical use for heavy ion treatments at HIT. This was necessary, as the Hounsfield look-up table, converting photon absorption into water equivalent path length, used for treatments at HIT was also applied for the treatment planning of the feasibility study. Further investigations showed that range uncertainties due to the different protocols are negligible as a good agreement of the Hounsfield units was found [Rica].

Two 4DCTs were recorded for every pig. The first CT was a native cardiac-gated 4DCT and the second one was a contrast-agent enhanced cardiac-gated 4DCT. This was necessary as several sub-structures of the heart are not visible in native CT scans. In addition, the correct motion of the cardiac sub-structures can only be determined in contrast-agent enhanced CT scans [Con14], while treatment planning is only possible on native imaging data. All CTs were recorded with a field of view of 500 mm to allow skin-to-skin images, necessary for treatment planning, and with a slice spacing of 1 mm.

For the contrast enhanced CT, 50 cc of a contrast agent (Omnipaque 350 mg, GE Healthcare, USA) was injected with a rate of 4 cc/s. The scan was recorded 8-10 seconds after the injection of the medication to ensure a homogeneous distribution of the contrast-agent within the pig.

2.1.5 Treatment Planning

The treatment planning was carried out using TRiP4D, a treatment planning system (TPS) developed at GSI for ion therapy [Ric13]. TRiP4D is a treatment planning software capable of calculating 4D dose distributions and incorporating different motion mitigation techniques in the planning process for particle therapy (for details see Section 1.1.2.5 or [Ric12]).

In all treatment plans the raster point distance in horizontal and vertical direction was chosen to be 2 mm with a distance of 3 mm between two iso-energy slices (IESs). A minimum number of 5,000 particles per raster point is needed to obtain a position and intensity feedback from the treatment control system (TCS) for successful irradiations at GSI. Thus, the absolute minimum particle number during the optimization was 75,000 as a rescanning scheme with up to 15 rescans was applied. However, as the speed of the irradiation is mainly determined by the particle intensity, which is fixed for the whole IES and depends on the raster point with the lowest particle number, the minimal particle number per raster point was increased until the target coverage started to decrease in order to reduce the irradiation time. Thus, 125,000 particles were chosen as minimal particle number per raster point for 12 treatment plans. For two out of the eight AVN pigs, the minimum number of particles had to be reduced to 75,000 in order to obtain a homogeneous dose distribution in the target volume. For Pig 1 a satisfactory treatment plan using 200,000 particles as a minimum particle number per raster point was obtained.

To ensure the robustness of the treatment, all irradiations were planned using two opposing horizontal fields with angles of 90° and 270°. This reduced the sensitivity to slight displacements and deformations of the heart due to the heartbeat or positioning uncertainties. The treatment plans for the AVN and LV irradiation were both optimized as single field uniform dose (SFUD). Hence, each field was separately optimized with half of the planned target dose. This approach increases the robustness of the treatment plans, as it removes gradients within the overlapping fields. In case of the SPV irradiations, the proximity of the target volume to several OARs required the usage of intensity-modulated particle therapy (IMPT), even though this reduced the plans' robustness. For the optimization of the SPV treatment plans the AVN was included in the optimization as OAR. The aim was to reduce the maximum point dose in the AVN below 30 Gy to avoid severe side effects as, for instance, AV-blocks. Hence, for Pig 12 and 14 the maximum dose allowed in the OAR was set to 70 % and for pig 13 to 80 % of the planned target dose. The weighting factor for the OAR was chosen to be 0.9 for all SPV pigs.

Prior to the treatment not only standard 3D, but also 4D dose simulations were carried out. All 4D dose calculations were compared to the 3D simulations, which served as reference for successful motion mitigation. The motion effect on the delivered dose distribution was estimated to ensure a successful irradiation in the presence of the heart motion.

In order to calculate 4D dose distributions [Ric12], each phase of the 4DCT had to be registered to the reference phase and vice versa using a deformable image registration (DIR). Slicer3D (Version 4.3) [Fed12] and Plastimatch (Version 1.15.17) [Sha10a] were used to perform this important process.

The goal of the treatment planning was to reach a median D_{95} value, greater than 95 % in the target volume (TV) and ensure that the minimum of the inner quartile range of D_{95} is above 80 % for all performed and motion mitigated 4D simulations in the planning target volume (PTV).

Contouring and Target Definition

Target structures and OARs were contoured prior to the treatment planning by a physician. The contouring process, also important for the risk evaluation, was conducted using Syngo PRT Planning (VC11B, Siemens AG, Erlangen, Germany) and Eclipse (Varian Medical, Palo Alto, CA, USA) treatment planning software. Prior to the treatment, only critical structures for the treatment planning were contoured due to the limited amount of time between image acquisition and irradiation. For a full analysis additional structures were added retrospectively. For each pig up to 21 OARs were available. For catheter-free ablation of the AVN a 5 mm sphere contoured in the AV junction was used as TV. For SPV as well as LV irradiation, targets were defined by polygons in transverse CT slices.

Margins

Safety margins were added to the TV to account for systematic errors and anatomical changes between treatment planning and the actual treatment. In the first step, isotropic 5 mm margins were added to the TV for the AVN and SPV target group to contruct the PTV. In the second step a range internal target volume (ITV) was created using the envelope of the PTV transformed to all motion states. For the treatment of the LV group margins of 2 mm + 2 % of the beam range in water were added in beam's eye view. A range ITV was calculated considering the applied range margins. Further details on the range ITV can be found in [Gra12]. The differences in the margins chosen for AVN and SPV ablation on the one side and LV irradiations on the other side can be explained with the different aims of the treatment. While a precise ablation of anatomical structures was necessary for AVN and SPV, the aim for the LV irradiation was an induction of a transmural lesion in the free-wall of the left ventricle.

Organs at Risk

The targeted sub-structures in the heart were in close proximity to several OARs. Hence, it was necessary to determine a certain number of critical structures for each target. The mean and max doses were investigated for lungs, left coronary artery (LCA), right coronary artery (RCA), myocardium, pericardium and skin. Depending on the target volume, additional critical structures were analysed. For the AVN group, aorta and pulmonary artery (PA) were examined. For the SPV group, trachea, esophagus, AVN as well as superior vena cava (SVC) and for the LV group PA were analyzed.

	Dose Volume Limit		
OAR	Volume Threshold [cm^3]	Dose Threshold [Gy]	Max. Point Dose [Gy]
Aorta	10.0	31.0	37.0
Trachea	4.0	10.5	22.0
Esophagus	5.0	11.9	19.0
Skin	10.0	23.0	26.0
Myocardium	15.0	16.0	22.0

Table 2.2.: Dose-volume and maximal point dose constraints of the most affected OARs [Gri11, Ben10].

In addition to mean and max doses, dose volume constraints were investigated for certain structures, as recommended by the Radiation Therapy Oncology Group (RTOG) for patients undergoing radiosurgery. The OAR limits applied throughout this study are listed in Table 2.2. For the maximum point dose deposited in the LCA and RCA 30 Gy were assumed as acceptable. No data is published on the radiation sensitivity of these structures. Therefore the limit is adapted from the known constraints for great vessels and was approved by the physicians conducting the study.

Motion Mitigation

To avoid overdosage in OARs and underdosage in the TV due to interplay effects, it was necessary to apply motion mitigation techniques as explained in Section 1.1.2.5. The first motion type that requiring mitigation is the breathing motion. As the pigs had to be anesthetized throughout the procedure and were externally ventilated using a respirator anyhow, repeated breath-holds were used to suppress the breathing motion completely. A remotely controlled respirator could be paused up to 120 seconds allowing consecutive breath-holds at a reproducible lung volume.

The second motion type, which was more difficult to compensate, was the heartbeat. In contrast to breathing, the heart cannot be stopped during the irradiation. Hence, it was necessary to compensate for the heartbeat by applying a motion mitigation technique during treatment and treatment planning. A planning study showed that rescanning is a promising method to account for heart motion while keeping the technical effort and the irradiation time as small as possible [Con14,Con16]. However, as the amount of beamtime was limited and the preparation for the pigs, including anesthesia and positioning, was lengthy, it was important to keep the irradiation time short. Thus, a new, inhomogeneous rescanning scheme was applied. A schematic of the rescanning strategy is shown in Figure 2.3.

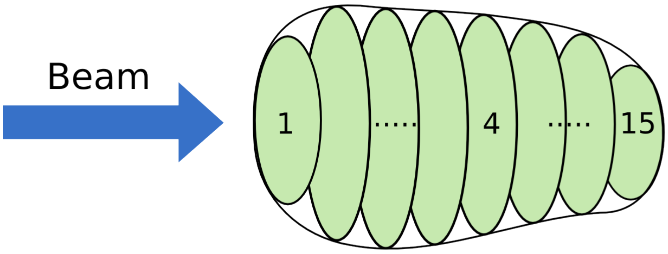

Figure 2.3.: Schematic of the inhomogeneous rescanning scheme used for the irradiation. The numbers in the IESs indicate the number of rescans for each IES.

In the standard scheme every IES is rescanned a specific number of times, usually between 5 and 20, depending on the present motion amplitude. The new, inhomogeneous scheme assumes that the proximal slices are already partly rescanned by the irradiation of the distal slices. This allows a reduction of the number of rescans in the proximal IESs . Hence, an polynomial decay of rescans was applied and the number of rescans decreased from the distal slice with 15 rescans to the proximal one with only one rescan following Equation 2.1.

$$N_{\text{Rescans}}(i) = N_{\text{Max}} - \left\lfloor 0.5 + \left(\frac{i}{N_{\text{Slices}} - 1} \right)^{0.3} \cdot (N_{\text{Max}} - N_{\text{Min}}) \right\rfloor \tag{2.1}$$

N_{Max} stands for the maximum, N_{Min} for the minimum number of rescansr and N_{Slices} is the number of IESs. Furthermore, i corresponds to the chosen IES.

Simulation Parameters

To investigate the effectiveness of the applied motion mitigation technique, different sets of dose calculations were performed, determining target coverage and doses deposited in several OARs in close proximity of the target volume. After optimization and calculation of a 3D dose distribution, additional 4D simulations were carried out to estimate the influence of motion effects on the uncompensated and compensated treatment. Therefore three different sets of 4D simulations were realized:

1. **Interplay** - 4D Simulations taking into account the motion effects assuming no motion mitigation technique for the heartbeat is applied.
2. **Homogeneous Rescanning** - 4D Simulations applying a conventional homogeneous rescanning scheme with 15 rescans in each IES.
3. **Inhomogeneous Rescanning** - 4D Simulations applying the inhomogeneous rescanning scheme developed for the feasibility study.

To investigate the sensitivity of the dose distribution with respect to changes in the motion period and to ensure the robustness of the treatment plan, all simulations were performed using variations of three different parameters: heart frequencies, regularity of the heartbeat and spill structure. For all pigs the heart frequency was simulated using two different motion surrogates, both are shown in Figure 2.4.

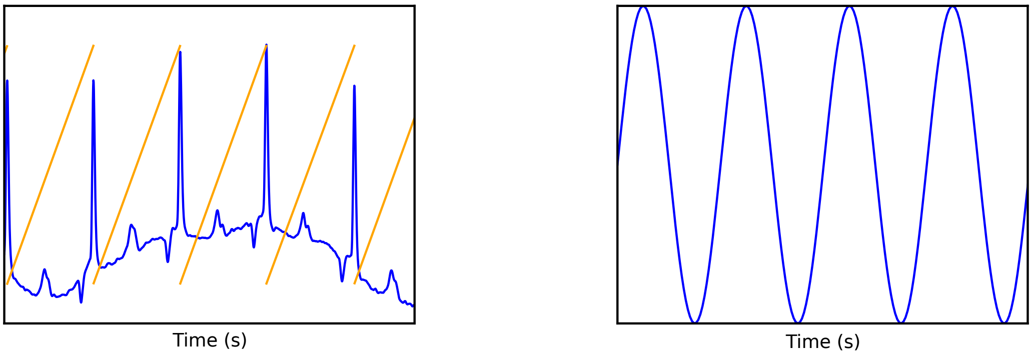

(a) Irregular ECG motion. The blue line correspond to the measured voltage and the orange line represent the corresponding motion surrogate used for the treatment planning as input data.

(b) Regular sine wave motion surrogate. Each period of the sine wave corresponds to one heartbeat.

Figure 2.4.: Scheme of the two different types of motion surrogates.

One was a measured ECG trajectory recorded of an arbitrarily chosen pig at Mayo Clinics (Mayo), the second one is a regular sinus function. These trajectories were scaled to an average value of 60, 70 and 80 beats per minute, corresponding to heart rates expected during the irradiation. As the timing of the sinus function is regular, a sinusoidal motion surrogate represents constant heart rate during the full treatment time. In contrast to this, the measured and scaled ECG trajectory shows an irregular behavior and, hence, corresponds to a slightly varying heart rate over the time of the treatment.

In addition, the 4D simulations were carried out for 8 different starting phases to investigate the outcome for different temporal correlations between the beam delivery sequence (BDS) and the target motion. One spill structure is a constant particle intensity over the whole extraction time, while the other one is a Gaussian shaped intensity behavior. Combining all simulation parameters yielded 96 simulations per pig for each of the interplay, inhomogeneous and homogeneous rescanning scenarios. Hence, in total 14 3D simulations, 1344 interplay and 2688 rescanning simulations were conducted to ensure plan robustness, a satisfying target coverage and an efficient sparing of the OARs.

Data Analysis

Several parameters were used to verify the quality of a treatment plan. The main aim of the treatment planning presented in this work was to reach a homogeneous dose distribution avoiding underdosage in the target volume, while overdosage was seen as less critical. Furthermore, the dose deposited in the OARs was examined to avoid overdosage. The main parameters for the analysis of the target coverage are the minimum dose to 95 % of the target volume (D_{95}), the volume that received at least 95 % of the planned dose (V_{95}) and, finally, D_5-D_{95}, as a measure for the dose homogeneity of the target volume. In addition, the dose to the OARs was assessed as dose volume, maximum point dose and mean dose. The results for the PTV could only be only determined for the AVN and SPV irradiation. Due to the different margin approach for the LV, no geometric PTV was defined.

2.1.6 Quality Assurance

Prior to the experiment, quality assurance (QA) was carried out once, validating the focal spot size, beam position and range, dose homogeneity and selected safety features. In addition, a daily QA was carried out every morning checking the beam position and dosimetry.

The nights before treatment, treatment plan QA was performed. All treatment plans were irradiated into a water phantom equipped with 24 pin-point ionization chambers (Type 31009, PTW, Freiburg, Germany). The pin-points were placed in a plastic holder with a distance of 12 mm in lateral direction and 10 mm in depth. Furthermore, the 24 pin-point ionization chambers were arranged at three different heights with a 6 mm distances between each level to avoid shielding of the distal chambers by the proximal ones. To increase the resolution of the measurement, it was repeated 2 to 3 times on average with the pin-point holder at different positions allowing a minimal resolution of 4 mm.

The pin-point holder was attached to an industrial robotic arm (Kuka KR5 sixx R850, Augsburg, Germany), which was able to follow the trajectory of the target. The motion trajectories were extracted from the 4DCT registration and can be found in 2.9. This allowed 4D verification in addition to the standard 3D one. In Figure 2.5 the experimental set-up is shown.

To analyze the recorded verification data, two different tools were used. First of all, a read out software is available for the MP3 water phantom [Kar99], which allowed online read out and verification. On the other hand extract+, a command line based program developed at GSI, was used to analyze the data [Ric12]. This tool includes an optimization algorithm to determine the most probable position of the pinpoint holder corresponding to the best agreement between measurement and simulation. This algorithm was used to detect systematic set-up errors during the verification. Hence, a set-up error was determined in the final analysis for each night.

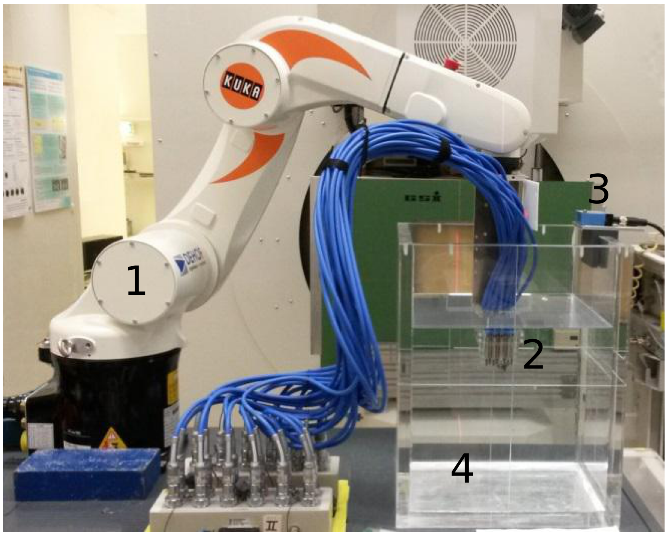

Figure 2.5.: Experimental set-up for 3D and 4D dose verification. 1) robotic arm, 2) ionization chambers, 3) Laser distance sensor, 4) water phantom

For the 3D analysis, an average agreement of all 24 pinpoints was calculated for each plan. In Section 2.2.1 the agreement of all plans is presented. For the 4D analysis, the dose at the average position of the ionization chamber was compared to the result of the calculated dose distribution.

To allow the irradiation of a treatment plan a maximum mean deviation of 5 % was accepted. Higher deviations for single ionization chambers were allowed due to the high gradients within and the small size of the fields. However, in case of higher deviations it was always double checked if the corresponding pinpoint was positioned in a gradient.

2.1.7 Positioning, Preparations and Treatment

After sedation, the animals were transported from the preparation room to the irradiation room. The respirator and the propofol infusion were connected before positioning the pigs. After a pig was adjusted to all markers, supporting structures were double checked for the correct vertical and horizontal position of the hip to avoid contortion of the pig. Immediately before the treatment, the exact position was controlled using orthogonal X-rays. The recorded images were compared with the projections of the CT scans used for treatment planning. In Figure 2.6 the whole set-up of the experiment in the irradiation room is shown.

Data Acquisition during Treatment

Three different data acquisition systems (DAQs) were used during the treatment. The ECG signal and the BDS were recorded with a real-time data acquisition system, a Beckhoff EtherCAT system (Beckhoff Automation. Verl, Germany), to provide a time correlation between the BDS and the heart motion for 4D dose reconstruction. In addition, a second Labview based DAQ system (National Instruments, Austin, TX, USA) was used to redundantly store identical information. Furthermore, the Labview system was applied as a remote control for the respirator.

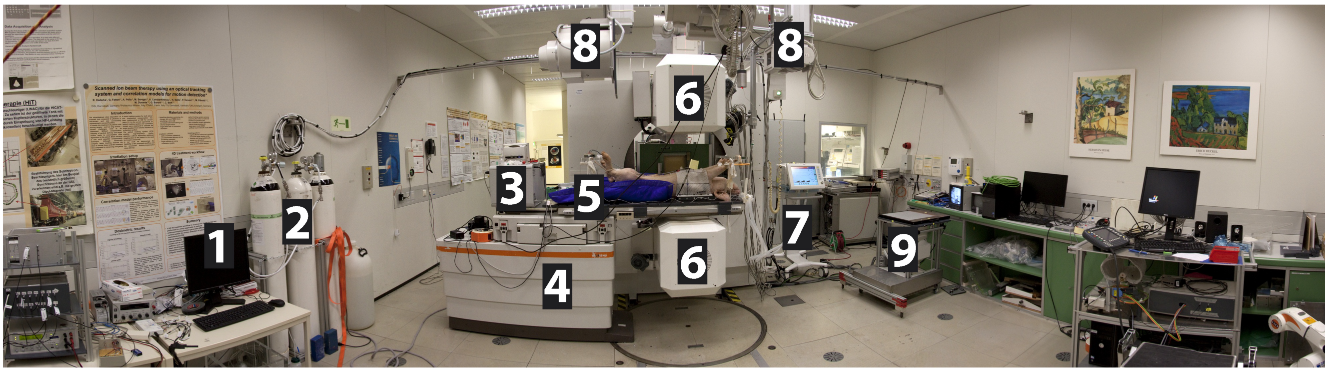

Figure 2.6.: Panoramic view of the treatment room at GSI. 1) DAQs and respirator control, 2) oxygen and medical air for ventilation, 3) pulsoxymeter and ECG monitor, 4) patient couch, 5) pig immobilization device, 6) PET cameras, 7) ventilator, 8) horizontal X-ray system, 9) vertical X-ray system. Figure courtesy of Matthias Prall.

Information about the delivered treatment plans was recorded by the TCS, which stored the actual position of the pencil beam in horizontal and vertical direction as well as the number of particles delivered to each raster point.

ECGs

The ECGs recorded during the irradiation were analyzed to investigate the change in the heart rate during the treatment. Additionally, the analysis was used to check the correct conversion of the recorded ECG to the motion surrogate used for the 4D dose reconstruction. Therefore the average, minimum and maximum heart rates were determined for each field and pig during the irradiation. In addition, the change in the heart rate between field 1 and field 2 and the behavior of the heart rate during the irradiation was investigated.

2.1.8 Dose Verification Methods

Two different types of dose verification methods, in-room positron emmission tomography (PET) imaging and 4D dose reconstruction, were applied to gain information on the quality of the treatment. Nevertheless, both methods cannot conclusively verify the success of the treatment. While the 4D dose reconstruction cannot include positioning uncertainties, PET imaging can only display deviations to the planned dose position, as both techniques rely on the 4DCT used for the treatment planning. Furthermore, the activity maps obtained from the PET imaging are not proportional to the deposited dose.

In-Room PET Imaging

A two-head in-room PET (CTI PET Systems Inc., Knoxville, TN, USA) was installed in the irradiation room, which allowed a measurement of the actual beam penetration depth. Therefore reconstructed activity maps are overlaid with the treatment planning CTs to visualize the position of the deposited dose. To gain the activity maps radioactive fragments produced due to fragmentation processes during treatment, emitting β^+-activity, are measured. In-room PET can be successfully used as a quality control for the irradiation with carbon ions providing valuable information about the actual penetration depth of the ions [Par07].

The PET images were taken in the spill pauses and after the irradiation under breath-hold. The measurement time for the PET analysis was between 10 and 39 min. During this time the respiration of the pigs was frequently stopped and data was taken. The measurement always took place after the irradiation of the first field. More details can be found in [Hel14, Leh16b].

4D Dose Reconstruction

The ECGs of all pigs were recorded during the treatment. On the one hand, ECGs gave information on the health status of the pigs. On the other hand, these ECGs were used as motion surrogate for 4D dose reconstructions to gain information on the actual dose delivered during the treatment. Besides the ECG also the BDS was recorded providing the temporal correlation between the irradiated raster point and the corresponding motion phase.

To conduct the 4D dose reconstruction, the data already used for the treatment planning is needed, including the DIR and the planning CT. This data is combined with the data recorded during irradiation to calculate the actual delivered 4D dose distribution. These steps could be performed in less than one hour after the treatment, allowing a first feedback on the quality of the irradiation. Furthermore, a 4D dose reconstruction using the actual delivered particle number and position of each raster point recorded by the TCS was performed to also account for uncertainties of the beam delivery.

For the 4D dose reconstruction a graphical user interface (GUI) was developed to facilitate the processing of the data and the creation of the files for the treatment planning. A more detailed description of the general process of a 4D dose reconstruction can be found in [Ric14]. Further details on the GUI and the reconstruction procedure for this experiment will be published in [Ricb].

2.1.9 Biological Endpoints

The biological endpoints investigated are: fibrosis, cell death to eliminate cardiomyocytes, dysfunctions of cardiomyocytes, inflammation processes and vascular damage in the irradiated area. For detailed descriptions of the biological processes the reader is referred to [Pre10, See12, Boe11, Fan12, Sag13].

All of these processes are considered to be meaningful for the interruption of the conductivity of the targeted structures. Therefore a pathological examination was carried out directly after the withdrawal of the heart and lung package. To facilitate the identification of the scar tissue within the heart muscle, a redox indicator (triphenyltetrazolium chloride) was used to improve the visibility of the fibrotic tissue.

For a deeper understanding a histological and a protein analysis was carried out afterward in the laboratories of GSI and UCHD. If possible, two different samples were taken for each anatomical structure. For preservation, samples for the histological analysis were fixed in 4 % formaldehyde and samples for the protein analysis were shock frozen with dry ice. The further processing methods of both probes are described in detail in [Fou04, Sim10].

For the histological analysis the tissue samples were embedded in paraffin and cut in slice. Afterwards a Hemotoxylin-Eosin as well as Mallorys Trichrome staining was performed. The analysis allowed the investigation of the amount of bleeding in the tissue and the examination of structural changes in the cardiomyocytes. Further details on the techniques used for the histological analysis can be found in [Sim10].

In addition, a protein analysis was carried out to investigate the presence of apoptosis at two time points, 3 and 6 months after irradiation. This was done by determining the amount of cleaved caspase 3, which is a common marker for apoptosis, in the protein extractions. The protein expression was visualized using chemiluminescence (ECL, Amersham Biosciences) and detected on films (ECL-Hyperfilm, Amersham Biosciences). Further details on the protein analysis in general can be found in [Fou04].

2.2 Results

The following section provides an overview of the experimental results. A detailed analysis is given for the treatment planning process and the results of all other topics are summarized. Further details and analysis of the latter sections can be found in [Leh16b, Erb15, Gra14, Eic15] or will be published in [Pra, Kad, Ricb]. Throughout this chapter all results are either given as mean values with standard deviation (mean ± standard deviation) or as median values with the range between the 25th and 75th percentile (median (25 % - 75 %)).

2.2.1 Quality Assurance

The set-up error of the 3D and 4D dose verification were determined to be between 0.3 and 2.5 mm in depth, 0.6 - 1.4 mm in vertical and 0.0 - 0.8 mm in horizontal direction. The former are relatively large and were caused by the limited time to set-up the verification equipment.

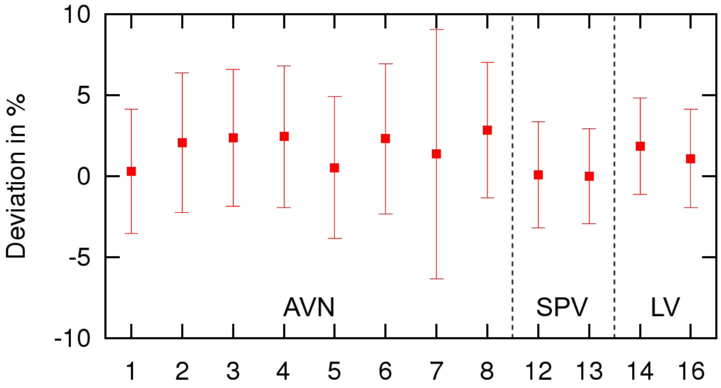

Figure 2.7.: Deviations of the 3D verification measurements in the water phantom from the planned dose. For each pig the mean value of both fields including all 24 pinpoint ionization chambers and the standard deviation of the deviations is shown. The different target groups are indicated with dashed lines. From left to right, the results for AVN, SPV and LV irradiations are shown.

Verification was carried out for all 14 irradiated pigs. For Pigs 15 and 17, only a 4D QA was performed due to limited beamtime and promising results of the previous 4D verifications. For the remaining 12 pigs a 3D verification was performed in addition to a 4D verification. After the correction of the systematic positioning errors, the overall deviations between measured and planned dose were 1.9 ± 4.6 %

and 0.8 ± 5.3 % for 3D and 4D dose verification, respectively. The calculated standard deviation was increasing with decreasing field size due to the high gradients and the poor resolution of the set-up. In Figure 2.7 the results for the 3D verification for each pig are shown. Detailed results for the 3D verification showing the results for each pig and field can be found in Table A.1. All plans were within the stated limits and therefore accepted for treatment.

2.2.2 ECGs

The average heart rate was found to vary between 50 bpm and 89 bpm during. For all pigs combined the average heart rate was 65 ± 10 bpm. A detailed overview of heart rates for all pigs and fields can be found in the Table A.2. An exemplary ECG behavior during irradiation is displayed in Figure 2.8(a). A similar behavior was found for the majority of the pigs, although not always as pronounced as shown in the figure. While the heart rate is regular before the treatment starts, it decreases during the breath-holds and increases again when the respirator is turned on.

The differences in the average heart rate between field 1 (90 degrees) and field 2 (270 degrees) can be found in Figure 2.8(b). In general, a increase of the heart rate between the irradiation of field one and field two was found. This can be explained by the reduced impact of the premedication, which is known to reduce the heart rate [Aza].

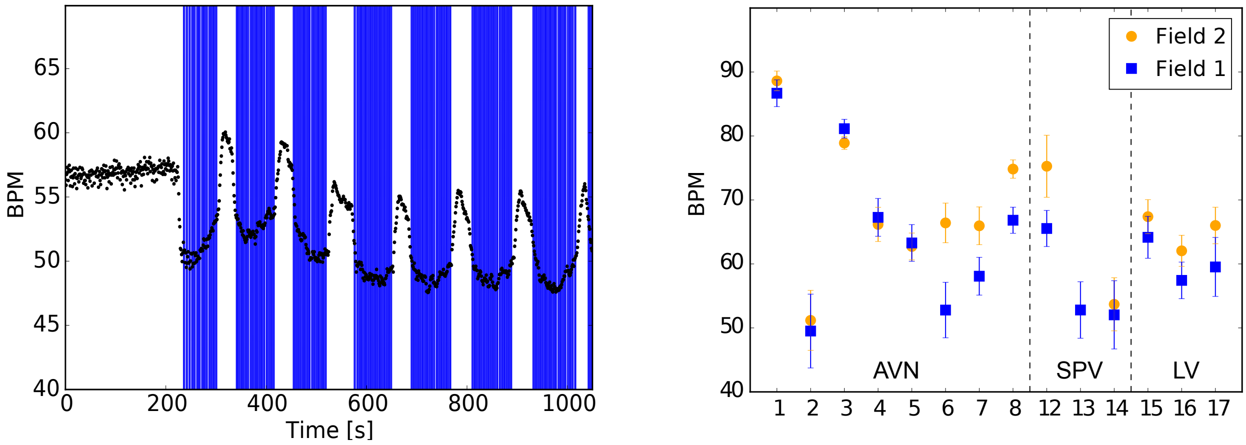

(a) Exemplary time dependent behavior of the ECG during irradiation. The displayed trajectory was measured in Pig 13 during the irradiation of the first field. While in black the heart rate is visualized, the blue areas correspond to the time windows when the respirator was switched off.

(b) Average heartbeat and standard deviation for each pig and field. Different target groups are indicated with a dashed line. From left to right AVN, LV and SPV are shown.

Figure 2.8.: Analysis of the measured heart rates during the irradiation.

2.2.3 Motion of Targeted Substructures

The displacement of the center of mass of the three target areas due to the heartbeat is shown in Figure 2.9 for all pigs. The absolute value of the motion amplitude vector is plotted as a function of the motion phase, relative to the reference phase.

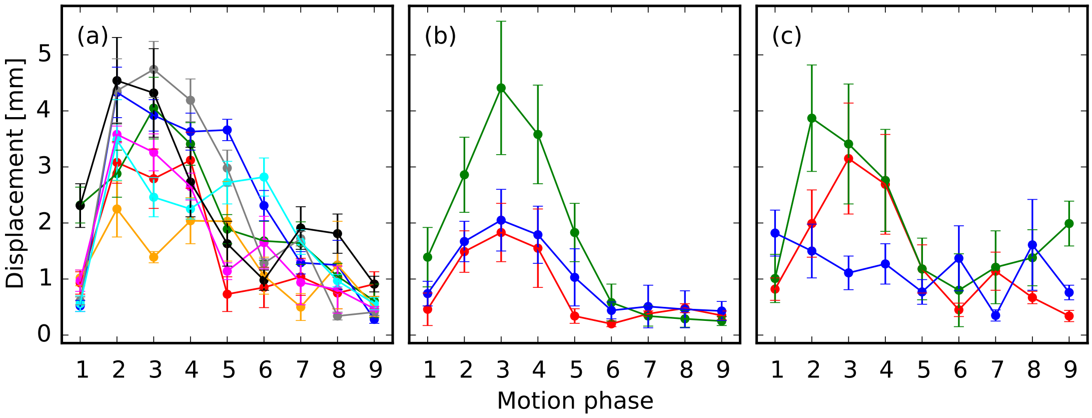

Figure 2.9.: The displacement of the center of mass of the target volume for all motion phases relative to the reference phase. The figures corresponds to the three different targets, the AVN group (a), the LV group (b) and the SPV group (c). Each pig is represented by one line. The depicted uncertainties shown for all motion phases are the calculated standard deviation.

The displacement of all target volumes is chaotic and varies strongly between the different pigs for all motion directions. In the studied animal cohort, the AVN group showed the biggest motion amplitude with maximal displacements of 3.8 ± 0.5 mm. For SPV and LV maximal displacements of 3.9 mm and 4.4 mm were determined, respectively. For the AVN, the motion direction with the largest displacement was found to be anterior-posterior with a mean value of -3.0 ± 0.5 mm. For the LV and the SPV group it was not possible to determine a major direction of the motion amplitude. The maximal displacement from the reference phase is stated for each pig and each motion phase in Table A.3. It was found that the maximal displacement for all target volumes is occurring in motion phase 2 or 3, at 20 % or 30 % of the cardiac cycle. These motion phases correspond to the ventricular systole, where the maximum of the ventricular contraction is reached. However, Pig 14 shows a different behavior lacking any clear maximum motion amplitude.

The presented motion trajectories express the knowledge at the time of the experiment. In Chapter 3 further details are given on the displacement of the targets and the accuracy of the applied DIR used to determine the displacements of the heart structures.

2.2.4 Treatment Planning

The following section summarizes the results of the treatment planning process for the feasibility study. All results presented are calculated with the level of the knowledge before and shortly after the experiment. To facilitate the understanding a consistent color scheme is applied throughout this section. In all figures orange, green, blue and light blue are used for static, interplay, inhomogeneous and homogeneous rescanning simulations, respectively.

Target Coverage

Exemplary dose distributions of rescanned 4D simulations for all three targets are shown in Figure 2.10. Detailed results for the target coverage of the different simulations types are given in the corresponding subsections.

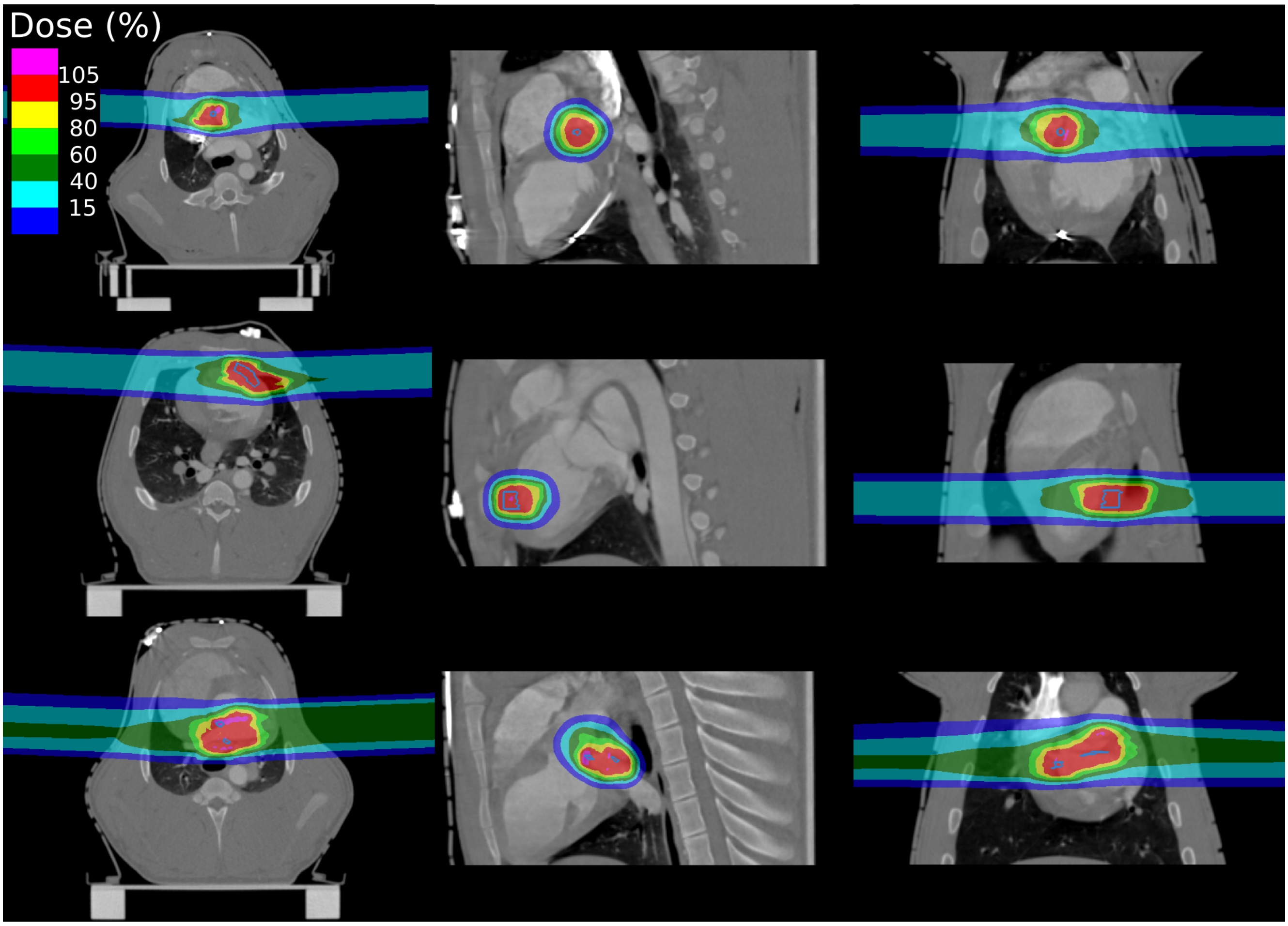

Figure 2.10.: Exemplary dosecuts for all targets in axial (left), sagittal (middle) and coronal (right) view. Dose distributions for AVN, LV and SPV are shown in the top, middle and bottom row, respectively. The targeted area is marked in blue, while the red and pink areas display the areas with more then 95 % of the planned dose.

Static Simulations

D_{95} and V_{95} are greater or equal to 100 % for TV and PTV in all pigs. The homogeneity index D_5-D_{95} varies between 0.06 % and 4.46 % for all pigs. In Figure 2.11 D_{95}, V_{95} and D_5-D_{95} values are shown for all static simulations. An overview of the results is given in Table 2.3. Further results can be found in Figure A.1 and Table A.4.

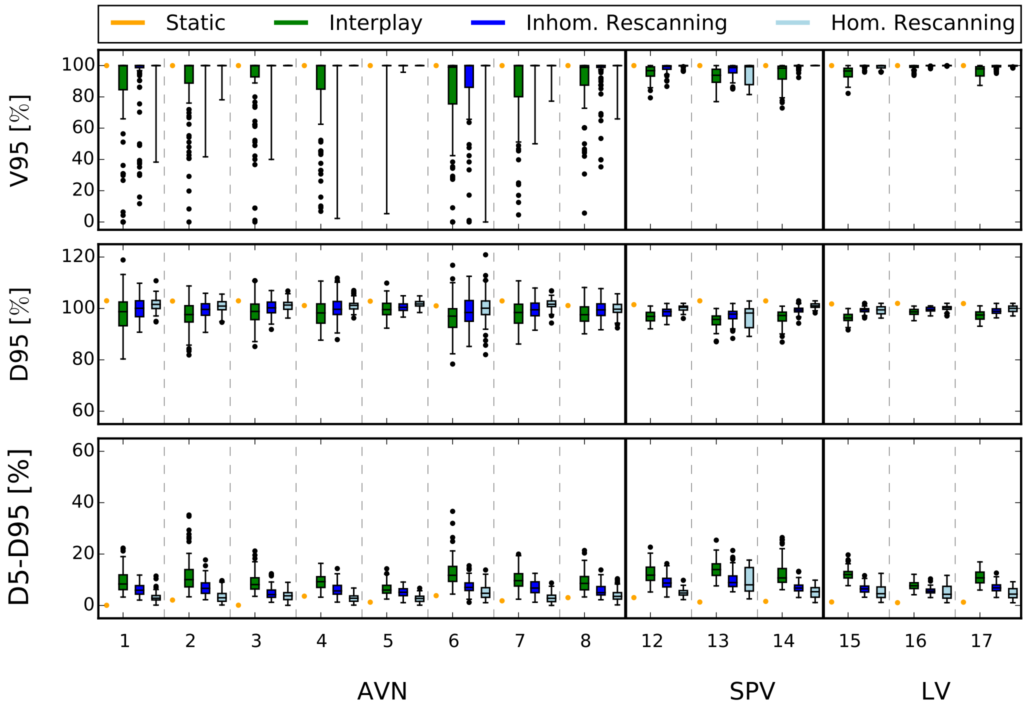

(a) Simulation results for the TV.

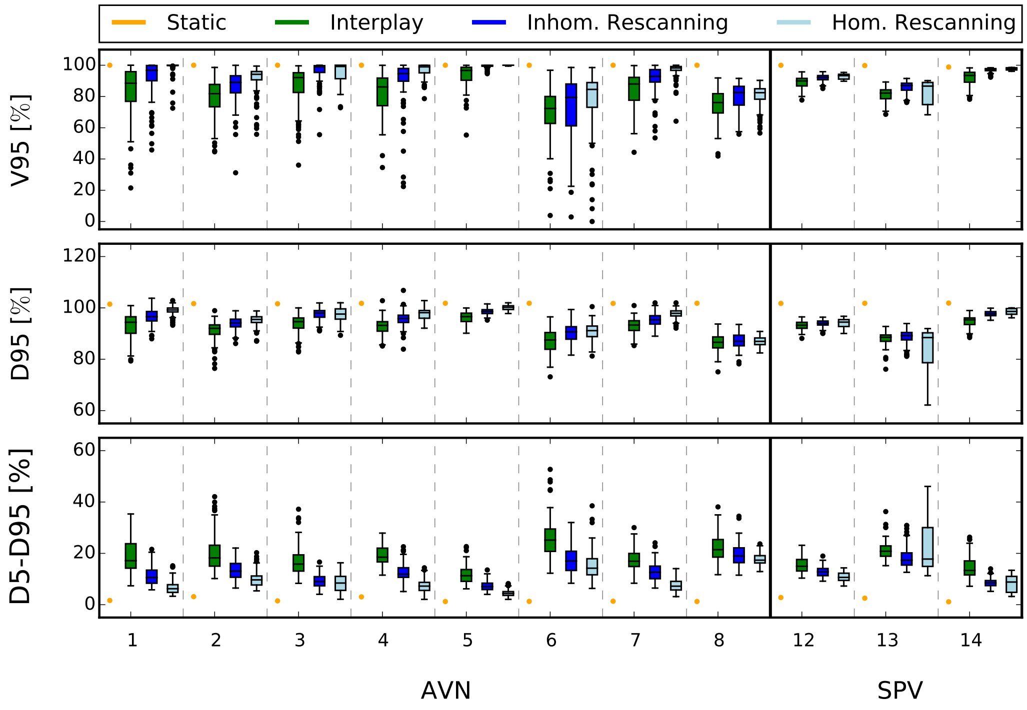

(b) Simulation results for the PTV.

Figure 2.11.: The results for V95, D95 and D5-D95 for TV and PTV are shown for static, interplay, inhomogeneous and homogeneous rescanning simulations. From left to right AVN, LV and SPV results are shown. Single target groups are separated by solid black lines, single pigs are separated by dashed gray lines. Static, interplay, inhomogeneous and homogeneous rescanning results are shown in orange, green, blue and light blue, respectively. The median value is indicated with a solid line, the boxes represent 25 - 75 % of the data and the whiskers showing 1.5 times the inner quartile range. Outliers are indicated with dots.

		TV	PTV
D_{95} [%]	AVN	102.8 (101.1 - 102.9)	101.8 (101.7 - 101.8)
	SPV	102.9 (102.2 - 103.0)	101.8 (101.8 - 101.8)
	LV	101.9 (101.8 - 101.9)	-
V_{95} [%]	AVN	100.0 (100.0 - 100.0)	100.0 (100.0 - 100.0)
	SPV	100.0 (100.0 - 100.0)	99.8 (99.3 - 99.9)
	LV	100.0 (100.0 - 100.0)	-
D_5-D_{95} [%]	AVN	2.0 (1.0 - 3.2)	1.4 (1.3 - 2.0)
	SPV	1.6 (1.5 - 2.3)	2.5 (1.8 - 2.7)
	LV	1.3 (1.2 - 1.3)	-

Table 2.3.: Results showing the target coverage and dose homogeneity of all static simulations. Results are given as median values with the range between the 25th and 75th percentile.

Interplay Simulations

In Figure 2.11 the results for the interplay simulations are displayed in green. Compared to the static simulations, the interplay calculations showed reduced values for the median D_{95} as well and the median V_{95} in the TV. In addition, the dose homogeneity values are decreased. The reduction of the median V_{95} and D_{95} values as well as the increase of the median D_5-D_{95} is more pronounced for the PTV. Further details stating the uncertainties of the results of the interplay simulations are listed in Table 2.4.

		TV	PTV
D_{95} [%]	AVN	98.1 (94.9 - 101.6)	92.6 (88.6 - 95.2)
	SPV	96.4 (94.8 - 98.1)	92.4 (89.4 - 94.8)
	LV	97.6 (96.0 - 98.8)	-
V_{95} [%]	AVN	100.0 (88.9 - 100.0)	85.0 (74.0 - 92.9)
	SPV	96.2 (91.3 - 99.2)	88.0 (83.1 - 92.4)
	LV	98.3 (95.0 - 99.7)	-
D_5-D_{95} [%]	AVN	8.8 (6.5 - 11.9)	18.0 (14.4 - 22.6)
	SPV	12.0 (9.9 - 15.7)	16.8 (13.2 - 20.2)
	LV	10.2 (8.0 - 12.3)	-

Table 2.4.: Results showing the target coverage and dose homogeneity of interplay simulations. Results are given as median values with the range between the 25th and 75th percentile.

In general, no significant differences in the TV and PTV between different combinations of spill structure and regularity of the heartbeat were found, as it can be seen in Figure 2.12. Nevertheless, the influence of the BDS and the motion trajectory on 4D dose distributions are visible. In the appendix detailed results for the interplay simulations are given in Figure A.2, in Table A.5 and in Tabel A.8.

Homogeneous Rescanning Simulations

For the TV the median D_{95} is 101.1 % , 100.1 % and 100.3 % for AVN, LV and SPV, respectively. The median values for the PTV are 97.0 % and 94.5 % for AVN and SPV, respectively. A similar behavior can be seen for the median V95, which is 100 % in the TV for AVN, LV and SPV and decreases to 97.3 % and 93.3 % for the PTV for AVN and SPV, respectively. The median D_5-D_{95} increases from 3.1 % to 8.3 % for AVN and from 5.5 % to 11.3 % for SPV. The D_5-D_{95} for LV is 4.0 %. A reduction of the PTV coverage was

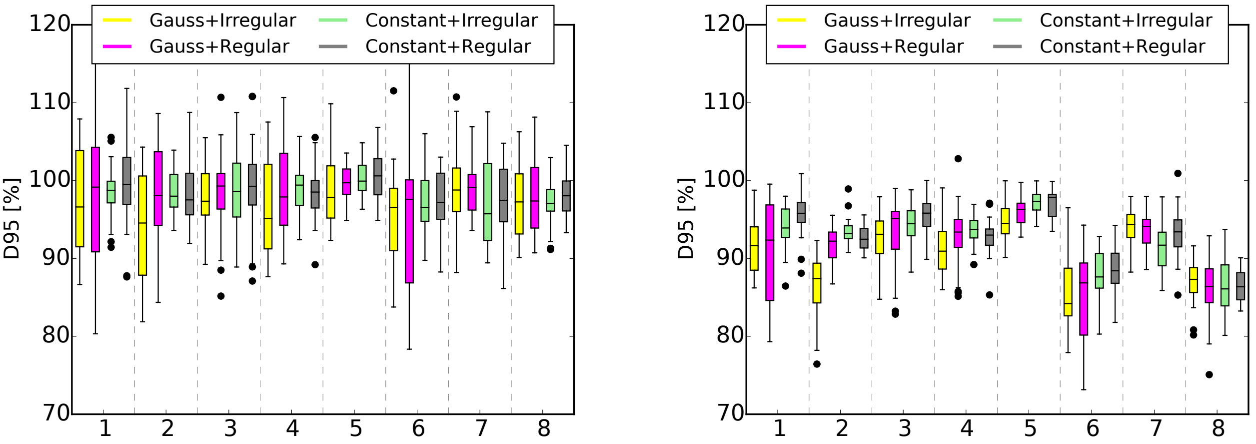

(a) AVN - TV (b) AVN - PTV

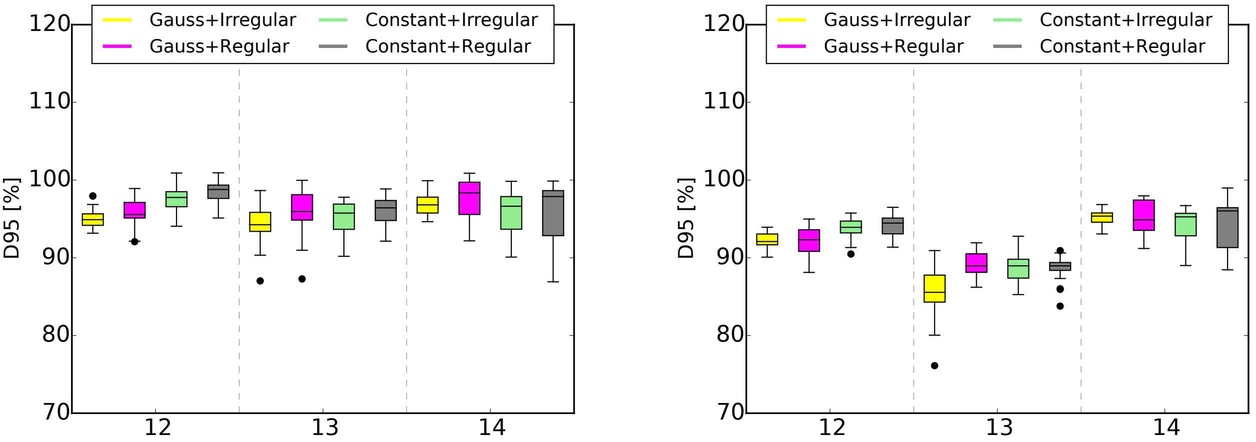

(c) SPV - TV (d) SPV - PTV

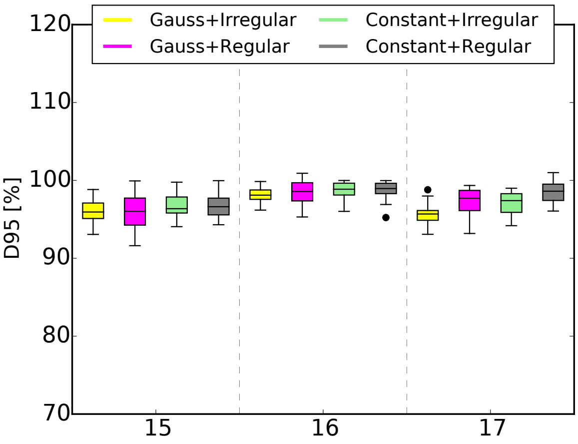

(e) LV - TV

Figure 2.12.: Results for D_{95} for the interplay simulations split by the three different target volumes and TV and PTV. For all pigs the data is separated into the four possible combinations of the spill structure and regularity of the the heartbeat. Each boxplot contains 24 4D simulations. The median value is indicated with a solid line, the boxes represent 25 - 75 % of the data, whiskers show 1.5 time the inner quartile range. Outliers are indicated by dots.

found for some pigs. For Pig 6, 8, 12 and 13 median V_{95} and D_{95} are below 95 %, indicating underdosing within the targeted volume.

More detailed results for the homogeneous rescanning simulations can be found in Table 2.5 and in the appendix in Figure A.3 and Table A.6, stating for V_{95}, D_{95} and D_5-D_{95} the median values and the first and third quartile for each pigs.

		TV	PTV
D_{95} [%]	AVN	101.1 (99.6 - 102.6)	97.0 (92.9 - 99.3)
	SPV	100.3 (99.0 - 101.0)	94.5 (90.1 - 97.5)
	LV	100.1 (98.7 - 100.8)	-
V_{95} [%]	AVN	100 (100.0 - 100.0)	97.3 (87.5 - 100.0)
	SPV	100.0 (99.7 - 100.0)	93.3 (89.0 - 97.0)
	LV	100.0 (99.7 - 100.0)	-
D_5-D_{95} [%]	AVN	3.1 (2.1 - 4.5)	8.3 (5.6 - 12.7)
	SPV	5.5 (4.0 - 7.6)	11.3 (9.4 - 14.6)
	LV	4.0 (3.0 - 7.0)	-

Table 2.5.: Results showing the target coverage and dose homogeneity of homogeneous rescanning simulations. Results are given as median values with the range between the 25th and 75th percentile.

Inhomogeneous Rescanning Simulations

The target coverage of the inhomogeneous rescanning scheme is reduced compared to the homogeneous scheme. Mean D_{95} of the TV was found to be 99.8 % , 99.4 % and 98.7 % for AVN, LV and SPV, respectively. In the PTV, D_{95} is 95.4 % (AVN) and 94.0 % (SPV). The TV results show a V_{95} and D_{95} above 95 %, the results for the PTV are still above the acceptance level. The same trend can be seen for the median values of V_{95}, which are 100 % for the TV for AVN and LV and 99.7 % for SPV. For the PTV V_{95} decreases to 92.9 % and 92.2 % for AVN and SPV, respectively, which is below the aspired threshold of 95 %. Compared to the interplay simulations, inhomogeneous rescanning could improve the target coverage by increasing the median values of the D_{95} and V_{95} by 2 % and 3 %, respectively. The dose homogeneity was improved, indicated by decreasing the median D_5-D_{95} values by a factor of 0.41. The details can be seen in Figure 2.11, where the overview of the results for all simulations is shown.

		TV	PTV
D_{95}	AVN	99.8 (97.4 - 102.0)	95.4 (91.8 - 97.7)
	SPV	98.7 (97.2 - 99.8)	94.0 (90.3 - 96.9)
	LV	99.4 (98.5 - 100.0)	-
V_{95}	AVN	100.0 (100.0 - 100.0)	92.9 (83.9 - 98.9)
	SPV	99.7 (98.0 - 100.0)	92.2 (88.1 - 96.5)
	LV	100.0 (99.7 - 100.0)	-
D_5-D_{95}	AVN	5.8 (4.2 - 7.8)	12.0 (9.0 - 16.4)
	SPV	8.0 (6.7 - 10.1)	12.8 (9.4 - 15.9)
	LV	6.2 (5.2 - 7.3)	-

Table 2.6.: Results showing the target coverage and dose homogeneity of inhomogeneous rescanning simulations. Results are given as median values with the range between the 25th and 75th percentile.

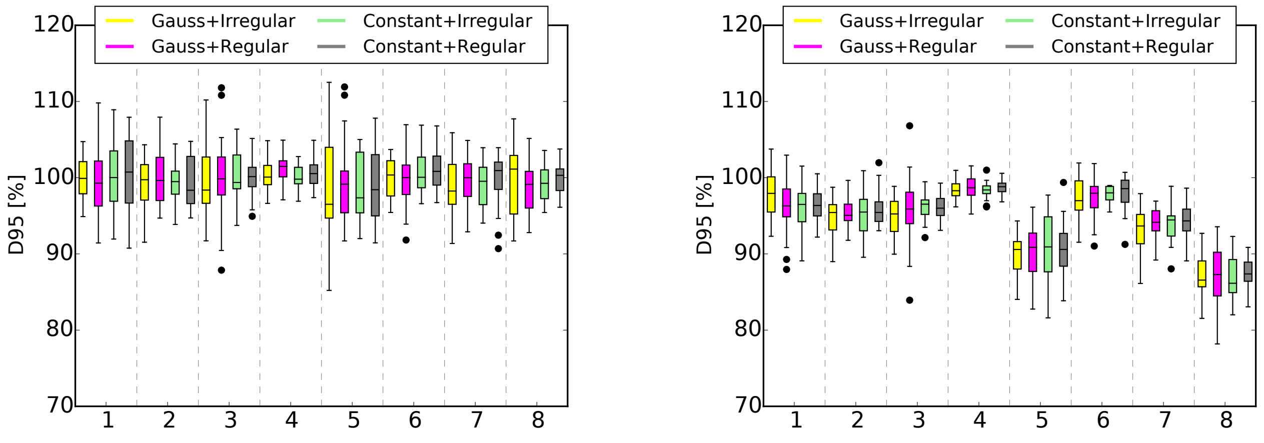

(a) AVN - TV

(b) AVN - PTV

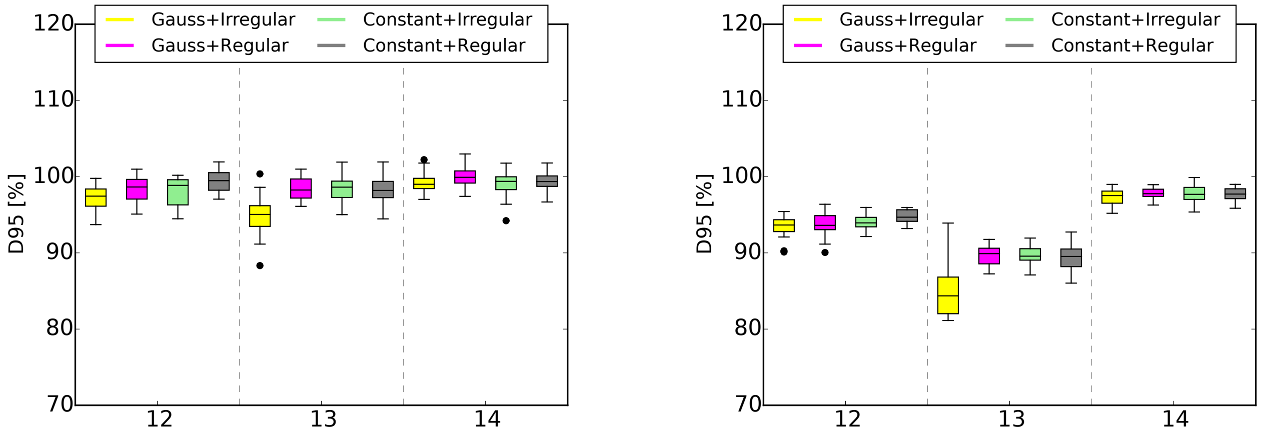

(c) SPV - TV

(d) SPV - PTV

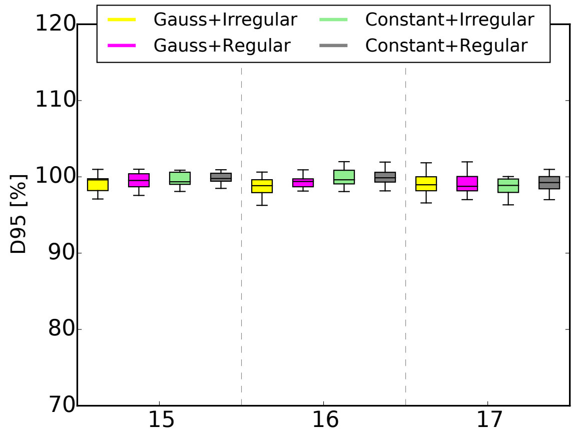

(e) LV - TV

Figure 2.13.: Results for D_{95} for the inhomogeneous rescanning simulations split by the three different target volumes and TV and PTV. For all pigs the data is separated into the four possible combinations of the spill structure and regularity of the heartbeat. Each boxplot contains 24 4D simulations. The median value is indicated with a solid line, the boxes represent 25 - 75 % of the data and the whiskers show 1.5 times the inner quartile range. Outliers are indicated by dots.

None of the combinations of spill structure and heartbeat regularity showed an improved target coverage for all pigs. However, for some pigs slight increases in the target coverage could be found for one of the combinations, as it can be seen in Figure 2.13. For Pig 13 the combination of a Gaussian spill structure and a irregular motion shows a dramatic worsening of the results compared to the other combinations with a significant decrease of median D_{95}. Further details are given in Table 2.6 and in the appendix, where target coverage and dose homogeneity is shown for each pig in Table A.7. Table A.9 gives more details on the influence of the spill structure and the BDS on the 4D simulations.

Irradiation Times

On average, using the inhomogeneous rescanning scheme, the treatment time could be reduced by 66.7 ± 4.1 % compared to the homogeneous schemes. As the time reduction potential depends on the size of the target volume, time savings are increasing with increasing field size. In Figure 2.14 the differences for the irradiation times for homogeneous and inhomogeneous rescanning are shown as well as the treatment time reduction for each pig. In Table A.10 an overview of the time savings achieved by using the inhomogeneous rescanning scheme is given.

The results shown in Figure 2.14 are pure irradiation times from 4D simulations. In the experiment the times necessary for the respiration of the pigs have to be added too. The average treatment time for the irradiation including the respiration time was found to be 10.7 ± 3.6 min, 23.9 ± 8.6 min and 36.2 ± 11.9 min for AVN, LV and SPV, respectively. A detailed analysis of the irradiation times per field and per pig can be found in A.11.

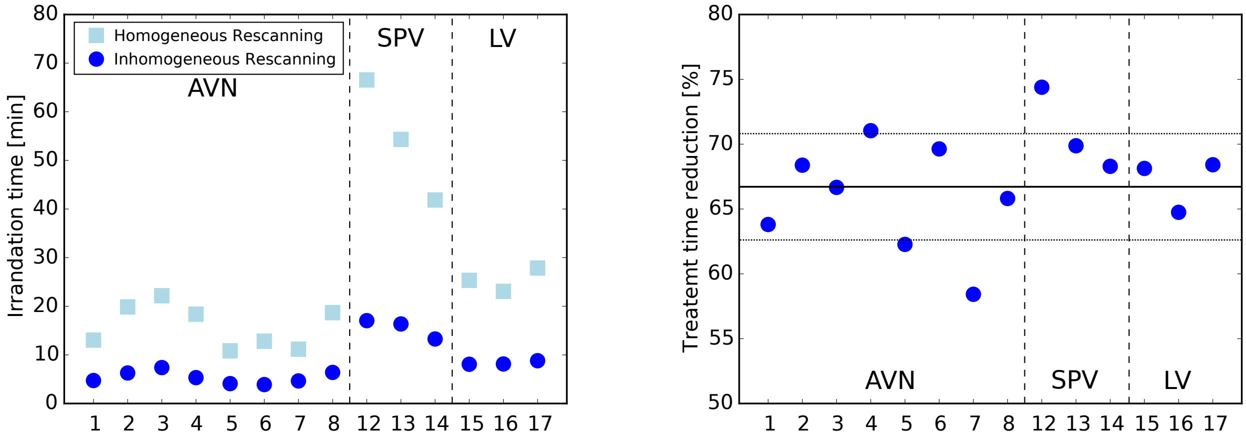

(a) Absolute treatment times for all pigs with homogeneous and inhomogeneous rescanning.

(b) Treatment time reduction for all pigs from homogeneous to inhomogeneous rescanning. Mean value and standard deviation indicated by horizontal solid and dotted lines, respectively.

Figure 2.14.: Differences in the treatment time between homogeneous and inhomogeneous rescanning.

Organs at Risk

For all pigs with an irradiation of the AVN and LV, the maximum dose deposited in the LCA and RCA could be kept below 30 Gy. The maximum point dose in the Aorta and, in general, the maximum point doses in the substructures of the heart were in the region of the target dose due to their anatomical proximity to the targeted area. However, the mean doses in all investigated structures were below the target dose. In addition, dose volume constraints were analyzed for certain OARs. It was shown that for all structures stated in Table 2.2 the dose volume constraints could be kept. Figures A.5, A.7 and A.6 illustrate the excellent sparing of the critical structures due to the use of carbon ions.

Furthermore, several critical structure as, for instance, the trachea and the esophagus could be completely spared for the AVN and the LV irradiation. Respective doses for the SPV treatments were far below the limits. An overview of the maximum and mean doses in the most important OARs is given in Figure 2.15, where the expected doses deposited in the OARs are given for static as well as rescanning simulations.

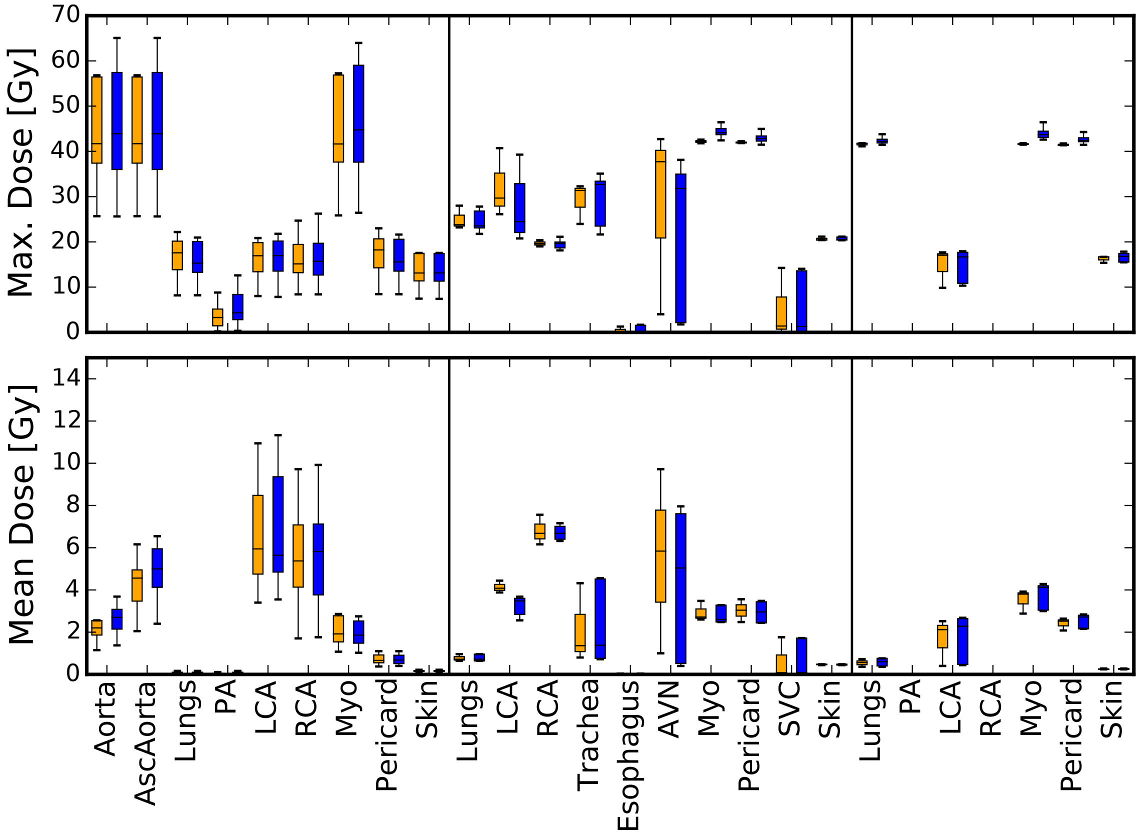

Figure 2.15.: Mean and max dose deposited in the OARs during rescanned 4D treatments (blue) and ideal static treatments (orange). The results are shown for AVN, SPV and LV from left to right. The static boxes summarize the results for all pigs of the corresponding target groups, while the blue boxes include all results of the 96 4D simulations for all pigs of the corresponding target group. The median value is indicated with a solid line, the boxes represent 25 - 75 % of the data, whiskers show 1.5 times the inner quartile range. The ascending aorta and myocardium are abbreviated as AscAorta and Myo, respectively.

The doses deposited in the OARs vary only slightly. While for some structures a dose reduction is found in the 4D simulations, for instance, for the AVN during the treatment of the SPV pigs, slight dose increases could be found for the LCA and RCA for the AVN target group. However, no severe overdosage was found due to the used motion mitigation technique. A detailed overview of the doses deposited in all OARs for static and 4D simulations is given in Tables A.12 and A.18.

2.2.5 In-room PET

The in-room PET was successfully used for online verification of the beam range. A 3D measurement was performed for one field of 12 pigs. Figure 2.16 shows exemplary activity distributions for all three target volumes.

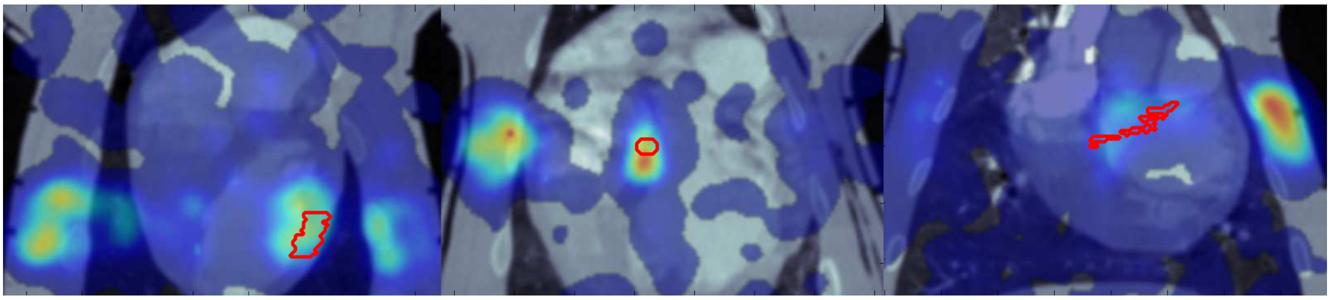

Figure 2.16.: Activity maps for all three target volumes. The activity is given in arbitrary units and is increasing from blue to red. From left to right a LV, an AVN and a SPV example is shown. The activity map is overlaid with the contrast enhanced CT used for contouring and DIR. For the first two targets the beam entrance is on the left side of the CT, while the beam enters the pig from the right side for the SPV irradiation. Figure adapted from [Hel14]

The activity maps were overlaid with the planning CT for all measured fields. Good correlations between the activity hot spots corresponding to the Bragg peak region and the targeted structures, marked with red contours, can be seen. The high activity in the chest indicates the entrance channel of the beam. The reduced activity in the targeted structure compared to the entrance channel is due to the strong blood flow causing a biological washout of the radioactive fragments in the heart. This effect has the biggest influence on the PET images of the SPV pigs.

2.2.6 4D Dose Reconstruction

A successful 4D reconstruction was possible for 11 pigs. The reconstruction of the remaining pigs failed due to technical problems with the DAQ. First preliminary results were available 30 min after the irradiation. Final results were calculated offline. An overview of the results for the target coverage in TV and PTV is given in Figure 2.17.

Apart from Pig 8, where D_{95} is 89.55 %, the D_{95} was found to be greater 95 % for the TV. The reduced TV coverage for Pig 8 can be explained by technical problems with the DAQ and the accelerator during the irradiation. The target coverage in the PTV is generally lower, especially for pigs 2 and 6. The small D_{95} value for Pig 8 in the PTV reconstruction is a direct consequence of the result in the TV reconstruction and it is founded in the same technical problems.

For the OARs, all dose volume constraints stated in Table 2.2 could be kept and were comparable to the 4D simulations shown above. This is also the case for the maximum and the mean dose deposited in the critical structures. In general, no significant deviation between the simulations and the 4D reconstructions was found for the target coverage as well as for the doses deposited in the OARs.

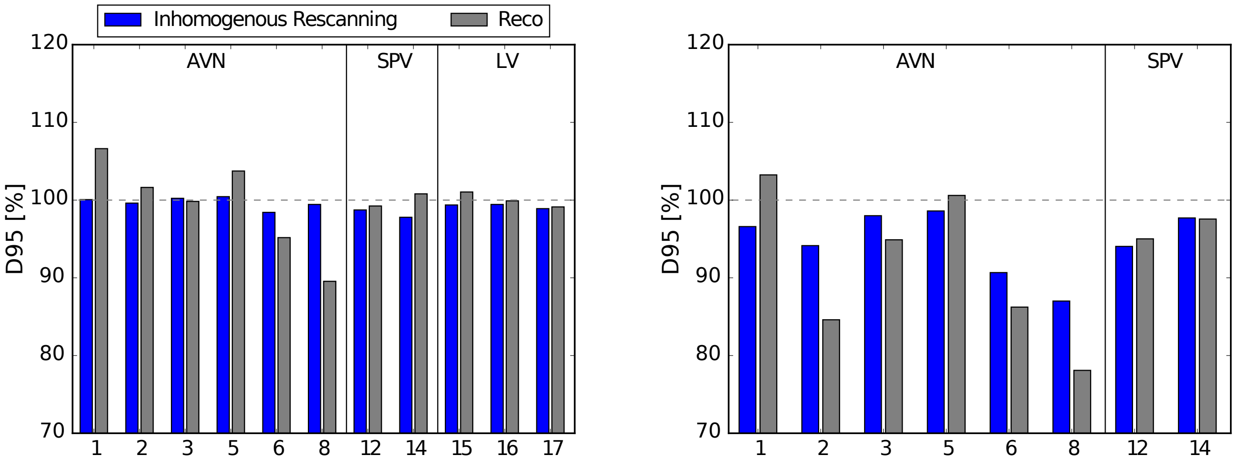

(a) TV

(b) PTV

Figure 2.17.: Results of 4D dose reconstruction for TV and PTV. The blue bar represents the median value of all 96 inhomogeneous rescanning simulations for the corresponding pig. The gray bar shows the results for the 4D dose reconstruction. A critical target coverage reduction between TV and PTV was found for pigs 2, 6 and 8. Figure courtesy of Daniel Richter.

2.2.7 Biological and Medical Study Outcome

After the experiment, the animals were kept for up to 24 weeks. During the follow-up, three animals (3, 5 and 6) died due to inflammation around the pacemaker electrodes. For Pig 1 and 4, complete AV-blocks were found 17 weeks after the irradiation. While the AV-block was permanent for Pig 1 and could be still recorded during the final follow-up examination 24 weeks after the irradiation, the complete AV-block vanished for Pig 4 and only a persistent slowing of the conduction could be found during the final follow up.

Skin toxicity was investigated during the first 9 weeks of the follow up. No changes of the skin within the entrance channels were found. Critical structures like esophagus, trachea and coronary arteries were carefully examined during the final follow-up. No radiation related side effects were observed during the whole study.

While for Pig 13 and 14 only sporadic fibrotic tissue could be found within the targeted volume, Pig 12 showed an almost complete isolation of the SPV. However, the electrophysiological examinations of Pig 13 and 14 showed statistically significant decreases in the conductivity.

For all LV animals, changes in the electrical conductivity of the left ventricle were found. Even though the histological analysis showed structural changes in the cardiomyocytes within the whole thickness of the heart muscle, epi- and endocardial fibrosis was only found in parts of the targeted area. The extent of fibrotic tissue varied between pigs, ranging from tiny fibrotic spots in pig 17 to clear fibrotic areas in pig 14 with epi- and endocardial scars.

Different biological endpoints were investigated by specialists, in the following a short summary will be given for completeness.

Pathological Results

For all targets it was possible to identify macroscopic lesions within the targeted area in the heart muscle. No additional lesions were created in the surrounding critical structures for any pig, except Pig 12, where fibrotic tissue was found throughout the left atrium. In Figure 2.18 an exemplary result is shown for each target volume.

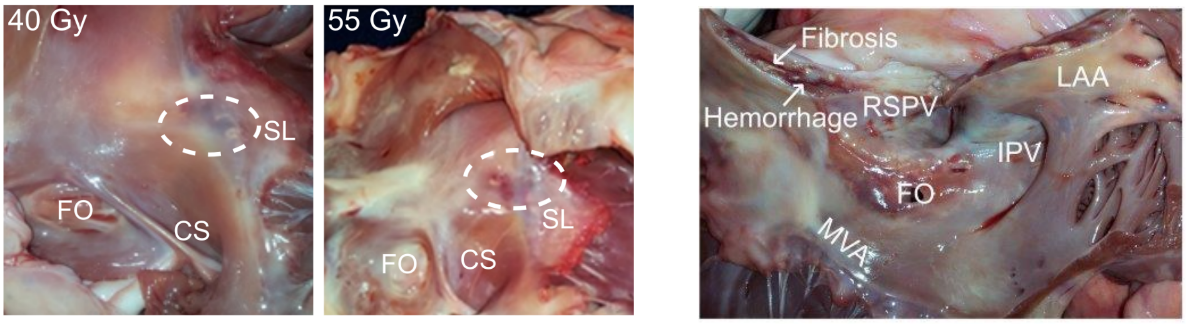

(a) Lesions (marked with dashed lines) after irradiation of the AVN.

(b) Lesion after the SPV irradiation, showing fibrosis and bleeding.

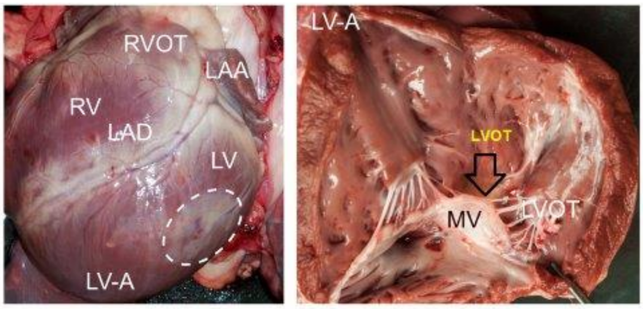

(c) Epi- and endocardial lesion after the irradiation of the left ventricle. Targeted area marked with dashed lines.

Figure 2.18.: Pathological analysis for all three target groups 6 month after the irradiation. Important anatomical structures are marked. In (a) and (c) lesions are indicated with dashed lines. Figure adapted from [Leh16b].

Histological Results

For all animals with macroscopically visible lesions, fibrotic tissue and persistent bleeding was found in the target area, as is can be seen in Figure 2.19b. The amount of hemorrhage was reduced after 6 months compared to the findings after 3 months. The amount of scar tissue was increased after 6 month compared to 3 month indicated by the reduced number of pink and the increased number of blue areas between Figure 2.19 b and c, as the blue color corresponds to an increased amount of collagen indicating fibrosis.

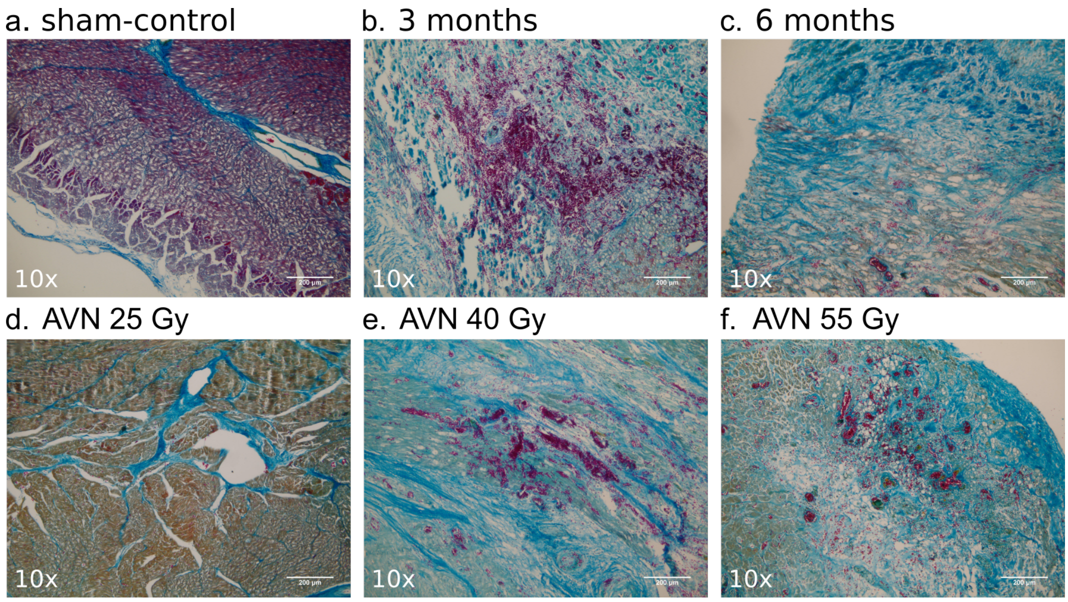

Figure 2.19.: Histological results showing the outcome of a Mallory Trichrome staining. Figure adapted from [Leh16b].

Protein Analysis

Western blots from the protein analysis are shown in Figure 2.20. Three months after the irradiation apoptosis was found in tissues samples of the irradiated animals. However, no apoptosis could be found in the control animals and the apoptosis peak was already over in the animals euthanized 6 months after the treatment. These findings indicate that the process of apoptosis finished between 3 and 6 months after irradiation.

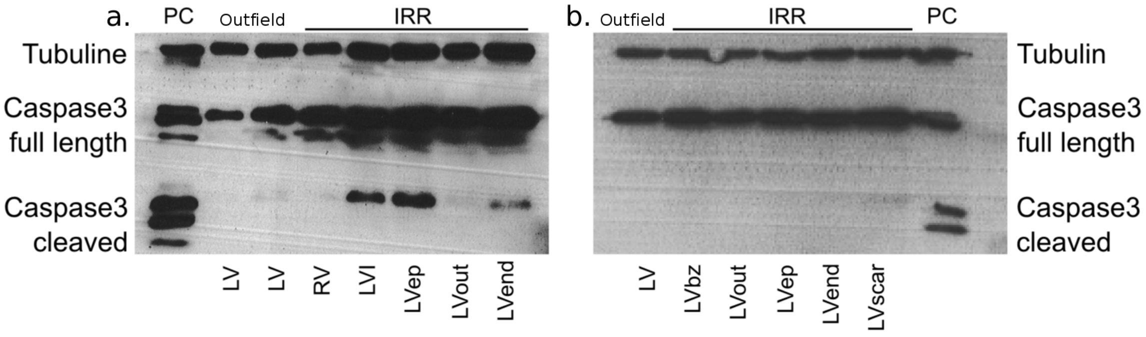

Figure 2.20.: Results of Western blotting. The left Western blot shows the results for an irradiated pig, while the right one shows the results for the same analysis for a sham irradiated pig. Figure adapted from [Leh16b].

The dose dependence is shown in Figure 2.19d-f were tissue slices for AVN targets are shown for all three dose groups. Effects in the organization of the cardiomyocytes and apoptosis can be seen for all dose groups. However, the findings are more pronounced for 40 and 55 Gy, where a strong fibrotic response is visible, while only minor changes could be found for 25 Gy.

2.3 Summary and Discussion

This is the first in-vivo study showing the potential of carbon ions to alter electrical pathways in the heart muscle. The study was carried out at GSI irradiating 15 pigs in total. The successful application of 4D treatment planning was demonstrated, including the feasibility to conduct such a treatment with the standard equipment available in heavy ion centers. The presented data suggests a homogeneous dose deposition to the targeted structures and shows an excellent sparing of the OARs, which was also confirmed by the examination of the removed heart and lung of the euthanized animals. In addition, the used motion mitigation techniques, repeated breath-holds and rescanning, could successfully account for the interplay effect for the majority of the pigs. Overall, the study showed that carbon ion therapy is a reasonable alternative to radio-frequency catheter ablation. It allows to induce persistent changes of the cardiomyocyte conductivity using doses of 40 Gy and higher.

Motion Mitigation - Homogeneous Rescanning vs. Inhomogeneous Rescanning Simulations

As it is necessary for carbon ion irradiations to account for the motion caused by the heartbeat, rescanning was selected as the most promising motion mitigation technique. It combines an easy to implement approach with an effective reduction of interplay effects. Nevertheless, all this comes at the cost of an increased target volume and prolonged treatment times. Other motion mitigation alternatives, such as, cardiac gating, could reduce the treated volume as already investigated in [Con14, Con16]. However, rescanning is simpler and less prone to technical problems whereas the drawback of an increased treatment time is known for both approaches. In addition, due to the short spill durations at GSI, the treatment time prolongation is more pronounced for cardiac gating than for rescanning. Even though a standard homogeneous slice-by-slice rescanning scheme significantly improves the target coverage and dose homogeneity, simulations of the BDS showed that it was not fast enough to irradiate all pigs during the available beamtime. Therefore, a new inhomogeneous rescanning scheme was to the number of rescans from the distal to the proximal slice. This shortened the treatment time to approximately one third and allowed the irradiation of 15 pigs during 5 days including quality assurance, positioning and PET imaging.

A slight reduction of the target coverage could not be avoided due to the use of the inhomogeneous rescanning scheme compared to a homogeneous one, increasing the susceptibility of the treatment plans to motion effects. However, no significant changes in the success rate of the study are expected due to the use of the inhomogeneous scheme. In TV and PTV the found reduction in the median D_{95} and V_{95} values of the single pigs were below 2.5 % and 5.3 %, respectively. The largest reduction in the target coverage is seen in Pig 2 and 7. In contrast to this, for Pig 13, the use of the inhomogeneous rescanning scheme even seems advantageous, showing a slight increase in the median D_{95} as well as in V_{95} and a reduced inner quartile range for the 4D simulations. Even though this can occur due to a temporal correlation between the target motion and the scanning motion of the beam, it is a surprising finding. However, it is unlikely to appear during a real treatment as several additional random fluctuations, such as, the fluctuations of the particle flux and the irradiation breaks due to the repeated breath-holds, influence the irradiation. Using the inhomogeneous rescanning enabled a successful irradiation of all 15 pigs within the limited beamtime. However, the target coverage is varying for some pigs, for instance, Pig 6, indicating residual motion effects. The drawbacks of the inhomogeneous rescanning scheme, a higher sensitivity to motion effects, slightly reduced target coverage and higher variations within the 4D simulation, were accepted with the goal to irradiate as many pigs as possible for a reliable study outcome.

Treatment Planning

The applied margin strategy differed from the ones used in the studies of [Sha10b] and [Bla14]. During the irradiation at GSI, reproducible repeated breath-holds were applied, which allowed to neglect the breathing motion during the treatment planning. In previous studies, either a CyberKnife was used, which can follow the breathing motion [Sha10b], or the breathing motion was considered in an ITV margin approach for the study using a linear accelerator [Bla14]. However, for both photon studies it was not necessary to compensate the heart motion as photon treatments are much more robust against inter-fractional motion. This was an additional challenge for the treatment with carbon ions. The applied margins in the presented study were relatively small to avoid radiation related side effects, as they were later reported for the ITV margin approach in [Bod15]. This can be explained by the high amount of OARs in close proximity to the target.

For all pigs, the mean doses deposited to the OARs were extremely low and well within the published dose volume constraints [Gri11, Ben10]. The maximum point doses allowed were only exceeded for structures close to the targeted volume or even within the applied margins. For instance, the maximum point dose in the aorta was as high as the planned target dose or even higher. For the RCA it was also not possible to stay below the self-imposed maximum point dose of 30 Gy for Pig 12 targeting the SPV. In the 4D simulations for this pig, doses deposited in RCA were up to 20 % higher than the allowed maximum point dose. However, no structural changes in the OARs were found during the follow-up and pathological examination. Furthermore, it was possible to successfully spare critical structures during the irradiation due to the inverse depth dose profile of carbon ions compared to photons as, for instance, the esophagus [Con14]. In contrast to previous findings [Zac97, Ham00], the skin did not show any reactions. A dose volume effect is discussed, as the targeted areas were small with a maximum diameter of approximately 5 cm for the SPV and LV group and 3 cm for the AVN group. Alternatively, the radio-sensitivity of the used pig breed might be lower compared to the breed used in previous studies.

However, the success rate of this study is low, especially when comparing the results with a twin study using photons carried out at Mayo [Leh16a]. In the present study only 2 out of 6 animals of the AVN group, that were irradiated with doses likely high enough to induce AV-blocks, showed a persistent AV-block or extensive slowing in the signal conduction. While 3 animals out of this group died because of a pacemaker infection, Pig 2 irradiated with 55 Gy did not show any incidence for a successful irradiation. The reasons are likely to be found in the positioning, treatment planning or a combination of both. In addition, dose volume effects could have an impact on the irradiation outcome due to the sharp dose gradients compared to photon irradiations. A general problem in the AVN target group during the imaging, treatment planning and treatment were the image artifacts caused by the implanted pacemakers, although the image artifacts were reduced as much as possible by the use of the thinnest available pacemaker leads (7 fr). Prior to the irradiation, dose calculations were carried out for an electrode placed in a water phantom, which showed that the employed margins should be sufficient to compensate for potential range changes due to the varying position of the electrodes in the heart. However, as the position of the leads during the irradiation is unknown, a displacement of the leads in combination with positioning uncertainties could significantly alter the treatment outcome and can, in the worst case, cause a complete target miss. Even though all pigs of the LV and SPV group received the same dose, the results for the LV and SPV group are heterogeneous. Especially the LV pigs did not show homogeneous transmural fibrotic tissue on a macroscopic scale and even the amount of patchy fibrotic tissue was highly varying. This is most likely caused due to registration problems underestimating the thickening of the left ventricular wall during the heart contraction. The low success rates for the SPV pigs can be explained more easily. Pig 14 was irradiated with a reduced target dose of 30 Gy as the dose deposited in the trachea was otherwise exceeding the limitations. Therefore, the physicians decided to reduce the target dose to not risk severe radiation induced side effects. In addition, for Pig 13 the irradiation was aborted due to technical problems of the accelerator causing a reduction of the target dose.

Another reason for the low success rate of the study could be the relative low results for D_{95} and especially V_{95} in the PTV of some pigs. Pig 2, contrary to the expectations showing no AV-block, is one of the animals with significantly reduced target coverage in the PTV with median D_{95} and V_{95} values of 94.1 % and 89.0 %, respectively. In addition, the low D_{95} result in the PTV was confirmed by the 4D dose reconstruction with a D_{95} of only 84.6 %. As the number of surviving pigs is limited, it cannot be completely ensured that the result of the 4D dose reconstruction allows a prediction of a successful treatment. However, comparing the results of the 4D dose reconstruction combined with the final outcome of Pig 1 and 2 indicates a connection between both. This would support the findings of [Ric14] that a 4D dose reconstruction is extremely valuable and can give information on the dose deposited in targeted structures. Nevertheless, the PTV coverage is important in 4D dose reconstruction as the approach relies on the treatment planning CT and cannot take positioning uncertainties into account.

In general, the reduced target coverage in TV and PTV indicates a lacking robustness of the treatment plans. However, due to the use of a rescanning scheme with 15 rescans the low robustness is unexpected, as the applied motion mitigation strategy should be sufficient to compensate any present interplay effects [Ber08b]. One possibility could be, that the found reduction in the target coverage is only a simulation artifact. During further analysis of the experiment problems with the image registration were detected, especially for the inverse consistency, which could cause a insufficient propagation of the dose from each motion phase to the reference phase. To verify this, the AVN position was marked by a physician in each motion phase and the dose of all motion phases was accumulated to check if the target coverage is satisfying over the full motion cycle. This topic is discussed in more detail in Chapter 3.

Furthermore, treatments using carbon ions are always prone to range deviations, due to anatomical changes of the patient between the recording of the treatment planning CT and the irradiation. Especially the position and the volume of the heart can cause uncertainties throughout the presented study. Further studies are necessary to determine the reproducibility of the heart volume and position over a longer time frame and for more then 3 pigs, as it was done during the preparation of this experiment. Another problem for this experiment could be the growth and the weight changes of the pigs due to the young age. In-between the planning CT and the treatment the highest weight changes were 13 % and -11 %

for Pig 3 and Pig 8, respectively. While the weight gain is due to the growth of the pigs the weight loss is due to the stress of the baseline examinations and pacemaker implantation.

One method to check for range changes is in-room PET [Par07, Bau13], which was applied during the presented study. Other possibilities to determine range uncertainties during the irradiation can be the detection of prompt gammas or prompt particles emitted during the irradiation [Pie14, Pri15]. Increasing the robustness would also be possible by improving the imaging modalities at the treatment location. Instead of the use of orthogonal x-rays, either installing a CT on rails or using cone beam CTs to gain a 3D position feedback would significantly increase the outcome. In addition, 3D imaging at the treatment position would enable an improved outcome prediction using the 4D dose reconstruction approach.

A step further is the consideration of all possible uncertainties during the treatment planning. In the case of the presented study it is likely that the chosen margins were too small and could not account for all possible error sources. A possibility to overcome this problem and to introduce margins covering all situations, also taking into account range changes, is the use of a robust optimization. Robust optimization allows an incorporation of potential range changes and positioning uncertainties in the treatment optimization. Several approaches are available to use robust optimization in proton therapy [Pfl08, Fre11, Liu12]. The integration of robust optimization in TRiP4D is under development and will offer new possibilities for carbon ion treatment planning in the future [Wol16].

Another possible uncertainty is the RBE. Carbon ions are known to have an increased biological effectiveness compared to photons [Kra00a]. However, the knowledge of the RBE for high single-fraction doses and the irradiation of cardiomyocytes is extremely limited since no reliable data is available so far. Therefore, the whole treatment planning process was performed using physically optimized treatment plans. The RBE for such high doses is expected to be only slightly above 1, allowing the treatment planning with physical dose.

Use of Carbon Ions - Promising Non-Invasive Alternative?

The use of carbon ions for catheter-free ablations of cardiac substructures offers great perspectives. Carbon ions are an extremely effective tool for radiotherapy due to their inverse depth-dose profile and the low lateral scattering in the entrance channel. This offers high precision and allows to successfully spare critical structures, which are a potential show stopper for comparable photon treatments.

However, the success rate of the presented study was not sufficient to directly transfer the treatment into clinical routine. Further animal experiments are necessary to investigate new margin and optimization strategies, such as, robust optimization, 4D optimization or a combination of both. In addition, it would be important to investigate the change of the heart volume of the pigs over several weeks and to investigate the corresponding positioning reproducibility over a longer time frame. For further treatments without 3D imaging in the treatment location larger margins should be useful to increase the success rate. In general, the use of 3D imaging at the treatment room is highly recommended. Furthermore, it would be beneficial to critically examine the possibility to increase the margins considering the doses deposited in the OARs.

For further experiments, alternative approaches without additional metal artifacts during imaging and irradiation should be carefully investigated. However, metal artifacts are a highly critical problem for the translation of catheter-free ablation to clinical routine, as patients suffering from severe cardiac disorders most likely have ICDs or pacemakers implanted. Therefore more research is needed to reduce metal artifacts within the planning CT and to determine the position of the leads prior to the treatment [Jäk07].

Comparing both methods, photon and carbon ion irradiation, photons are advantageous in the robustness against breathing and heart motion. Necessary compensation strategies for interplay effects make the application of carbon ions more challenging compared to photons. Before a clinical application is possible more animal experiments are necessary, to further understand the biological reactions of the high doses delivered in a single fraction to a small volume. To finally reach the aim of a non-invasive treatment modality also the beam delivery needs to be modified to combine, for instance, gating for the breathing motion and rescanning or gating for the cardiac motion. To date, no carbon ion facility is able to perform motion mitigation for both motion types without anesthesia. In general, it is not possible to apply radiotherapy as a stand-alone therapy for people suffering from severe cardiac arrhythmia. Regarding the findings of all published animal studies, the time until an effect is expected lies somewhere between 3 and 6 months. Hence, radiotherapy always needs to be applied in combination with an ICD.

In summary, catheter-free ablation using carbon ions can be a possible alternative to radio-frequency catheter ablations in the future. The presented study demonstrates the feasibility and shows possibilities to overcome the heart and breathing motion. A first and important step is done and now further research is needed to apply the presented techniques in clinical routine. In addition, no radiation induced side effects were observed over the whole follow-up time of 6 months. The success rates can be increased using 3D imaging in the treatment room and applying new margin strategies or treatment plan optimization methods such as 4D optimization [Gra14, Gra13] or robust optimization [Liu16]. Nevertheless, a first in-vivo study was conducted and the success of carbon ion therapy in cancer treatment could be continued in treatment of cardiac arrhythmia.

3 Deformable Image Registration for Beating Hearts and Influence on the In-Vivo Feasibility Study

Image registration is a widely used tool in clinical routine nowadays. As it is necessary to compare the outcomes of different image modalities, such as magnetic resonance imaging (MRI), positron emmission tomography (PET), computed tomography (CT) and cone-beam CT (CBCT) or of image data taken at different time points, commercial treatment planning software provides registration algorithms able to match the imaging data. In radiotherapy deformable image registration (DIR) opens a wide field of opportunities and new fields of applications are already described in literature, such as 4D optimization [Tro05], 4D dose calculation [Fla06] and contour propagation [Lu06]. Several years ago, 4D dose calculations became available for protons [Pag05] as well as for carbon ions [Ber07a]. Even though these methods are sensitive to uncertainties in DIR, they are a powerful tool to determine dose distributions of moving targets.

In TRiP4D the calculation of 4D dose distributions works as follows. A temporal correlation between the raster points and the corresponding motion phase is determined using a beam delivery sequence (BDS) and the dose contributions of all raster points to each CT voxel. For this step, the voxel position of the reference phase is modified according to the DIR, considering the Hounsfield unit (HU) of the actual motion phase. The overall physical dose is calculated as a summation of all dose contributions from all motion states projected onto the reference phase. For biological dose calculations the particle spectra initial and secondary particles are accumulated over all motion phases projected onto reference phase. Furthermore, contour propagation can be carried out transforming the contours from the reference phase to any arbitrary motion phase. For further details the reader is referred to [Ric12].

The transformation from reference to each motion phase and vice versa is carried out separately to avoid uncertainties due to a simple inversion. Thus, a lacking inverse consistency of the registration is possible and points to a poor DIR outcome. Large inverse consistency error (ICE) can cause severe deviations between reality and 4D simulations such as under- and overdosage within the target volume and the organs at risk (OARs). Thus, the inverse consistency of DIR should be checked for all motion phases to gain important information about DIR quality.

For the application in lung and liver cancer therapy, DIR has already been in use for several years [Ric14, And16b]. To carry out catheter-free ablations, DIR is essential to mimic the complex motion of the heart allowing 4D dose simulations and even 4D dose optimization in future. In a previous treatment planning study, a DIR approach was established for the registration of human and pig hearts [Con14, Con16] using Plastimatch [Sha10a]. A similar approach was used for the in-vivo feasibility study presented in Chapter 2. However, a detailed retrospective analysis showed insufficiencies of B-spline DIR for beating hearts. The registration of the heart motion is incorrect and especially lacking inverse

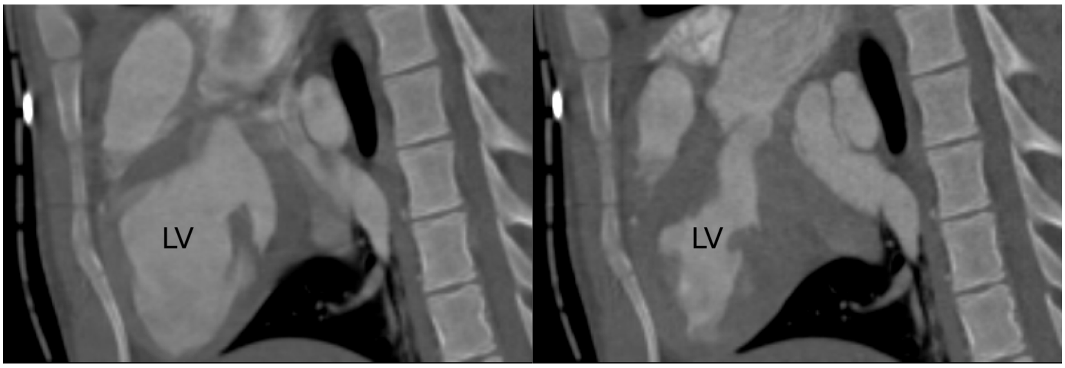

Figure 3.1.: Diastole and systole of the contrast enhanced 4DCT of Pig 16. The thickness of the left ventricular free-wall is clearly increasing. Even though the deformation of the heart muscle occurs in 3D, the strong influence of the heart contraction on its anatomy is clearly visible in the 2D slice.

consistency [And16a]. The problems are among others, the complex motion with an extreme contraction of the left ventricle as shown in Figure 3.1, imaging artifacts present due to the irregular flow of the contrast agent, the fast contraction of the heart and the implanted pacemakers in the atrioventricular node (AVN) pigs.

Therefore, the following chapter will present the result of two approaches trying to increase the quality of DIR using Plastimatch. In the first approach the registration parameters are varied and in the second one a stepwise registration is tested. In addition, an estimation of the effect of the DIR uncertainties on the feasibility study presented in Chapter 2 is given. Finally, further approaches to increase DIR quality are discussed.

3.1 Material and Methods

3.1.1 Registration method

The registration process was carried out using Plastimatch [Sha10a] included in Slicer3D [Fed12]. Plastimatch is an open-source commandline based software, often used in medical research. It is included in a Slicer3D plugin, called SlicerRT [Pin12], that offers fast parameter adaption and prompt visual feedback. SlicerRT was used to carry out the original DIRs for the feasibility study as well as for the new approaches presented in this chapter trying to improve the DIR for beating hearts.

Registration parameters and nomenclature

A short summary of the nomenclature for the different images created during a registration process is given in the following:

- **Reference Image**: As the name already states, this image is used as a reference for the registration process.

- **Moving Image**: The image that needs to be transformed to the reference image.

- **Warped Image**: After the registration, the warped image is the transformed moving image which should resemble the reference image as close as possible.

- **Forward Registration**: Registration of each moving phase to the reference phase.

- **Backward Registration**: Registration of the reference phase to all moving phases.

In all cases, the original registration was performed as a two-step process using the registration parameters stated in Table 3.1. A detailed descriptions of the parameters can be found in [Pla].

Parameter	Stage 1	Stage 2
Resolution	4,4,2	2,2,1
Grid Size	50	15
Regularization Lambda	0.005	0.005
Iterations	200	100

Table 3.1.: Parameters used for the deformable image registration for the pig study.

3.1.2 Quality Assurance of a Deformable Image Registration

After acquisition of the 4DCTs, a time frame of several days was available to perform registration, registration quality assurance, contouring, treatment planning and 4D dose simulations to prepare the irradiation of all 15 pigs. Due to the limited time and large amount of data, automated processes were used for registration, registration quality checks, treatment planning and 4D dose simulations. In addition, the registration quality checks were performed only on one motion phase to reduce the workload as previously reported in [Con14]. For each pig an overlaid image of reference and warped image was created using inverse colors. Furthermore, a square shaped region of interest (ROI) around the body was determined manually. Within this region the mean value of the absolute difference, the Jacobian determinant and the ICE were calculated. In the following paragraphs the quantities used for the deformable image registration quality assurance (DIRQA) are explained in detail.

To estimate the agreement of reference and warped image it is useful to apply an **inverse color** code to both images. The differences are usually small between reference and warped image and the gray scale of the recorded CTs makes it difficult to determine slight deviations. Overlaying both images with inverse color codes, as, for instance, red and cyan, facilitates to recognize deviations. After the overlaying process, matching areas will be displayed in gray and non matching ones in red and cyan. This allows a fast visual quality check of the registration.

In addition, the **absolute difference** is a measure to determine the agreement of two images quantitatively. The difference of the Hounsfield units is calculated for each voxel and can then be used to calculate the mean, standard, minimum and maximum deviation in the selected ROI across all voxels. For an ideal registration the results would be 0. As a registration is typically used for single motion phases and minimizes the mean square error, the absolute difference indicates if an image registration was carried out successfully.

Besides analytical and visual checking of the reference and warped image, an analysis of the determined vector fields is necessary. One important quantity is the **Jacobian determinant** to validate the physical properties of the registration process [Leo07]. The Jacobian determinant is defined as

$$J = \begin{vmatrix} \frac{\partial u_x}{\partial x} & \frac{\partial u_x}{\partial y} & \frac{\partial u_x}{\partial z} \\ \frac{\partial u_y}{\partial x} & \frac{\partial u_y}{\partial y} & \frac{\partial u_y}{\partial z} \\ \frac{\partial u_z}{\partial x} & \frac{\partial u_z}{\partial y} & \frac{\partial u_z}{\partial z} \end{vmatrix} \tag{3.1}$$

where u is the calculated vector field, which assigns each voxel in the reference image a new voxel in the moving image. The Jacobian determinant should be greater than 0 for all voxels, as values below correspond to mirroring voxels within the patient, which is impossible [Rey99, Che08]. Values above or below 1 correspond to an expansion or contraction of the volume, respectively. For an analysis, mean, standard deviation, minimum and maximum of the Jacobian determinants can be calculated similar to the approach for the absolute difference. Hence, the minimum value of all Jacobian determinants gives a quick overview whether the registration outcome is realistic.

Another important quantity of the vector field is the **inverse consistency error**. The ICE checks if the forward and backward transformation, which are carried out independently, are defined consistently. Therefore an arbitrary starting point of the reference image x is transformed to the moving image using the vector u_{AB} leading to x'. After that x' is transformed to the reference image using the vector u_{BA} leading to x''. The distance between x and x'' gives the ICE. In other words, the ICE is defined as the Euclidean norm between x and x''. This process is performed for all voxels of the CT and again a mean, standard deviation, minimum and maximum can be calculated.

In general, it is important not to focus solely on the mean results. Instead, increased attention should be given to the minimum and maximum values. The extreme values are able to point out certain areas within the total ROI which need further investigation.

3.1.3 In-Vivo Feasibility Study

A detailed retrospective analysis of the DIR calculated prior to the pig study can be found in [And16a]. In summary, the analysis showed that the registration was not able to reproduce the complex motion of the heart contraction. The minimization of the absolute difference, which is the goal of the optimizer in the applied B-Spline registration, was satisfying. However, this is not a clear indication for a good registration as organ folding and maximum ICE values greater than 20 mm were found for some pigs. In addition, the DIR was not able to reproduce the thickening of the left ventricular free-wall (LV) and the opening and closing of the valves. In Figure 3.2 the false color image of systole and diastole is shown, indicating the complexity of the heart motion. In Figure 3.3 false color images after DIR, according warped images and vector fields are shown.

The DIRQA prior to the in-vivo study was not sufficient and, in general, an improved registration of all pigs is necessary to gain reliable results from the 4D dose calculation. Hence, two different registration approaches were carried out to improve the DIR and to reach satisfying results for the absolute difference, the Jacobian, the ICE as well as for the inverse color images.

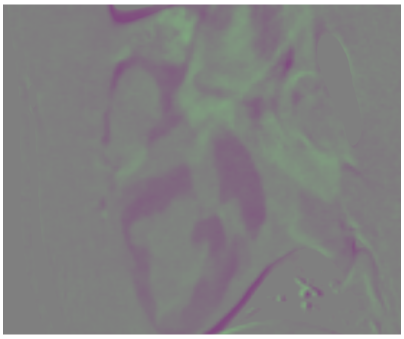

Figure 3.2.: False color image of the motion phases 3 and 0 before registration representing the two extreme phases of systole and diastole.

Different parameter combinations were investigated for the two-step DIR used prior to the experiment. The grid size was reduced twice, first a rough resolution was chosen with grid sizes of 30 and 10 mm in stage 1 and 2, respectively. After that a finer resolution was chosen, with grid sizes of 20 and 5 mm. Besides the original value of 0.005, the regularization lambda was changed to 0.0005, 0.001, 0.050, 0.010 and 0.015.

In addition, it was investigated if the registration outcome of complex motion types, such as the heartbeat, is increased when applying a stepwise registration approach. Thus, neighboring phases were

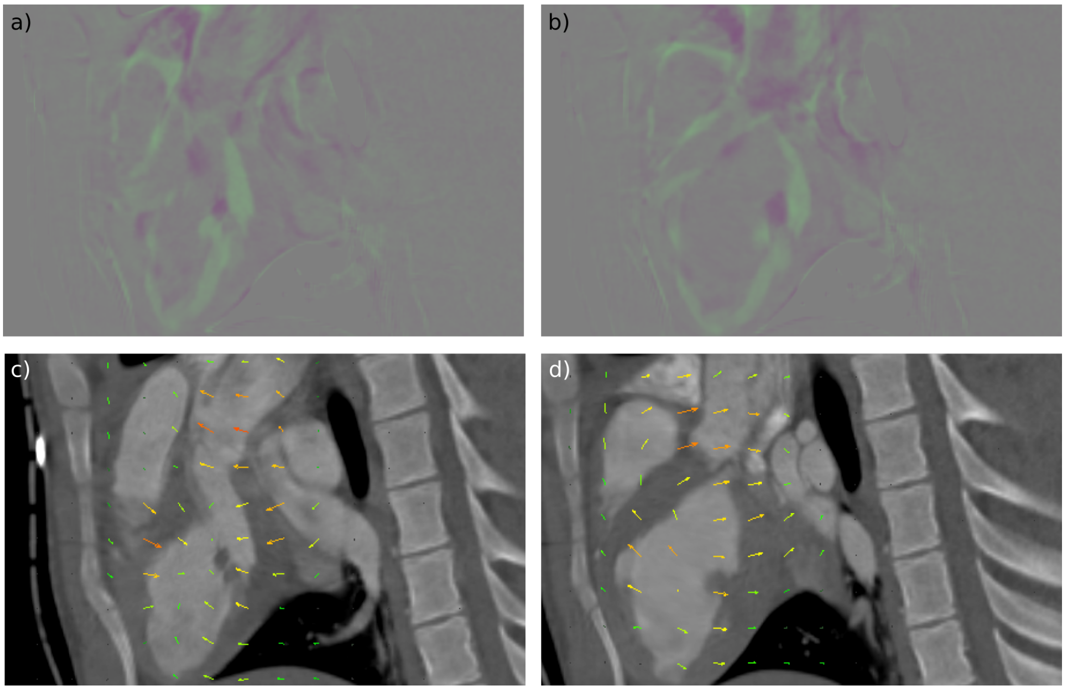

Figure 3.3.: Results of the forward and backward DIR of diastole and systole are presented corresponding to reference phase and motion phase 3, respectively. In a) the false color image overlaying phase 3 (systole) with the warped image of the reference phase (diastole) is shown. The corresponding vector field overlaid on the warped image of phase 0 is shown in c). In b) and d) the same images are shown for the forward registration. It can be seen that the deformation of the left ventricle is extreme and that motion amplitudes of the forward and the backward registration differ.

registered onto each other and, in the end, adding the transformation vector fields for each registration to obtain the transformation from each motion phase to the reference phase and vice versa. Instead of registering each motion phase directly to the reference phase, as it is usually done in a standard DIR.

To improve the results of the DIR, different approaches were tested. These studies were carried out for Pig 16, which was part of the LV group. The latter was selected due to the good quality of the 4DCT without pacemaker and reconstruction artifacts. Furthermore, a homogeneous contrast agent distribution was available. It was assumed that a successful registration of all 4DCTs is only possible, if an approach for the 4DCT of Pig 16 is found. In addition, for all pigs of the AVN group the position of the AVN was manually determined in each motion phase of the 4DCT to estimate the influence of the inexact DIR. The manual contouring was carried out by a physician blinding the study outcome. This study was necessary to investigate if the inhomogeneous results throughout the target and dose groups can be correlated with the applied DIR. Two important examples for this examination were Pig 1 and Pig 2. Both pigs were irradiated with 55 Gy, while Pig 1 developed a complete AV-block, Pig 2 did not even show a slowing of the conductivity of the AVN.

3.1.4 Perfect Rescanning

Idealized 4D treatment simulation neglecting the influence of interplay effects are possible using perfect rescanning (PRSC) [Bre15]. In a PRSC simulation the deposited dose is equally distributed to all motion states of the treatment planning 4DCT. This allows to simulate a treatment without interplay effects and yields the maximum target coverage possible in a 4D simulation. A PRSC simulation is independent of the BDS and does not need a motion surrogate.

Throughout this chapter PRSC was applied to clarify if the reduced target coverage found in Chapter 2 is due to residual interplay effects or the underlying registration. If the motion was mitigated sufficiently, the median values found from the rescanning simulations should be comparable to the results of the PRSC simulation. However, if the target coverage is reduced in PRSC simulations as well, the reason lies in the insufficient registration quality, specifically a lacking inverse consistency, and not in residual interplay effects.

Therefore a PRSC simulation was performed for each of the 14 investigated pigs. From the simulations D_{95}, V_{95} and D_5-D_{95} values were determined and compared to the corresponding median values for homogeneous and inhomogeneous rescanning presented in Chapter 2.

3.1.5 Target Coverage for Manual AVN Contours

To investigate the influence of the found registration uncertainties on the 4D dose calculations the AVN position was determined by a physician in each motion phase. The manual contouring was carried out blinding the study results. Afterwards a sphere of 5 mm diameter was created around the determined location, comparable to the target volume (TV) used throughout Chapter 2. As the uncertainties for determining the correct position within each single motion phase are in the order of several millimeters, the target coverage was calculated only for the TV.

A static dose distribution depositing 10 % of the target dose in each motion phase of the 4DCT was calculated. The target coverage and dose homogeneity in the TV was analyzed determining V_{95}, D_{95}

and D_5-D_{95} values. To estimate the target coverage in a 4D dose simulation without uncertainties due to the DIR, the values of V_{95}, D_{95} and D_5-D_{95} over all motion phases were determined using a rigid transformation of the target sphere. This procedure cannot replace a full 4D simulation, especially considering the dose deposited within the OARs. However, it allows a rough statement about the actual target coverage as well as an estimation if the DIR uncertainties caused a poor target coverage due to a wrong internal target volume (ITV).

3.2 Results

The following sections present the results of two new registration approaches and an estimation of the influence of the DIR uncertainties on the study outcome. Throughout this chapter results are either given as mean values with standard deviation (mean ± stdev) or as median values with the range between the 25th and 75th percentile (median (25 % - 75 %)).

3.2.1 New Registration Approaches

Parameter Variation

The parameter variation showed a clear influence on the registration outcome. In general, the calculations indicate that a small grid can cause negative Jacobians and large ICEs. However, when investigating absolute differences between the warped and the reference image, a small grid seems to be the optimal choice. For the two larger grids the results showed comparable outcome for all used regularization lambdas, but the results of the absolute difference were poor. For all parameter combinations the resulting minimum Jacobian, maximum ICE and absolute difference are displayed in Figure 3.4.

Even though the results of the vector field analysis look satisfying for certain parameter combinations, the corresponding inverse color images displayed in Figure 3.5 cannot confirm the good results of the vector field analysis. Compared to the inverse color image of phase 0 and 3 without registration (see Figure 3.2) it can be seen that the deviations at the outer contours of the heart muscle are reduced. However, none of the parameter combinations were able to model the thickening of the left ventricle and the deformation of the heart at the superior edge satisfyingly. In addition, the deviations are tremendous in the area of the right atria, where the contrast agent is flooding the heart muscle.

Stepwise Registration

Based on the findings of the parameter variation the stepwise registration approach was tested for two parameter combinations. Grid sizes of 30 mm in the first and 10 mm in the second stage and 20 mm in the first and 5 mm in the second stage were combined with regularization lambdas of 0.015 and 0.00005, respectively. Even though the vector field quality of both was not satisfying due to large maximum ICE and negative Jacobians, both parameter combinations showed the most promising false color images, indicated by a reduction of the absolute difference.

In Table 3.2 the quantitative analysis of the stepwise registration is shown. The homogeneity of the vector field was increased using the stepwise approach and the inverse consistency benefited from this approach as well. For the combination with the small grid also the absolute difference benefited for the stepwise registration approach. However, comparing the results of the false color images for both

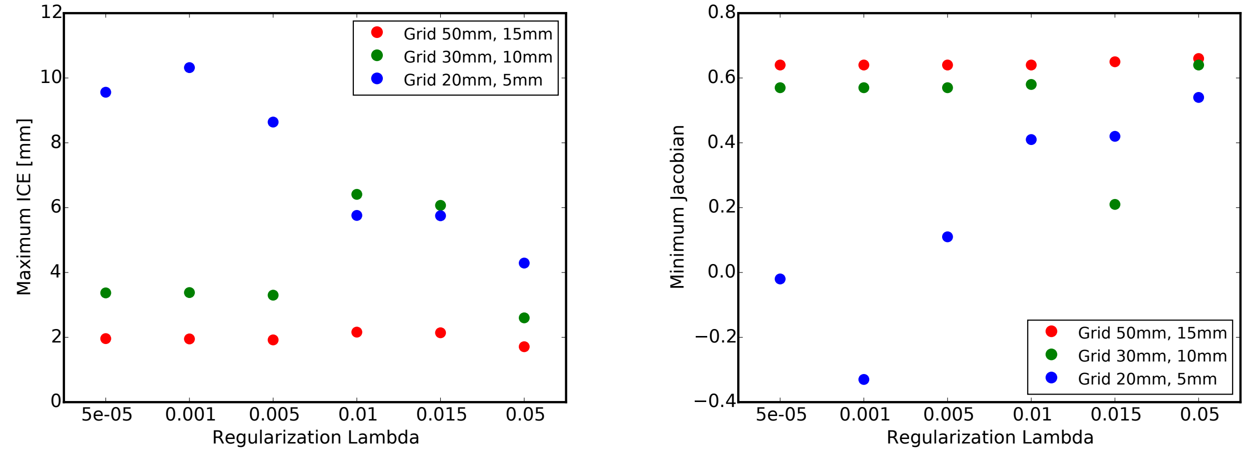

(a) Maximum inverse consistency error

(b) Minimum Jacobian

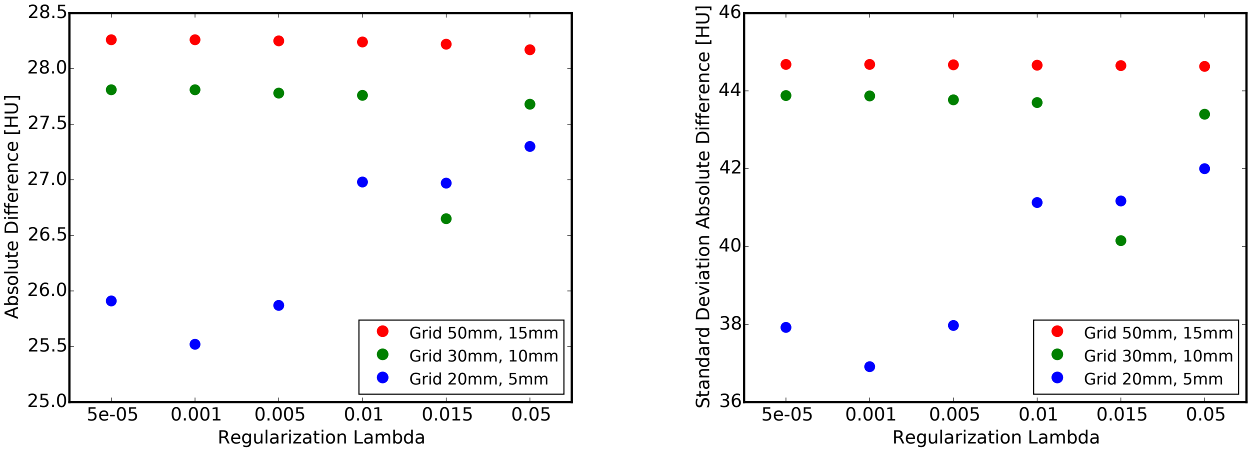

(c) Mean absolute difference

(d) Standard deviation of the absolute difference

Figure 3.4.: Results of the parameter variation approach. The maximum ICE, the minimum Jacobian, the absolute difference and the standard deviation of the absolute difference are plotted over 6 different values for the regularization lambda and for 3 different grid sizes.

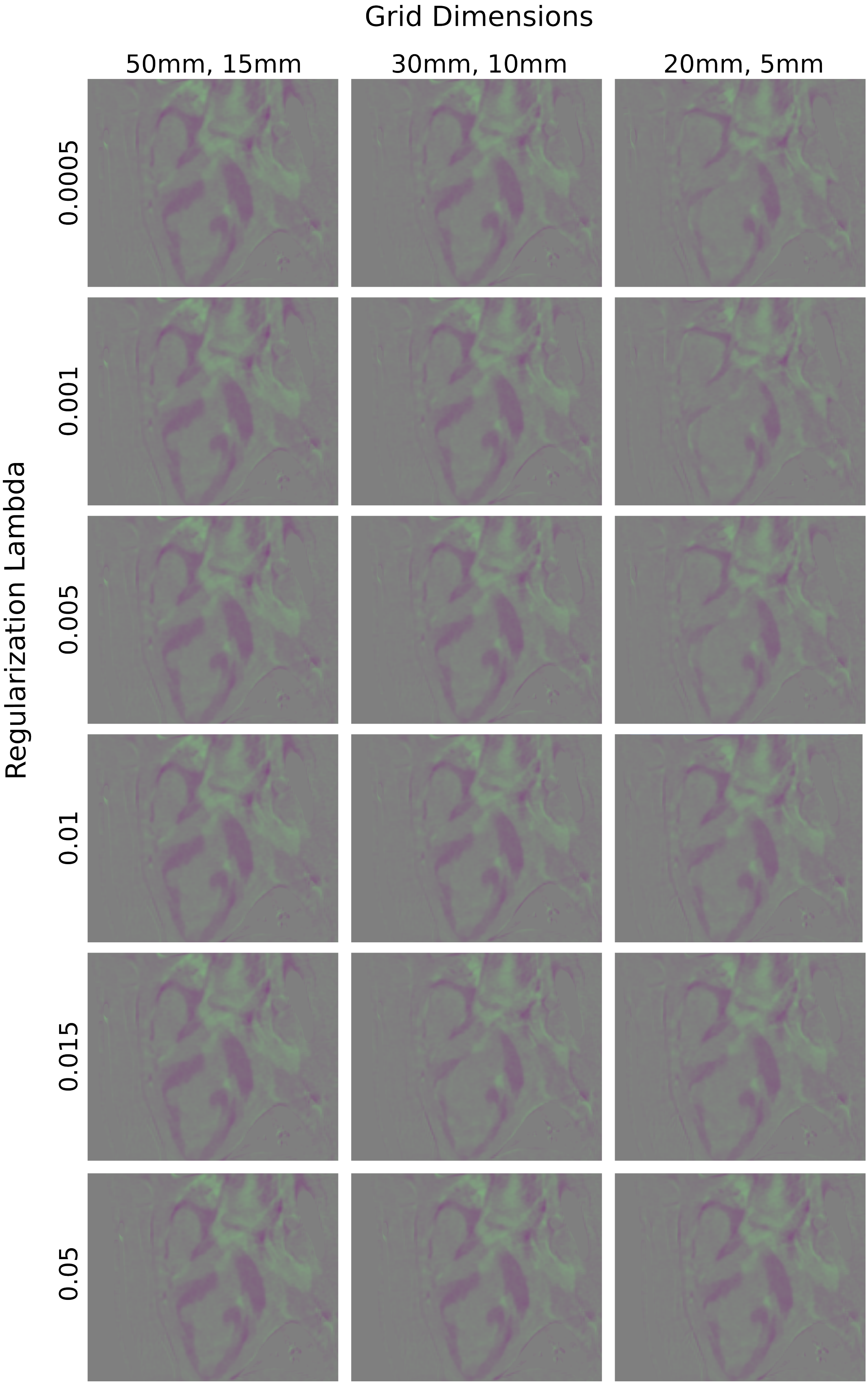

Figure 3.5.: Overview of the false color images gained with all different combinations of regularization lambda and grid sizes. All images show an overlay of sagittal cuts from phase 0 and 3 from forward registration.

	Grid: 20mm, 5mm Regularization λ: 0.0005		Grid: 30mm, 10mm Regularization λ: 0.015	
	One Step	Stepwise	One Step	Stepwise
Mean Absolute Difference [HU]	25.91	14.76	26.65	27.54
Standard Deviation Absolute Difference [HU]	37.92	24.42	40.15	45.07
Maximum Inverse Consistency Error [mm]	9.56	3.06	6.07	1.98
Minimum Jacobian	-0.02	0.39	0.21	0.25

Table 3.2.: Results comparing the one step and the stepwise registration approach.

registration approaches in Figure 3.6, it can be seen that the overall outcome is not satisfying. The stepwise registration is able to avoid negative Jacobians and to reduce the ICE. Nevertheless, the stepwise registration approach could not sufficiently improve the transformation from moving phase to reference phase and vice versa. Especially the changes of the heart anatomy due to the opening and closing of the valves and the thickening of the left ventricle cannot be represented.

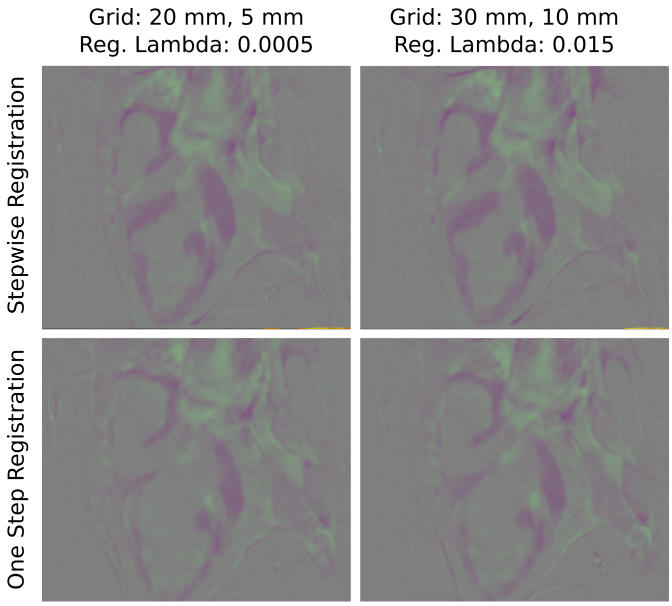

Figure 3.6.: Overview of the false color images for the stepwise and the original registration approach gained with two different combinations of regularization lambda and grid size.

3.2.2 Perfect Rescanning

The simulations carried out with PRSC are in good agreement with median values of the inhomogeneous and homogeneous rescanning simulations presented in Chapter 2. In Figure 3.7 the results are compared.

The target coverage expressed by the D_{95} and V_{95} as well as the dose homogeneity show reduced values for the same pigs. Nevertheless, for some pigs, for instance Pig 1, 3 and 4, the dose homogeneity is better for the perfect rescanning simulations. Furthermore, for some pigs, for instance, Pig 6, a larger variance in the results for the target coverage was found, which cannot be explained by the results of the perfect rescanning simulations and indicate residual interplay effects for these animals. The 4D

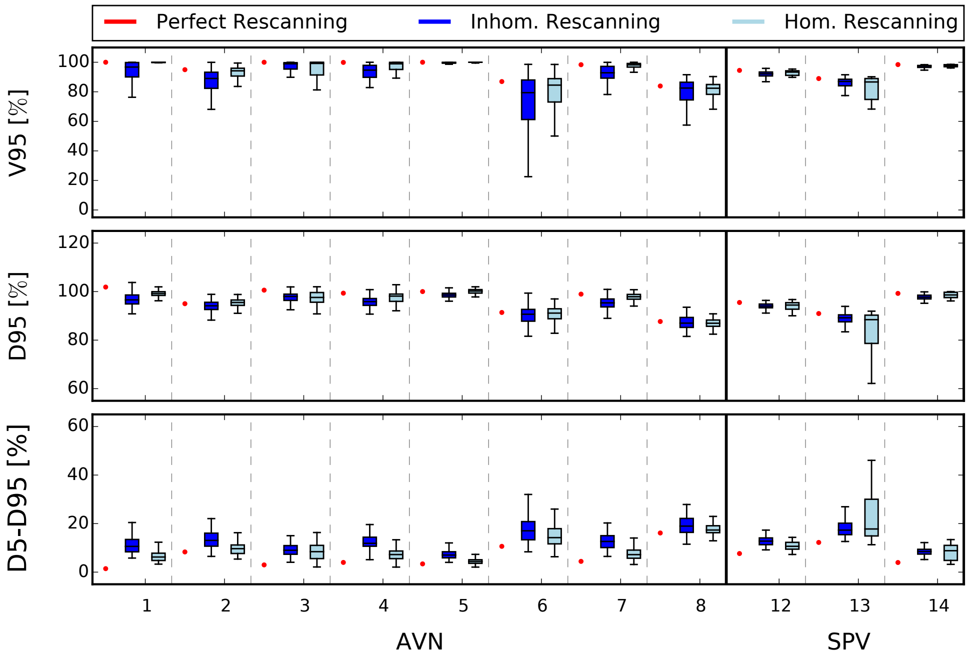

Figure 3.7.: V_{95}, D_{95}, D_5-D_{95} results of the PTV. Comparison for the results of the perfect, inhomogeneous and homogeneous rescanning simulations. For inhomogeneous and homogeneous rescanning simulations the box represents the 25 to 75 % of the data of 96 simulations including different motions and beam delivery sequences. The median is given by a solid line and the whiskers represent 1.5 times the inner quartile range.

rescanning simulations presented in Chapter 2 could successfully compensate the motion for most of the pigs and the found reductions in the target coverage are due to registration problems.

3.2.3 Influence of Deformable Image Registration on Study Outcome

The analysis of the manually drawn contours showed a good target coverage for all AVN pigs in all motion phases. Single outliers were found for some pigs, which could be identified calculating the motion vector showing unnatural changes between single motion phases.

The overall target coverage in all motion phases was determined by shifting the target point for each motion phase. The results were satisfying, showing D_{95} values above 94 % without corrections for identified outliers. Especially, when considering the contouring uncertainties of several millimeters, a good target coverage was reached indicating a correct treatment planning process for the AVN group. In Table 3.3 the D_{95} values are shown for each pig of the AVN group using the manual contours in all motion phases.

Pig	1	2	3	4	6	7	8
D95 [%]	94	98	95	101	98	103	101

Table 3.3.: Results for D_{95} values for the hand drawn contours.

In addition, dose cuts of the reference phase and the motion phase with the largest contraction were visually analyzed for the LV group. This allowed to check for the transmural dose coverage of the left ventricular free-wall during the motion phase with the largest contraction. The analysis incorporates 3D images of the static dose distribution for each phase. In Figure 3.8 the dose distribution is shown for Pig 15 in the reference motion phase and in motion phase 3, corresponding to the ventricular systole. The dose cuts show that full dose coverage of the entire thickness of the left ventricular free-wall in the motion phases with extreme contractions was not achieved. Hence, a reduced target dose within the TV is likely.

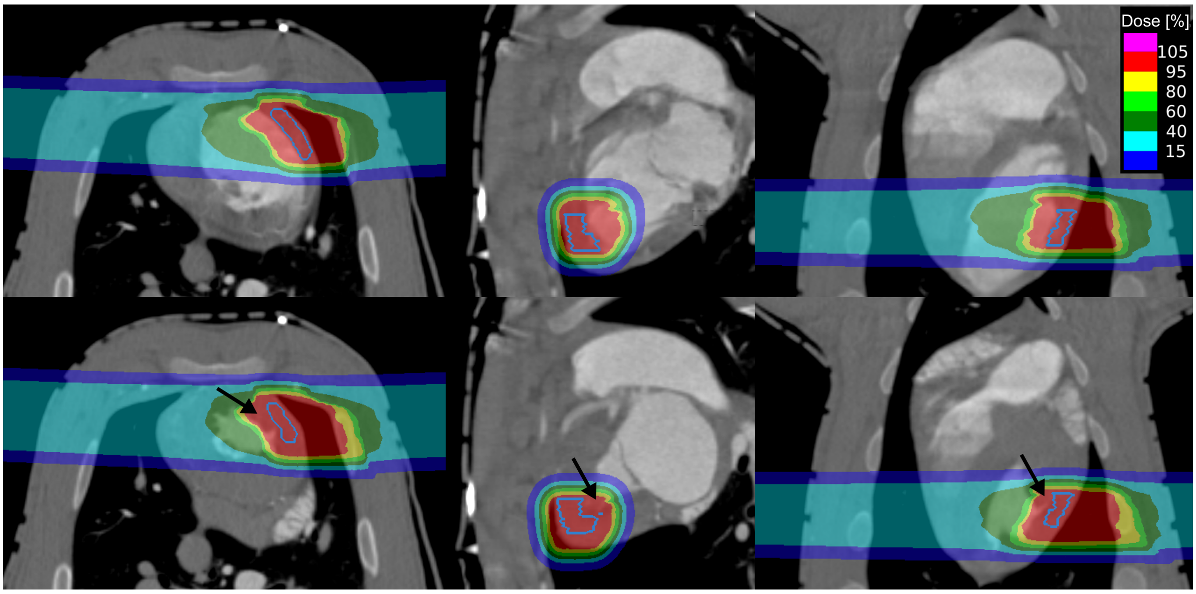

Figure 3.8.: Axial, sagittal and coronal views of the dose distribution of Pig 15 in diastole (top) and systole (bottom). The corresponding propagated contours are marked in blue. The arrows indicate that during systole the contour is not large enough to cover the full myocardium. Thus, it is likely that it was not possible to deposit the full target dose in a transmural region.

3.3 Summary and Discussion

To overcome the DIR problems reported in [And16a], two new registration strategies were tested. An approach with adapted parameter combinations was applied as well as a stepwise registration. None of theses approaches could significantly improve the registration outcome. The DIR quality is still too low to be used as suitable input data for 4D simulations.

However, the results of PRSC simulations showed that the reduced target coverage in the 4D simulations, reported in Chapter 2, is due to the low quality of the registration's inverse consistency. This finding was especially pronounced within the planning target volume (PTV). Even though the interplay effects are mitigated by the applied rescanning strategy for the majority of the pigs, large variations within the target coverage indicate residual motion effects for specific pigs.

For the AVN group no impact on the study outcome is expected due to DIR uncertainties. This was investigated using manually drawn contours in all phases. Although it was not possible to contour each motion phase for the superior pulmonary vein (SPV) group, equal findings are expected due to the comparable deformation of the targeted volume. In contrast, the registration uncertainties likely had an influence on the LV group irradiation, as the thickening of the myocardium during the systole was not correctly modeled. Hence, target doses below the planned dose of 40 Gy are likely.

CT Quality

The in-vivo feasibility study presented in Chapter 2 was the first in-vivo study performing 4D treatment planning on cardiac gated contrast enhanced 4DCTs. In a retrospective analysis of the CT data, several irregularities were found within the 4DCTs used in treatment planning and DIR.

For almost all contrast enhanced 4DCTs the contrast agent was not homogeneously distributed, especially within the right atrium, see Figure 3.9. In addition, the concentration of the contrast agent was changing over time. Thus, the different rotations of the CT detectors resulted in different HU for the same anatomic structure. Furthermore, the reconstruction of the 4DCTs did not work reliably in all cases, hence, imaging artifacts are visible in different motion phases of certain pigs. These motion artifacts can be identified as edges in the CT and are caused by a fast and irregular motion of the imaged structure [Che04].

(a) Pig 2

(b) Pig 17

Figure 3.9.: Axial, sagittal and coronal view of the reference phase of two 4DCT are shown. All stated uncertainties in the 4DCT recording can be seen in this cuts. In both figures the inhomogeneous contrast agent distribution is visible, while in (a) the pacemaker and in (b) the strip artifacts can be seen.

Two additional problems occurred in the 4DCTs of the AVN group. First of all, the tip of the heart was not recorded for these pigs. Even though this was not critical for the DIR process carried out prior to the feasibility study, the missing heart tip could increase the difficulty to solve the DIR problem for the AVN group when applying motion models. In addition, metal artifacts due to the implanted pacemakers reduced the quality of the 4DCTs further and, hence, could alter the treatment planning outcome [Jäk07]. Especially for Pigs 2, 6 and 8 the metal artifacts could cause problems during DIR as well as irradiation, as they are in close proximity to the target volume.

The determination of necessary improvements of the CT protocol is essential to be able to develop a reliable DIR algorithm. As the 4DCTs are used as base data for DIR, a low quality of the 4DCTs is strongly connected to uncertainties of the DIR outcome. A first necessary step is a CT protocol that guarantees a homogeneously distributed contrast agent throughout the whole heart. Secondly, the use of a metal artifact reduction during the reconstruction of the CT is highly recommended [Abd16]. And finally, to overcome the motion artifacts, a heart rate reduction combined with an increased regularity of the heart beat by the use of drugs should be studied [Kal16]. Alternatively, the employment of an advanced and iterative CT reconstruction algorithm [Hah16] or the use of a CT scanner with 320 detector rows [Coo09] could increase the imaging quality and at the same time avoid image artifacts.

Deformable Image Registration

Catheter-free ablation is the first application of DIR in beating hearts for 4D treatment planning in particle therapy. Prior to the feasibility study presented in Chapter 2, no in-vivo experiment was carried out using deformation vector fields of cardiac-gated 4DCTs as input data for 4D treatment planning. Especially as innovative approaches are susceptible to uncertainties, careful consideration of error sources is necessary to allow a fast transition to clinical routine and enable a consequent improvement of the applied methods. Even though the presented study underestimated the complexity of the heart motion and overestimated the power of a B-Spline DIR, it is important to point out the uncertainties found in the retrospective analysis for the CT as well as the DIR data to support a prompt improvement of the described methods.

Considering the procedure of a DIR, trying to reduce the absolute difference between the reference and moving image, unsolvable challenges for the algorithm were found during the retrospective analysis. Extreme differences between the HUs, especially in the right atrium where the contrast agent was flooding the heart, as well as distinct changes of the anatomical structure, such as opening and closing of valves, cannot be correctly modeled by the applied DIR. One possibility to improve the outcome could be a segmentation of the contrast agent and afterwards a replacement with a constant HU value. This might increase the registration results, as strong gradients would vanish. Furthermore, a correct registration requires knowledge about deformable and non deformable areas of the CT. Especially the sternum and the spine should not be affected by the registration of the heart motion, as the 4DCT was recorded under breath-hold. To solve this problem, a segmentation of the heart should be considered for future simulations.

To estimate the effect of the DIR uncertainties on the treatment planning, contours of the AVN were manually created in each motion phase for all pigs of the AVN group blinded to the study outcome. Even though the precision of the target location is only within several millimeters, this approach allows an estimation of the actually deposited dose in the targeted area. The D_{95} values were above 94 % using the manual contours indicating that the reduced target coverage for some pigs in Chapter 2 is due to the poor inverse consistency of the registration and not due to residual motion effects. However, due to the described uncertainties in the target location of several millimeters in all three dimensions, manual contouring did not allow to calculate motion trajectories of the AVN throughout all motion phases.

Nevertheless, the manual contours can be used as an indication for new DIR algorithms to validate the contour propagation.

For the development of a DIR algorithm suitable for cardiac motion, incorporating biomechanical heart models should be considered. Several models for the heart motion are available. However, most of them are focusing on specific properties and anatomical structures of the heart due to the high complexity of the motion. The high complexity is caused by the contractions of atria and ventricles, which occur slightly shifted in time and moving the atrioventricular plane up- and downwards, as well as the complex interaction of myocardium and pericardium [Fri14b]. A review of different models is given in [Ker06].

One model of the atrioventricular plane motion was published in [Mak15], describing the atrioventricular plane as a piston unit. In addition, models of the left ventricular motion are published, but due to the high workload to develop them the number of models is still low. To overcome the extreme workload, MRI and diffusion tensor MRI approaches were proposed as a new class of anatomically accurate electromechanical models [Gur11]. Even though all these models are species dependent, left ventricular motion models are available for humans, canine as well as pigs [Ste03, Gur11]. Realistic ventricular models are more complex, as it is necessary to consider the interaction of atria and ventricles as well as the interaction of both with the pericardium. A first cardiac model for the full heart including the impact of the pericardium is published in [Fri14b]. In addition, first approaches for patient specific models, allowing an improved personalized treatment are available [Kri13]. These heart models are important and could provide support to overcome the registration problem for the heart motion discussed throughout this chapter. An integration of a biomechanical model, ideally a patient-specific biomechanical model, into a new DIR strategy should be tested in future, although this is a challenging approach.

Furthermore, the development of reliable DIRQA should be continued. While it is possible to check the success of contour propagation visually, a reliable quality assurance (QA) of the vector field outcome needs a dedicated software and a good understanding of the calculated results as it is not always obvious to distinguish between successful and unsuccessful vector field outcomes. In addition, it is useful to not only determine all quantities in the whole ROI, but also in the target volume and the entrance channel. This improves the knowledge of the vector field within the actual irradiated region. The mean values of the total body ROI can be influenced by the good results of the non deformable structures such as the chest wall and the spine.

For clinical transition, it is important to improve the knowledge of cardiac motion. One method could be ultrasound measures of AV plane displacement [Slø04]. In addition, ultrasound guidance [Sch14, Pra14a] could be an option for future experiments to gain baseline data as well as for real-time motion monitoring. As since 2015 MRI compatible implantable cardioverter-defibrillators (ICDs) are available [Med], MRI could be a powerful tool for the determination of scar tissue within the heart muscle for baseline data and treatment planning as well as for success control of the treatment [Ips14].

Reliability of the 4D simulations

During the manual contouring of the AVN position within all motion phases, it was found that Pig 5 had a malformation of the heart. Due to a defect in the myocardium, the pacemaker electrode was positioned in the left ventricle instead of the right one. This caused an inappropriate pacemaker electorde position in close proximity to the AVN. Furthermore, the timing of the contrast-agent enhanced 4DCT was lacking and, hence, the amount of contrast agent was reduced causing a poor quality of the vector field with underestimated motion amplitudes. This small vector amplitudes explain the superior target coverage for Pig 5 compared to all other pigs shown in Chapter 2.

The results of the PRSC simulations are comparable to the median values of the 4D simulations carried out in Chapter 2. Reduced values for the target coverage within the PRSC simulations indicate problems of the inverse consistency of the applied DIR, as the general idea of the perfect rescanning approach is performing 4D simulations neglecting interplay effects. Thus, the results should yield a good target coverage. However, a realistic 4D simulation considering a motion surrogate and a BDS should give comparable results on average. Based on the results of the PRSC simulations, it was not possible to achieve a satisfying target coverage for several pigs due to the poor inverse consistency. Thus, all results should be analyzed relative to the PRSC results. Within these limitations, the observed target coverage in TV and PTV indicates a successful interplay mitigation in most pigs. However, for some pigs large variations were found that are due to residual motion effects. Nevertheless, the DIR uncertainties do not allow a correct 4D simulation for the in-vivo experiment presented in Chapter 2.

Influence on Study Outcome

Even though the poor inverse consistency diminishes the value of 4D simulations, the repeated manual contouring indicates that the treatment planning for the AVN group was correct. The area of the AVN was fully irradiated within all motion phases taking the location uncertainties into account. Hence, the heterogeneous study results are not necessarily correlated with the registration problems. However, several other possible reasons are known. One of the main reasons might be missing 3D imaging at the treatment location. This did not allow to determine a position of the pacemaker leads during the irradiation. Furthermore, anatomical changes, such as the heart or lung volume, are not exactly known. The situation is assumed to be comparable for the irradiation of the SPV group. However, due to the complex contouring process for the SPV irradiation, it was not possible to carry out contouring for each phase.

The effect of the low quality DIR on the outcome of the LV group is different. As shown in Figure 3.8, the DIR does not successfully model the thickening of the left ventricular free-wall, which caused too small ITVs and, hence, did not allow a transmural irradiation within all motion phases. Especially during the systole the spread-out Bragg was not deep enough to penetrate the whole myocardium. However, in this case it was not possible to determine the actual target coverage as carried out for the AVN group. Due to the strong contraction and deformation of the myocardium it was not possible to follow the arbitrarily determined target volume over the full cardiac cycle. This would be different for patients, as in a real case, an already existing scar, visible in MRI and ultrasound, would be irradiated. This would allow a correct contouring in all motion phases.

In summary, more advanced DIR methods are necessary. Existing strategies from other fields, especially image fusion and biomechanical motion modeling, can be adapted. In clinical routine, irradiation can be carried out if all phases of a 4DCT are contoured, but 4D dose simulations would strongly benefit from better DIR approaches.

4 Fast Rescanning Strategies for Hypofractionated Ion Beam Therapy

The trend in radiotherapy is moving from fractionated treatments to hypofractionated or even single-fraction treatments also known as radiosurgery [Whe08, Whe10, Fri16]. In addition, the use of radiotherapy is spreading to treatments of non-cancerous disease, such as cardiac arrhythmia, trigeminal neuralgia, arterial aneurism and arteriovenous malformations [Ber12]. In recent years, this trend is supported by technical developments, allowing a treatment with an increased conformity of the dose distribution [Bra00, Sal12]. Furthermore, especially in scanned particle therapy, the treatment of moving targets is becoming more common. Besides handling range changes, this frequently requires the use of motion mitigation techniques to avoid interplay effects due to an interference of the scanned ion beam and the target motion. One possible motion mitigation approach in particle therapy is rescanning. It can be applied easily with just minor technical changes and it is more robust compared to gating or tracking. However, both, the increased doses due to hypofractionated treatments as well as the use of rescanning prolongs the treatment time. As longer treatment times decrease the number of patients treated per day and their comfort, for economical reasons as well as for more efficient and comfortable treatments new approaches are warranted to allow a faster irradiation.

In particle therapy, the main factor determining the treatment duration is the intensity of the particle beam. In an ideal system the allowed intensity for each iso-energy slice (IES) and raster point is the maximum intensity available at the accelerator. However, the several conditions are necessary to perform a controlled and high-quality treatment can cause an intensity reduction. The main source for the latter is the requirement to perform two beam position measurements during the irradiation of each raster point. Other reasons are a high loss of particles in the beam transition between two raster points or the limited measurement range of the ionization chambers which is fixed for each IES. All limitations need to be considered to guarantee the deposition of the correct amount of particles at the predetermined position. Further details can be found in [Sch15]. As particle numbers can vary between $5 \cdot 10^3$ and $1 \cdot 10^6$ within each IES, the previously stated limitations are necessary to guarantee a high quality treatment. Different attempts to overcome intensity limitations and to reduce the treatment time are already known. While the Paul Scherrer Institut (PSI) and the National Institute of Radiological Sciences (NIRS) reduced the time necessary for energy changes significantly [Ped01, Miz14] and implemented a dynamic intensity control (DIC), Heidelberg Ion-Beam Therapy Center (HIT) implemented only a DIC. The latter allows to adjust the particle intensity during each spill.

The following chapter presents new approaches to conduct faster rescanning irradiations by applying a scan path optimization (SPO) to overcome intensity limitations. Therefore, IESs are split according to the particle number of each raster point. In addition, the influence of the SPO as well as the DIC implemented at HIT on 4D dose distributions is investigated. Therefore the SPO as well as the DIC was implemented in a designated beam delivery sequence simulation (DSim) software to carry out realistic 4D simulations using TRiP4D [Ric12].

4.1 Material and Methods

4.1.1 Fixed Intensity

At facilities operating with a fixed intensity over the whole extraction time predetermined intensity levels are available for the irradiation. The standard procedure for determining the maximum possible intensity level for each IES is to identify the raster point with the lowest particle number. The particle flux is then scaled down until the intensity level is reached that allows the treatment control system (TCS) to perform a beam position measurement twice within the irradiation time of this raster point. After that, other intensity limitations, like the dose lost in transition between two raster points and the measurement range of the ionization chambers, are checked. If necessary, the intensity is further reduced until all constraints are fulfilled. As the intensity is kept constant for the whole IES, a long irradiation time for the whole IES can be caused by a single low intensity raster point. In this case most of the time is spent irradiating raster points with an unsuitable low intensity. These varying irradiation times cause an irregular motion of the beam over the targeted volume. The behavior of the beam intensity over time is schematically shown in Figure 4.1(a). This irregular time behavior has no effect on the treatment of static tumors other than prolonged irradiation time. Its effect on moving targets is investigated within this chapter.

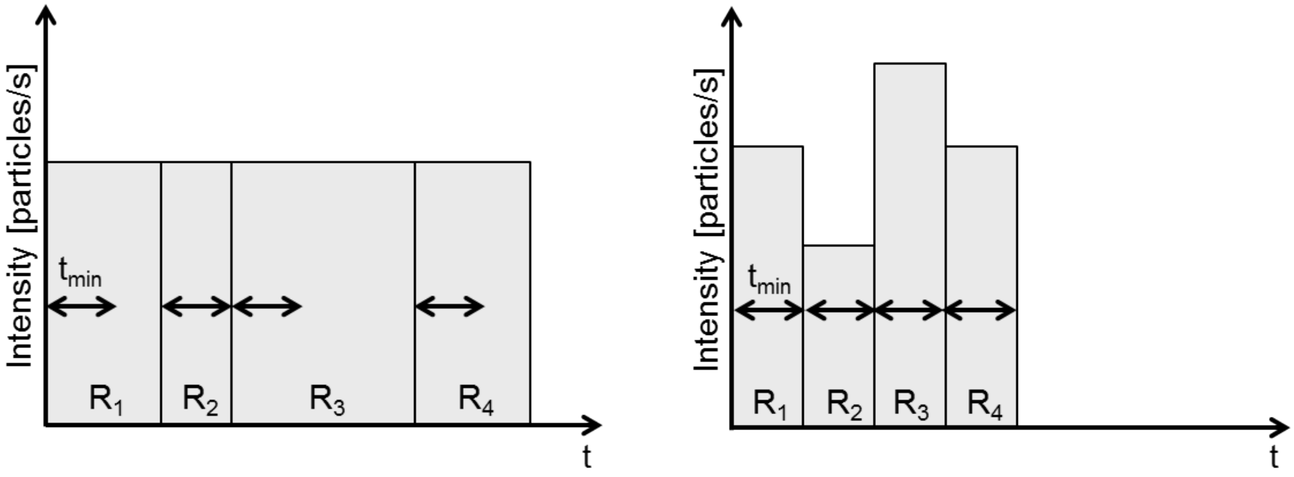

(a) Schematic behavior of the intensity over time for an irradiation carried out with a constant intensity.

(b) Schematic behavior of the intensity over time for an irradiation carried out with a dynamic intensity control.

Figure 4.1.: Comparison of the variation in time of raster points irradiated with a fixed and a dynamic intensity. R_1 to R_4 correspond to 4 raster points. Adapted from [Pan14].

4.1.2 Dynamic Intensity Control

A DIC allows altering of the beam intensity during the irradiation of a single IES and applies the highest possible intensity for each raster point [Fur07, Sch15]. The aim of DIC is to increase the efficiency and the stability of the accelerator and, hence, to reduce the treatment time. Prior to the treatment, the TCS needs to determine the maximum possible intensity for each raster point to be able to request the varying intensities from the accelerator. This allows a constant irradiation time for each raster point corresponding to the shortest treatment time possible with the used system. The intensity behavior over the treatment time for a system with a DIC is schematically shown in Figure 4.1(b) The DIC influences the beam delivery sequence (BDS) of a treatment plan and can therefore have an effect on the 4D dose distribution for moving tumors. Compared to a constant intensity, a more regular motion of the beam across the targeted volume is present applying a DIC. If this is more prone to interplay effects, is investigated throughout this chapter.

The technical implementation requires a feedback loop connected to the accelerator to automatically adjust and control the intensity. For the work of this chapter the model of the DIC at HIT is used. The simulated system is not able to use the maximum intensity allowed for each raster point, as increasing and decreasing the intensity cannot be done instantaneously. The treatment times are thus prolonged compared to an ideal case. In addition, comparable to the fixed intensity, several conditions need to be fulfilled to irradiate the IES with the highest possible intensity. Especially, if the particle numbers of the raster points are heterogeneous, the maximum allowed intensity can be reduced due to the dose lost in transition or the restricted measurement range of the ionization chambers. In general, two types of intensity fluctuations are always present and have to be considered. The feedback loop of the DIC needs milliseconds to adjust the intensity, hence, only intensity fluctuations on this time scale can be influenced. Fluctuation on the scale of microseconds are always present due to statistical variations and cannot be avoided by the use of a DIC as implemented at HIT. Further details about the described DIC can be found in [Sch11, Pan14, Sch15]. For more information about DIC in general and the implementation at the Heavy Ion Medical Accelerator in Chiba (HIMAC) the reader is referred to [Fur04, Fur05, Fur07, Sat07].

4.1.3 Scan-Path Optimization

To deliver a carbon ion treatment, the single raster points of an arbitrary IES are connected via a scan path determining the order of their irradiation. However, due to technical limitations of the raster scanning system, the gaps between two raster point must be smaller than a facility specific threshold, for instance, 2.2 times the FWHM of the beam at HIT, in the following called scanner limit. The standard scan path implemented in TRiP98 tries to connect all points using a meander path across the IES avoiding to change the x and the y coordinate of the position at the same time, an example is given Figure 4.2(a). The algorithm is divided into three steps. In the first one the algorithms starts at the top of the IES and determines lines of raster points. The latter are then connected with each other as long as the distance between two following raster points is smaller than allowed by the system. In case of a too large distance the algorithm starts searching for 'subpaths'. The final 'subpath' is the one which can connect the highest number of raster points. In the second step the algorithm tries to extend the previously found path with the residual points, which could not be included in the first step. Therefore it is checked if neighboring points, not included in the scan path yet but within the scanner limit, can be added to the path. If it is not possible to connect all raster points, the IES is subdivided into two separate slices. In the last step small subgroups of the path are permuted to smooth the path [Web]. An ideal scan path is as short as possible, avoids larger gaps to reduce the number of particles lost between two raster points and does not have any crossings [Kan07]. As the inhomogeneity of treatment plans is increasing, especially when using intensity-modulated particle therapy (IMPT), alternatives to the meander path are warranted.

An alternative method to optimize the scan path is to cast it as a traveling salesman problem trying to minimize the path length while neglecting the amount of direction changes, an example is given in Figure 4.2(b). The distance between the raster points can be determined by

$$d_i = \sqrt{(x_i - x_{i+1})^2 + (y_i - y_{i+1})^2}. \tag{4.1}$$

Thus, the objective function which needs to be minimized is given by

$$f = \sum_{i=1}^{N-1} d_i. \tag{4.2}$$

In Figure 4.2 the two different scan path optimization methods are compared. A SPO as a traveling salesman problem is a NP-hard problem. It needs high computational power to be solved exactly for a non-trivial sample size. Several different polynomial-time algorithms can be found in the literature for approximating the optimal solution [Rei94]. Sengoku et al. and Dias et al. proposed the use of a genetic algorithm with heuristics [Sen98, Dia12, Dia15]. A genetic algorithm is a metaheuristic, which is inspired by the survival of the fittest, the process of natural selection, and belongs to the large group of evolutionary algorithms [Raw91]. For this work a genetic algorithm is combined with a mutation and a crossover method [Sen98, Dia12, Dia15]. This combination allows to perform an efficient calculation of a scan path with minimized length. The use of a genetic algorithms allows to overcome a locally found minimum and approach the global minimum. In comparison to the traditionally used meander algorithm, the genetic algorithm provides better optimization especially for inhomogeneous raster point distributions. The traveling salesman algorithm manages to optimize a connected scan path in cases where the meander algorithm fails. During the work of this thesis a genetic algorithm was implemented in the DSim software.


(a) Meander algorithm (b) Traveling salesman algorithm

Figure 4.2.: Comparison of the two scan path optimization methods, showing that a traveling salesman algorithm produces shorter scan paths' than the meander algorithm.

Generally, the following steps have to be performed to minimize a scan path with a genetic algorithm:

1. Determination of a starting population P_0 with a certain number (N_0) of random paths.

2. Determination of the fitness value of all paths (e.g. the path length) and removing a certain fraction, $p_d \times N_0$, of the paths with the worst fitness values. This yields a new path population P_1.

3. From the path population P_1 a predetermined percentage, p_c, is selected for the greedy-subtour crossover. The newly created paths are added to P_1 to obtain again N_0 paths in total.
4. For the mutation, a predetermined percentage, p_m, of the population P_1 is selected. The modified paths replace the selected ones in P_1.
5. Finally, the whole process is repeated from step two using P_1 instead of P_0. The loop ends when either the maximum number of iterations is reached or no improvement is found within a certain number of iterations.

For the mutation the 2-opt method [Cro58] was chosen and for the crossover the greedy-subtour crossover was selected, proposed in [Sen98].

2-Opt method

The 2-opt method was proposed by Croes in 1958 to solve the traveling salesman problem (TSP) [Cro58]. The approach is able to create paths without intersections, but it cannot consider global optimization goals. To reduce the path length intersections are identified and removed. Equation 4.3 can be used to identify an intersection comparing the distance between two pairs of neighboring points. If exchanging the partners of the pairs reduces the sum of the distances the exchange is kept.

$$\overline{W_{i+r}W_{i+r+1}} + \overline{W_i W_{i+1}} > \overline{W_{i+r}W_i} + \overline{W_{i+r+1}W_{i+1}} \tag{4.3}$$

This approach neglects all optimizations that take into account more than the exchange of two subparts. In addition, the runtime is rather long, as the algorithms need to calculate the distances between all raster points yielding a $O(n^2)$ complexity. The algorithm needs to run several times as new crossings can be induced by the 2-opt method. A scheme of the application of the 2-Opt method is given in Figure 4.3, where the exchange of neighboring pairs is illustrated.

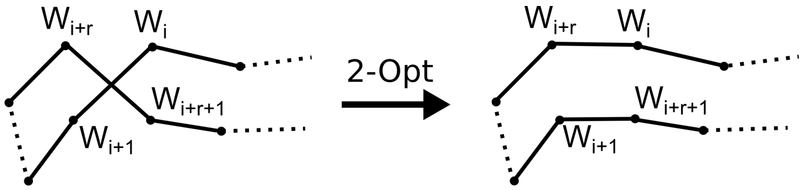

Figure 4.3.: Schematic of the 2-Opt method. Adapted from [Dia12]

Greedy-Subtour Crossover

The greedy-subtour crossover was proposed in [Sen98] to add new paths to the existing path population. While the 2-Opt method can only perform local optimizations, the greedy-subtour crossover allows to combine two paths, changing their global structure, to approach the optimal solution. A schematic of the method is shown in Figure 4.4. Performing the greedy-subtour crossover involves the following steps:

1. Two random parent paths are selected.

2. A random entry of the first parent is chosen, the position is stored (x_1) and the entry is added to the child path.

3. The position of the same entry in the seconds parent path is searched(x_2).

4. x_1 is changed to x_1-1 and x_2 to x_2+1. The entry of x_1 is placed on the left of the existing entry in the child path and x_2 is placed on the right.

5. The previous procedure (step 4) is continued until one entry is already part of the child path.

6. In case the child path is still shorter than the parent paths, the remaining entries are added in random order to the end of the child path.

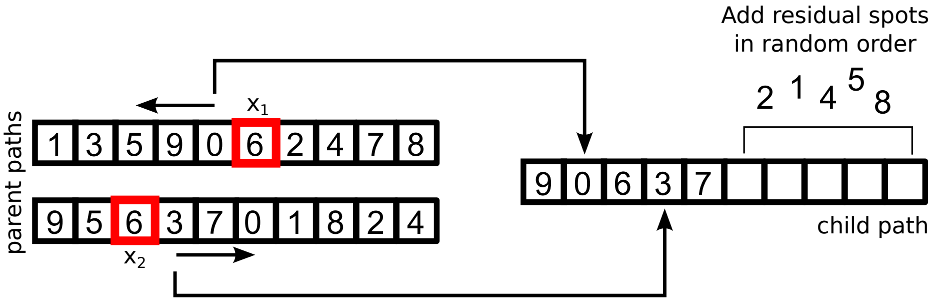

Figure 4.4.: Schematic of the greedy-subtour crossover method. The red boxes indicate the positions x_1 and x_2. Figure adapted from [Sen98]

4.1.4 Separate Iso-Energy Slices

As pointed out in the previous sections, the irradiation time is prolonged by the large differences in particle numbers of the raster points in a single IES. In the case of a fixed intensity, time is lost irradiating raster points with an unsuitable low intensity. In the presence of DIC, the perpetual increasing and decreasing of the intensity is responsible for a prolonged treatment times due to the finite intensity gradient. Both problems can be handled by categorizing the raster points of a single IES into sets of *small* and *large* points, which have a small or high particle number, respectively. With a fixed intensity irradiation, these two sets are placed on two different slices, from here on called SPO I. Using DIC both sets can be irradiated within one slice, but due to the new scan path considerably less intensity ramping is needed. This approach is named SPO II in the following. However, when applying a SPO it must be ensured that the adapted scan path can be irradiated. For instance, the distance between two raster points that are irradiated in succession must not be greater than the limit given by the scanning magnets.

In the following the SPO developed during this thesis is explained. A schematic of the SPO algorithm is given in Figure 4.5. In addition, the outcome of SPO I and SPO II is shown in Figure 4.6(a) and Figure 4.6(b), respectively.

At the beginning the raster points are separated by a threshold, which is proportional to the mean particle number of the raster points within the IES. To exploit the potential of the algorithm the threshold is slightly increased until the maximum particle number of the chosen intensity level is reached. If the separation of the raster points does not lead to a shortened irradiation time, the IES is irradiated in the

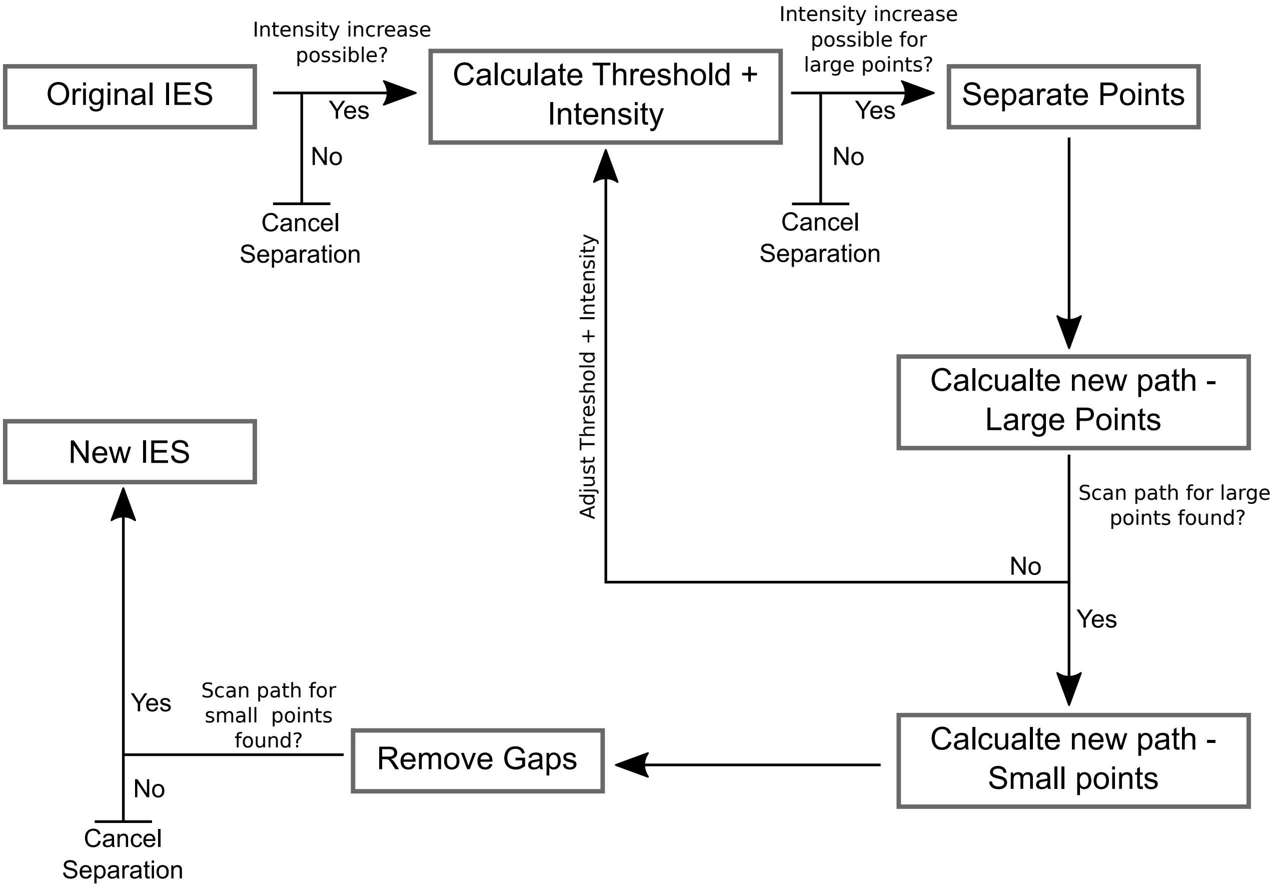

Figure 4.5.: Scheme of the SPO.

original form. This is only the case, if all raster points in the original IES can be irradiated with the same intensity level.

Subsequently, the algorithm tries to find and optimize a scan path for the large raster points. If a scan path can be constructed, the algorithm proceeds with the next step. If it is not possible to optimize a new scan path due to gaps, the intensity threshold is reduced to the next intensity level provided by the accelerator and the optimization is started again. This procedure is repeated until a scan path is found for a subset with an increased intensity. Otherwise the IES is irradiated with the original scan path and intensity.

If the algorithm is successful, it continues with the optimization of the scan path of the small raster point set. The number of small points is usually significantly lower than the number of large raster points, hence, gaps are more likely. For the set of small points gaps can be closed by creating additional raster points. The additional raster points are generated by splitting some of the large raster points. During this process it must be ensured that the number of particles for any of the large points is higher than the minimum number allowed by the current intensity level. Hence, a subset of large raster points with a sufficiently high particle number to deduct new beam spots is identified. Then the A*-algorithm [Har68] is used to bridge every gap in the small points by using the subset of the large points. If no path is found for one of the gaps, the whole separation of the IES is canceled. Otherwise, the points used by the A* algorithm are added to the set of small points and the corresponding particle number is subtracted

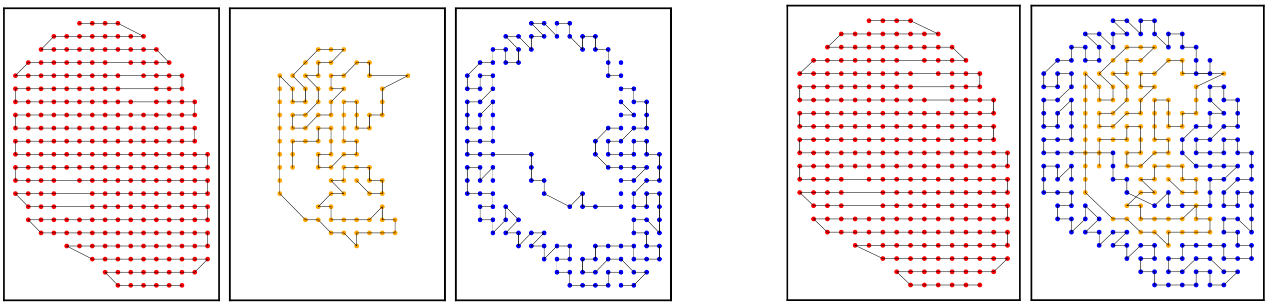

(a) Example for SPO I. On the left (red) the original IES is shown with the meander scan path. In the middle (orange) the raster points with the low number of particles are shown with the corresponding scan path and on the right (blue) the same is shown for the large raster points. This SPO can be applied with a constant intensity as well as using ac DIC

(b) Example for called SPO II. On the left (red) the original scan path is shown, while on the right the combination of the scan paths of the small (orange) and large (blue) raster points is displayed.

Figure 4.6.: Examples for the outcome of the SPO algorithm.

from the corresponding large point, yielding a successful separation of the IES. The plan can now be irradiated, either within one slice for a DIC or in two separated ones applying a constant intensity.

4.1.5 Simulation Software

To simulate treatment time and intensity, the software DSim, developed at GSI Helmholtz Center for Heavy Ion Research (GSI), was used and extended. The software allows the simulation of a beam delivery taking into account the different parameters for different accelerators. Up to now simulations for HIT and GSI are possible and an extension for Marburg Ion-Beam Therapy Center (MIT) is planned. The DSim is a necessary step for 4D simulations carried out with TRiP4D.

DSim can simulate different modes like static, rescanning and 4D optimized irradiations and can combine all modes with gating. The software is command line based and written in C++. It was originally developed by Daniel Richter and Peter Steidl [Ric12, Ste12]. A modularization was carried out by Sebastian Hild in 2014. The latter allows the fast implementation of additional features such as DIC and SPO, which are independent of the optimization of a treatment plan but are reordering the raster points.

The aim of the DSim is to predict the speed and timing of an irradiation. Correct treatment simulations are especially important for irradiations of moving targets to gain a correct temporal correlation between the irradiation and the target motion. Thus, 4D dose distributions can be calculated and the possible interplay effects as well as the efficiency of the motion mitigation techniques can be assessed. Therefore DSim processes all IESs and corresponding raster points and determines the intensities and irradiation times per raster point. The list of intensities and treatment times is merged with the spill structure of the accelerator, providing a full temporal simulation of a specific accelerator. To allow the correct determination of the accelerator settings and corresponding irradiation times, libraries representing the different available accelerator parameters are included. In addition, the tool is able to correlate the irradiation timepoints of the beam spots and a motion surrogate to simulate 4D optimized and gated treatments.

For the results described in this chapter, the irradiation time was determined using DSim. The raster point order was modified by applying the previously described SPO. The particle number per raster point was kept constant to not change the static dose deposition optimized by the treatment planning system (TPS).

4.1.6 Patient Data

The use and influence of the fast rescanning strategies presented within this chapter was investigated using three different data sets. First of all, the algorithm was applied to the data set of the pig feasibility study presented in Chapter 2, consisting of 14 pigs, divided in three different target and dose groups. Further details can be found in section 2.1.1.

In addition, a data set of five patients for the catheter-free ablation of the pulmonary veins in humans was used. A corresponding treatment planning study was published in [Con14,Con16]. As the irradiation times of the published data are long, the benefit of the approaches described above was investigated. However, to successfully apply the SPO, the spacing between the raster points had to be increased from 1 mm to 2 mm to gain a more homogeneous grid of raster points.

To show the efficiency of the approaches not only for catheter-free ablations, the use of the proposed techniques for hypofractionated cancer treatments was investigated. Hence, five lung cancer patients were used out of the patient group of a study published in [And16b]. Finally, the SPO efficiency is investigated during experiments using three clinical plans for liver and one clinical plan for pancreas treatments provided by HIT.

4.1.7 Experimental Set-up

To measure the exact timing and to benchmark DSim for further simulations studies, an experiment was carried out in the quality assurance cave at HIT. Two different experimental set-ups were used, see Figure 4.7. For the first one, called 2D-setup, a prototype of the Octavius SRS1000 (PTW, Freiburg, Germany) capable of proton dosimetry recorded the dose of single IESs in shoot-through measurement. In addition, a Beckhoff system and the machine beam records provided information on the timing of the accelerator [Ric12]. The Octavius SRS1000 was mounted on top of a sliding table to be able to perform 4D measurements. The motion amplitude in horizontal direction was 2 cm and the motion period was chosen to be approximately 5 seconds to investigate the effect of DIC on 4D dose distributions. In second set-up, called 3D-setup, the Octavius SRS1000 detector was replaced with a water phantom (PTW, Freiburg, Germany) and 24 pinpoint ionization chambers to measure the accuracy of 3D dose distributions. As in the first set-up, the Beckhoff system and the machine beam records were used to gain the timing information.

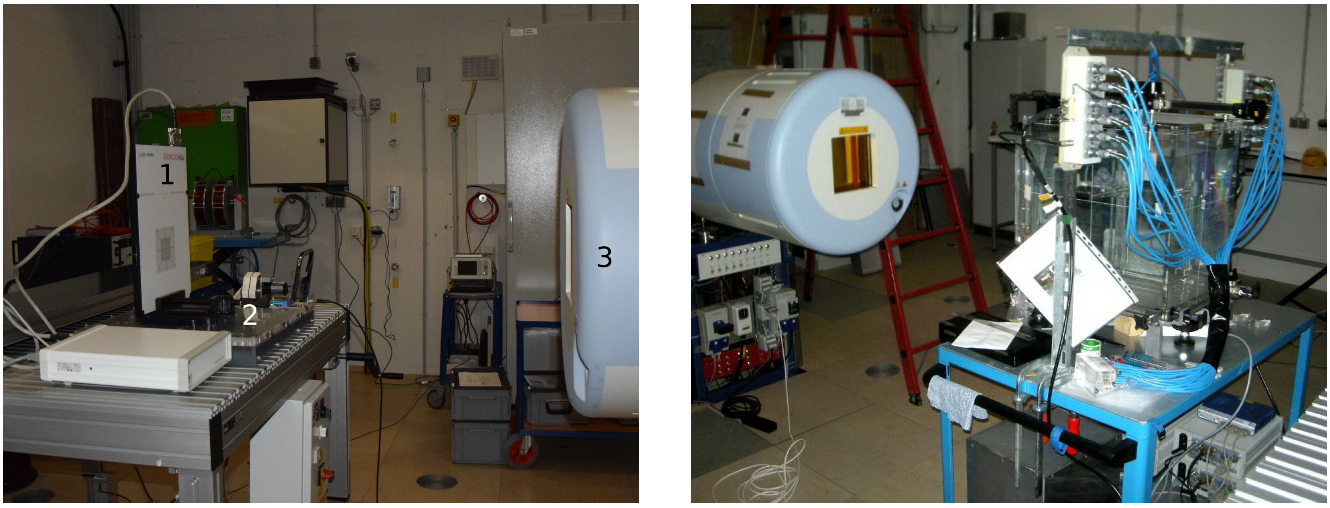

(a) The experimental set-up of the 2D measurements is shown. The Octavius SRS1000 (1) was mounted on top of a sliding table (2) to be able to perform 4D measurements and reconstructions. The set-up was positioned up stream of the beam exit window (3) without additional material in-between.

(b) An experimental set-up comparable to the one used for the 3D measurements is shown, including the 24 pinpoint ionization chambers and the water phantom, both manufactured by PTW. Figure taken from [Kad11].

Figure 4.7.: Experimental set-up of both parts of the experiment in the QA-room at HIT.

4.1.8 Data Analysis

The data analysis carried out for the 4D simulations as well as for the measurements is described within this section. For an easier understanding the used methods are split in two parts. First the data analysis of the simulations will be explained followed by the analysis of the measurements.

Simulations

For all patient cohorts, treatment plans were optimized using TRiP4D [Ric13]. The resulting treatment plans were then modified using the SPO and corresponding BDS were determined using the DSim software to create the necessary input data for 4D dose calculations. Afterwards a set of interplay and rescanning simulations was carried out for each patient cohort.

In the pig cohort, for each animal simulations were performed combining three different heart rates with 60, 70 and 80 bpm, 8 different starting phases (0°, 45°, 90°, 135°, 180°, 225°, 270°, 315°) and a regular and irregular heartbeat. All described options were simulated for a constant and a dynamic intensity for rescanning as well as for interplay irradiations. For the rescanning simulations, also calculations for the SPO were carried out for both intensity patterns, yielding in total 2688 simulations for the pig cohort. For the human patient cohort interplay and rescanning simulations for two different heartbeats with 60 and 86 bpm and 4 different starting phases (0°, 90°, 180°, 270°) were conducted, comparable to the simulations performed in [Con14, Con16]. In total, 240 simulations were carried out for a constant and a dynamic intensity for rescanning as well as for interplay irradiations. For the rescanning simulations, also calculations for the SPO were carried out for both intensity patterns. Also two motions of 17 and 12 breathing cycles per minute were used for the lung cancer data combined with 4 different starting phases (0°, 90°, 180°, 270°), comparable to the simulation performed in [And16a, And16b]. The total number of simulations was 240, as for the catheter-free ablation in humans.

For all simulations, the expected irradiation times for the different scan paths were extracted from the logfiles of the DSim. The resulting irradiation time of the simulation without DIC and without SPO was treated as a reference. All time savings were calculated relative to this reference time, if not stated differently. In addition, for all different simulation types and patient cohorts a two-sided paired T-test was carried out.

V_{95}, D_{95} and D_5-D_{95} were calculated for all simulations comparable to chapter 2, to determine changes in the target coverage and dose homogeneity. The found results were compared for the different approaches using SPO, applying DIC and combining both approaches.

Measurements

For the readout of the Octavius SRS1000, the software delivered by the manufacturer (BeamAdjust 1.9, PTW Freiburg, Germany) was used, while for the pin-point ionization chambers a software written by C. Karger was applied [Kar99], providing a graphical feedback. The differences between measured and simulated irradiation times were determined using the machine beam records and the log files of the DSim. To compare the deviations for the simulated and measured treatment time for each raster point, the root-mean-square error (RMSE) was determined for each treatment plan. For the measurements with the water phantom and the pinpoint ionization chambers, the mean and the standard deviation of all pinpoints for each measurement was determined. The results for the original plans without SPO were taken as reference. For all irradiated 2D and 3D plans the actual time savings of DIC and SPO was determined.

To compare the outcome of the static measurements with the Octavius 1000SRS, the measured doses of 60 plans were analyzed. The similarity of the measured dose distributions was investigated by determining the γ index [Low03, Low98]. For each plan the γ-index was calculated to compare DIC and constant intensity measurements, measured dose distributions with and without rescans as well as SPO I and SPO II dose distributions. In addition, the measured dose was plotted for all irradiated plan types to visually compare the results. For γ-indices smaller than 0.95 (2mm/2 %) the total deviation of the measured doses was determined.

For the 3D dose measurements the deviations in each pinpoint were analyzed and deviations for each field, pinpoint and patient were determined. In total 35 measurements were carried out investigating treatment plans of 5 different patients. However, due to technical problems, such as, interlocks and aborted measurements, only 30 measurements could be analyzed.

For the 2D measurements 7 single IESs of liver cancer and cardiac ablation plans in pigs were used. For the 3D measurement one pancreas plan, two liver plans (Liver1, Liver2) and both fields of a cardiac ablation plan in pigs was measured. In total 270 measurements were carried out during the experiment.

4.2 Results

In the following chapter results of simulations as well as measurements investigating the influence of DIC and SPO on 4D dose distributions are presented. In addition, possible time savings for both speed-up techniques are analyzed. Throughout this chapter results are either given as mean values with standard deviation (mean ± stdev) or as median values with the range between the 25th and 75th percentile (median (25 % - 75 %)).

4.2.1 Simulations

Simulated time savings

For all patient cohorts combined, average time savings of 50 ± 10 %, 55 ± 7 %, 51 ± 11 % and 59 ± 8 % were found for the use of a DIC, SPO I, SPO II and for SPO I with DIC, respectively. Applying SPO II for a plan delivered with DIC could further reduce the treatment time by 5 ± 2 %, 8 ± 1 % and 1 ± 1 % for the pig feasibility study, human pulmonary vein ablations and lung cancer treatments, respectively. In addition, the time reduction was increased using DIC and SPO I, as originally proposed for facilities with constant intensity. In this case additional time savings of 27 ± 7 %, 3 ± 1 % and 18 ± 3 % were found compared to a irradiation without SPO for the pig feasibility study, human pulmonary vein ablations and lung cancer treatments, respectively, were found. An overview of the time savings separated for each patient cohort is given in Table 4.1.

	DIC	SPOI	SPOII + DIC	SPOI + DIC
Cardiac Ablation - Pigs	51 ± 5 %	45 ± 6 %	49 ± 5 %	38 ± 7 %
Cardiac Ablation - Humans	33 ± 2 %	39 ± 2 %	30 ± 2 %	32 ± 2 %
Lung Cancer Patients	58 ± 8 %	50 ± 8 %	58 ± 9 %	48 ± 8 %

Table 4.1.: Simulated relative irradiation times compared to rescanned irradiation with constant intensity for each IES

Target Coverage

The target coverage for all simulation types of the pig feasibility study are shown in Figure B.1. While for some pigs, for instance, 4, 6 and 8, deviations in the interplay pattern can be seen between a delivery with constant intensity and one with DIC, no differences can be found for the different rescanning simulations. Comparing the results to the simulations with constant intensity and traditional scan path, no clinical relevant reduction in the target coverage and dose homogeneity was found, neither for applying the SPO nor using a DIC or a combination of both. However, for all simulation types statistical significant deviations ($p < 0.05$) were found, especially for the planning target volume (PTV) coverage. Detailed results are listed in Table B.3.

As for the pig study, also the human heart cohort showed differences in the interplay pattern between a delivery with and without varying intensity. The rescanning results are comparable for both kinds of accelerator specifications and the different applied SPOs. In Figure B.2 detailed results for the 4D simulations of the pulmonary vein isolation in humans can be found. In Table B.5 the p-values, comparing the target coverage and dose homogeneity for all different simulation types are given. Even though all deviations are not clinically relevant, statistically significant ($p < 0.05$) changes were found in D_{95} and D_5-D_{95} values.

The interplay patterns for the lung cancer patients vary between simulations with constant intensity and with DIC, especially for Patient 1, 3 and 4. There was no relevant difference in the target coverage for the different types of rescanning simulations. In summary, the changes in the BDS have no relevant influence on the outcome of the motion compensated 4D simulations. For a detailed analysis of the 4D simulations the reader is referred to Figure B.3. Statistically significant changes ($p < 0.05$) were found for all simulations types in the V_{95} results. However, none of the deviations are clinically relevant.

4.2.2 Measurements

In the following sections the results of the measurements at HIT are presented, showing the actual time savings and validating the DSim. In addition, comparisons of the measured doses are performed in 2D as well as in 3D to verify the comparable dose distribution for different scan paths and delivery intensities. In total 270 plans were irradiated, 235 2D and 35 3D plans.

Validation of DSim

The agreement between measured and simulated irradiation times is good, showing average deviations below 5 %. However, the deviations are larger for the short single IES plans measured with the Octavius set-up. In this measurements deviations above 4 seconds were found, neglecting interlocks during the irradiation. This can be traced back to the number of spill pauses, as they differed between the simulation and the measurements. The extraction time varied between 4.4 and 5.1 seconds deviating from the expected and simulated extraction time of 5 seconds.

	Median [%]
3D	4 (1 - 7)
Static	-1 (-6 - 4)
Rescanning	-1 -6 - 2)
NewPath	0 (-2 - 1)
Large Points	-14 (-21 - -4)
Small Points	-17 (-62 - -6)
All 2D Plans	-4 (-18 - 1)

Table 4.2.: Temporal agreement between simulated and measured irradiation time of the complete treatment plan including spill pauses but neglecting interlocks. Negative values correspond to an underestimation of the treatment time in the simulations. In column 2 median values are given with the correspond 25^{th} and 75^{th} percentile given in brackets.

An overall agreement of 4% (1% - 7%) and of -4% (-18% -1%) was found for the total treatment times for 2D and 3D plans, respectively, neglecting irradiation with interlocks. Detailed results separated according to the different plan properties are shown in Table 4.2.

For all plans the RMSE of the simulated and measured treatment times was determined, quantifying the agreement of simulations and measurements. For all following calculations, all raster points influenced by spill pauses were ignored due to a varying duration of the latter. In addition, the data was fitted with a line through the origin to determine systematic deviations between simulation and measurement. It was found that for the 2D measurements a significant deviation of 3 % and 4 % is present for DIC and constant intensity, respectively, whereas the simulated treatment time is always overestimating the actually necessary time. For the 3D measurements delivered with DIC a deviation of 3 % was found as well. In Table 4.3 the RMSE is given for all plan types and for DIC as well as for a constant intensity.

	Constant Intensity			Dynamic Intensity		
	RMSE [ms]	Incline	RMSE$_{cor}$ [ms]	RMSE [ms]	Incline	RMSE$_{cor}$ [ms]
3D	-	-	-	1.43	0.97	1.43
Static	2.34	0.96	0.91	3.44	0.99	3.41
Rescanning	1.74	0.96	0.70	1.24	0.97	1.13
NewPath	-	-	-	1.03	0.96	0.87
Large Points	0.51	0.95	0.39	0.58	0.96	0.53
Small Points	0.67	0.95	0.53	1.00	0.98	0.99
All 2D Plans	1.56	0.96	0.67	1.25	0.97	1.17

Table 4.3.: RMSE for the temporal agreement between simulated and measured treatment times splitted by constant and dynamic intensity for the 2D measurements. The first column states the RMSE comparing the simulated and the measured values. The second column states the incline of a fitted line through the origin and the third column states the corrected RMSE considering the fit as truth. All results neglect the raster points influenced by the varying spill pause timepoints. Incline smaller 1 corresponds to an overestimation of the treatment time by the simulations.

Furthermore, the incline of the fit is stated to indicate the systematic deviations. The uncertainty of the incline was below 0.001. The largest deviations are found for heterogeneous treatment plans irradiated with high intensities (static). Furthermore, the RMSE for DIC is higher compared to deliveries with a constant intensities.

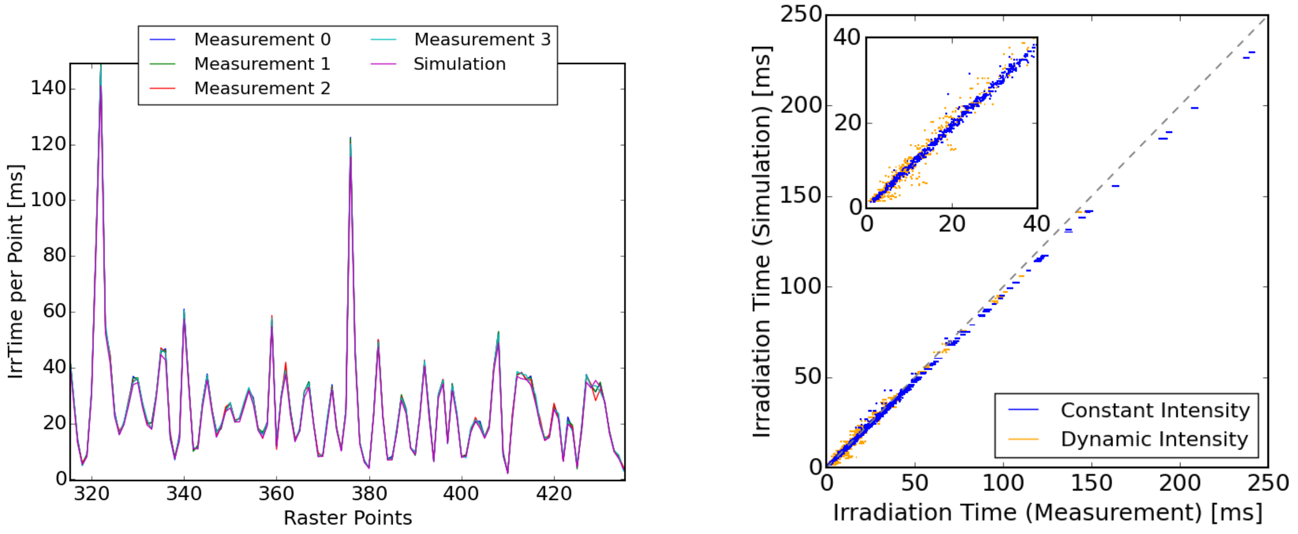

(a) Irradiation times for each raster point displayed for 4 different measurements using a fixed intensity and the simulation.

(b) Simulated irradiation time of each raster point plotted over the corresponding measured irradiation time. Data points appear almost as line through origin. Strips for the simulations appear due to fixed possible irradiation times.

Figure 4.8.: Comparison of the simulated and measured irradiation times for each raster point.

Differences between constant intensity and DIC are caused on the one hand by larger RMSE errors of the dynamic intensity due to the time necessary for DIC to adjust the intensity, which is in the order of 10 ms [Sch15]. On the other hand, a slight systematic overestimation of the irradiation times for raster points with irradiation times greater 100 ms is present. Both deviations can be seen in Figure 4.8(b). The agreement between simulations and measurement are good and the DIC at HIT works stable and reproducible. In Figure 4.8 the agreement between measured and simulated irradiation times is shown.

Measured Time Savings due to SPO and DIC

The time savings of the measured treatment plans were determined for DIC, SPO I, DIC+SPO I and DIC+SPO II. The results show significant time savings as expected from the simulations. For the 2D plans the total time saving due to DIC was determined to be 34 ± 26 %. For the 2D plans the use of the separated SPO saves 59 ± 6 % of the treatment time, while with combined path saves 15 ± 9 % for DIC. For a constant intensity, SPO I was able to save 79 ± 10 % of the treatment time. For the 3D plans applying SPO I saves 28 ± 13 % of the treatment time compared to 13 ± 5 % for using SPO II on average.

Dose Comparison in 2D

A good agreement between the measurments was found for the high dose IES taken from pig 12 and pig 14. For this plans all calculated γ-indices were 0.99 or 1.00. However, deviations were found for the IESs taken from a treatment plan of a liver cancer. Here γ-indices below 0.7 were found for the rescanned plans with constant intensity compared to the rescanned plan with DIC and compared to the non-rescanned plan with constant intensity. The deviations were determined to vary between 9 and 17 % depending on the measured plan. All calculated γ-indices and determined deviations can be found in Table B.1 and B.2. In Figure 4.9 the measured doses of pig 12 are displayed for all situations.

Dose Comparison in 3D

The found deviations of the pinpoint measurements were in average smaller than 2 percent, except for one patient. The exact values can be found in table 4.4. For Liver 2, a dose error due to path crossings in the new scan path cannot be completely excluded. However, due to results of the other plans and the good agreement of all other measurement of Liver 2, a technical problem is more likely.

Plan	Deviations [%]
Pancreas	0.1 ± 0.0
Liver 1	1.0 ± 0.8
Liver 2	-9.2 ± 0.0
Pig 14 - Field 1	0.5 ± 0.4
Pig 14 - Field 2	-0.2 ± 0.9

Table 4.4.: Deviations of the measurement for all 5 irradiated treatment plans.

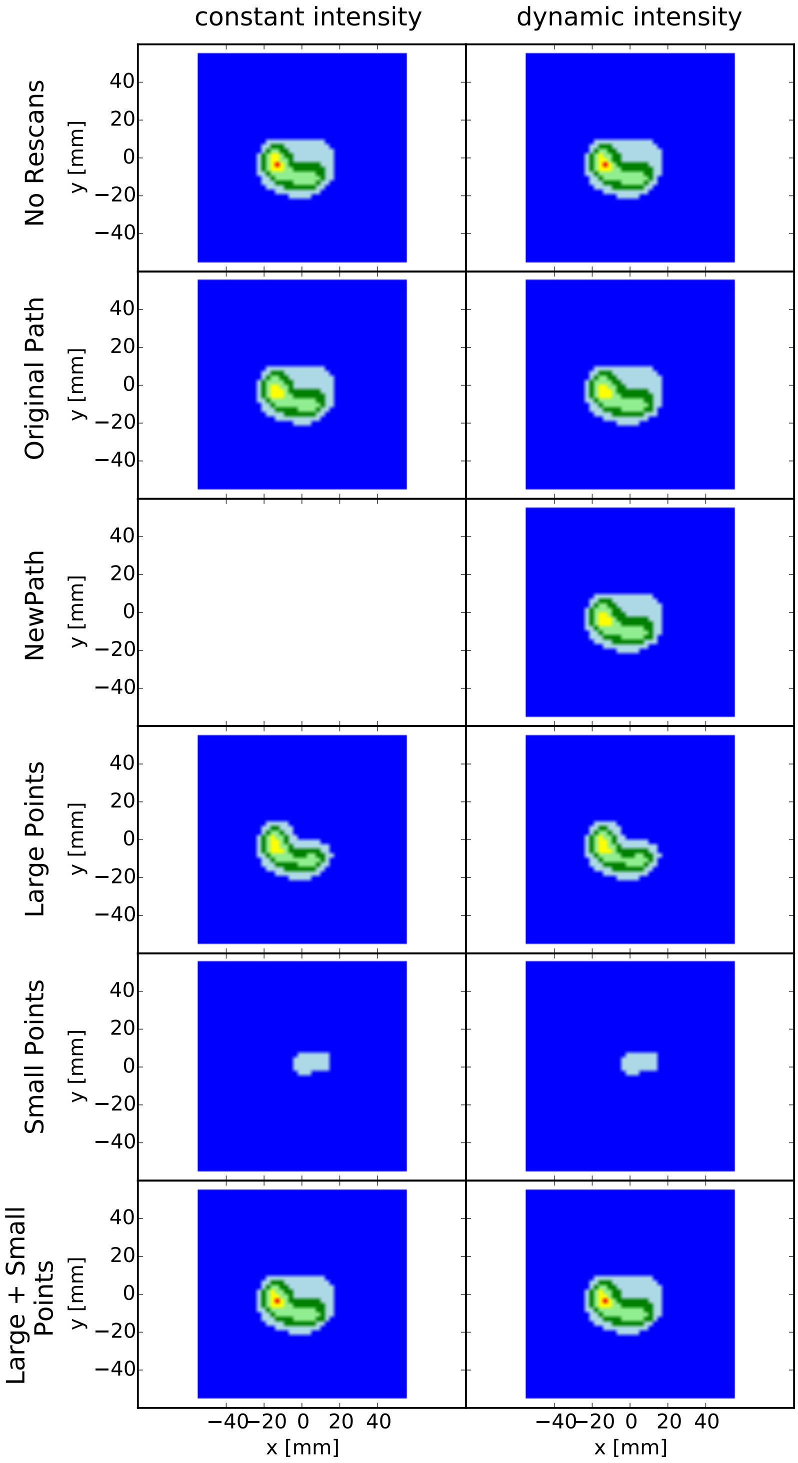

Figure 4.9.: Comparison of measured doses with different delivery methods, showing results for a constant intensity on the left and for DIC on the right. All different modalities to delivery the dose are shown including the standard path with and without rescans, the modified one, the delivery with raster points split in large and small particle number and, finally, the sum of the large an the small dose. Apart from the top row all plans were delivered with 15 rescans.

4.3 Summary and Discussion

In this chapter, new developments for faster rescanning techniques in ion beam therapy were presented. It was shown that a significant reduction of the treatment time is possible without reducing the the target coverage by using DIC, SPO or a combination of both. Even though changes in the BDS are present and have influence on the interplay patterns, the same motion mitigation strategies could be applied for all approaches. In addition, the software DSim used throughout this chapter was successfully validated for irradiations at the accelerator at HIT allowing realistic 3D and 4D simulations, which can serve as a platform to develop new treatment and motion mitigation strategies.

Agreement between Measured and Simulated Treatment Times

The deviations of the number of spill pauses between simulations and measurements had a significant influence on the treatment time for short 2D plans, as irradiation times for the single IES measurements were in the order of one spill duration. The reason for the extraction time variation is not clear yet and further investigations are necessary. For reliable 4D simulations a correct prediction of the spill pause is important to correctly correlate the irradiated raster point with the actual motion phase. Deviations in the correlation can have severe influence on the final dose distribution, as one unexpected spill pause is sufficient to change the temporal correlation of all following raster points of one IES. Some increased understanding of the accelerator behavior is necessary to fully adapt the DSim to the HIT accelerator. Nevertheless, it is possible to conduct realistic simulations of the irradiation time as well as the delivered dose with the current version of the DSim. The behavior of the HIT accelerator is well reproducible and stable. Irradiation time predictions of an arbitrary raster point are possible with median RMSE of 1.56 ms, 1.25 ms and 1.43 ms for 2D constant intensity, 2D DIC and 3D measurements, respectively. Especially for motion mitigated simulations, different starting phases can be used to verify that the irradiation is independent of slight changes in the temporal correlation.

Dose Comparison in 2D and 3D

Good agreements were found in the 2D dose distributions for Pig 12 and 14 between all application methods, indicated by γ-indices of 1.0. However, for the single IES measurements of the liver plan deviations were found in a certain plan. Especially, the measurement for the rescanned plan delivered with constant intensity shows deviations from the rescanned plan delivered with DIC and non rescanned plan delivered with constant intensity. Even though the shape of the recorded dose distribution were equal, deviations in the absolute values of around 10 % were found as already stated in Section 4.2.2.

A possible explanation for such deviations was the different particle flux between the measurements. All measurements showing a good agreement between all different modalities were irradiated with a flux of $1{\cdot}10^7$ particles per second and higher, whereas all measurements showing deviations were irradiated with a particle flux of $5{\cdot}10^6$ particles per second. The used detector is a prototype manufactured by PTW (Freiburg, Germany). At the German Cancer Research Center (DKFZ) in Heidelberg a study showed that, for smaller intensities measuring a homogeneous field without rescans, the measured dose deviates by about 1 % from the expected outcome on average [Dol]. Further investigations are necessary to ensure that the measured deviations for the 2D dose distributions are not correlated with the use of DIC or SPO and only occur due to detector properties.

For the 3D dose measurements the relative agreement between different scan paths was calculated and did not show deviations between different modalities except for one plan. For a pancreas plan, a deviation was found between the original and all modified plans. As all other plans showed a good agreement, it is assumed that something went wrong with the data acquisition for the reference plan. However, to completely ensure that the new scan paths or the application of a homogeneous rescanning scheme did not alter the results, a repetition of the measurement should clarify the situation.

Potential Time Savings

Both methods described throughout this chapter offer excellent time savings. The described SPO provides an opportunity for facilities without DIC to reach treatment times that were only possible by using DIC before. In addition, facilities already using DIC can further reduce the time necessary for irradiation. Furthermore, the possible time savings are comparable to the ones reached by applying the inhomogeneous rescanning scheme. While time savings of 58 ± 8% were possible for an irradiation of the inhomogeneous rescanning plans at HIT accepting a slightly reduced target coverage (see Chapter 2), SPO allows a time reduction of 55 ± 5% with target coverage comparable to the original plan.

However, the presented SPO works only when small intensity levels are used and the variation of the particle number between the raster points is large. All this is typically avoided in the clinical routine, where, especially for static tumors, the dose delivered per fraction is low and the minimum particle number per plan can be increased until the maximum intensity is allowed for each IES without any influence on the target coverage. Even though increasing the minimum particle number works for static cases with a normal fractionation scheme and also for hypofractionated ones, this approach is not possible anymore when it comes to rescanned treatments. Rescanning reduces the minimum particle numbers significantly. In addition, it is typically not possible to irradiate rescanned plans with particle numbers high enough to allow the maximum available intensity without a significant influence on the target coverage and dose homogeneity. To overcome the intensity limitations DICs were implemented in different particle facilities [Fur07, Sch15]. However, it is shown in this chapter that the presented SPO can be effective even in the presence of DIC. If SPO I or SPO II is more effective depends on the implementation of DIC and is therefore facility specific. In case of the DIC implemented at HIT increased time savings are possible using SPO I due to the chosen settings of the ionization chambers. To ensure a correct beam position measurement for all raster points independent of the particle number, a sensitive setting of the ionization chambers is chosen which does not allow the DIC to use the full range of available intensities. This causes the superior time savings of SPO I combined with DIC compared to SPO II. Hence, it would be interesting to perform comparable measurements at facilities with different DIC algorithms and compare the found time savings.

The time savings found for DIC in combination with hypofractionated treatment plans are in the order of 60 % for rescanned treatment plans and, hence, significantly higher as the possible reduction of approximately 10 % described in [Sch11, Pan14]. However, the time savings are expected to be less prominent in clinical routine. Especially for the liver and pancreas treatment plans, which were optimized for a static irradiation but then delivered with 4 rescans. Thus, the minimum particle number was extremely heterogeneous. For more valid time saving results, clinical treatment plans optimized for rescanned irradiations should be investigated.

The results for the 2D measurements show that time savings depend strongly on the structure of the treatment plan. Potential time savings are limited for plans with high intensities, but are very prominent for plans with mixed intensities. These plans can benefit from DIC as well as SPO.

Outlook

Due to the excellent time savings and unchanged target coverage the use of SPO and, if possible, DIC to overcome intensity limitations is highly recommended. Depending on the facility and the characteristics of a present DIC, additional time savings could be possible by further separating and optimizing the scan path. An ideal scan path is facility dependent and tries to sort the raster points in a way that the irradiation time is minimized. Thereby an automatic choice between SPO I and SPO II depending on the IES properties would be beneficial. For a clinical transition further tests are necessary to ensure the comparable dose distribution in more experiments. Furthermore, the implementation of the SPO in a commercial treatment planning system is required.

In addition, the presented DSim offers great opportunities investigating new possibilities to overcome interplay effects, to further reduce the treatment time using new techniques and to carry out realistic 4D simulations. A possible step for future developments is to combine simulated 4D optimized treatments [Gra14] with the presented SPO. This would further improve the treatment options and hence improve the treatment outcome of carbon ion therapy. In future, the extension and validation of the DSim software is planned for more ion beam therapy centers. To compare different implementations of DICs, comparable experiments as presented in this chapter should be carried out at the Marburg Ion-Beam Therapy Center, at the Shanghai Proton and Heavy Ion Center as well as at Centro Nazionale di Adroterapia Oncologica.

5 Discussion and Outlook

A first in-vivo study treating cardiac arrhythmia with scanned carbon ions was successfully conducted at GSI Helmholtz Center for Heavy Ion Research (GSI) in July 2014. This was not only the first study using particle therapy, but also the first one employing a full 4D treatment planning approach based on cardiac time-resolved computed tomographys (4DCTs) as well as a respiratory gating strategy. Fibrosis and tissue modifications were induced at predetermined locations showing the potential of scanned carbon ions as a non-invasive treatment modality for cardiac disorders. Electrical pathways were altered in the heart muscle without observing radiation induced side effects. Due to the inverse depth-dose profile of carbon ions and the raster scanning technique, highly conformal dose distributions were delivered successfully, sparing critical structures.

Nevertheless, the use of 4D treatment planning and dose calculations was necessary to ensure a correct mitigation of interplay effects. As carbon ions delivered by an active scanning system are prone to motion effects, repeated breath-holds were combined with rescanning to account for breathing and heart motion, respectively. A new, inhomogeneous rescanning scheme was applied to reduce the necessary treatment time, allowing the irradiation of all pigs within a limited time frame. However, the inhomogeneous rescanning approach came with the drawback of a reduced target coverage.

Even though a large effort was invested to achieve comparable treatments of all pigs, the study results were heterogeneous and differed between animals of identical target and dose groups [Leh16b]. As shown in Chapter 3, retrospective analysis showed that the quality of the recorded 4DCTs was poor and that the applied B-spline deformable image registration (DIR) was not sufficient to correctly model the heart motion. Thus, the target volume of the left ventricular free-wall (LV) group was likely not irradiated with the full planned target dose. For the atrioventricular node (AVN) group, manual re-contouring blinded to the study outcome was done for each motion phase to study the effects of DIR on the treatment planning. In this scenario, it was shown that the treatment planning for the AVN group was correct. The same result is expected for the superior pulmonary vein (SPV) group, although a validation study was not possible as the contours were too complex and could not be reliably transformed to each motion phase manually.

The poor quality of the DIR is also the reason for a reduced median target coverage in the 4D simulations. The reduced median target coverage in the planning target volume (PTV) found in Chapter 2 is mainly not due to residual motion effects. Instead, the uncertainties of the DIR, especially the large errors of the inverse consistency, shown in [And16b], did not allow realistic 4D simulations. However, the large variation in the target coverage for single pigs, for instance, Pig 6 shows that the used rescanning scheme was not sufficient to completely mitigate interplay effects. Future treatment planning studies should carry out perfect rescanning (PRSC) simulations first, before 4D simulations using beam delivery sequences (BDSs) and motion surrogates are performed. This allows to calculate the ideal 4D dose distribution not influenced by motion effects. In case of a poor target coverage for PRSC simulations, problems of the DIR are likely and a careful consideration of the DIR is necessary prior to the conduction of full 4D simulations.

In addition, new and faster delivery methods were developed and implemented in the beam delivery sequence simulation (DSim) software. The treatment time was a critical quantity during the feasibility study as the beam time was limited and, hence, fast application of each plan was necessary. The same problem occurs during clinical routine in particle therapy. In the clinics the treatment time of each individual patient should be as short as possible, not only to increase the number of patients treated per day, but also to increase the patients' comfort. Furthermore, baseline drifts and other irregular motion effects are known to increase with treatment time, deteriorating the treatment outcome [Wöl14]. Hence, a scan path optimization was developed to reduce the treatment time. The scan path optimization as well as the dynamic intensity control (DIC), developed at Heidelberg Ion-Beam Therapy Center (HIT), was implemented in the DSim software to enable reliable 4D simulations using TRiP4D [Ric13].

The scan path optimization allows a reduction of the treatment time, comparable to the inhomogeneous rescanning scheme used during the feasibility study, while target coverage and dose homogeneity are not altered on a clinically relevant level. The DSim software was also validated in experiments at HIT and can be the base for future developments for the irradiation of moving targets. The DSim validation showed a good agreement between measured and simulated irradiation times of each raster point. Only the timing of the spill pauses needs some further investigation to allow correct prediction of the BDS.

5.1 Possible Improvements for Future Studies

The feasibility study was successful and new approaches were developed to further reduce the treatment time in following in-vivo studies. Even though the reported study could induce tissue modifications in the targeted areas, the heterogeneous results suggest the need for further experiments in animal models. Image acquisition, DIR and treatment planning should be appropriately adapted considering the knowledge gained from the reported study. Furthermore, the schedule of a following study should be adapted. The time span between each irradiation should be prolonged to allow an iterative approach increasing the knowledge from pig to pig. The first in-vivo study was carried out with several boundary conditions. The available beam time was limited, the positioning equipment not state-of-the-art and the infrastructure too complex and labor intensive. Additionally, an iterative approach would allow to shorten the time between recording of the treatment planning computed tomography (CT) and the irradiation. This reduces the possibility of anatomical changes in the still growing animals. Hence, several improvements are possible and necessary for future in-vivo studies as well as for a fast transition of catheter-free ablations into clinical routine.

Image Guidance

The first and most important aim for a following study must be an enhanced image guidance, throughout the whole workflow from recording of the treatment planning CTs to real-time imaging during the irradiation. For an improved outcome new protocols for the 4DCTs recording are necessary, as they are the base for a correct DIR. The timing of the contrast agent, the 4D reconstruction and the suppression of metal artifacts must be improved. Furthermore, a reliable DIR for cardiac-gated 4DCTs needs to be developed. A correct DIR is essential to carry out 4D dose calculations and 4D treatment planning using vector fields connecting the single motion phases. However, a reliable DIR can be only determined on the basis of high quality 4DCTs. While for abdominal and lung cancer treatments B-Spline algorithms provided by Plastimatch [Sha10a] are sufficient, more advanced strategies are necessary to model the complex motion of the heart, especially the thickening of the left ventricular free-wall during the ventricular systole. To gain a correct description of the heart motion incorporating a biomechanical model is necessary. Several heart models are known, however, most of them display only a certain area of the heart due to the complex interaction of atria and ventricles. The first model considering all chambers and the pericardium was published in [Fri14b]. The model is also able to consider patient specific data, such as voltage maps from electrophysiological mapping examinations, which would be necessary for individual radiotherapy treatment planning. In addition, it would be necessary to develop a DIR algorithm which can include the information of a biomechanical model.

Furthermore, it is not only necessary to understand and model the heart motion of the 4DCT recorded for treatment planning. A deeper understanding of anatomical changes between data sets recorded at different time points - such as the treatment planning CT, the actual treatment as well as possible changes during the treatment - would be important for a reliable 4D treatment planning and 4D simulations. The time between treatment planning and irradiation was several days for the feasibility study, which is also the case for cancer treatments, as a certain amount of time to plan and approve the treatment plans is necessary. However, it was found that within this time the heart volume can change causing range errors [Pra14b]. In addition, it was found that the heart frequency varied during the treatment. The heart frequency was increased between field 1 and field 2 due to a decreasing impact of the premedication. Furthermore, variations during each breath-hold were found. Hence, a study should be carried out investigating how a changing heart rate or a changed heart volume influence the heart motion. This could be investigated by magnetic resonance imaging (MRI) in healthy volunteers and patients. Alternatively, ultrasound imaging could be used, especially for patients with MR incompatible implantable cardioverter-defibrillators (ICDs). The found data could then be included in a patient-specific heart model.

The positioning is another crucial point, where image guidance plays an important role and needs to be improved for future studies, especially for an extremely range sensitive treatment, such as carbon ion therapy. For the presented feasibility study only orthogonal x-rays could be used due to the available infrastructure. The use of a CT on rails or a cone-beam CT (CBCT) would increase the positioning accuracy significantly [Ben15]. In addition, it would allow to recognize changes of the anatomy prior to the irradiation, especially the position of pacemaker electrodes and the heart volume. This information could be either used to re-plan and postpone the treatment or, in case of smaller changes, to gain a more meaningful feedback from 4D dose reconstruction. Volumetric imaging at the treatment location would enable dose calculations using the actual treated patient anatomy. Retrospective dose calculations would be possible, without any further work, using a CT on rails. The use of CBCTs would require more effort, but several different strategies are already published calculating particle dose distributions on CBCTs [Lan15, Par15].

Finally, the application of image guidance as real-time monitoring of the motion would be another important improvement. Ultrasound could be used as a possible motion control, since it is a powerful tool to visualize heart motion and was already used in cancer therapy to track intra-fractional changes

[Sch14, Pra14a]. However, the delays are still in the order of 200 ms and, hence, too large for a 4D beam delivery. Thus, for motion guidance, it would be necessary to have a prediction model forecasting the actual position of the target volume [Pra14a].

Treatment Planning and Delivery

Besides an improved image guidance also the treatment planning process as well as the beam delivery could be improved. One possible option would be the use of 4D optimization strategies as proposed in [Gra13, Gra14]. This approach determines individual treatment plans for each motion phase, allowing a more conformal dose distribution further reducing doses deposited in the organs at risk (OARs). However, 4D optimization, especially 4D rescanning [Gra14], requires an exact knowledge of the actual motion phase and a specialized treatment control system (TCS). Therefore, a real-time motion surrogate would be necessary for the delivery of a 4D optimized treatment plan, showing again the importance of improved image guidance. A further option to improve the treatment would be the use of a robust 4D optimization. Robust optimization was proposed in [Unk04] for photons and in [Unk07] first approaches for protons were published. Robust optimization allows to incorporate different scenarios in the optimization, such as range changes and positioning errors. The number of scenarios can be adapted to further uncertainties, which are, for example, extracted from the new DIR approach. Different types of robust optimization algorithms are known [Liu12, Cha06]. An algorithm using the worst case optimization approach proposed in [Pfl08, Liu12, Liu16] is under development for carbon ions [Wol16].

So far, all the stated improvements are concerning the treatment planning process and online imaging. However, also the beam delivery is susceptible to errors and several improvements are possible. To further reduce the treatment time and increase the target coverage, the developed scan path optimization could be used, as shown in Chapter 4. Especially the combination of the scan path optimization and DIC offers excellent possibilities to carry out the treatment in a reasonable time frame of below 15 minutes. The extended and validated DSim software is capable to carry out realistic 4D simulations. Possible future delivery techniques can easily be tested and simulated extending DSim. One possibility would be the combination of a 4D optimized treatment, such as 4D rescanning [Gra14] and the scan path optimization. For this task the determination of the optimal scan path has to be possible within milliseconds, connecting the different phases without scanner jumps and ordering the raster points according to the necessary intensities at the same time.

5.2 Clinical Transition

The goal of the described feasibility study is the transition of catheter-free ablation using carbon ions into clinical routine. While the feasibility of this approach was shown, further research is still needed to achieve this goal. Considering the results of the described animal study, the outcome is too heterogeneous to directly move from the reported in-vivo study to patient trials. Especially the irradiation of the LV, as the target offering the highest potential gain for the patients, still comes with several challenges and shows the most puzzling results of all three irradiated targets. Patients suffering from ventricular tachycardia (VT) cannot be cured with the available treatments nowadays, as the penetration depth of radio-frequency catheters is not high enough. Episodes of VT are interrupted by ICD shocks, but this significantly reduces quality of life. In severe cases, including the so-called electrical storm with more than 3 events per day, mortality is markedly increased in spite of the ICD. However, in none of the irradiated pigs out of the LV group a homogeneous transmural scar was observed, in contrast to the original aim. As the fibrotic tissue induced in the LV is patchy for carbon ion as well as photon irradiation [Leh16b, Leh16a], also experiments investigating the biological processes occurring after the irradiation of cardiomyocytes are needed. Several other functional changes were observed besides fibrosis, which led, for instance, to a full AV-block. These changes might also be sufficient to eliminate the causes of VT in inhomogeneous infarct scars. Further studies are needed to confirm this hypothesis, preferably in an animal model of myocardial infarction or otherwise induced VT [Tao16]. In the animals in this study, a homogeneous section of the LV was targeted. In actual patient cases, scars or other substrates would be the target offering a visible contrast in both MR and ultrasound imaging. Contouring and following this scar in all motion phases would be considerably easier, simplifying the task of both physician and the DIR algorithm. Nevertheless, this requires reliable 4D imaging prior to the treatment, combining CT, ultrasound and MRI data. These data also have to be fused using DIR, which poses new challenges, though these are often already solved in clinical routine. However, one limitation is that MRI is only possible for a subgroup of patients, as ICDs are a necessary step in the treatment of VT, but only a limited number of MR compatible ICDs are in the market [Med]. Even though the goal is to introduce radiotherapy as a non-invasive treatment for VT, due to the time needed to induce the scar tissue, the use of an ICD cannot be avoided in most cases.

Furthermore, the use of radiotherapy would be extremely useful for patients who cannot undergo surgery. For this patient group it would be advantageous to provide a non-invasive treatment without anesthesia. Hence, it would be necessary to actively account for heart and breathing motion at the same time. The approach used during the feasibility study relied on anesthesia as this was necessary in an animal study anyway. An alternative, a combination of respiratory as well as cardiac gating was already proposed in [Con14, Con16]. In photon radiotherapy, irradiation in deep-inspiration breath-hold is not uncommon [BH16], also combined with patient coaching and visual feedback to stabilize the inspiration endpoint. Even though this would reduce the stress of the patient, the technical complexity would be increased even further.

5.3 Conclusions

In conclusion, this work reported the first in-vivo study showing the feasibility of carbon ions to change electrical path ways in the mycoardium using pigs as an animal model. Catheter-free ablation using carbon ions could induce an AV-block, an almost full isolation of the SPV and significant slowing of the conduction. Furthermore, fibrosis as well as tissue modifications were created in the myocardium. However, retrospectively uncertainties within the DIR were found and the influence on 4D treatment planning and simulations was determined. The AVN and, according to the available data, also the SPV group treatment planning was correct, although uncertainties in DIR were present. In contrast to this, the treatment planning of the LV group likely could not achieve a transmural irradiation of the left ventricular free-wall during all motion phases. Hence, for the LV group DIR uncertainties might have caused a reduced target coverage.

A new inhomogeneous rescanning scheme was applied reducing the treatment time by more than 60 % while slightly reducing target coverage. As a clinically more acceptable and more robust alternative, a scan path optimization was developed to similarly reduce the treatment time, while keeping target coverage. This method can also be highly useful for single-fraction and hypofractionated cancer treatments. The scan path optimization, as well as a DIC developed at HIT, were implemented in a DSim software to carry out realistic 4D simulations. In addition, the DSim software was validated in experiments throughout this thesis.

4D treatment planning as well as 4D dose calculations are important for a successful treatment of moving targets. However, it was demonstrated throughout this work that 4D simulations rely heavily on DIR and are thus are highly sensitive to errors in the DIR. As DIR is prone to errors, especially for complex motion types such as the heartbeat, a careful investigation of each DIR on all motion phases is necessary prior to treatment planning and dose simulations steps.

A future repetition of the pig study is necessary to bring catheter-free ablations using carbon ions into clinical routine. For realistic 4D simulations and treatments, a reliable DIR is necessary and a new registration algorithm needs to be developed based on a biomechanical model of the heart motion, incorporating patient-specific information, such as ultrasound and MRI data.

From a physics point of view more in-vivo experiments are necessary to establish a reliable 4D treatment planning approach especially for the LV patients. Major steps forward were done by conducting the feasibility study presented in this work, developing the scan path optimization and extending and validating DSim. The specific challenges of cardiac DIR became apparent for the first time in this unique study setting. Even though they could not be solved completely during this work, their characterization will enable future researchers to contribute to a successful clinical transition.

Radiotherapy, especially using carbon ions, is a promising non-invasive alternative which has the potential to become a routinely used tool for the treatment of cardiac arrhythmia, opening new opportunities for patients who cannot be cured with radio-frequency catheter ablation. The remaining challenges, described in detail in this work, can be overcome within the next years to make catheter-free ablation of cardiac substructures using carbon ions as successful as carbon ion cancer therapy.

A Appendix Chapter 3

Table A.1.: Mean values and standard deviation is given in [%] for the 3D verification. Results are given for all pigs and fields as well as for the combination of both fields.

ID	both fields	90°	270°
1	0.30 ± 3.84	0.80 ± 3.91	1.90 ± 3.78
2	2.06 ± 4.30	2.43 ± 4.28	1.68 ± 4.32
3	2.38 ± 4.21	2.64 ± 4.20	2.13 ± 4.22
4	2.44 ± 4.36	1.82 ± 4.16	3.05 ± 4.55
5	0.54 ± 4.36	0.09 ± 3.94	0.99 ± 4.73
6	2.31 ± 4.62	2.02 ± 4.12	2.49 ± 4.93
7	1.36 ± 7.69	2.32 ± 4.98	-0.08 ± 12.40
8	2.86 ± 4.18	3.21 ± 4.04	2.16 ± 4.45
12	0.10 ± 3.27	-0.42 ± 2.80	0.62 ± 3.68
13	0.00 ± 2.95	-0.51 ± 2.49	0.52 ± 3.35
14	1.87 ± 2.97	1.87 ± 2.97	-
16	1.10 ± 3.05	0.54 ±3.30	1.95 ± 3.56

Table A.2.: Mean, max and min heart rate for all pigs during the irradiation for both fields.

ID	90° field			270° field		
	Mean BPM	Max BPM	Min BPM	Mean BPM	Max BPM	Min BPM
1	86.68	94.64	80.86	88.61	95.69	82.64
2	49.51	59.464	44.09	51.18	58.14	45.98
3	81.14	86.33	76.34	78.90	83.68	76.24
4	67.28	81.41	62.96	66.18	73.44	61.92
5	63.28	68.97	58.14	62.73	66.52	58.48
6	52.79	61.29	47.51	66.41	73.35	59.88
7	58.08	63.90	53.43	65.96	73.08	60.42
8	66.83	71.94	61.79	74.83	79.47	70.59
12	65.54	76.24	58.31	75.27	96.00	63.56
13	52.80	60.12	47.58	-	-	-
14	52.04	60.98	45.35	53.69	61.73	47.96
15	64.16	78.43	56.55	67.39	76.82	60.30
16	57.43	63.16	52.17	62.05	68.89	58.25
17	59.53	70.92	51.72	66.01	78.74	56.71

Table A.3.: Maximum motion amplitudes and corresponding motion phases of all pigs.

	ID	Max. Amplitude [mm]	Motion Phase
AVN	1	3.58	2
	2	4.54	2
	3	3.48	3
	4	4.33	2
	5	2.25	2
	6	4.74	3
	7	3.08	2
	8	4.05	3
SPV	12	3.15	3
	13	3.87	3
	14	1.82	1
LV	15	4.41	3
	16	1.83	3
	17	2.05	3

Figure A.1.: Results of the static simulations for TV (a)and PTV (b). For all three target volumes (AVN, LV, SPV) the values for V_{95}, D_{95} and D_5-D_{95} are given.

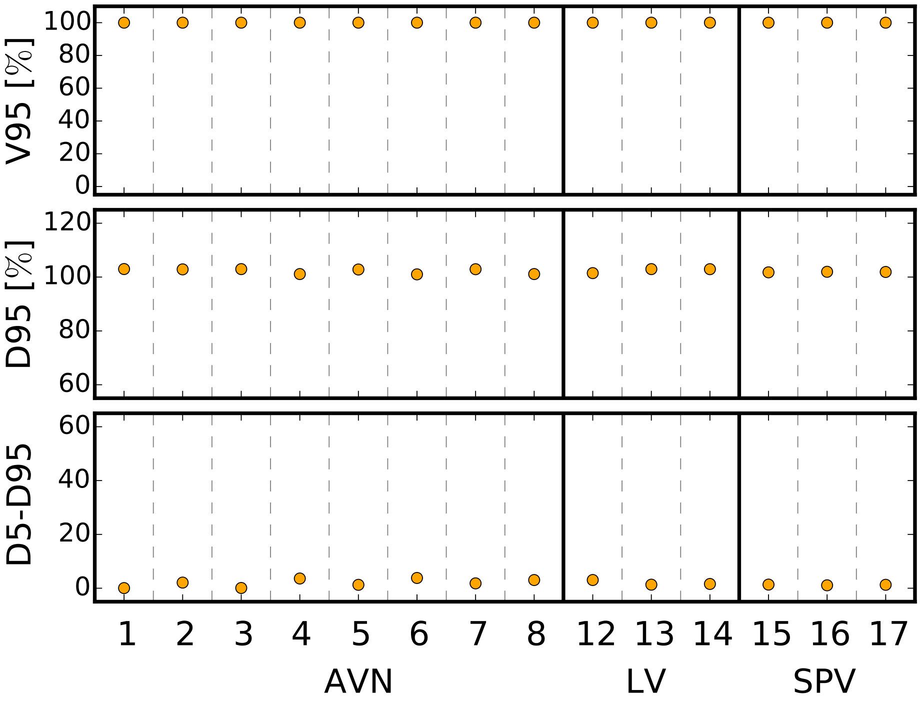

(a) Static simulation results for TV

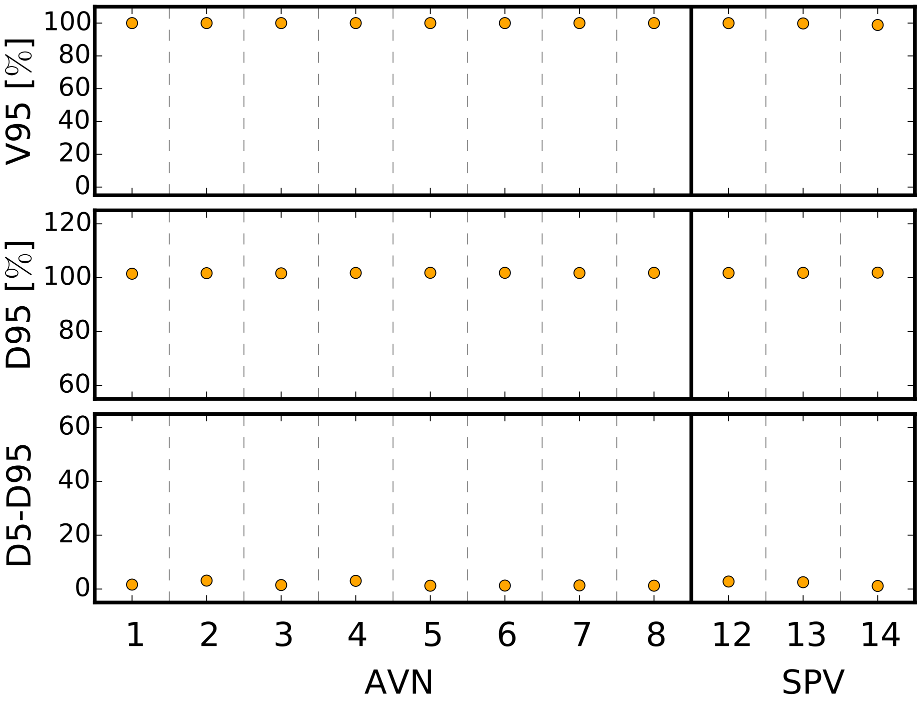

(b) Static simulation results for PTV

Table A.4.: Results of the static simulations for V_{95}, D_{95} and D_5-D_{95}.

		ID	V_{95} [%]	D_{95} [%]	D_5-D_{95} [%]
TV	AVN	1	103.0	100.0	0.1
		2	102.9	100.0	2.1
		3	103.0	100.0	0.1
		4	101.1	100.0	3.6
		5	102.8	100.0	1.3
		6	101.0	100.0	3.8
		7	102.9	100.0	1.8
		8	101.1	100.0	3.0
	SPV	12	101.5	100.0	3.1
		13	103.0	100.0	1.3
		14	102.9	100.0	1.6
	LV	15	101.8	100.0	1.3
		16	102.0	100.0	1.1
		17	101.9	100.0	1.3
PTV	AVN	1	101.5	100.0	1.7
		2	101.7	100.0	3.1
		3	101.6	100.0	1.5
		4	101.8	100.0	3.0
		5	101.8	100.0	1.2
		6	101.8	100.0	1.3
		7	101.7	100.0	1.3
		8	101.8	100.0	1.2
	SPV	12	101.7	100.0	2.8
		13	101.8	99.8	2.5
		14	101.9	98.8	1.1

Figure A.2.: Results of the interplay simulations for TV (a) and PTV (b). For all pigs the values for V_{95}, D_{95} and D_5-D_{95} are given. Each box includes 96 simulations per pig, including different motion patterns, regularity of the heartbeat and spill structures.

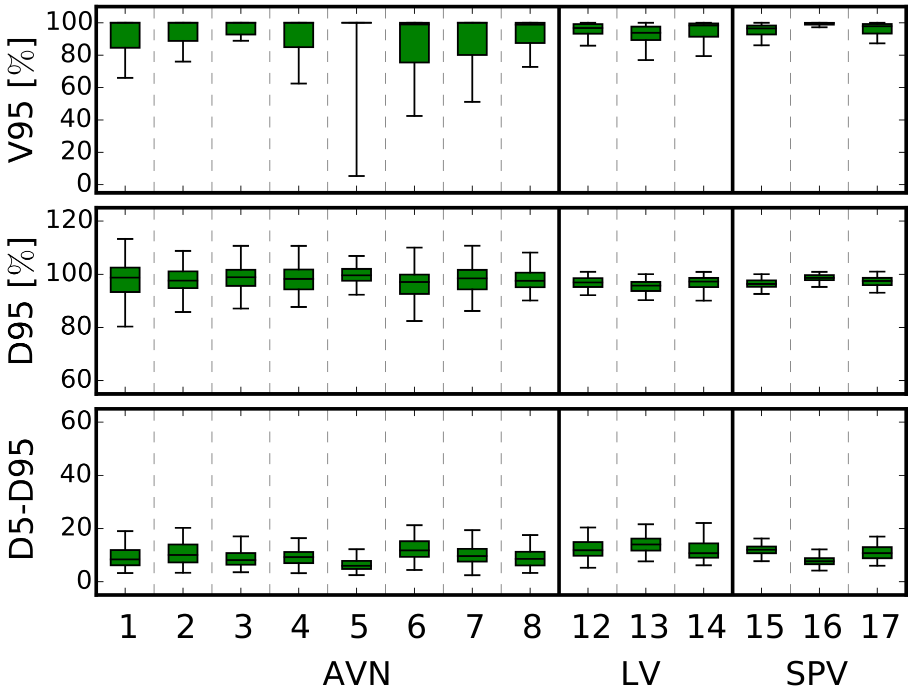

(a) Results of the interplay simulations of the TV

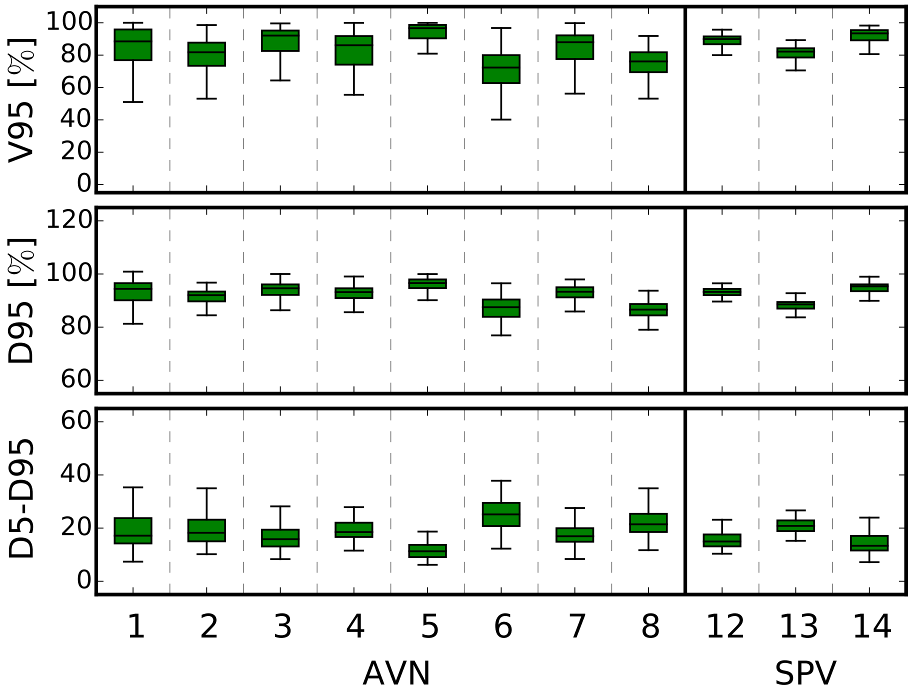

(b) Results of the interplay simulations of the PTV

Table A.5.: Results for the interplay simulations for V_{95}, D_{95} and D_5-D_{95}. For all pigs and volumes the median values for all 96 simulations are given and in brackets the 25th -75th percentiles are shown.

		ID	V_{95} [%]	D_{95} [%]	D_5-D_{95} [%]
TV	AVN	1	100.0 (84.6-100.0)	98.7 (93.2-102.5)	8.4 (6.2-11.9)
		2	100.0 (88.8-100.0)	97.6 (94.7-101.1)	10.1 (7.2-14.0)
		3	100.0 (92.8-100.0)	98.8 (95.6-101.7)	8.1 (6.4-10.8)
		4	100.0 (84.9-100.0)	98.2 (94.3-101.8)	9.3 (7.0-11.2)
		5	100.0 (100.0-100.0)	99.6 (97.6-102.0)	6.0 (4.8-7.8)
		6	99.0 (75.5-100.0)	97.0 (92.6-99.9)	11.7 (9.4-15.2)
		7	100.0 (80.1-100.0)	98.4 (94.3-101.6)	9.6 (7.5-12.4)
		8	98.9 (87.5-100.0)	97.6 (95.1-100.6)	8.6 (6.1-11.3)
	SPV	12	96.8 (93.3-99.2)	96.9 (95.2-98.5)	11.8 (9.8-14.9)
		13	93.8 (89.3-97.6)	95.7 (93.7-97.1)	14.0 (11.7-16.2)
		14	98.4 (91.4-99.6)	97.2 (95.1-98.6)	10.7 (9.0-14.4)
	LV	15	96.5 (92.8-98.3)	96.3 (95.3-97.7)	12.0 (10.7-13.2)
		16	99.8 (98.9-100.0)	98.7 (97.7-99.6)	7.7 (6.6-8.8)
		17	97.9 (93.4-99.2)	97.5 (95.8-98.6)	10.7 (8.8-13.0)
PTV	AVN	1	88.5 (76.9-95.9)	94.4 (90.1-96.6)	17.1 (14.2-23.8)
		2	81.8 (73.4-87.7)	92.0 (89.7-93.4)	18.2 (15.0-23.2)
		3	92.1 (82.6-95.2)	94.6 (92.1-96.1)	15.8 (13.1-19.4)
		4	86.1 (74.1-91.8)	93.2 (90.9-94.6)	18.5 (16.7-22.0)
		5	96.7 (90.4-98.7)	96.6 (94.7-98.0)	11.3 (9.1-13.7)
		6	72.3 (62.8-80.0)	87.5 (83.9-90.4)	25.2 (20.8-29.5)
		7	88.0 (77.6-92.2)	93.3 (91.2-95.0)	16.9 (14.9-20.0)
		8	76.1 (69.5-81.8)	86.6 (84.4-88.7)	21.4 (18.5-25.4)
	SPV	12	89.9 (86.7-91.6)	93.3 (92.1-94.4)	15.0 (13.1-17.6)
		13	82.2 (78.6-84.3)	88.6 (87.0-89.5)	20.8 (18.9-22.9)
		14	93.5 (89.2-95.5)	95.4 (93.5-96.1)	13.3 (11.6-17.1)

Figure A.3.: Results of the homogeneous rescanning simulations for TV (a) and PTV (b). For all pigs the values for V_{95}, D_{95} and D_5-D_{95} are given. Each box includes 96 simulations per pig, including different motion patterns, regularity of the heartbeat and spill structures.

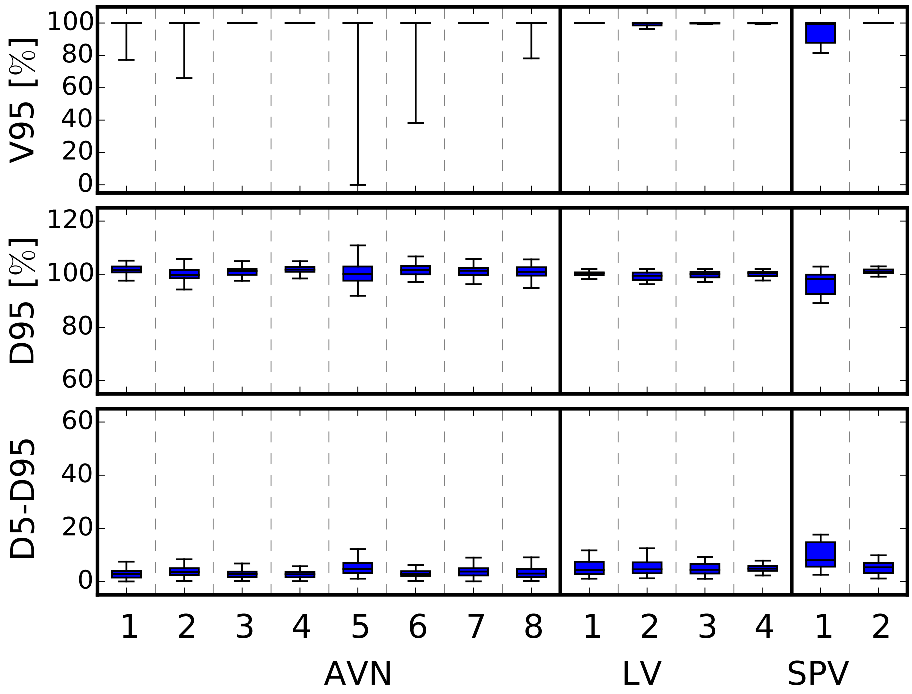

(a) Results of the homogeneous rescanning simulations of the TV

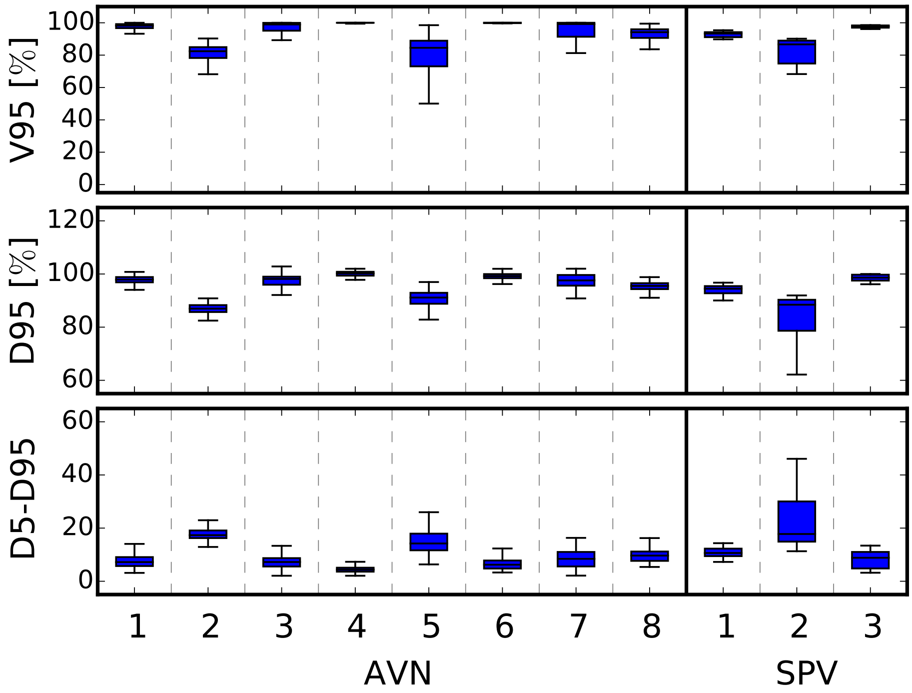

(b) Results of the homogeneous rescanning simulations of the PTV

Table A.6.: Results for the homogeneous rescanning simulations for V_{95}, D_{95} and D_5-D_{95}. For all pigs and volumes the median values for all 96 simulations are given and in brackets the 25th -75th percentiles are shown.

		ID	V_{95}[%]	D_{95}[%]	D_5-D_{95}[%]
TV	AVN	1	100.0 (100.0-100.0)	101.6 (100.0-103.1)	2.8 (2.1-3.9)
		2	100.0 (100.0-100.0)	100.9 (99.5-102.6)	3.0 (1.6-4.7)
		3	100.0 (100.0-100.0)	101.3 (99.7-102.4)	3.8 (2.3-5.0)
		4	100.0 (100.0-100.0)	101.2 (99.8-102.0)	2.8 (1.6-3.7)
		5	100.0 (100.0-100.0)	101.7 (100.9-102.7)	2.7 (1.6-3.6)
		6	100.0 (100.0-100.0)	100.1 (97.6-102.9)	4.7 (3.2-6.9)
		7	100.0 (100.0-100.0)	101.6 (100.7-102.9)	2.8 (1.5-4.0)
		8	100.0 (100.0-100.0)	99.7 (98.5-101.6)	3.5 (2.5-5.0)
	SPV	12	100.0 (99.8-100.0)	100.4 (99.4-100.9)	4.9 (4.0-5.8)
		13	99.2 (87.8-100.0)	98.2 (92.5-99.9)	8.0 (5.6-14.8)
		14	100.0 (100.0-100.0)	101.0 (100.4-101.8)	5.3 (3.2-6.9)
	LV	15	99.8 (98.5-100.0)	99.4 (97.9-100.6)	4.6 (3.1-7.2)
		16	100.0 (100.0-100.0)	100.3 (99.7-100.7)	4.3 (2.8-7.4)
		17	100.0 (99.7-100.0)	100.0 (98.8-100.9)	4.4 (3.0-6.5)
PTV	AVN	1	100.0 (99.8-100.0)	99.2 (98.4-100.0)	6.2 (4.8-7.8)
		2	94.2 (90.6-96.0)	95.5 (94.3-96.5)	9.7 (7.7-11.2)
		3	99.2 (91.4-100.0)	97.6 (95.6-99.6)	8.4 (5.6-11.0)
		4	99.0 (95.1-99.9)	98.1 (96.0-99.0)	7.2 (5.6-8.7)
		5	100.0 (100.0-100.0)	100.2 (99.4-100.8)	4.4 (3.6-5.1)
		6	84.5 (73.1-88.9)	91.1 (88.8-92.9)	14.2 (11.6-17.9)
		7	98.2 (96.7-99.2)	97.9 (96.9-98.8)	7.2 (5.7-9.1)
		8	82.4 (78.3-84.9)	87.0 (85.7-88.3)	17.3 (16.2-19.1)
	SPV	12	93.3 (91.1-94.2)	94.5 (92.7-95.4)	10.6 (9.5-12.3)
		13	86.7 (74.8-89.0)	88.4 (78.6-90.3)	17.8 (14.9-30.0)
		14	97.8 (97.0-98.4)	98.6 (97.5-99.7)	8.8 (4.8-11.0)

Figure A.4.: Results of the inhomogeneous rescanning simulations for TV (a) and PTV (b). For all pigs the values for V_{95}, D_{95} and D_5-D_{95} are given. Each box includes 96 simulations per pig, including different motion patterns, regularity of the heartbeat and spill structures.

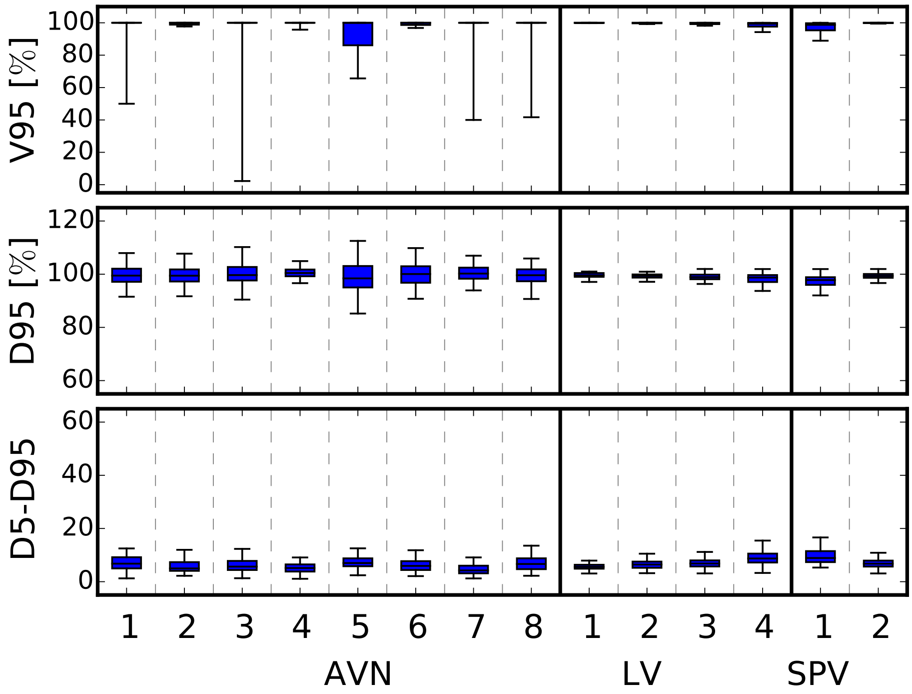

(a) Results of the inhomogeneous rescanning simulations of the TV

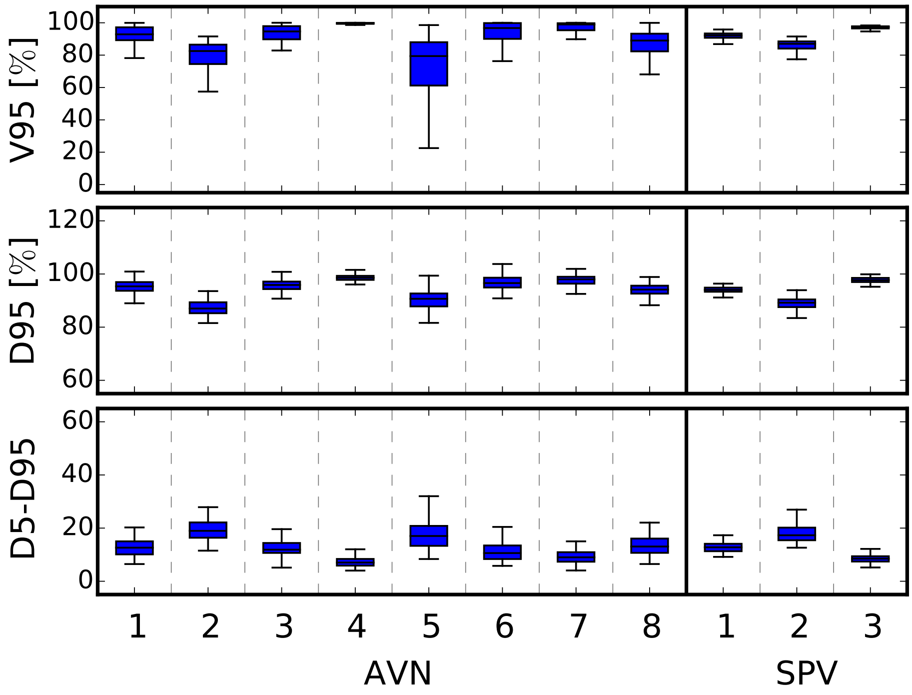

(b) Results of the inhomogeneous rescanning simulations of the PTV

Table A.7.: Results for the inhomogeneous rescanning simulations for V_{95}, D_{95} and D_5-D_{95}. For all pigs and volumes the median values for all 96 simulations are given and in brackets the 25th -75th percentiles are shown.

		ID	V_{95} [%]	D_{95} [%]	D_5-D_{95} [%]
TV	AVN	1	100.0 (98.7-100.0)	100.1 (96.8-103.0)	5.9 (4.4-7.7)
		2	100.0 (100.0-100.0)	99.6 (97.3-101.8)	6.7 (4.7-8.8)
		3	100.0 (100.0-100.0)	100.2 (98.3-102.5)	4.2 (3.2-6.0)
		4	100.0 (100.0-100.0)	99.7 (97.6-102.7)	5.7 (4.4-7.8)
		5	100.0 (100.0-100.0)	100.4 (99.2-101.8)	5.1 (3.8-6.5)
		6	100.0 (86.1-100.0)	98.4 (95.0-103.1)	7.0 (5.8-8.8)
		7	100.0 (100.0-100.0)	99.5 (97.1-102.1)	6.8 (5.0-9.2)
		8	100.0 (98.9-100.0)	99.4 (97.3-101.8)	5.0 (4.1-7.4)
	SPV	12	99.4 (97.6-99.9)	98.7 (97.1-99.7)	8.7 (7.2-10.6)
		13	98.7 (95.3-99.7)	97.8 (96.0-98.9)	8.9 (7.4-11.5)
		14	100.0 (99.8-100.0)	99.4 (98.7-100.1)	6.8 (5.7-7.9)
	LV	15	100.0 (99.7-100.0)	99.4 (98.7-99.9)	6.4 (5.2-7.5)
		16	100.0 (99.9-100.0)	99.6 (99.0-100.4)	5.6 (4.9-6.4)
		17	99.9 (99.2-100.0)	98.9 (98.1-99.8)	6.8 (5.7-8.0)
PTV	AVN	1	96.7 (90.1-99.8)	96.6 (94.9-98.6)	10.6 (8.4-13.5)
		2	89.0 (82.3-93.3)	94.1 (92.6-95.6)	13.1 (10.7-16.1)
		3	99.0 (95.4-99.7)	98.0 (96.4-99.0)	9.0 (7.4-10.9)
		4	94.7 (89.8-97.9)	95.9 (94.3-97.1)	11.9 (10.7-14.4)
		5	99.8 (99.3-99.9)	98.6 (97.8-99.3)	7.0 (5.9-8.4)
		6	79.4 (61.2-88.0)	90.7 (87.8-92.7)	17.0 (13.3-20.8)
		7	92.9 (89.2-97.2)	95.4 (93.7-97.0)	12.6 (10.1-15.0)
		8	82.5 (74.5-86.5)	87.0 (85.2-89.4)	19.0 (16.4-22.1)
	SPV	12	92.2 (90.7-93.4)	94.0 (93.3-94.9)	12.8 (11.3-14.1)
		13	87.0 (84.1-88.5)	89.2 (87.5-90.4)	17.3 (15.4-20.2)
		14	97.4 (96.5-97.8)	97.7 (97.0-98.5)	8.5 (7.4-9.4)

Table A.8.: Interplay results split by motion and spill structure type. Each row is based on 24 simulations. Median values are stated as well as in brackets the 25th -75th percentile range.

Target	Volume	Spill	Motion	D_{95} [%]	V_{95}[%]	D_5-D_{95} [%]
AVN	CTV	Gaussian	measured	97.07 (92.32 - 101.55)	98.94 (72.07 - 100.0)	10.75 (7.7 - 13.91)
		Gaussian	regular	98.53 (94.93 - 101.79)	100 (88.07 - 100.0)	8.31 (6.3 - 11.42)
		constant	measured	98.06 (95.96 - 101.26)	100 (95.33 - 100.0)	8.88 (6.41 - 11.57)
		constant	regular	98.52 (95.96 - 101.62)	100 (95.33 - 100.0)	8.21 (5.84 - 10.88)
	PTV	Gaussian	measured	90.74 (87.32 - 94.15)	80.02 (66.53 - 89.77)	20.84 (16.39 - 25.14)
		Gaussian	regular	92.74 (87.69 - 95.2)	86.26 (73.23 - 93.42)	18.05 (13.49 - 24.7)
		constant	measured	92.98 (89.62 - 95.53)	85.29 (76.9 - 93.31)	17.59 (13.97 - 21.36)
		constant	regular	93.29 (90.04 - 95.78)	86.39 (76.72 - 94.29)	16.51 (13.52 - 19.92)
SPV	CTV	Gaussian	measured	95.38 (94.18 - 96.64)	94.08 (89.73 - 96.61)	13.41 (11.29 - 16.28)
		Gaussian	regular	96.32 (94.92 - 98.33)	95.99 (91.23 - 99.33)	13.02 (10.23 - 16.13)
		constant	measured	96.79 (95.03 - 97.87)	96.77 (92.08 - 98.82)	12.02 (10.09 - 15.6)
		constant	regular	97.51 (95.57 - 98.78)	98.6 (94.18 - 99.63)	10.39 (8.36 - 13.15)
	PTV	Gaussian	measured	92.09 (87.88 - 94.52)	86.54 (81.27 - 91.63)	17.21 (14.48 - 21.26)
		Gaussian	regular	92 (90.06 - 93.99)	87.34 (83.02 - 91.26)	17.95 (14.04 - 19.88)
		constant	measured	92.83 (89.68 - 94.8)	89.15 (83.4 - 92.63)	15.31 (13.15 - 19.91)
		constant	regular	92.6 (89.37 - 95.54)	89.73 (84.33 - 94.1)	13.83 (11.68 - 19.89)
LV	CTV	Gaussian	measured	96.32 (95.41 - 97.97)	96.92 (92.91 - 98.71)	12.07 (10.26 - 13.18)
		Gaussian	regular	97.64 (95.74 - 98.79)	98.17 (94.5 - 99.63)	10.26 (8.63 - 11.9)
		constant	measured	97.79 (96.28 - 98.86)	99 (96.35 - 99.79)	9.57 (7.96 - 12.26)
		constant	regular	98.31 (96.89 - 99.54)	99.14 (97.59 - 99.88)	8.66 (7.3 - 11.22)

Table A.9.: Inhomogeneous rescanning results split by motion and spill structure type. Each row is based on 24 simulations. Median values are stated as well as in brackets the 25th -75th percentile range.

Target	Volume	Spill	Motion	D_{95} [%]	V_{95}[%]	D_5-D_{95} [%]
AVN	CTV	Gaussian	measured	99.71 (96.84 - 102.44)	100 (98.94 - 100.0)	6.14 (4.64 - 7.99)
		Gaussian	regular	99.84 (97.41 - 101.93)	100 (100.0 - 100.0)	5.83 (4.37 - 7.67)
		constant	measured	99.56 (97.41 - 101.77)	100 (100.0 - 100.0)	6.01 (4.32 - 8.15)
		constant	regular	100.46 (98.05 - 102.43)	100 (100.0 - 100.0)	5.05 (3.63 - 7.24)
	PTV	Gaussian	measured	95.07 (91.3 - 97.46)	91.87 (83.68 - 98.67)	12.33 (8.76 - 17.7)
		Gaussian	regular	95.21 (92.32 - 97.74)	92.69 (84.14 - 98.4)	12.44 (8.94 - 16.24)
		constant	measured	95.81 (91.73 - 97.78)	94.54 (82.84 - 98.97)	11.93 (9.17 - 16.72)
		constant	regular	95.58 (92.74 - 97.95)	93.72 (85.05 - 99.09)	11.74 (8.95 - 15.18)
SPV	CTV	Gaussian	measured	97.57 (95.47 - 98.99)	98.94 (94.27 - 100.0)	9.66 (7.66 - 12.53)
		Gaussian	regular	98.96 (97.67 - 99.88)	99.7 (98.82 - 100.0)	8.25 (6.7 - 9.42)
		constant	measured	98.83 (97.08 - 99.72)	99.67 (98.01 - 100.0)	7.6 (6.51 - 10.05)
		constant	regular	99.31 (98.0 - 99.91)	99.93 (99.08 - 100.0)	7.31 (6.28 - 8.66)
	PTV	Gaussian	measured	93.77 (86.85 - 96.35)	91.34 (83.1 - 96.3)	13.43 (9.1 - 20.5)
		Gaussian	regular	93.61 (90.54 - 97.27)	91.79 (87.87 - 97.01)	12.97 (8.58 - 15.85)
		constant	measured	93.94 (90.71 - 96.86)	91.71 (88.85 - 96.2)	12.94 (9.43 - 15.11)
		constant	regular	94.68 (90.65 - 96.94)	93.11 (89.14 - 96.45)	11.02 (9.63 - 15.41)
LV	CTV	Gaussian	measured	99.07 (98.17 - 99.75)	99.92 (99.32 - 100.0)	6.98 (5.99 - 8.02)
		Gaussian	regular	99.21 (98.5 - 99.81)	99.88 (99.68 - 100.0)	6.52 (5.65 - 7.25)
		constant	measured	99.23 (98.48 - 100.14)	100 (99.87 - 100.0)	5.62 (4.78 - 7.13)
		constant	regular	99.59 (99.22 - 100.53)	100 (99.95 - 100.0)	5.54 (4.79 - 6.44)

Table A.10.: Simulated irradiation times for homogeneous and inhomogeneous rescanning neglecting necessary time for breath holds. The results show the values for each field as well as the total time for the combination of both fields.

Target	ID	homogeneous rescanning			inhomogeneous rescanning		
		90° [min]	270° [min]	total [min]	90° [min]	270° [min]	total [min]
AVN	1	6.98	6.06	13.04	2.40	2.31	4.72
	2	10.71	9.15	19.86	3.14	3.15	3.28
	3	10.57	11.60	22.17	3.52	3.87	7.39
	4	8.07	10.30	18.37	2.75	2.57	5.32
	5	5.82	5.02	10.84	2.37	1.72	4.09
	6	5.84	6.97	12.81	1.86	2.02	3.89
	7	5.23	5.94	11.16	2.23	2.41	4.64
	8	9.35	9.34	18.69	3.12	3.26	6.39
SPV	12	30.11	36.43	66.54	8.21	8.83	17.04
	13	23.26	31.05	54.31	7.06	9.30	16.36
	14	20.92	20.93	41.85	7.27	6.01	13.27
LV	15	18.23	7.09	25.32	5.78	2.29	8.04
	16	12.77	10.29	23.06	4.59	3.54	8.13
	17	18.28	7.09	25.32	5.98	2.83	8.80

Table A.11.: Total irradiation times during the experiment including the time needed for the repeated breathholds.

Target	ID	90° total [min]	270° total [min]
AVN	1	4.82	4.01
	2	5.63	5.10
	3	5.71	7.18
	4	6.78	-
	5	4.50	3.39
	6	3.32	3.32
	7	5.55	12.06
	8	6.08	7.76
SPV	12	16.28	17.15
	13	13.51	38.47*
	14	13.22	9.97
LV	15	12.91	4.99
	16	10.42	7.35
	17	15.98	20.16

Table A.12.: Doses deposited in the OARs for the static simulations of the AVN patient cohort. Corresponding dose volume limits are given in Table 2.2.

OAR		Pig 1	Pig 2	Pig 3	Pig 4	Pig 5	Pig 6	Pig 7	Pig 8
Aorta	Dmean [Gy]	3.69	1.82	2.36	2.56	2.04	1.88	1.15	2.55
	Dmax [Gy]	56.82	56.48	56.43	41.76	41.20	41.64	25.67	25.97
	DoseVolume [Gy]	10.94	8.55	10.48	7.27	11.49	11.28	10.35	16.42
Skin	Dmean [Gy]	0.17	0.28	0.22	0.16	0.12	0.16	0.10	0.15
	Dmax [Gy]	17.44	17.49	17.55	13.88	11.88	12.36	7.45	9.88
	DoseVolume [Gy]	3.40	3.36	3.30	3.53	3.11	3.41	3.21	3.69
Myo	Dmean [Gy]	2.86	2.75	2.86	1.64	1.44	2.20	1.08	1.58
	Dmax [Gy]	56.87	57.25	56.87	41.52	41.68	41.60	25.85	26.00
	DoseVolume [Gy]	8.06	6.60	5.68	6.41	5.68	6.51	6.19	6.98
AscAorta	Dmean [Gy]	6.16	3.52	4.95	4.52	4.60	3.32	2.05	4.95
	Dmax [Gy]	56.82	56.48	56.43	41.76	41.20	41.64	25.67	25.97
Lungs	Dmean [Gy]	0.00	0.11	0.17	0.00	0.04	0.04	0.05	0.10
	Dmax [Gy]	18.81	20.13	20.24	16.36	13.40	14.00	8.18	22.18
PA	Dmean [Gy]	0.00	0.06	0.11	0.00	0.04	0.04	0.00	0.05
	Dmax [Gy]	0.22	6.05	8.80	1.72	3.04	3.52	0.65	4.85
LCA	Dmean [Gy]	6.05	10.95	9.79	5.84	4.00	8.04	3.40	5.00
	Dmax [Gy]	20.63	20.85	19.58	15.52	12.92	13.56	8.03	18.35
RCA	Dmean [Gy]	1.71	9.02	6.44	2.28	9.72	4.80	5.95	4.75
	Dmax [Gy]	19.31	19.80	24.70	15.84	13.88	14.44	8.40	11.13
Pericard	Dmean [Gy]	1.10	0.88	1.05	0.64	0.48	0.68	0.38	0.58
	Dmax [Gy]	20.29	20.68	20.68	16.16	13.76	14.44	8.45	23.00

Table A.13.: Doses deposited in the OARs for the static simulations of the SPV patient cohort. Corresponding dose volume limits are given in Table 2.2.

OAR		Pig 12	Pig 13	Pig 14
Skin	Dmean [Gy]	0.48	0.48	0.44
	Dmax [Gy]	21.16	20.40	20.40
	DoseVolume [Gy]	6.80	6.18	5.77
Myo	Dmean [Gy]	2.60	2.72	3.48
	Dmax [Gy]	42.60	42.16	41.80
	DoseVolume [Gy]	9.84	8.63	10.89
Trachea	Dmean [Gy]	0.80	1.36	4.32
	Dmax [Gy]	23.96	31.36	32.28
	DoseVolume [Gy]	1.07	1.25	2.26
Esophagus	Dmean [Gy]	0.00	0.00	0.04
	Dmax [Gy]	0.00	0.04	1.28
	DoseVolume [Gy]	0.00	0.00	0.00
Lungs	Dmean [Gy]	0.72	0.64	0.96
	Dmax [Gy]	23.20	23.80	28.00
LCA	Dmean [Gy]	3.88	4.44	4.08
	Dmax [Gy]	40.72	26.12	29.68
RCA	Dmean [Gy]	6.16	6.68	7.56
	Dmax [Gy]	19.60	20.36	19.00
AVN	Dmean [Gy]	9.72	5.84	1.00
	Dmax [Gy]	42.72	37.72	4.00
Pericard	Dmean [Gy]	3.04	2.48	3.56
	Dmax [Gy]	42.24	41.88	41.84
SVC	Dmean [Gy]	1.76	0.00	0.08
	Dmax [Gy]	14.24	0.00	1.40

Table A.14.: Doses deposited in the OARs for the static simulations of the LV patient cohort. Corresponding dose volume limits are given in Table 2.2.

OAR		Pig 15	Pig 16	Pig 17
Skin	Dmean [Gy]	0.24	0.24	0.28
	Dmax [Gy]	15.36	16.68	16.68
	DoseVolume [Gy]	3.99	3.83	4.12
Myo	Dmean [Gy]	3.80	2.88	3.92
	Dmax [Gy]	41.80	41.60	41.48
	DoseVolume [Gy]	10.04	9.56	10.26
Lungs	Dmean [Gy]	0.72	0.36	0.56
	Dmax [Gy]	41.76	41.12	41.80
PA	Dmean [Gy]	0.00	0.00	0.00
	Dmax [Gy]	0.00	0.00	0.00
LCA	Dmean [Gy]	0.40	2.12	2.52
	Dmax [Gy]	9.84	17.68	17.04
RCA	Dmean [Gy]	0.00	0.00	0.00
	Dmax [Gy]	0.00	0.00	0.00
Pericard	Dmean [Gy]	2.64	2.08	2.52
	Dmax [Gy]	41.36	41.36	41.76

Table A.15.: Doses deposited in the OARs for the inhomogeneous rescanning simulations of the AVN pig 1 - 4. Corresponding dose volume limits are given in Table 2.2.

OAR		Pig 1	Pig 2	Pig 3	Pig 4
Aorta	Dmean [Gy]	3.55 (3.52 - 3.58)	2.20 (2.15 - 2.20)	3.08 (3.07 - 3.08)	2.98 (2.96 - 3.01)
	Dmax [Gy]	59.54 (58.55 - 61.41)	57.20 (55.94 - 57.53)	57.70 (56.91 - 59.84)	43.66 (43.01 - 44.39)
	DoseVolume [Gy]	10.36 (10.30 - 10.54)	8.44 (8.37 - 8.50)	12.00 (11.96 - 12.06)	12.90 (12.86 - 13.01)
Skin	Dmean [Gy]	0.17 (0.17 - 0.17)	0.28 (0.28 - 0.28)	0.22 (0.22 - 0.22)	0.16 (0.16 - 0.16)
	Dmax [Gy]	17.38 (17.38 - 17.43)	17.43 (17.42 - 17.43)	17.49 (17.49 - 17.55)	13.84 (13.84 - 13.92)
	DoseVolume [Gy]	3.38 (3.38 - 3.38)	3.35 (3.35 - 3.35)	3.31 (3.30 - 3.31)	3.53 (3.53 - 3.53)
Myo	Dmean [Gy]	2.53 (2.52 - 2.53)	2.53 (2.53 - 2.53)	2.75 (2.75 - 2.75)	1.62 (1.60 - 1.64)
	Dmax [Gy]	60.09 (58.85 - 61.53)	60.03 (58.34 - 61.94)	59.43 (58.99 - 60.17)	43.96 (43.37 - 45.11)
	DoseVolume [Gy]	7.24 (7.22 - 7.28)	6.13 (6.11 - 6.15)	5.51 (5.49 - 5.53)	6.13 (6.12 - 6.20)
AscAorta	Dmean [Gy]	5.91 (5.87 - 5.95)	4.18 (4.13 - 4.18)	6.38 (6.33 - 6.39)	5.26 (5.20 - 5.29)
	Dmax [Gy]	59.54 (58.55 - 61.41)	57.20 (55.94 - 57.53)	57.70 (56.91 - 59.84)	43.66 (43.01 - 44.39)
Lungs	Dmean [Gy]	0.06 (0.06 - 0.06)	0.11 (0.11 - 0.11)	0.17 (0.17 - 0.17)	0.00 (0.00 - 0.00)
	Dmax [Gy]	20.07 (19.51 - 20.20)	20.27 (20.07 - 20.73)	20.32 (20.24 - 20.47)	16.66 (16.00 - 17.04)
PA	Dmean [Gy]	0.00 (0.00 - 0.00)	0.14 (0.11 - 0.17)	0.17 (0.17 - 0.17)	0.04 (0.04 - 0.04)
	Dmax [Gy]	0.47 (0.44 - 0.51)	8.06 (7.75 - 8.29)	11.99 (11.88 - 12.17)	3.32 (3.22 - 3.55)
LCA	Dmean [Gy]	5.25 (5.16 - 5.34)	11.14 (11.10 - 11.22)	9.49 (9.46 - 9.51)	5.92 (5.91 - 6.00)
	Dmax [Gy]	20.60 (20.38 - 21.00)	21.09 (20.80 - 21.31)	19.94 (19.70 - 20.10)	15.72 (15.31 - 15.91)
RCA	Dmean [Gy]	1.82 (1.82 - 1.87)	8.66 (8.62 - 8.70)	6.54 (6.49 - 6.56)	2.76 (2.72 - 2.80)
	Dmax [Gy]	19.72 (19.55 - 19.98)	19.61 (19.35 - 19.91)	24.28 (23.47 - 25.37)	16.12 (15.71 - 16.47)
Pericard	Dmean [Gy]	1.04 (1.04 - 1.04)	0.88 (0.88 - 0.88)	0.99 (0.99 - 0.99)	0.64 (0.64 - 0.64)
	Dmax [Gy]	20.60 (20.45 - 20.71)	20.71 (20.60 - 20.90)	20.63 (20.54 - 20.86)	16.42 (15.96 - 16.65)

Table A.16.: Doses deposited in the OARs for the inhomogeneous rescanning simulations of the AVN pig 5 - 8. Corresponding dose volume limits are given in Table 2.2.

OAR		Pig 5	Pig 6	Pig 7	Pig 8
Aorta	Dmean [Gy]	2.12 (2.12 - 2.13)	2.32 (2.31 - 2.40)	1.40 (1.38 - 1.40)	3.10 (3.08 - 3.10)
	Dmax [Gy]	41.90 (41.60 - 42.23)	44.46 (42.89 - 46.65)	27.29 (26.59 - 28.09)	27.13 (26.65 - 27.24)
	DoseVolume [Gy]	11.34 (11.29 - 11.47)	12.40 (12.15 - 12.73)	10.59 (10.49 - 10.65)	18.68 (11.67 - 18.94)
Skin	Dmean [Gy]	0.12 (0.12 - 0.12)	0.16 (0.16 - 0.16)	0.10 (0.10 - 0.10)	0.15 (0.15 - 0.15)
	Dmax [Gy]	11.92 (11.91 - 11.92)	12.46 (12.42 - 12.52)	7.49 (7.47 - 7.50)	9.53 (9.50 - 9.57)
	DoseVolume [Gy]	3.11 (3.11 - 3.11)	3.42 (3.42 - 3.42)	3.21 (3.21 - 3.21)	3.69 (3.69 - 3.70)
Myo	Dmean [Gy]	1.52 (1.52 - 1.52)	2.12 (2.12 - 2.12)	1.05 (1.03 - 1.05)	1.35 (1.34 - 1.35)
	Dmax [Gy]	42.72 (42.26 - 43.90)	44.94 (43.97 - 45.86)	27.83 (27.14 - 28.67)	27.45 (27.06 - 27.58)
	DoseVolume [Gy]	5.91 (5.89 - 5.92)	6.21 (6.17 - 6.25)	6.00 (5.97 - 6.03)	6.03 (6.00 - 6.11)
AscAorta	Dmean [Gy]	4.80 (4.79 - 4.84)	4.10 (4.04 - 4.21)	2.46 (2.43 - 2.48)	5.97 (5.95 - 6.00)
	Dmax [Gy]	41.90 (41.60 - 42.23)	44.46 (42.89 - 46.65)	27.29 (26.59 - 28.09)	27.13 (26.65 - 27.24)
Lungs	Dmean [Gy]	0.04 (0.04 - 0.04)	0.08 (0.08 - 0.08)	0.05 (0.05 - 0.05)	0.10 (0.10 - 0.10)
	Dmax [Gy]	13.44 (13.38 - 13.65)	14.62 (14.11 - 14.86)	8.40 (8.29 - 8.66)	12.30 (11.92 - 12.46)
PA	Dmean [Gy]	0.04 (0.04 - 0.04)	0.04 (0.04 - 0.04)	0.00 (0.00 - 0.00)	0.10 (0.10 - 0.10)
	Dmax [Gy]	3.54 (3.48 - 3.56)	5.46 (5.33 - 5.57)	1.71 (1.57 - 1.76)	8.55 (8.41 - 8.64)
LCA	Dmean [Gy]	4.00 (4.00 - 4.01)	8.88 (8.83 - 9.00)	3.65 (3.59 - 3.70)	5.26 (5.25 - 5.28)
	Dmax [Gy]	12.88 (12.84 - 12.96)	14.00 (13.87 - 14.22)	8.23 (8.03 - 8.26)	18.43 (18.21 - 18.56)
RCA	Dmean [Gy]	9.78 (9.75 - 9.81)	5.44 (5.30 - 5.50)	6.16 (6.10 - 6.18)	4.17 (4.15 - 4.23)
	Dmax [Gy]	13.98 (13.70 - 14.17)	15.20 (14.27 - 15.65)	8.49 (8.44 - 8.90)	11.03 (10.74 - 11.34)
Pericard	Dmean [Gy]	0.48 (0.48 - 0.48)	0.72 (0.72 - 0.72)	0.40 (0.40 - 0.40)	0.53 (0.53 - 0.53)
	Dmax [Gy]	13.82 (13.76 - 14.13)	15.00 (14.24 - 15.45)	8.72 (8.54 - 8.88)	12.10 (11.95 - 12.21)

Table A.17.: Doses deposited in the OARs for the inhomogeneous rescanning simulations of the SPV patient cohort. Corresponding dose volume limits are given in Table 2.2.

OAR		Pig 12	Pig 13	Pig 14
Skin	Dmean [Gy]	0.48 (0.48 - 0.48)	0.48 (0.48 - 0.48)	0.44 (0.44 - 0.44)
	Dmax [Gy]	21.12 (21.11 - 21.12)	20.40 (20.36 - 20.40)	20.44 (20.40 - 20.44)
	DoseVolume [Gy]	6.67 (6.67 - 6.67)	6.18 (6.18 - 6.18)	5.77 (5.77 - 5.77)
Myo	Dmean [Gy]	2.48 (2.48 - 2.48)	2.60 (2.59 - 2.60)	3.28 (3.28 - 3.28)
	Dmax [Gy]	44.56 (44.16 - 45.90)	44.18 (43.75 - 45.24)	43.70 (43.45 - 44.11)
	DoseVolume [Gy]	9.49 (9.48 - 9.50)	8.24 (8.20 - 8.25)	10.41 (10.39 - 10.41)
Trachea	Dmean [Gy]	0.76 (0.76 - 0.76)	1.38 (1.36 - 1.40)	4.54 (4.52 - 4.56)
	Dmax [Gy]	22.72 (22.38 - 23.48)	32.68 (32.32 - 33.09)	33.80 (33.26 - 34.33)
	DoseVolume [Gy]	1.00 (1.00 - 1.01)	1.26 (1.26 - 1.27)	2.37 (2.35 - 2.37)
Esophagus	Dmean [Gy]	0.00 (0.00 - 0.00)	0.00 (0.00 - 0.00)	0.04 (0.04 - 0.04)
	Dmax [Gy]	0.04 (0.04 - 0.04)	0.04 (0.04 - 0.04)	1.60 (1.56 - 1.64)
	DoseVolume [Gy]	0.00 (0.00 - 0.00)	0.00 (0.00 - 0.00)	0.00 (0.00 - 0.00)
Lungs	Dmean [Gy]	0.72 (0.72 - 0.72)	0.64 (0.64 - 0.64)	0.96 (0.96 - 0.96)
	Dmax [Gy]	23.04 (22.95 - 23.13)	23.54 (23.29 - 23.68)	27.02 (26.86 - 27.12)
LCA	Dmean [Gy]	2.80 (2.71 - 2.84)	3.48 (3.47 - 3.52)	3.64 (3.60 - 3.64)
	Dmax [Gy]	34.64 (32.93 - 35.46)	22.00 (21.81 - 22.12)	24.48 (23.98 - 24.85)
RCA	Dmean [Gy]	6.40 (6.36 - 6.40)	6.68 (6.63 - 6.72)	7.04 (7.03 - 7.13)
	Dmax [Gy]	19.78 (19.62 - 19.87)	20.14 (19.71 - 20.40)	18.56 (18.27 - 18.65)
AVN	Dmean [Gy]	7.72 (7.63 - 7.76)	5.04 (5.00 - 5.08)	0.52 (0.48 - 0.52)
	Dmax [Gy]	36.08 (35.02 - 36.82)	31.80 (30.28 - 32.23)	2.10 (2.05 - 2.16)
Pericard	Dmean [Gy]	2.96 (2.96 - 2.96)	2.44 (2.44 - 2.44)	3.44 (3.44 - 3.44)
	Dmax [Gy]	42.94 (42.52 - 43.47)	42.24 (41.75 - 42.84)	43.00 (42.60 - 43.68)
SVC	Dmean [Gy]	1.72 (1.72 - 1.72)	0.00 (0.00 - 0.00)	0.08 (0.08 - 0.08)
	Dmax [Gy]	13.68 (13.63 - 13.77)	0.08 (0.08 - 0.08)	1.30 (1.24 - 1.48)

Table A.18.: Doses deposited in the OARs for the inhomogeneous rescanning simulations of the LV patient cohort. Corresponding dose volume limits are given in Table 2.2.

OAR		Pig 15	Pig 16	Pig 17
Skin	Dmean [Gy]	0.24 (0.24 - 0.24)	0.24 (0.24 - 0.24)	0.28 (0.28 - 0.28)
	Dmax [Gy]	15.52 (15.48 - 15.52)	16.80 (16.76 - 16.80)	17.56 (17.44 - 17.68)
	DoseVolume [Gy]	4.00 (4.00 - 4.00)	3.82 (3.82 - 3.83)	4.13 (4.13 - 4.13)
Myo	Dmean [Gy]	4.12 (4.12 - 4.12)	3.04 (3.04 - 3.04)	4.22 (4.20 - 4.24)
	Dmax [Gy]	43.76 (43.32 - 44.59)	43.10 (42.87 - 43.74)	44.12 (43.22 - 45.36)
	DoseVolume [Gy]	10.42 (10.40 - 10.46)	9.78 (9.75 - 9.80)	10.65 (10.62 - 10.72)
Lungs	Dmean [Gy]	0.76 (0.76 - 0.76)	0.40 (0.36 - 0.40)	0.60 (0.60 - 0.60)
	Dmax [Gy]	42.54 (42.20 - 42.90)	41.72 (41.55 - 41.85)	42.58 (42.44 - 42.89)
PA	Dmean [Gy]	0.00 (0.00 - 0.00)	0.00 (0.00 - 0.00)	0.00 (0.00 - 0.00)
	Dmax [Gy]	0.00 (0.00 - 0.00)	0.00 (0.00 - 0.00)	0.00 (0.00 - 0.00)
LCA	Dmean [Gy]	0.44 (0.44 - 0.45)	2.28 (2.28 - 2.28)	2.64 (2.64 - 2.68)
	Dmax [Gy]	10.68 (10.63 - 10.81)	17.70 (17.68 - 17.77)	16.68 (16.50 - 16.84)
RCA	Dmean [Gy]	0.00 (0.00 - 0.00)	0.00 (0.00 - 0.00)	0.00 (0.00 - 0.00)
	Dmax [Gy]	0.00 (0.00 - 0.00)	0.00 (0.00 - 0.00)	0.00 (0.00 - 0.00)
Pericard	Dmean [Gy]	2.80 (2.80 - 2.80)	2.16 (2.16 - 2.16)	2.72 (2.72 - 2.72)
	Dmax[Gy]	42.58 (42.26 - 43.02)	42.08 (41.92 - 42.22)	42.98 (42.44 - 43.56)

Figure A.5.: Dose volume limits for the AVN irradiation. The corresponding dose threshold for each OAR is marked with a horizontal dashed gray line.

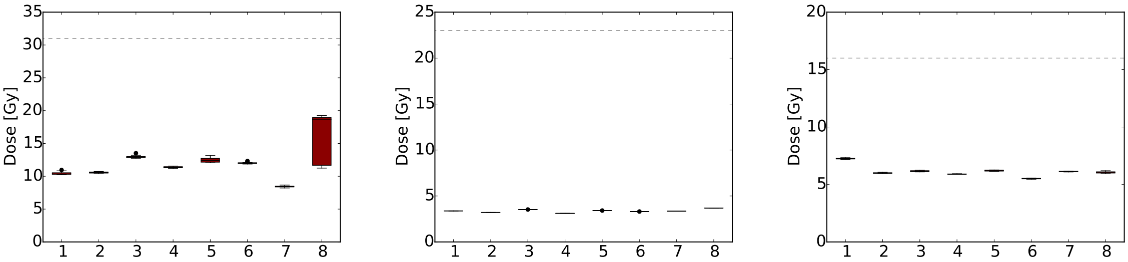

(a) Aorta (b) Skin (c) Myocardium

Figure A.6.: Dose volume limits for the LV irradiation. The corresponding dose threshold for each OAR is marked with a horizontal dashed gray line.

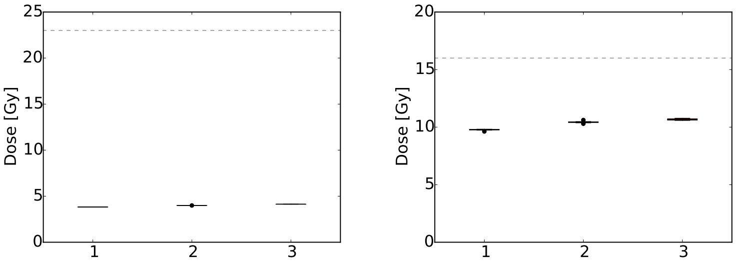

(a) Skin (b) Myocardium

Figure A.7.: Dose volume limits for the SPV irradiation. The corresponding dose threshold for each OAR is marked with a horizontal dashed gray line.

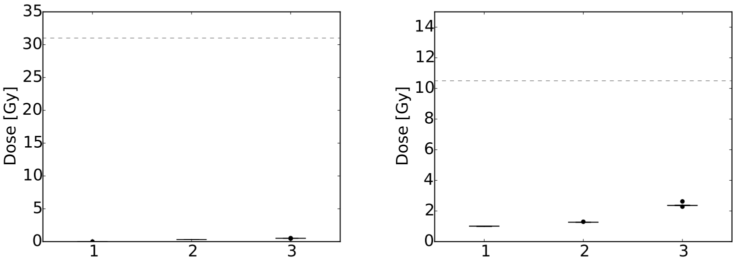

(a) Aorta (b) Trachea

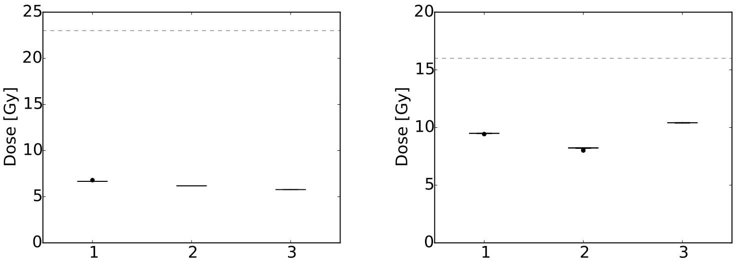

(c) Skin (d) Myocardium

B Appendix Chapter 5

Table B.1.: γ-Indices (2mm + 2%) for the 2D dose measurements carried out at HIT. Technical problems during the measurements not allowing the calculation of the γ-index are indicated by a dash.

	Pig 12	Pig 14	Liver A	Liver B	Liver C	Liver D	Liver E
DICI vs DICII - Original	1.00	-	0.98	0.92	0.99	0.99	0.99
DICI vs DICII - Rescanning	1.00	1.00	0.66	-	0.66	0.74	0.61
DICI vs DICII - Large Points	1.00	1.00	1.00	1.00	1.00	1.00	1.00
DICI vs DICII - Small Points	1.00	1.00	0.71	0.99	0.41	0.24	0.10
DICI vs DICII - Large + Small	1.00	1.00	1.00	1.00	1.00	1.00	1.00
DICI - Original vs Rescanning	1.00	1.00	0.68	-	0.67	0.63	0.63
DICII - Original vs Rescanning	1.00	-	1.00	0.94	1.00	0.97	1.00
DICII - NewPath vs Rescanning	1.00	1.00	0.34	1.00	1.00	1.00	1.00
DICII - Original vs NewPath	1.00	-	0.27	0.88	0.95	0.94	0.94
DICII - Rescanning vs Large+Small	0.99	1.00	0.60	-	0.73	0.69	0.70
DICII - Original vs Big+Small	1.00	-	1.00	0.94	1.00	1.00	1.00
DICII - NewPath vs Big+Small	1.00	1.00	0.31	0.98	0.98	0.98	0.97

Table B.2.: Deviations found in the 2D dose measurements between the constant intensity rescanning plan and other plans delivering the same dose with higher intensities.

	Pig 12	Pig 14	Liver A	Liver B	Liver C	Liver D	Liver E
DICI vs DICII - Rescanning	0.02 (0.01 – 0.15)	0.01 (0.00 – 0.09)	0.12 (0.09 – 0.15)	0.78 (0.77 – 0.94)	0.12 (0.08 – 0.17)	0.09 (0.07 – 0.15)	0.12 (0.10 – 0.18)
DICI vs DICII - Small	0.01 (0.00 – 0.03)	0.00 (0.00 – 0.02)	0.18 (0.11 – 0.26)	-0.06 (-0.18 – 0.0)	0.25 (0.17 – 0.35)	0.37 (0.28 – 0.51)	0.31 (0.24 – 0.43)
DICI - Original vs Rescanning	-0.03 (-0.11 – -0.02)	-0.03 (-0.10 – -0.01)	-0.17 (-0.23 – -0.12)	-3.51 (-4.14 – -3.31)	-0.17 (0.23 – -0.12	-0.16 (-0.25 – -0.12)	-0.16 (-0.23 – -0.12)
DICI - Rescanning vs Big+Small	0.02 (0.01 – 0.09)	0.01 (0.00 – 0.04)	0.13 (0.08 – 0.19)	0.78 (0.76 – 0.81)	0.10 (0.05 – 0.15)	0.10 (0.06 – 0.17)	0.11 (0.07 – 0.17)

Figure B.1.: For all three target groups the results for interplay and rescanning simulations showing the influence of SPO and DIC on the target coverage. Each box includes 48 simulations, median values are indicated by solid lines. The whisker represent 1.5 times the inner quartile range and outliers are marked with dots. The legend shown in part (a) is valid for all subfigures.

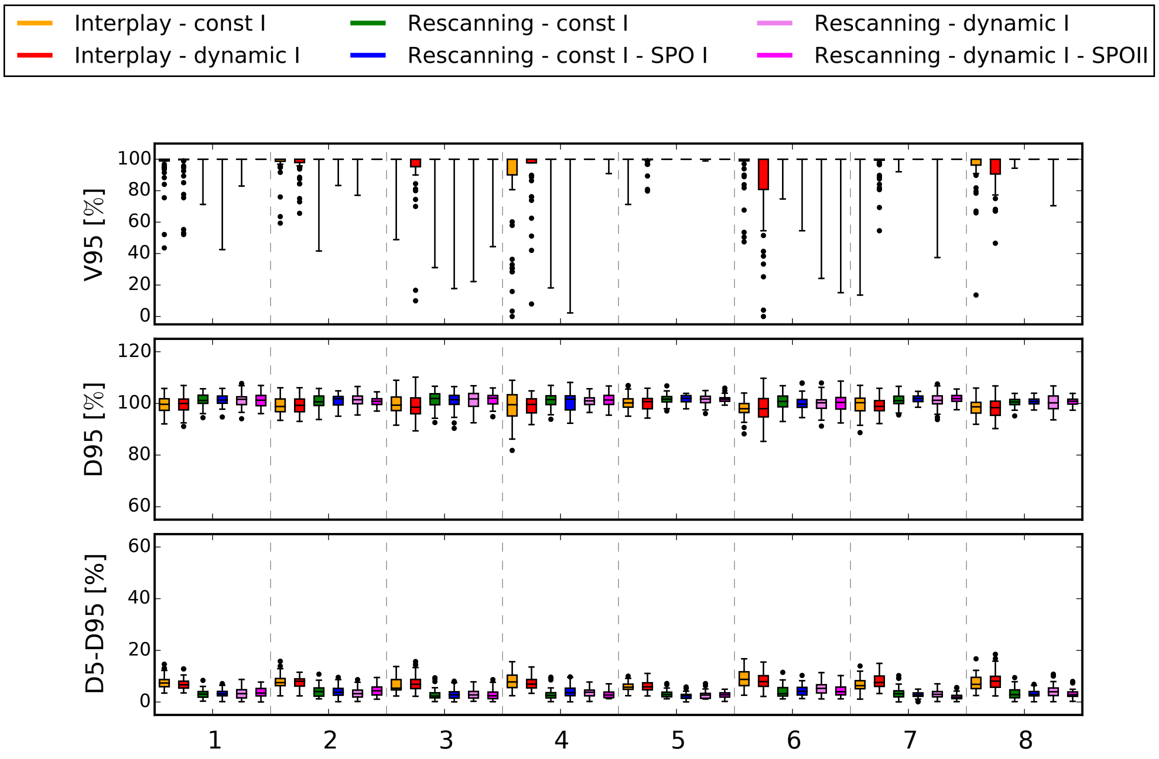

(a) AVN - CTV

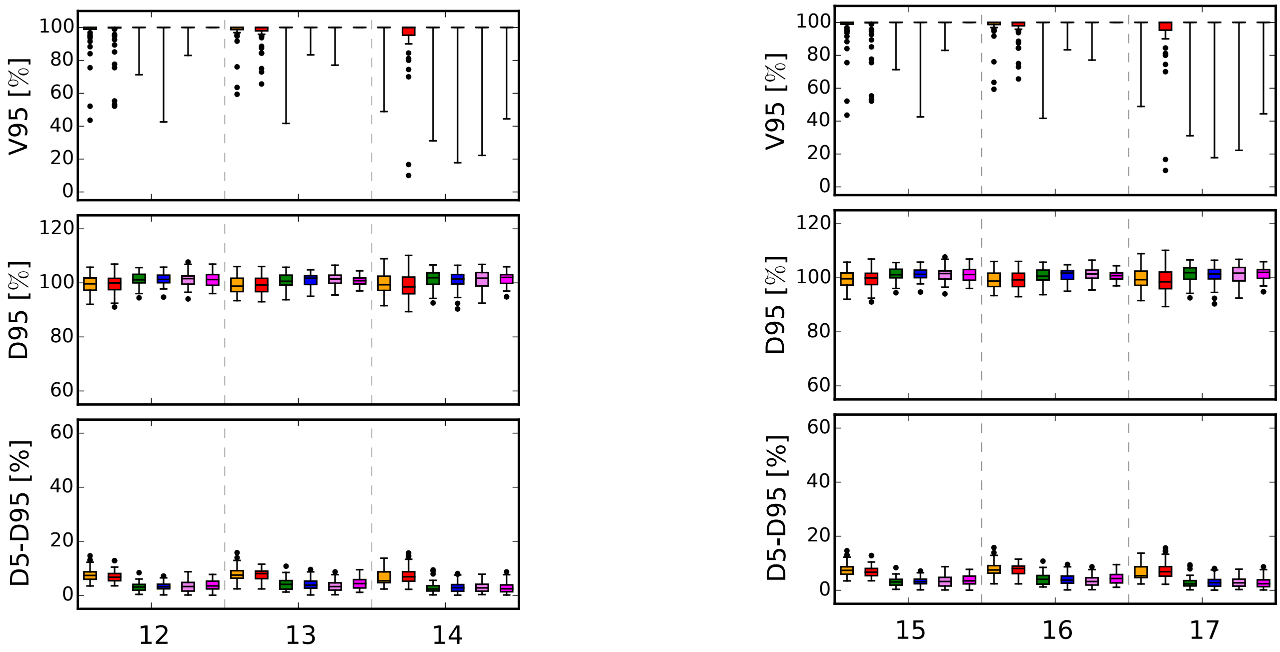

(b) SPV - CTV

(c) LV - CTV

Figure B.2.: Results for interplay and rescanning simulations of catheter-free ablations in humans showing the influence of SPO and DIC on the target coverage in five patients. Each box includes 8 simulations, median values are indicated by solid lines. The whisker represent 1.5 times the inner quartile range and outliers are marked with dots.. The legend shown in part (a) is valid for all subfigures.

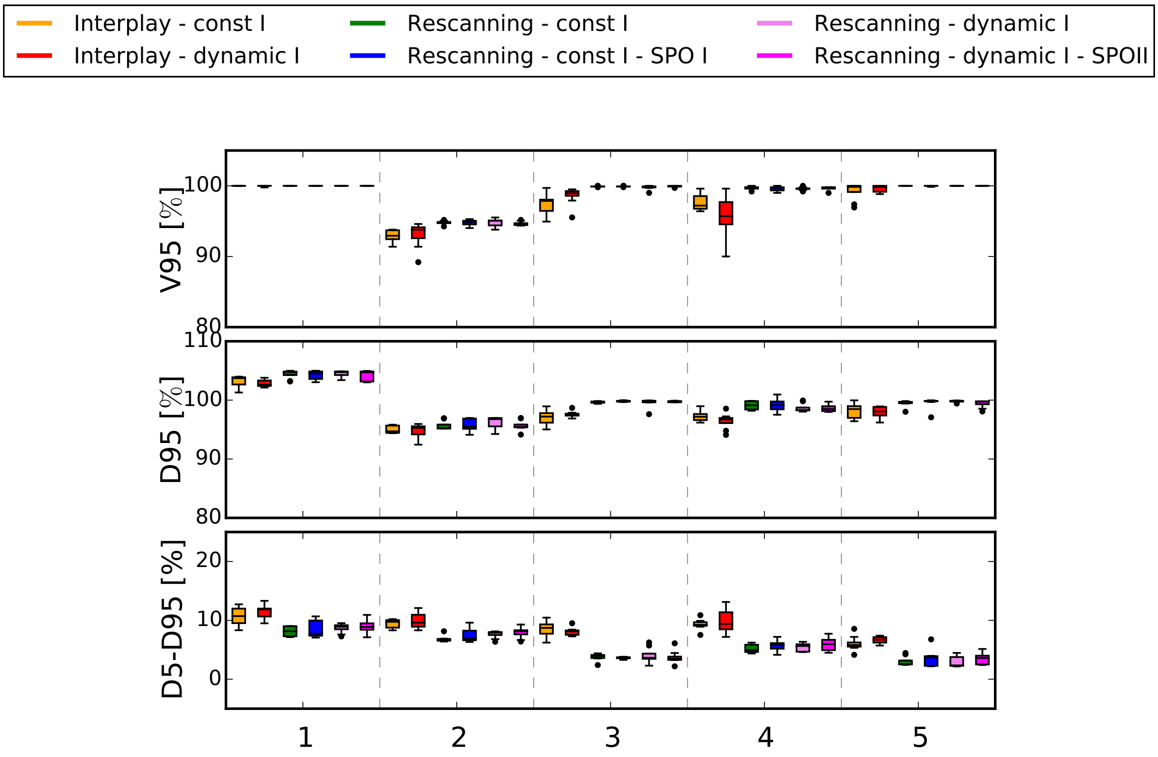

(a) Right Pulmonary Vein

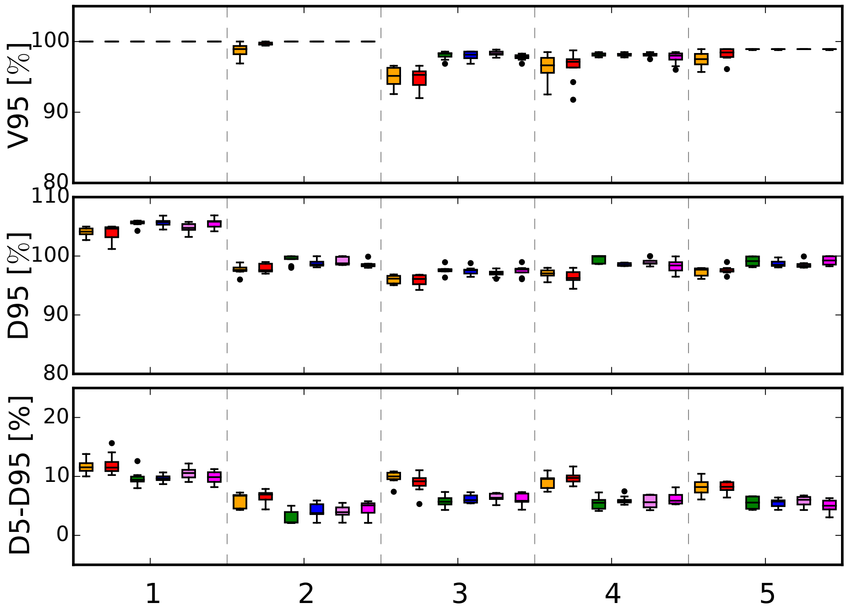

(b) Left Pulmonary Vein

Figure B.3.: Results for interplay and rescanning simulations of five lung cancer patients showing the influence of SPO and DIC on the target coverage. Each box includes 8 simulations, median values are indicated by solid lines. The whisker represent 1.5 times the inner quartile range and outliers are marked with dots.. The legend shown in part (a) is valid for all subfigures.

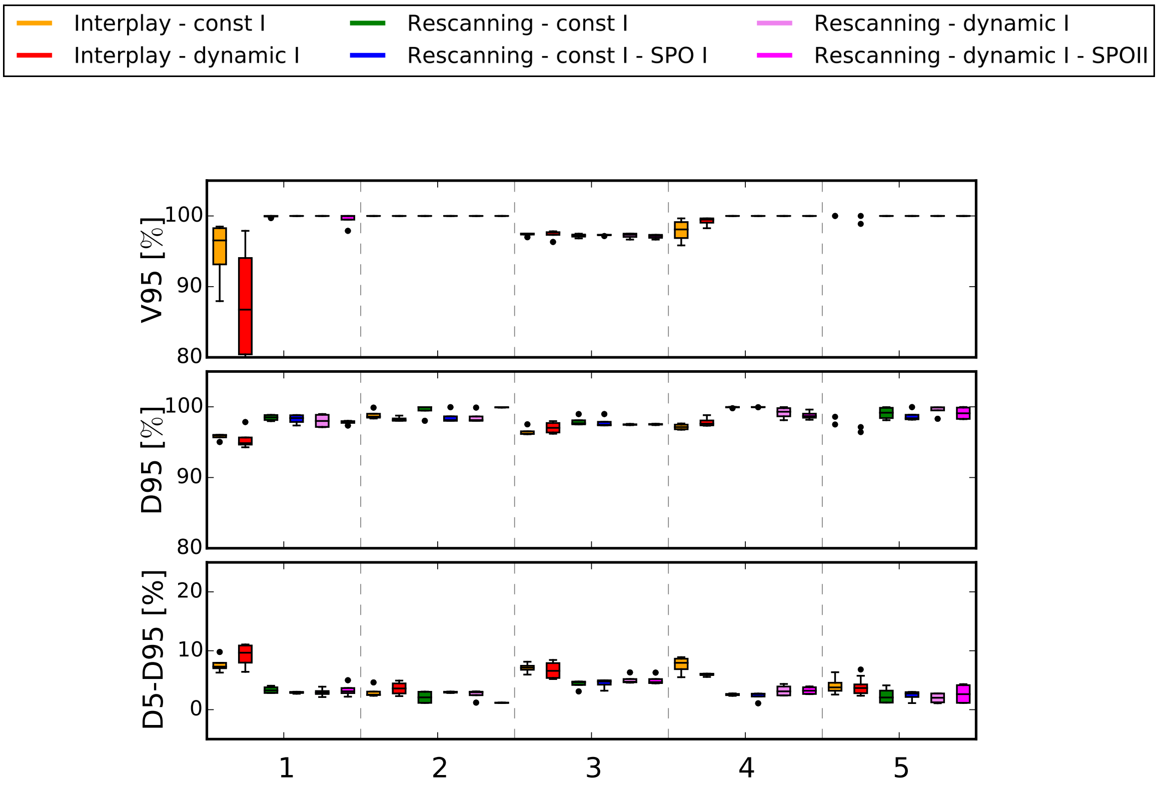

Table B.3.: Resulting p-values comparing the target coverage and dose homogeneity of the pig cohort between different speed-up methods

Target	Simulation Type	D_{95}	V_{95}	D_5-D_{95}
CTV	SPOI	0.898	0.504	0.000
	DIC	0.002	0.259	0.395
	DIC + SPO II	0.272	0.647	0.000
PTV	SPOI	0.000	0.066	0.000
	DIC	0.000	0.763	0.037
	DIC + SPO II	0.00	0.011	0.000

Table B.4.: Resulting p-values comparing the target coverage and dose homogeneity of the human cohort between different speed-up methods

Target	Simulation Type	D_{95}	V_{95}	D_5-D_{95}
LPV	SPOI	0.024	0.853	0.075
	DIC	0.002	0 548	0.017
	DIC + SPO II	0.034	0.122	0.105
RPV	SPOI	0.812	0.482	0.055
	DIC	0.552	0.265	0.046
	DIC + SPO II	0.364	0.229	0.007

Table B.5.: Resulting p-values comparing the target coverage and dose homogeneity of the lung caner patient cohort between different speed-up methods

Simulation Type	D_{95}	V_{95}	D_5-D_{95}
SPOI	0.003	0.172	0.679
DIC	0.012	0.271	0.218
DIC + SPO II	0.046	0.130	0.532

Bibliography

[Abd16] Abdoli M et al., ‘Assessment of metal artifact reduction methods in pelvic CT’, Medical Physics, **vol. 43(4)**, pp. 1588–1597, 2016

[Ama05] Amaldi U et al., ‘Recent applications of Synchrotrons in cancer therapy with Carbon Ions’, Europhysics News, **vol. 36(4)**, pp. 114–118, 2005

[And16a] Anderle K, ‘In silico comparison of photons versus carbon ions in single fraction therapy of lung cancer’, Ph.D. thesis, TU Darmstadt, 2016

[And16b] Anderle K et al., ‘In silico comparison of photons versus carbon ions in single fraction therapy of lung cancer.’, Physica Medica, **vol. 32(9)**, pp. 1118–1123, 2016

[Aza] Azaperon, http://www.pharmazie.com/graphic/A/97/8-14797.pdf, assessed 2016/11/14

[Bah13] Baher A et al., ‘Management of ventricular tachycardia in heart failure.’, Methodist DeBakey cardiovascular journal, **vol. 9(1)**, pp. 20–25, 2013

[Bar63] Barkas WH, ‘Nuclear Research Emulsions’, Vols I and II, Academic Press, New York, 1963

[Bau13] Bauer J et al., ‘An experimental approach to improve the Monte Carlo modelling of offline PET/CT-imaging of positron emitters induced by scanned proton beams.’, Physics in Medicine and Biology, **vol. 58(15)**, pp. 5193–5213, 2013

[Ben10] Benedict SH et al., ‘Stereotactic body radiation therapy: the report of AAPM Task Group 101’, Medical Physics, **vol. 37(8)**, pp. 4078–4101, 2010

[Ben15] Bentefour EH et al., ‘Using CBCT for pretreatment range check in proton therapy: A phantom study for prostate treatment by anterior-posterior beam’, Journal of Applied Clinical Medical Physics, **vol. 16(6)**, pp. 472–483, 2015

[Ber07a] Bert C et al., ‘4D treatment planning for scanned ion beams.’, Radiation Oncology, **vol. 2(24)**, 2007

[Ber07b] Bert C et al., ‘Target motion tracking with a scanned particle beam’, Medical Physics, **vol. 34(12)**, pp. 4768–4771, 2007

[Ber08a] Bert C et al., ‘Quantification of interplay effects of scanned particle beams and moving targets’, Physics in Medicine and Biology, **vol. 53(9)**, pp. 2253–2265, 2008

[Ber08b] Bert C et al., ‘Rescanning to mitigate the impact of motion in scanned particle therapy’, GSI Scientific Report, 2008

[Ber10] Bert C et al., 'Dosimetric precision of an ion beam tracking system.', Radiation Oncology, **vol. 5(61)**, 2010

[Ber11] Bert C et al., 'Motion in radiotherapy: particle therapy.', Physics in Medicine and Biology, **vol. 56(16)**, pp. 113–144, 2011

[Ber12] Bert C et al., 'Scanned carbon beam irradiation of moving films: comparison of measured and calculated response', Radiation Oncology, **vol. 7(1)**, pp. 1–13, 2012

[Bet30] Bethe H, 'Zur Theorie des Durchgangs schneller Korpuskularstrahlung durch Materie', Annalen der Physik, **vol. 5(5)**, pp. 325–400, 1930

[BH16] Boda-Heggemann J et al., 'Deep Inspiration Breath Hold—Based Radiation Therapy: A Clinical Review', International Journal of Radiation Oncology Biology Physics, **vol. 94(3)**, pp. 478–492, 2016

[Bla14] Blanck O et al., 'Dose-escalation study for cardiac radiosurgery in a porcine model', International Journal of Radiation Oncology Biology Physics, **vol. 89(3)**, pp. 590–598, 2014

[Bod15] Bode F et al., 'Pulmonary vein isolation by radiosurgery: Implications for non-invasive treatment of atrial fibrillation', Europace, **vol. 17(12)**, pp. 1868–1874, 2015

[Boe11] Boerma M et al., 'Preclinical Research into Basic Mechanisms of Radiation-Induced Heart Disease', Cardiology Research and Practice, **vol. 2011**, pp. 1–8, 2011

[Bor13] Borne RT et al., 'Implantable cardioverter-defibrillator shocks: epidemiology, outcomes, and therapeutic approaches.', JAMA Internal Medicine, **vol. 173(10)**, pp. 859–865, 2013

[Bra00] Brahme A, 'Development of Radiation Therapy Optimization', Acta Oncologica, **vol. 39(2)**, pp. 579–595, 2000

[Bre15] Brevet R, 'Optimized treatment parameters to account for interfractional variability in scanned ion beam therapy of lung cancer', Ph.D. thesis, TU Darmstadt, 2015

[Cam10] Camm A et al., 'Guidelines for the management of atrial fibrillation: the task force for the management of atrial fibrillation of the European Society of Cardiology', European Heart Journal, **vol. 31**, pp. 2369–2429, 2010

[Cap05] Cappato R et al., 'Worldwide survey on the methods, efficacy, and safety of catheter ablation for human atrial fibrillation', Circulation, **vol. 111(9)**, pp. 1100–1105, 2005

[Cap10] Cappato R et al., 'Updated worldwide survey on the methods, efficacy, and safety of catheter ablation for human atrial fibrillation', Circulation: Arrhythmia and Electrophysiology, **vol. 3(1)**, pp. 32–38, 2010

[Cha76] Chatterjee A et al., 'Microdosimetric structure of heavy ion tracks in tissue.', Radiation and Environmental Biophysics, **vol. 13(3)**, pp. 215–227, 1976

[Cha06] Chan TCY et al., ‘A robust approach to IMRT optimization.’, Physics in Medicine and Biology, **vol. 51(10)**, pp. 2567–2583, 2006

[Che04] Chen GTY et al., ‘Artifacts in Computed Tomography Scanning of Moving Objects’, Seminars in Radiation Oncology, **vol. 14(1)**, pp. 19–26, 2004

[Che08] Chen M et al., ‘A simple fixed-point approach to invert a deformation field.’, Medical Physics, **vol. 35(1)**, pp. 81–88, 2008

[Chu93] Chu WT et al., ‘Instrumentation for treatment of cancer using proton and light-ion beams’, Review of Scientific Instruments, **vol. 64(8)**, pp. 2055–2122, 1993

[Chu14] Chugh SS et al., ‘Worldwide Epidemiology of Atrial Fibrillation’, Circulation, **vol. 129(8)**, pp. 837 – 847, 2014

[Con09] Connell PP et al., ‘Advances in radiotherapy and implications for the next century: A historical perspective’, Cancer Research, **vol. 69(2)**, pp. 383–392, 2009

[Con14] Constantinescu A, ‘Planning studies for a non-invasive treatment of atrial fibrillation with scanned ion beams’, Ph.D. thesis, TU Darmstadt, 2014

[Con16] Constantinescu A et al., ‘Treatment Planning Studies in Patient Data with Scanned Carbon Ion Beams for Catheter-Free Ablation of Atrial Fibrillation’, Journal of Cardiovascular Electrophysiology, **vol. 27(3)**, pp. 335–344, 2016

[Coo09] Coolens C et al., ‘Implementation and characterization of a 320-slice volumetric CT scanner for simulation in radiation oncology’, Medical Physics, **vol. 36(11)**, pp. 5120–5127, 2009

[Cri98] Crick S et al., ‘Anatomy of the pig heart: comparisons with normal human cardiac structure’, Journal of Anatomy, **vol. 193(1)**, 1998

[Cro58] Croes GA, ‘A Method for Solving Traveling-Saleman Problems’, Operations Research, **vol. 6(6)**, pp. 791–812, 1958

[Cur50] Curie E, ‘Marie and Pierre Curie and the discovery of radium.’, The British Journal of Radiology, **vol. 23(271)**, pp. 409–412, 1950

[Cve14] Cvek J et al., ‘Cardiac Radiosurgery for Malignant Ventricular Tachycardia’, Cureus, **vol. 6(7)**, pp. 5–11, 2014

[Di 12] Di Biase L et al., ‘Endo-epicardial homogenization of the scar versus limited substrate ablation for the treatment of electrical storms in patients with ischemic cardiomyopathy’, Journal of the American College of Cardiology, **vol. 60(2)**, pp. 132–141, 2012

[Dia12] Dias M, ‘Scan path optimization for active beam delivery in charged particle therapy’, Ph.D. thesis, University of Lisbon, 2012

[Dia15] Dias MF et al., ‘Scan path optimization with/without clustering for active beam delivery in charged particle therapy’, Physica Medica, **vol. 31(2)**, pp. 130–136, 2015

[Din14] Dinov B et al., ‘Outcomes in catheter ablation of ventricular tachycardia in dilated nonischemic cardiomyopathy compared with ischemic cardiomyopathy: Results from the prospective heart centre of leipzig vt’, Circulation, **vol. 129(7)**, pp. 728–736, 2014

[Dol] Doll L, Personal Communication, 2016/11/02

[ECG] ECG, http://a-fib.com/treatments-for-atrial-fibrillation/diagnostic-tests/the-ekg-signal/, assessed 2016/11/04

[Eic15] Eichhorn A et al., ‘SU-C-303-06: Treatment Planning Study for Non-Invasive Cardiac Arrhythmia Ablation with Scanned Carbon Ions in An Animal Model’, Medical Physics, **vol. 42(6)**, p. 3198, 2015

[Els07] Elsässer T et al., ‘Cluster effects within the local effect model.’, Radiation Research, **vol. 167(3)**, pp. 319–329, 2007

[Erb15] Erbeldinger N et al., ‘Vascular and fibrotic changes in irradiated myocard after cardiac ablation with carbon ions in a pig model’, GSI Scientific Report, 2015

[Fan12] Fan D et al., ‘Cardiac fibroblasts, fibrosis and extracellular matrix remodeling in heart disease.’, Fibrogenesis & tissue repair, **vol. 5(1)**, p. 15, 2012

[Fed12] Fedorov A et al., ‘3D Slicer as an image computing platform for the Quantitative Imaging Network’, Magnetic Resonance Imaging, **vol. 30(9)**, pp. 1323–1341, 2012

[Fib] Fibrillation A, http://www.health.harvard.edu/heart-health/atrial-fibrillation-common-serious-treatable, assessed 2016/11/04

[Fla06] Flampouri S et al., ‘Estimation of the delivered patient dose in lung IMRT treatment based on deformable registration of 4D-CT data and Monte Carlo simulations.’, Physics in Medicine and Biology, **vol. 51(11)**, pp. 2763–2779, 2006

[Fok04] Fokdal L et al., ‘Impact of changes in bladder and rectal filling volume on organ motion and dose distribution of the bladder in radiotherapy for urinary bladder cancer’, International Journal of Radiation Oncology Biology Physics, **vol. 59(2)**, pp. 436–444, 2004

[Fou04] Fournier C et al., ‘Accumulation of the cell cycle regulators TP53 and CDKN1A (p21) in human fibroblasts after exposure to low- and high-LET radiation.’, Radiation Research, **vol. 161(6)**, pp. 675–684, 2004

[Fre11] Fredriksson A et al., ‘Minimax optimization for handling range and setup uncertainties in proton therapy’, Medical Physics, **vol. 38(3)**, pp. 1672–1684, 2011

[Fri12] Friedrich T et al., ‘Calculation of the biological effects of ion beams based on the microscopic spatial damage distribution pattern’, International Journal of Radiation Biology, **vol. 88(1)**, pp. 103–107, 2012

[Fri14a] Friedrich T et al., ‘RBE of ion beams in hypofractionated radiotherapy (SBRT)’, Physica Medica, **vol. 30(5)**, pp. 588–591, 2014

[Fri14b] Fritz T et al., ‘Simulation of the contraction of the ventricles in a human heart model including atria and pericardium.’, Biomechanics and modeling in mechanobiology, **vol. 13(3)**, pp. 627–641, 2014

[Fri16] Frischer JM et al., ‘Gamma Knife Radiosurgery in Recurrent Glioblastoma.’, Stereotactic and functional neurosurgery, **vol. 94(4)**, pp. 265–272, 2016

[Fur04] Furukawa T et al., ‘Global spill control in RF-knockout slow-extraction’, Nuclear Instruments and Methods in Physics Research, Section A: Accelerators, Spectrometers, Detectors and Associated Equipment, **vol. 522(3)**, pp. 196–204, 2004

[Fur05] Furukawa T et al., ‘Intensity control in RF-knockout extraction for scanning irradiation’, Nuclear Instruments and Methods in Physics Research, Section B: Beam Interactions with Materials and Atoms, **vol. 240(1)**, pp. 32–35, 2005

[Fur07] Furukawa T et al., ‘Design study of a raster scanning system for moving target irradiation in heavy-ion radiotherapy’, Medical Physics, **vol. 34(3)**, pp. 1085–1097, 2007

[Gra12] Graeff C et al., ‘Motion mitigation in intensity modulated particle therapy by internal target volumes covering range changes’, Medical Physics, **vol. 39(10)**, pp. 6004–6013, 2012

[Gra13] Graeff C et al., ‘A 4D-optimization concept for scanned ion beam therapy’, Radiotherapy and Oncology, **vol. 109(3)**, pp. 419–424, 2013

[Gra14] Graeff C et al., ‘Multigating, a 4D Optimized Beam Tracking in Scanned Ion Beam Therapy.’, Technology in cancer research and treatment, **vol. 13(6)**, pp. 497–504, 2014

[Gra15] Graeff C et al., ‘Catheter-free arrhythmia ablation using scanned carbon ion beams in a porcine model’, GSI Scientific Report, 2015

[Gri11] Grimm J et al., ‘Dose tolerance limits and dose volume histogram evaluation for stereotactic body radiotherapy.’, Journal of Applied Clinical Medical Physics, **vol. 12(2)**, p. 3368, 2011

[Grö06] Grözinger SO et al., ‘Simulations to design an online motion compensation system for scanned particle beams.’, Physics in Medicine and Biology, **vol. 51(14)**, pp. 3517–3531, 2006

[Gur11] Gurev V et al., ‘Models of cardiac electromechanics based on individual hearts imaging data’, Biomech Model Mechanobiol, **vol. 10(3)**, pp. 295–306, 2011

[Hab93] Haberer T et al., ‘Magnetic scanning system for heavy ion therapy’, Nuclear Instruments and Methods in Physics Research Section A: Accelerators, Spectrometers, Detectors and Associated Equipment, **vol. 330(1)**, pp. 296–305, 1993

[Hah16] Hahn K et al., ‘A comparison of linear interpolation models for iterative CT reconstruction’, Medical Physics, **vol. 43(12)**, pp. 6455–6473, 2016

[Hai16] Haissaguerre M et al., ‘Ventricular arrhythmias and the His–Purkinje system’, Nature Reviews Cardiology, **vol. 13(3)**, pp. 1–12, 2016

[Ham00] Hamm PCJ et al., 'Single dose irradiation response of pig skin: A comparison of brachytherapy using a single, high dose rate iridium-192 stepping source with 200 kV X-rays', British Journal of Radiology, **vol. 73(871)**, pp. 762–770, 2000

[Har68] Hart P et al., 'A Formal Basis for the Heuristic Determination of Minimum Cost Paths', IEEE Transactions on Systems Science and Cybernetics, **vol. 4(2)**, pp. 100–107, 1968

[Hea] Heart, https://www.interactive-biology.com/3619/heart-contractions-simplified/, assessed 2016/11/04

[Hel96] Hellman S, 'Radiation Oncology Centennial Series Discovering the Past, Inventing the Future', International Journal of Radiation Oncology Biology Physics, **vol. 35(1)**, pp. 15–20, 1996

[Hel14] Helmbrecht S et al., 'PT-PET imaging during arrhythmia ablation in porcine hearts using carbon ion beams', GSI Scientific Report, 2014

[ICR93] ICRU, 'Prescribing, recording and reporting photon beam therapy', ICRU report no 50, 1993

[ICR95] ICRU, 'Quantities and units in radiation protection dosimetry', ICRU report no 51, 1995

[ICR99] ICRU, 'Prescribing, recording, and reorting photon beam therapy', ICRU report no 62, 1999

[Ips14] Ipsen S et al., 'Radiotherapy beyond cancer: Target localization in real-time MRI and treatment planning for cardiac radiosurgery.', Medical Physics, **vol. 41(12)**, p. 120702, 2014

[Jäk07] Jäkel O et al., 'The influence of metal artefacts on the range of ion beams.', Physics in Medicine and Biology, **vol. 52(3)**, pp. 635–644, 2007

[Kad] Kaderka R et al., 'Quality asssurance for 4D dose delivery in radiotherapy: 4D dose verification with target trajectories extracted from 4DCT', In preparation

[Kad11] Kaderka R, 'Out-of-field measurements in radiotherapy', Ph.D. thesis, 2011

[Kad12] Kaderka R et al., 'Out-of-field dose measurements in a water phantom using different radiotherapy modalities.', Physics in Medicine and Biology, **vol. 57(16)**, pp. 5059–5074, 2012

[Kal16] Kalisz K et al., 'Artifacts at Cardiac CT: Physics and Solutions', RadioGraphics, **vol. 1**, p. 160079, 2016

[Kan07] Kang JH et al., 'Demonstration of scan path optimization in proton therapy', Medical Physics, **vol. 34(9)**, pp. 3457–3464, 2007

[Kar99] Karger CP et al., 'A system for three-dimensional dosimetric verification of treatment plans in intensity-modulated radiotherapy with heavy ions.', Medical Physics, **vol. 26(10)**, pp. 2125–2132, 1999

[Kat99] Katz R et al., 'Tracks to therapy', Radiation Measurements, **vol. 31(1)**, pp. 379–388, 1999

[Ker06] Kerckhoffs RCP et al., 'Computational methods for cardiac electromechanics', Proceedings of the IEEE, **vol. 94(4)**, pp. 769–782, 2006

[Kie86] Kiefer J et al., ‘A model of ion track structure based on classical collision dynamics’, Physics in Medicine and Biology, **vol. 31(11)**, pp. 1201–1209, 1986

[Kra00a] Kraft G, ‘Tumor therapy with heavy charged particles’, Progress in Particle and Nuclear Physics, **vol. 45(2000)**, pp. 473–544, 2000

[Krä00b] Krämer M et al., ‘Treatment planning for heavy-ion radiotherapy: calculation and optimization of biologically effective dose’, Physics in Medicine and Biology, **vol. 45(11)**, pp. 3319–3330, 2000

[Krä00c] Krämer M et al., ‘Treatment planning for heavy-ion radiotherapy: physical beam model and dose optimization.’, Physics in Medicine and Biology, **vol. 45(11)**, pp. 3299–3317, 2000

[Krä05] Krämer M et al., ‘Biological dose optimization using ramp-like dose gradients in ion irradiation fields.’, Physica Medica, **vol. 21(3)**, pp. 107–11, 2005

[Krä06] Krämer M et al., ‘Rapid calculation of biological effects in ion radiotherapy’, Physics in Medicine and Biology, **vol. 51(8)**, pp. 1959–1970, 2006

[Krä09] Krämer M, ‘Swift ions in radiotherapy - Treatment planning with TRiP98’, Nuclear Instruments and Methods in Physics Research, Section B: Beam Interactions with Materials and Atoms, **vol. 267(6)**, pp. 989–992, 2009

[Krä10] Krämer M et al., ‘Ion beam transport calculations and treatment plans in particle therapy’, European Physical Journal D, **vol. 60(1)**, pp. 195–202, 2010

[Kri13] Krishnamurthy A et al., ‘Patient-specific models of cardiac biomechanics’, Journal of Computational Physics, **vol. 244**, pp. 4–21, 2013

[Lan15] Landry G et al., ‘Investigating CT to CBCT image registration for head and neck proton therapy as a tool for daily dose recalculation.’, Medical Physics, **vol. 42(3)**, pp. 1354–1366, 2015

[Leh15] Lehmann HI et al., ‘AV Node Ablation in Langendorff-Perfused Porcine Hearts Using Carbon Ion Particle Therapy: Methods and an In vivo Feasibility Investigation for Catheter-Free Ablation of Cardiac Arrhythmias’, Circulation: Arrhythmia and Electrophysiology, **vol. 8(2)**, pp. 429–438, 2015

[Leh16a] Lehmann HI et al., ‘External arrhythmia ablation using photon beams: Ablation of the atrioventricular junction’, Circulation: Arrhythmia and Electrophysiology, accepted, 2016

[Leh16b] Lehmann HI et al., ‘Feasibility Study on Cardiac Arrhythmia Ablation Using High-Energy Heavy Ion Beams’, Nature Scientific Reports, **vol. 6**, p. 38895, 2016

[Leo07] Leow AD et al., ‘Statistical properties of Jacobian maps and the ralization of unbiased large-deformation nonlinear image registration’, IEEE Transactions on Medical Imaging, **vol. 26**, 2007

[Liu12] Liu F et al., ‘Evaluation of deformable image registration and a motion model in CT images with limited features.’, Physics in Medicine and Biology, **vol. 57(9)**, pp. 2539–2554, 2012

[Liu16] Liu W et al., 'Exploratory Study of 4D versus 3D Robust Optimization in Intensity Modulated Proton Therapy for Lung Cancer', International Journal of Radiation Oncology Biology Physics, **vol. 95(1)**, pp. 523–533, 2016

[Loo15] Loo BW et al., 'Stereotactic Ablative Radiotherapy for the Treatment of Refractory Cardiac Ventricular Arrhythmia', Circulation: Arrhythmia and Electrophysiology, **vol. 8(3)**, pp. 748–750, 2015

[Low98] Low DA et al., 'A technique for the quantitative evaluation of dose distributions.', Medical Physics, **vol. 25(5)**, pp. 656–661, 1998

[Low03] Low DA et al., 'Evaluation of the gamma dose distribution comparison method', Medical Physics, **vol. 30(9)**, pp. 2455–2464, 2003

[Lu06] Lu W et al., 'Automatic re-contouring in 4D radiotherapy.', Physics in Medicine and Biology, **vol. 51(5)**, pp. 1077–1099, 2006

[Mak15] Maksuti E et al., 'Modelling the heart with the atrioventricular plane as a piston unit', Medical Engineering and Physics, **vol. 37(1)**, pp. 87–92, 2015

[Med] Medtronic, https://www.medtronic.com/us-en/healthcare-professionals/mri-surescan/implantable-cardiac-devices/sure-scan-ICD-system.html, assessed 2016/11/29

[Mit15] Mittnacht AJC et al., 'Ventricular Tachycardia Ablation: A Comprehensive Review for Anesthesiologists', Anesthesia and Analgesia, **vol. 120(4)**, pp. 737–748, 2015

[Miz14] Mizushima K et al., 'Experimental studies of systematic multiple-energy operation at HIMAC synchrotron', Nuclear Instruments and Methods in Physics Research, Section B: Beam Interactions with Materials and Atoms, **vol. 331**, pp. 243–247, 2014

[Moh95] Mohan R, 'Field shaping for three-dimensional conformal radiation therapy and multileaf collimation', Seminars in Radiation Oncology, **vol. 5(2)**, pp. 86–99, 1995

[Mol48] Moliere G, 'Theorie der Streuung schneller geladener Teilchen II Mehrfach-und Vielfachstreuung', Zeitschrift fur Naturforschung - Section A Journal of Physical Sciences, **vol. 3(2)**, pp. 78–97, 1948

[Mor14] Mori S et al., 'Amplitude-based gated phase-controlled rescanning in carbon-ion scanning beam treatment planning under irregular breathing conditions using lung and liver 4DCTs', Journal of Radiation Research, **vol. 55(5)**, pp. 948–958, 2014

[Mun14] Munger TM et al., 'Atrial fibrillation', Journal of Biomedical Research, **vol. 28(1)**, pp. 1–17, 2014

[Pag05] Paganetti H et al., '4D Monte Carlo simulation of proton beam scanning: modelling of variations in time and space to study the interplay between scanning pattern and time-dependent patient geometry', Physics in Medicine and Biology, **vol. 50**, pp. 983–990, 2005

[Pan14] Panse R et al., ‘Abstract O36: Reduction of the Irradiation Time of Patient Treatment Plans Using Dynamic Intensity Control of the Ion Beam’, PTCOG 53, **vol. 1(2)**, pp. 449–450, 2014

[Par86] Paretzke HG, ‘Physical events of heavy ion interactions with matter’, Advances in Space Research, **vol. 6(11)**, pp. 67–73, 1986

[Par07] Parodi K et al., ‘Patient study of in vivo verification of beam delivery and range, using positron emission tomography and computed tomography imaging after proton therapy’, International Journal of Radiation Oncology Biology Physics, **vol. 68(3)**, pp. 920–934, 2007

[Par15] Park YK et al., ‘Proton dose calculation on scatter-corrected CBCT image: Feasibility study for adaptive proton therapy’, Medical Physics, **vol. 42(8)**, pp. 4449–4459, 2015

[Pat48] Paterson R, ‘The Treatment of Malignant Disease by Radium and X-rays’, London, Edward Arnold, 1948

[Ped95] Pedroni E et al., ‘The 200-MeV proton therapy project at the Paul Scherrer Institute: conceptual design and practical realization.’, Medical Physics, **vol. 22(1)**, pp. 37–53, 1995

[Ped01] Pedroni E et al., ‘A novel gantry for proton therapy at the Paul Scherrer Institute’, AIP Conf Proc, **vol. 600**, pp. 13–17, 2001

[Pfl08] Pflugfelder D et al., ‘Worst case optimization: a method to account for uncertainties in the optimization of intensity modulated proton therapy.’, Physics in Medicine and Biology, **vol. 53(6)**, pp. 1689–1700, 2008

[Pie14] Piersanti L et al., ‘Measurement of charged particle yields from PMMA irradiated by a 220 MeV/u C12 beam.’, Physics in Medicine and Biology, **vol. 59(7)**, pp. 1857–1872, 2014

[Pin12] Pinter C et al., ‘SlicerRT: radiation therapy research toolkit for 3D Slicer.’, Medical Physics, **vol. 39(10)**, pp. 6332–6338, 2012

[Pla] Plastimatch, http://plastimatch.org, assessed 2016/11/04

[Poo08] Poole JE et al., ‘Prognostic importance of defibrillator shocks in patients with heart failure.’, The New England Journal of Medicine, **vol. 359(10)**, pp. 1009–1017, 2008

[Pra] Prall M et al., ‘Immovilization for carbon-beam albation of cardiac structures in a pig model’, In preparation

[Pra14a] Prall M et al., ‘Ion beam tracking using ultrasound motion detection’, Medical Physics, **vol. 41(4)**, p. 041708, 2014

[Pra14b] Prall M et al., ‘Reproducible immobilization for porcine heart irradiations’, GSI Scientific Report, 2014

[Pra15] Prall M et al., ‘Treatment of arrhythmias by external charged particle beams: A Langendorff feasibility study’, Biomedizinische Technik, **vol. 60(2)**, pp. 147–156, 2015

[Pre10] Prech M et al., 'Apoptosis as a Mechanism for the Elimination of Cardiomyocytes After Acute Myocardial Infarction', American Journal of Cardiology, **vol. 105(9)**, pp. 1240–1245, 2010

[Pri15] Priegnitz M et al., 'Detection of mixed-range proton pencil beams with a prompt gamma slit camera', Physics in Medicine and Biology, **vol. 60(12)**, pp. 4849–4871, 2015

[PTC] PTCOG, https://www.ptcog.ch, assessed 2016/11/04

[Rah14] Rahman F et al., 'Global epidemiology of atrial fibrillation', Nature Reviews Cardiology, **vol. 11(11)**, pp. 639–654, 2014

[Raw91] Rawlins GJE, Foundations of Genetic Algorithms, vol. 21, 1991

[Ray] Raysearch, https://raysearchlabs.com/press/?year=2013&cisionid=1301095, assessed 2016/11/04

[Red07] Reddy V et al., 'Prophylactic Catheter Ablation for the Prevention of Dfibrillator Therapy', The New England Journal of Medicine, **vol. 357(26)**, pp. 2657–2665, 2007

[Rei94] Reinelt G, The Traveling Salesman: Computational Solutions for TSP Applications, vol. 840, 1994

[Rey99] Rey D et al., 'Automatic Detection and Segmentation of Evolving Processes in 3D Medical Images: Application to Multiple Sclerosis', Information Processing in Medical Imaging, **vol. 1613**, pp. 154–167, 1999

[Rica] Richter D, Personal Communication, 2016/10/16

[Ricb] Richter D et al., 'ECG-based 4D dose reconstruction of carbon ion beam cardiac ablation in a pig model', In preparation

[Ric12] Richter D, 'Treatment Planning for tumors with residual motion in scanned ion beam therapy', Ph.D. thesis, TU Darmstadt, 2012

[Ric13] Richter D et al., 'Upgrade and benchmarking of a 4D treatment planning system for scanned ion beam therapy.', Medical Physics, **vol. 40(5)**, p. 51722, 2013

[Ric14] Richter D et al., 'Residual motion mitigation in scanned carbon ion beam therapy of liver tumors using enlarged pencil beam overlap', Radiotherapy and Oncology, **vol. 113(2)**, pp. 290–295, 2014

[Rön95] Röntgen WC, 'Über eine neue Art von Strahlen', Sitzungsberichte der Physikalisch-Medizinischen Gesellschaft Würzburg, 1895

[Ros52] Rossi BB, 'High energy particles', Prentice Hall, New York, 1952

[Ros15] Rossi S, 'The National Centre for Oncological Hadrontherapy (CNAO): Status and perspectives', Physica Medica, **vol. 31(4)**, pp. 333–351, 2015

[Sag13] Sag CM et al., 'Ionizing radiation regulates cardiac Ca handling via increased ROS and activated CaMKII', Basic Research in Cardiology, **vol. 108(6)**, 2013

[Sal12] Salama J et al., 'Stereotactic body radiotherapy treatment of extracranial metastases', Nature Reviews Clinical Oncology, **vol. 9(11)**, pp. 654–665, 2012

[Sat07] Sato S et al., 'Dynamic intensity control system with RF-knockout slow-extraction in the HIMAC synchrotron', Nuclear Instruments and Methods in Physics Research, Section A: Accelerators, Spectrometers, Detectors and Associated Equipment, **vol. 574(2)**, pp. 226–231, 2007

[Sch97] Scholz M et al., 'Computation of cell survival in heavy ion beams for therapy', Radiation and Environmental Biophysics, **vol. 36(1)**, pp. 59–66, 1997

[Sch10] Schardt D et al., 'Heavy-ion tumor therapy: Physical and radiobiological benefits', Reviews of Modern Physics, **vol. 82(1)**, pp. 383–425, 2010

[Sch11] Schömers C, 'Entwicklung einer dynamischen Intensitätsregelung für das Heidelberger Ionenstrahl-Therapiesynchrotron', Ph.D. thesis, University Frankfurt, 2011

[Sch14] Schwaab J et al., 'Ultrasound tracking for intra-fractional motion compensation in radiation therapy', Physica Medica, **vol. 30(5)**, pp. 578–582, 2014

[Sch15] Schömers C et al., 'The intensity feedback system at Heidelberg Ion-Beam Therapy Centre', Nuclear Instruments and Methods in Physics Research Section A: Accelerators, Spectrometers, Detectors and Associated Equipment, **vol. 795**, pp. 92–99, 2015

[SE07] Schulz-Ertner D et al., 'Effectiveness of Carbon Ion Radiotherapy in the Treatment of Skull-Base Chordomas', International Journal of Radiation Oncology Biology Physics, **vol. 68(2)**, pp. 449–457, 2007

[Sec09] Seco J et al., 'Breathing interplay effects during proton beam scanning: simulation and statistical analysis', Physics in Medicine and Biology, **vol. 54(14)**, pp. 283–294, 2009

[See12] Seemann I et al., 'Irradiation induced modest changes in murine cardiac function despite progressive structural damage to the myocardium and microvasculature', Radiotherapy and Oncology, **vol. 103(2)**, pp. 143–150, 2012

[Sen98] Sengoku H et al., 'A fast TSP solver using GA on JAVA', in Proc 3rd Int Symp Artif Life and Robot, 283–288, 1998

[Ser47] Serber R, 'Nuclear Reactions at High Energies', Physical Review, **vol. 72(11)**, pp. 1114–1115, 1947

[Sha10a] Shackleford JA et al., 'On developing B-spline registration algorithms for multi-core processors.', Physics in Medicine and Biology, **vol. 55(21)**, pp. 6329–6351, 2010

[Sha10b] Sharma A et al., 'Noninvasive stereotactic radiosurgery (CyberHeart) for creation of ablation lesions in the atrium', Heart Rhythm, **vol. 7(6)**, pp. 802–810, 2010

[Sim10] Simoniello P et al., ‘Responses to cadmium intoxication in the liver of the wall lizard Podarcis sicula’, Comparative Biochemistry and Physiology - C Toxicology and Pharmacology, **vol. 151(2)**, pp. 194–203, 2010

[Slø04] Slørdahl SA et al., ‘Atrioventricular plane displacement in untrained and trained females’, Medicine and Science in Sports and Exercise, **vol. 36(11)**, pp. 1871–1875, 2004

[Son08] Sonke JJSJ et al., ‘Variability of Four-Dimensional Computed Tomography Patient Models’, International Journal of Radiation Oncology Biology Physics, **vol. 70(2)**, pp. 590–598, 2008

[Ste03] Stevens C et al., ‘Ventricular mechanics in diastole: Material parameter sensitivity’, Journal of Biomechanics, **vol. 36(5)**, pp. 737–748, 2003

[Ste12] Steidl P, ‘Gating for scanned ion beam therapy’, Ph.D. thesis, TU Darmstadt, 2012

[Tao16] Tao B et al., ‘Preclinical modeling and multimodality imaging of chronic myocardial infarction in minipigs induced by novel interventional embolization technique’, EJNMMI Research, **vol. 6(1)**, 2016

[Tha12] Thariat J et al., ‘Past, present, and future of radiotherapy for the benefit of patients’, Nature Reviews Clinical Oncology, **vol. 10(1)**, pp. 52–60, 2012

[Tro05] Trofimov A et al., ‘Temporo-spatial IMRT optimization: concepts, implementation and initial results.’, Physics in Medicine and Biology, **vol. 50(12)**, pp. 2779–98, 2005

[Unk04] Unkelbach J et al., ‘Inclusion of organ movements in IMRT treatment planning via inverse planning based on probability distributions.’, Physics in Medicine and Biology, **vol. 49(17)**, pp. 4005–4029, 2004

[Unk07] Unkelbach J et al., ‘Accounting for range uncertainties in the optimization of intensity modulated proton therapy.’, Physics in Medicine and Biology, **vol. 52(10)**, pp. 2755–2773, 2007

[Var77] Varma MN et al., ‘Radial dose, LET, and W for 16O ions in N2 and tissue-equivalent gases.’, Radiation Research, **vol. 70(3)**, pp. 511–518, 1977

[VT] VT, assessed 2016/11/04

[Web] Weber U, Personal Communication, 2016/11/14

[Web99] Weber U et al., ‘Design and construction of a ripple filter for a smoothed depth dose distribution in conformal particle therapy.’, Physics in Medicine and Biology, **vol. 44(11)**, pp. 2765–2775, 1999

[Web00] Weber U et al., ‘Depth scanning for a conformal ion beam treatment of deep seated tumours.’, Physics in Medicine and Biology, **vol. 45(12)**, pp. 3627–3641, 2000

[Whe08] Whelan TJ et al., ‘Clinical Experience Using Hypofractionated Radiation Schedules in Breast Cancer’, Seminars in Radiation Oncology, **vol. 18(4)**, pp. 257–264, 2008

[Whe10] Whelan TJ et al., 'Long-term results of hypofractionated radiation therapy for breast cancer.', The New England Journal of Medicine, **vol. 362(6)**, pp. 513–520, 2010

[Wil46] Wilson RR, 'Radiological use of fast protons.', Radiology, **vol. 47**, pp. 487–491, 1946

[Wis12] Wissner E et al., 'Catheter ablation of ventricular tachycardia in ischaemic and non-ischaemic cardiomyopathy: Where are we today? A clinical review', European Heart Journal, **vol. 33(12)**, 2012

[Wöl14] Wölfelschneider J et al., 'Quantification of an external motion surrogate for quality assurance in lung cancer radiation therapy', BioMed Research International, **vol. 2014**, 2014

[Wol16] Wolf M et al., 'Non linear robust optimization methods for (4D) treatment planning in carbon ion therapy', 4D Treatment Planning Workshop, 2016

[Zac97] Zacharias T et al., 'Acute response of pig skin to irradiation with 12C-ions or 200 kV X-rays.', Acta Oncologica, **vol. 36(6)**, pp. 637–642, 1997

[ZB14] Zoni-Berisso M et al., 'Epidemiology of atrial fibrillation: European perspective', Clinical Epidemiology, **vol. 6**, p. 213, 2014

[Zie99] Ziegler JF, 'The Stopping of Energetic Light Ions in Elemental Matter', Journal of Applied Physics, **vol. 85(1999)**, pp. 1249–1272, 1999

Publications related to this work

Peer-reviewed articles

H.I. Lehmann, C. Graeff, P. Simoniello, A. Constantinescu, M. Takami, P. Lugenbiel, D. Richter, **A. Eichhorn** , M. Prall , R. Kaderka, F. Fiedler , S. Helmbrecht, C. Fournier, N. Erbeldinger, A.-K. Rahm, R. Rivinius, D. Thomas, H. Katus, S. Johnson, K. Parker, J. Debus, S. Asirvatham, C. Bert , M. Durante, D. Packer, *Feasibility Study on Cardiac Arrhythmia Ablation Using High-Energy Heavy Ion Beams*, **vol 6**, Nature Scientific Reports, 2016

GSI scientific reports

A. Eichhorn, S. Hild, K. Anderle, C. Graeff, *Speed-up of scanned beam particle therapy by splitting iso-energy slices to optimize particle beam intensities*, GSI Scientific Report, 2015

Conference contributions

A. Eichhorn, A. Constantinescu, H.I. Lehmann, D. Richter, M. Prall, R. Kaderka, P. Lugenbiel, M. Takami, S. Helmbrecht, F. Fiedler, C. Bert, D. Thomas, M. Durante, D. L. Packer, C. Graeff, *Treatment planning for an experimental validation of non-invasive cardiac ablation with scanned carbon ions in a pig model*, 4D Treatment Planning Workshop, 2014, Poster Presentation

A. Eichhorn, A. Constantinescu, H.I. Lehmann, P. Lugenbiel, M. Takami, D. Richter, M. Prall, R. Kaderka, D. Thomas, C. Bert, D.L. Packer, M. Durante and C. Graeff, *Treatment planning study for non-invasive cardiac arrhythmia ablation with scanned carbon ions in an animal model*, AAPM, 2015, Oral Presentation

A. Eichhorn, A. Constantinescu, H.I. Lehmann, P. Lugenbiel, M. Takami, D. Richter, M. Prall, R. Kaderka, D. Thomas, C. Bert, D.L. Packer, M. Durante and C. Graeff, *Planungsstudie zur nicht-invasiven Ablation von Herzrhythmusstörungen mit einem gescannten Kohlenstoffstrahl*, DGMP, 2015, Oral Presentation

A. Eichhorn, S. Hild, K. Anderle, C. Graeff, *Speed-up of plan delivery for intensity modulated particle therapy by splitting iso-energy slices according to beam intensity levels*, PTCOG, 2016, Poster Presentation

A. Eichhorn, S. Hild, C. Graeff, *Untersuchung des Einflusses einer dynamischen Intensittskontrolle auf mehrfachbestrahlte 4D Pläne von Lungenkrebspatienten*, DGMP, 2016, Oral Presentation

A. Eichhorn, S. Hild, J. Naumann, *Fast rescanning strategies for hypofractionated therapy*, 4D Treatment Planning Workshop, 2016, Poster Presentation

Lebenslauf

Persönliche Daten

Name	Anna Vera Eichhorn
Geburtstag	10.02.1989
Geburtsort	Heppenheim

Ausbildung und Werdegang

seit 2010	**Technische Universität Darmstadt** Promotion
seit 2010	**GSI Helmholtzzentrum** Wissenschaftliche Hilfskraft
2011 - 2013	**Technische Universität Darmstadt** Master of Science in Physik Masterarbeit ’*Invesitgation of dose profile inhomogeneities at the interface between water and bone-like materials following irradiation with therapeutic carbon ions*’
2010 - 2011	**University of Bristol, UK** Erasmusaufenthalt
2008 - 2011	**Technische Universität Darmstadt** Bachelor of Science in Physik Bachelorarbeit ’*Attenuation of carbon ion in bone-like material*’
1999 - 2008	**Liebfrauenschule Bensheim** (Gymnasium)
1995 - 1999	**Wingertsberg Schule Lorsch** (Grundschule)

Nebentätigkeiten

2011 - 2015	Übungsleitung und Organisation der Veranstaltung ’*Physik für Biologen*’
2008 - 2013	Aktives Mitglied der Fachschaft Physik

Danksagungen

Bedanken möchte ich mich zuallererst bei all den Menschen, die zum Gelingen dieser Arbeit beigetragen haben. Mein Dank gilt vor allem Marco Durante, der mich mit offenen Armen in der Abteilung Biophysik aufgenommen hat und es mir ermöglicht hat an spannenden Forschungsprojekten zu arbeiten. Ganz besonders bedanken möchte ich mich bei Christian Graeff. Danke für die freundliche Aufnahme in das Motion Team und die Möglichkeit der Mitarbeit am Schweineexperiment. Danke auch, für deine Geduld und Ratschläge ohne die das Gelingen dieser Arbeit nicht möglich gewesen wäre. Und nochmals danke, für die vielen Möglichkeiten auf Konferenzen und an der NASA Summer School teilzunehmen. Außerdem möchte ich mich auch bei Thomas Aumann für die Übernahme des Zweitgutachtens bedanken.

Danke sagen möchte ich auch all denen Menschen, die mir die Zeit an der GSI so angenehm gemacht haben, nämlich all meinen Büromitbewohnern der letzten 6 Jahre. Ein weiteres Danke geht an die gesamten Mitglieder der Abteilung Biophysik, die eine sehr angenehme Arbeitsatmosphäre ermöglicht haben. Vor allem möchte ich mich auch bei den Sekretärinnen Maria Didonna-Schnellbächer und Julia Bellartz für ihre Arbeit und Unterstützung in allen Lebenslagen bedanken. Ein besonderes Danke geht an Stefan Schulz, Kristjan Anderle, Christian Graeff, Julia Wiedemann und Moritz Wolf für das geduldige Korreketurlesen dieser Arbeit! Ohne euch würde es immer noch von kleinwüchsigen Sections, kranken Überschriften und Schweinen in der Stadtmitte wimmeln! Bei Kristjan Anderle möchte ich mich auch für seine Hilfe beim Umgang mit Slicer bedanken. Ohne dich wären die ganzen Registrierungen, Auswertungen und Bilder nicht halb so schnell fertig geworden! Außerdem möchte ich Stefan Schulz für die Unterstützung beim Programmieren und seine Geduld danken. Ein Danke geht auch an alle aktuellen, ehemaligen und assoziierten Mitglieder des Motion Teams und der Mittagsessensgruppe, für die nette Zusammenarbeit und die kurzweiligen und abwechslungsreichen Mittagspausen. Auch dem gesamten '*SchweineTeam*' möchte ich ein großes Danke für diese unvergessliche Zeit aussprechen. Ihr alle habt maßgeblich dazu beigetragen, dass in dieser arbeitsintensiven Zeit der Spaß nie zu kurz kam! Danke Immo, für die unzähligen Konturen! Ein großes Danke geht auch an Daniel Richter, der mit seiner Erfahrung immer wieder wichtige Hinweise geben konnte und einen großen Anteil am Gelingen dieser Arbeit hat. Ganz besonders bedanken möchte ich auch bei Patrick Lugenbiel, der mir vor allem in der Endphase dieser Arbeit den nötigen Input aus medizinischer Sicht geben konnte. Danke dafür!

Bedanken möchte ich mich bei Stephan Brons, der bei mehreren Strahlzeiten immer unterstützend mitgewirkt hat und den reibungslosen Ablauf der Experiment unterstützt hat. Danke sagen möchte ich auch Jakob Naumann, der seine Bibliotheken für diese Arbeit zu Verfügung gestellt hat, immer ein offenen Ohr für Fragen hatte und die Experimente in Heidelberg unterstützt hat.

Bedanken möchte ich mich auch bei meinen Freunden für das Verständnis in stressigen Zeiten. Ein großes Dankeschön geht auch an die Ex-Unilerngruppe! Ohne euch wäre das Studium deutlich zäher und langweiliger gewesen!

Danken möchte ich auch bei meiner Famile, die mich immer unterstützt hat und mir gerade in stressigen Zeiten den Rücken freigehalten hat. Ein besonderes Dank geht auch an Stefan, der mich auch in stressigen Zeiten ertragen musste und der es immer geschafft hat mir wieder Mut zu machen und mich zu motivieren weiter meine Ziele zu verfolgen.

Erklärung zur Dissertation

Hiermit versichere ich, die vorliegende Dissertation ohne Hilfe Dritter nur mit den angegebenen Quellen und Hilfsmitteln angefertigt zu haben. Alle Stellen, die aus Quellen entnommen wurden, sind als solche kenntlich gemacht. Diese Arbeit hat in gleicher oder ähnlicher Form noch keiner Prüfungsbehörde vorgelegen.

Darmstadt, den March 10, 2017

(Anna Vera Eichhorn)